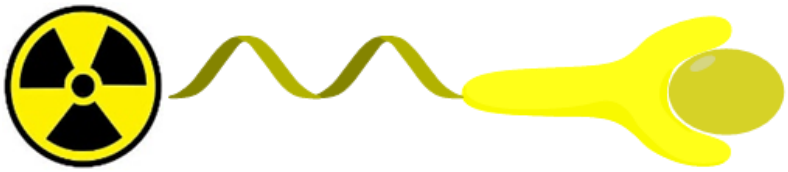
KU Leuven
Biomedical Science Group
Faculty of Pharmaceutical Sciences
Department of Pharmaceutical and Pharmacological Sciences

Development and preclinical evaluation of ^{161}Tb radiopharmaceuticals for cancer treatment



Irwin Cassells

In collaboration with

sck cen

Supervisory committee

Promotor	:	Prof. Dr. Frederik Cleeren
Co-promotors	:	Prof. Dr. Guy Bormans Prof. Dr. Thomas Cardinaels
SCK CEN mentor	:	Dr. Maarten Ooms
Jury Members	:	Prof. Dr. Sergei Strelkov Dr. Nick Geukens Dr. Kim Serdons Prof. Dr. Cristina Müller Prof. Dr. François Guêrard

Dissertation presented in partial fulfilment of the requirements for the degree of Doctor in Biomedical Sciences

Abbreviations

2-PMPA	:	2-(phosphonomethyl)pentanedioic acid
c-Met	:	Mesenchymal-epithelial transition factor
CT	:	Computed tomography
Da	:	Daltons
DFO	:	Desferrioxamine B
DNA	:	Deoxyribonucleic acid
DOTA	:	2,2′,2″,2‴-(1,4,7,10-tetraazacyclododecane-1,4,7,10-tetrayl)tetraacetic acid
DTPA	:	Diethylenetriaminepentaacetic acid
DTT	:	Dithiothreitol
EBRT	:	External beam radiation therapy
EC	:	Electron capture
EDTA	:	Ethylenediaminetetraacetic acid
EMA	:	European Medicines Agency
EMR	:	Electromagnetic radiation
ESI	:	Electrospray ionisation
FAPI	:	Fibroblast activated protein inhibitor
FBS	:	Fetal bovine serum
FDA	:	U.S Food and Drug Administration
[^{18}F]FDG	:	2-[^{18}F]Fluoro-2-deoxy-D-glucose
HER-2	:	Human epidermal growth factor receptor-2
HGF	:	Human growth factor
HPIC	:	High-pressure ion chromatography
HPLC	:	High-performance liquid chromatography
HSA	:	Human serum albumin
IT	:	Isomeric transition
iTLC	:	Instant thin-layer chromatography
LET	:	Linear energy transfer
m/z	:	mass/charge
mCRPC	:	Metastatic castration-resistant prostate cancer
MS	:	Mass spectrometry
MTS	:	3-(4,5-dimethylthiazol-2-yl)-5-(3-carboxymethoxyphenyl)-2-(4-sulfophenyl)-2H-tetrazolium
MTT	:	3-(4,5-dimethylthiazol-2-yl)-2,5-diphenyltetrazolium bromide
NETA	:	[4-[2-(bis-carboxymethyl-amino)-ethyl]-7-carboxymethyl-[1,4,7]triazonan-1-yl]-acetic acid

NOTA	:	1,4,7-triazacyclononane-1,4,7-triacetic acid
PET	:	Positron emission tomography
PRRT	:	Peptide receptor radionuclide therapy
PSMA	:	Prostate specific membrane antigen
RTK	:	Receptor tyrosine kinase
SPECT	:	Single photon emission computed tomography
SROSEM	:	Similarity-regulated ordered subsets expectation maximisation
SUV	:	Standardised uptake value
TAT	:	Targeted alpha therapy
TFA	:	Trifluoroacetic acid
TOF	:	Time-of-flight
TRNT	:	Targeted radionuclide therapy
v_HH	:	Variable domain heavy chain only

Acknowledgements

Firstly, I would like to start off expressing my gratitude to my supervisors, Prof. Dr. Frederik Cleeren, Prof. Dr. Guy Bormans, Dr. Maarten Ooms and Prof. Dr. Thomas Cardinaels for their advice and guidance throughout the project. I will never forget the knowledge and guidance you have shared with me, and for that, I am eternally grateful. Thank you for being patient with me, even through difficult times. I will miss all the informal meetings, lunches, sports, talks, and especially, the friendship with you. Additionally, I would like to thank my supervisory committee for their patience and contributions over the years of the project.

I would also like to extend my gratitude to Julie Cornelis, Koen Vermeulen, Michiel Van de Voorde, Andrew Burgoyne, Stephen Ahenkorah, Terrence Tshibangu, Nathalie Heynickx and Sunay Perez for all the assistance to the work performed in this thesis – a true "from atom to scanner bedside" piece of work. The work done in this project was a truly collaborative effort, and I have a lot to thank you for. Additionally, contributions from Pieter Haspeslagh, Ivan Sannen, Jeroen Peetroons, Sofie Celen, Noami Daems, Anthony Waked, Charlotte Segers and Amelie Coolkens are also very appreciated, and I thank you all.

I also would like to thank all the wonderful people I have met in the two research groups I was a part of: Radiopharmaceutical Research Group from KU Leuven and NURA team from SCK CEN. You have made a difficult and troubling journey a very pleasant one, and I would love to thank you for that. I also would love to thank all my friends I have made on this journey, namely Pol Laanen, Meng Li, Magy Salam, Stephen Ahenkorah, Terrence Tshibangu, Nathalie Heynickx, Anthony Waked, Diana Melis, Tom Lemaitre, Tomas Opsomer. Thank you so much for all the memories – and hopefully more to come.

During my time in Lisbon (chapter 4 work), I met some incredible people who took care of me and taught me so much from radiochemistry to culture. I thank Prof. Antonio Paulo, Prof. Filipa Mendes, Dr Celia Fernandes, Dr Paula Rasposinho, Ms Ana Rita Juliao and Ms Caterina Pinto for an amazing experience in Lisbon and thank you for all your help in the project.

This project, and this degree will not have been possible without the funding and support from SCK CEN and FWO. I would love to thank both establishments for their financial contributions and their support throughout the project. Additionally, I would like to extend my many thanks to Prof. Dr Thomas Cocolios and Prof. Dr Christophe Deroose (MD) for their contributions to the project, as supervisory members in the FWO: Tb IRMA-V project.

Lastly, and most importantly, I would like to thank my family, friends (Tavon, Remano, Muneebah, Shakeela) and Tameryn Stringer for all your support, care and love throughout this stressfully-joyous time in life. And for always being there for me – especially through the ups and downs. And I would like to thank 2018-2022 Irwin, for making this journey from South Africa to a foreign country, with a different culture, different language, pushing through all the trials and tribulations, and making it out at the end.

Table of Contents

Abbreviations ii

Acknowledgements iv

Chapter 1: General Introduction Targeted Radionuclide Therapy

1.1 Cancer and Active Treatment Avenue 1

1.1.1 Cancer 1

1.1.2 Current Treatment Strategies 1

1.2 Nuclear Medicine and Targeted Radionuclide Therapy 5

1.2.1 Radionuclides in radiopharmaceuticals 6

1.2.2 Attaching radionuclides to carrier molecule 14

1.2.3 Carriers used in radiopharmaceuticals 20

1.3 Theragnostic Approach 27

1.3.1 Homonuclear pairs 28

1.3.2 Heteronuclear pairs 28

1.3.3 Terbium Radionuclides for Medical Applications 29

1.4 References 33

Objectives 51

Chapter 2: Radiolabelling of human serum albumin with terbium-161 using mild conditions and evaluation of *in vivo* stability

2.1 Introduction 55

2.2 Material and Methods 57

2.2.1 Materials 57

2.2.2 Animals 58

2.2.3 Instrumentation and Characterisation 58

2.2.4 Production of [^{161}Tb]$TbCl_3$ 58

2.2.5 Human serum albumin (HSA) ligand constructs 59

2.2.6 Radiolabelling studies with [^{161}Tb]$TbCl_3$ 59

2.2.7 *In vitro* stability studies 60

2.2.8 Biodistribution studies 60

2.2.9 Statistical analysis 61

2.3 Results 61

2.3.1 Optimisation of radiolabelling conditions for low temperature labelling 61

2.3.2 In vitro stability of radiolabelled ligands 61

2.3.3 Synthesis, radiolabelling and in vitro stability of human serum albumin conjugates. 63

2.3.4 *Ex vivo* biodistribution of [^{161}Tb]$TbCl_3$ and ^{161}Tb-labeled HSA-conjugates. 64

2.4 Discussion 67

2.5 Conclusion 70

2.6 Ethical statement 70

2.7 Conflict of Interest 70

2.8 Supplementary information 70

2.9 References 70

Chapter 3: Preclinical evaluation of a terbium-161 labelled half-life extended anti-c-Met nanobody (v_HH)

3.1 Introduction 75

3.2 Materials and Methods 77

3.2.1 General 77

3.2.2 Animal Studies 78

3.2.3 Instrumentation and Characterisation 78

3.2.4 Isotope production 78

3.2.5 Synthesis of compounds 79

3.2.6 Radiolabelling 80

3.2.7 Cell binding of [^{161}Tb]Tb-DOTA-GA-v_HH 80

3.2.8 Cell viability and cytotoxicity screening 81

3.2.9 Clonogenic survival assay 82

3.2.10 Ex vivo biodistribution 82

3.2.11 µ-SPECT/ CT scans 82

3.2.12 Statistical Analyses 83

3.3 Results and Discussion 84

3.3.1 Conjugation and Radiolabelling with [^{161}Tb]$TbCl_3$ 84

3.3.2 Cell binding 85

3.3.3 In vitro cell viability 87

3.3.4 Clonogenic assays 88

3.3.5 *Ex vivo* biodistribution 90

3.3.6 µSPECT/ CT scans 92

3.4 Conclusion 95

3.5 Conflict of Interest Declaration 95

3.6 Ethical Statement 95

3.7 Acknowledgements 96

3.8 References 96

Chapter 4: Auger electron therapy of prostate cancer using ^{111}In and ^{161}Tb labelled compounds targeting the mitochondria of prostate specific membrane antigen (PSMA) overexpressing cells

4.1 Introduction 103

4.2 Material and Methods 105

4.2.1 General 105

4.2.2 Instrumentation and Characterisation 105

4.2.3 Cell Culture 107

4.2.4 Radioisotopes 107

4.2.5 Complexation reactions with $^{nat}InCl_3$ and $^{nat}TbCl_3$ 108

4.2.6 Radiolabelling with [^{111}In]$InCl_3$ and [^{161}Tb]$TbCl_3$ 108

4.2.7 Partition coefficient 109

4.2.8 In vitro stability studies 109

4.2.9 Cell and competitive binding assays 109

4.2.10 Mitochondria Uptake Assay 109

4.2.11 Cell viability assay 110

4.2.12 Clonogenic assay 110

4.2.13 Tumour inoculation 111

4.2.14 SPECT/CT scans and Image processing and analysis 111

4.2.15 Statistical analysis 111

4.3 Results and Discussion 112

4.3.1 Complexation with natural terbium chloride and indium chloride 112

4.3.2 Radiolabelling with [^{161}Tb]$TbCl_3$ and [^{111}In]$InCl_3$ and *in vitro* stability 113

4.3.3 Cell binding and sub-cellular uptake 113

4.3.4 Cell viability 117

4.3.5 Clonogenic Assay 117

4.3.6 Mechanism of action 119

4.3.7 µ-SPECT/CT imaging 122

4.4 Conclusion 125

4.5 Funding 125

4.6 Ethical Statement 125

4.7 Acknowledgements 125

4.8 References 126

Chapter 5: Terbium Radiopharmaceuticals: A perspective of the advances towards routine clinical application

5.1 General Discussion 131

5.2 References 140

Summary/Samenvatting 147

CV 153

Chapter 1 – General Introduction Targeted Radionuclide Therapy

1.1 Cancer and Active Treatment Avenues

1.1.1 Cancer

Tumours are cell masses characterised by uncontrolled cell growth (1). Tumours occur due to genetic interference with cell mitigation processes, causing growth of abnormal cellular masses. In many cases, cancer cells migrate to remote regions or invade nearby tissues, making treatment complicated. The five main types of cancers are carcinoma, sarcoma, leukaemia, lymphoma/myeloma and central nervous system cancers (2). During cancer progression, tumours can become highly heterogeneous, whereby a mixed population of cell types congregate (3). This heterogeneity is one of the key factors responsible for the development of treatment-resistant phenotypes (3), which make managing/treatment of the cancer complicated. Better diagnostic techniques improve early-stage detection of cancers, aiding the efficacy of available therapies. In addition, development of new and advanced therapeutic tools to treat cancers have shown a positive effect on patient survival. Herein, we discuss the current class of therapeutic techniques employed in oncology.

1.1.2 Current Treatment Strategies

Removal of tumours

Until now, the most common treatment strategy is the surgical removal of the tumour (4–6). Surgery is the first line of treatment, as large portions of the tumour can be removed, limiting the chance of metastasis. Often, surgery is not a viable option due to the location of the tumour (e.g. some brain tumours), or due to the presence of metastatic lesions (7). Additionally, surgery might leave microscopic cancer tissues in the surgical cavity, resulting in the recurrence of cancers. To avoid the recurrence of the cancer, combination therapies are used (4–6).

Though traditional scalpel-based surgery is used for large tumours, more advanced techniques have been developed for a higher precision removal of tumours (8–10):

- **Ablation therapies**. Ablation therapy involves the heating or freezing of the tumour tissue, or precancerous tissues (cells which grow abnormally causing appearance to be different than normal cells), which causes the cells to die. This method is effective in skin-related cancers since application of the cooling or heating source can be done effectively. The disadvantage of this therapy is it can often lead to irreparable scar tissue. Moreover, the extreme temperatures used can affect neighbouring cells and blood vessels, resulting in bleeding or to post-surgical infections.

- **Laser surgery.** Light beams are used to focus on small tumour lesions which cannot be targeted with traditional surgical tools. One advantage of using lasers is that blood vessels can be cauterised with the laser, preventing excessive blood loss during surgery.

Chemotherapy

Chemotherapy is a treatment strategy which use non-endogenous chemical reagents. Some of the first chemotherapy reagents were discovered in the early 1900s, where patients exposed to nitrogen mustard gas (chloroethylamine derivatives) had lowered leukocyte levels (3,6,7,11). In later years, pharmaceuticals with more direct mechanism of action were developed, which spearheaded the acceptance and administration of chemotherapeutics in the medicinal world (7,12). Because it is a systemic treatment, chemotherapy is a viable option for metastatic lesions, which can be troublesome to remove using surgical methods. Chemotherapy is also often used as an adjuvant therapy after surgery or radiation-based therapies (7,13). Conventional pharmaceuticals often don't selectively target cancer cells, leading to many side effects such hair loss, mild arthritis, general weakness and nausea (14,15). In recent years, the target-specificity of the pharmacophores have been improved, reducing the side effects often associated with chemotherapy. Additionally, to restore blood cell regeneration, which is often reduced due to treatments, stem cell transplants are performed to aid in the natural response to cancer treatment.

Immunotherapy

Immunotherapy is a type of cancer treatment which involves assisting or catalysing immune system responses to cancer. Several cancers are currently treated successfully using immunotherapy. The first immunotherapy target LAG-3 is currently used to treat advanced melanoma (7,16). There are various strategies within immunotherapy:

- **Immune checkpoint inhibitors.** Pharmaceuticals are introduced to block receptors which inhibit the potency of T-cells, causing the effect of T-cells to be more potent. Two common targets are CTLA-4 and PD-L1 (17), which cancer cells use to diminish the natural immune response to cancers.
- **T-cell transfer therapy.** T-cells are extracted from the individual and replicated in a laboratory. T-cells cannot distinguish between normal and cancer cells, therefore they are genetically modified to target cancer-specific biomarkers such as chimeric antigen receptor T-cells (CAR T-cells). These cells are intravenously reintroduced into the body, which increases the number of T-cells active in the immune response to cancer. This therapy is used in the treatment of leukaemia (16).
- **Monoclonal antibodies/antibodies.** Like T-cell transfer therapy, immune response proteins (such as β-lymphocyte CD20 antigens) are extracted and duplicated in a laboratory, which are

later re-introduced in the patient. These antibodies assist in bringing T-cells in closer proximity to the cancer cell, which increases the potency.

Though often seen as a safer alternative to chemotherapy, immunotherapy also has some disadvantages. In immune checkpoint inhibitor therapy, the immune response could also attack regular, healthy cells, or activate a broader range of immune cells which can have an autoimmune response, resulting in a lower response to treatment (18).

Radiation-based therapies

Radiation therapies have become a vital tool in the arsenal of cancer treatment strategies. One of the most common treatment methods is external beam radiation therapy (EBRT). EBRT is a radiation method which delivers high-energy X-ray, electron beams or gamma radiation to a tumour (19). These radiation beams are usually generated by a linear accelerator (X-ray, electrons), or decay emission from radionuclides such as ^{60}Co (gamma rays). The latter can be used for targeting non-superficial tumours (20). One of the major disadvantages of gamma or X-ray EBRT is the off-target dose to healthy tissues in between the tumour and the radiation source and healthy tissues downstream of the tumour. To overcome this limitation, energy deposits are performed from multiple angles to maximise the accumulative dose in the tumour and minimise the effect in healthy tissue (21). A theoretical example of this can be seen in **Figure 1.1**, where radiation is simulated at 5 different angles, and the accumulative dose is calculated from one of the angles. This results in a significant increase in the dose at the tumour site, where energy pathways cross.

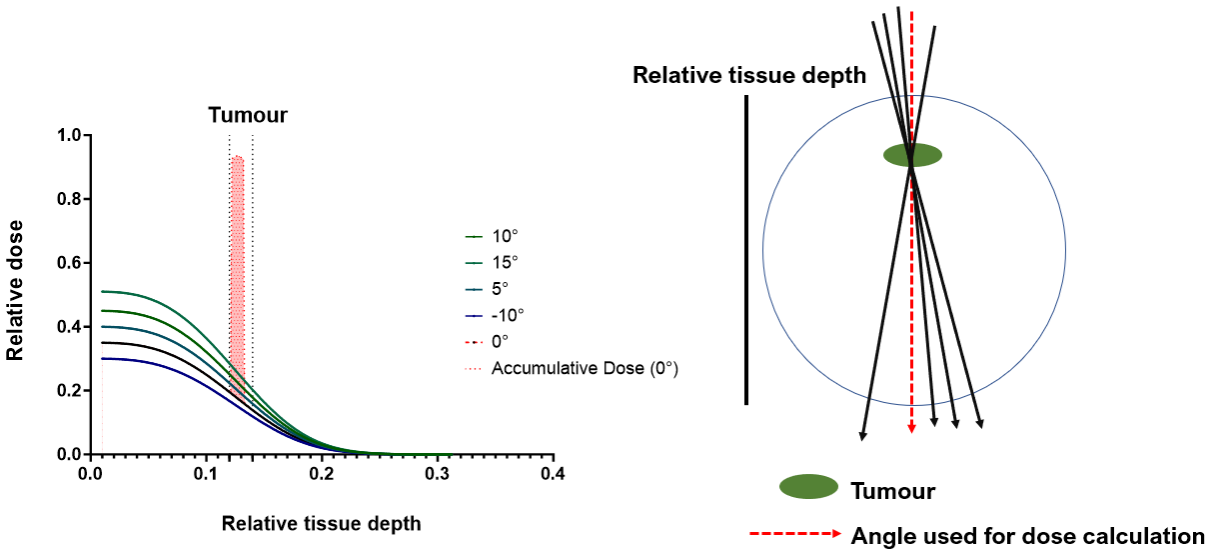


Figure 1.1. A theoretical figure showing the absorbed dose at the tumour site after applying an external radiation dose from 5 different angles. Accumulative dose is calculated along the vertical norm.

To further increase the selectivity with which the radiation dose is deposited in the tumour, heavier particles are used, such as protons (proton therapy) or carbon atoms (heavy-ion therapy) (22). Particles are accelerated and travel through tissue, where the energy gets deposited more selectively to the tumour region. It is important to note that this is also performed from multiple angles to increase efficiency and reducing healthy tissue irradiation (22). In addition, the energy of these particles can be adjusted to deposit the maximum dose at the tumour depth (**Figure 1.2**).

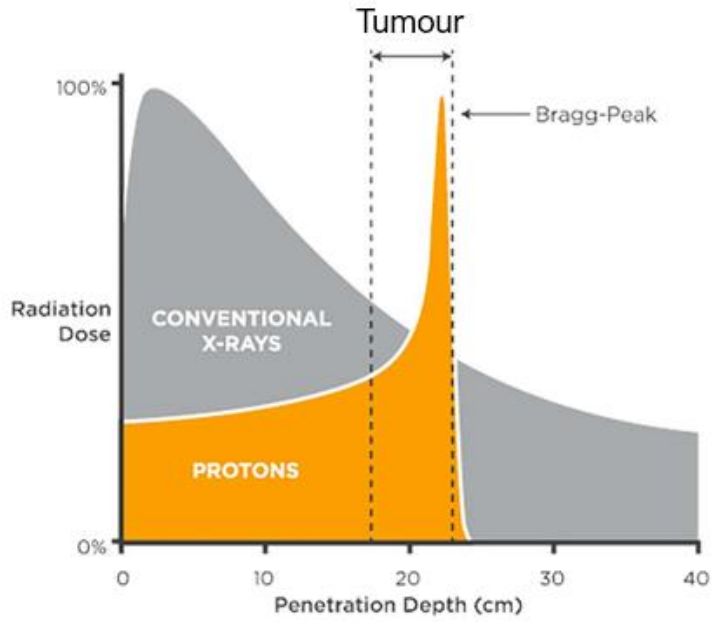


Figure 1.2. A theoretical figure showing the absorbed dose at the tumour site comparing a single irradiation of proton therapy and conventional EBRT. Image used from https://provisionhealthcare.com/about-proton-therapy/advantages-of-proton/ (Accessed on 17 January 2023)

Another approach is to implant a radioactive source in or on the tumour (brachytherapy) to deliver a localised radiation dose to kill the cancer cells in the immediate vicinity (21). This technique has shown to be highly effective against benign tumours found in neck, breast, cervix and eye cancers. In liver cancers, radioactive nanoparticles are injected into the hepatic artery (main supply of blood to tumour cells) and are trapped in the downstream tumour bed capillaries, resulting in a continuous local therapeutic dose. One major drawback of this therapy is the continuous dose delivery to healthy tissue in the vicinity of the implanted radiation source (21,23). Additionally, these methods are only effective against localised tumours, and cannot treat metastases.

Radiation therapies have two distinct effects, the deterministic and the stochastic effect. (24). The deterministic effect which occurs usually shortly after exposure to radiation has a sigmoidal relation with the radiation dose and is characterised by a threshold dose under which the biological effect (e.g. cell

death) is not occurring. Ideally, the radiation dose is deposited should be far above the threshold dose for tumour cells and below the threshold dose for healthy tissues. Ionising radiation will may however also cause stochastic effects which may occur with years of delay such as secondary tumours. The stochastic effect is directly proportional to the dose and does not have a threshold dose (24). Therefore, limiting the dose to healthy tissue and maximising the overall dose to the cancerous cells is of high importance.

Targeted radionuclide therapy (TRNT) is a highly specific radiation therapy which has been proven to be highly effective in clinics (25–27). The overall goal of TRNT is to direct the radiation source as close to cancer cells, whilst limiting the radiation dose received by healthy tissue. This notion is akin to brachytherapy, where a radiation source is implanted in the tumour. But unlike brachytherapy, a radiation source is introduced into the patient via intravenous or oral administration, and with selective molecular interaction to cancerous cells, the radionuclide will accumulate in the tumour and be cleared from other tissues.

1.2 Nuclear Medicine and Targeted Radionuclide Therapy

Using radioactive contrast agents (radiopharmaceuticals), the nuclear medicine imaging techniques single photon emission computed tomography (SPECT) and positron emission tomography (PET) have become useful tools in the diagnosis and follow-up of cancer (28–32). The use of these non-invasive approaches to image the primary tumour, as well as metastatic lesions, has been a crucial feature in the success of nuclear medicine. Additionally, radionuclides that selectively deposit ionising radiation via alpha, beta, or Auger/conversion electron (A/CE) emission to tumours have emerged as viable treatment strategies for cancer (26,33–36).

Radiopharmaceuticals are radioactive drugs which have a certain affinity towards targets in the tumour microenvironment or on the tumour cells to ensure selective accumulation of radioactivity in the target. The general structure of radiopharmaceuticals is illustrated in **Figure 1.3**. The radiopharmaceutical usually consists out of 1) a radionuclide with desired radioactive properties for imaging and/or therapy; 2) a linking group (prosthetic groups for non-metals or chelator for metal radionuclides) that links the radionuclide to the carrier molecule; and 3) a carrier molecule that has high specificity and high affinity for an overexpressed target. In some cases, a distinctive linker and/or carrier group is incorporated into a single framework/element. In very rare cases, radionuclides are administered without being bound to an additional pharmaceutical carrier since the radionuclide in question as such accumulates naturally at a biological target. These molecules often exploit biological processes to direct the radionuclides. For example, in thyroid cancers, Na[$^{123/131}$I]I is given to patients to diagnose or treat hyperthyroidism (37). Because iodine is chemically incorporated in thyroid hormones, a large fraction of [$^{123/131}$I]I$^-$ accumulates

in the thyroid, giving clinicians the ability to diagnose and treat thyroid related diseases. Metal salts, such as $^{223}RaCl_2$ (commercially known as Xofigo®) are currently used in the treatment of bone metastases (38). Similar to calcium, Ra^{2+} readily binds to bone and accumulates in regions of the bone that are characterised by a high bone turnover, from where they irradiate bone metastases tumour cells in their vicinity.

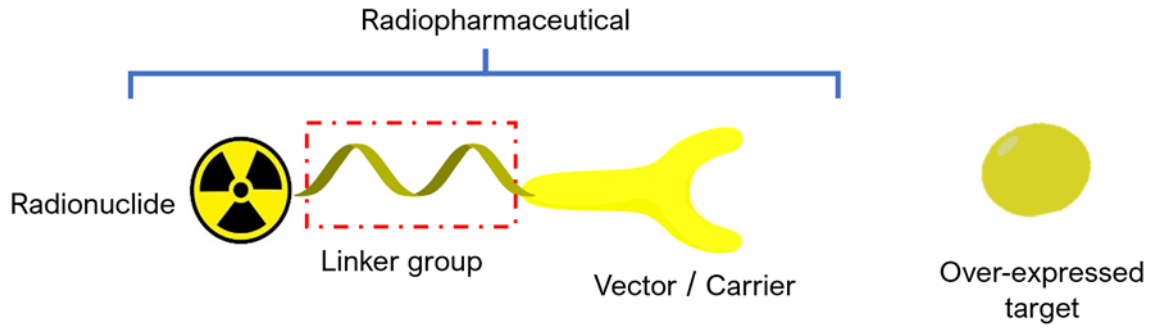


Figure 1.3. General structure of a radiopharmaceutical.

1.2.1 Radionuclides in radiopharmaceuticals

Elements that possess an imbalance in their proton-neutron ratio or exist in a metastable energy state will undergo radioactive decay. Unstable elements decay by releasing particles (α, $\beta^{+/-}$) and/or electromagnetic radiation (gamma ray photons (γ)) and/or secondary X-rays, conversion electrons and/or Auger electrons (39)). Radionuclides are either naturally-occurring, produced in particle accelerators, nuclear reactors or extracted from decay products (generators) (39–41). There are several radionuclides with decay properties suitable for application in radionuclide imaging and/or therapy.

1.2.1.1 Diagnostic radionuclides and applications

Diagnostic radionuclides emit electromagnetic radiation (EMR), in the form of X-rays or gamma rays (γ), which travel out of the body and are detected by a dedicated camera to determine the *in vivo* concentration of the radiopharmaceutical throughout the body. PET and SPECT are two main diagnostic frameworks which are used in the nuclear medicine space. Both these imaging modalities detect gamma radiation (up to 200 keV for SPECT, 511 keV for PET) or high energy X-rays (20-150 keV) to determine the location and the concentration of the radiopharmaceutical *in vivo* (42). It is important to note that PET and SPECT are often coupled with imaging devices that provide anatomical information, such as computed tomography (CT) or magnetic resonance imaging (MRI). Both PET and SPECT can be used in static imaging, where the uptake of the radiopharmaceutical can be determined within a specific time frame after administration. This is usually after a time lapse where the target tissue activity concentration is much higher than its background (high target-to-background ratio). Dynamic imaging acquires data

as a function of time (short time frames) post injection, which allows to determine exact *in vivo* pharmacokinetic parameters such as dissociation constants (K_d) and maximum receptor expression (B_{max}). These pharmacokinetic parameters can be determined by measuring the inverse binding potential at different concentration, which can be fitted to a straight line (Woolf-Hanes plot), with the B_{max} (-x intercept) and K_d (slope) values (43–45). An estimation of this can also be performed *ex vivo* and *in vitro*, however a binding to plasma protein correction needs to be performed. However, dynamic imaging is restricted to PET as the nature of obtaining and processing data on SPECT cameras make that dynamic imaging with high time resolution is difficult.

PET Radionuclides

PET radionuclides have an excess number of protons in the nucleus, making them neutron deficient. The excess proton spontaneously decays into a neutron, a positron (β^+) and neutrino, with the latter two particles being ejected from the nucleus. After slowing down, positrons combine with electrons generating a positronium that will “annihilate”. In the annihilation process, the mass of the electron and positron is converted in two near-coincident (~180°) γ-rays, with a characteristic energy of 511 keV each. A graphical illustration of the general principle of PET detection is provided in **Figure 1.4**. Before this annihilation can occur, the positron travels a short distance, which is proportional to the energy of the positron (46). This distance is crucial in the imaging space since it is important to have the annihilation as close to the target as possible to avoid loss of spatial resolution. A list of common PET radionuclides is provided in **Table 1.1**.

The proton excess is often artificially generated by irradiation of stable elements with protons that are accelerated in a cyclotron (47). Medical cyclotrons enable the on-site production of short-lived PET radionuclides. Radionuclides such as ^{15}O and ^{13}N, have very few radiopharmaceuticals in the clinical space since their short half-life is not compatible with long radiosynthesis procedures (48). ^{18}F-based radiopharmaceuticals are often preferred for their more suited half-life (^{18}F: 109.8 min) and ^{11}C-based radiopharmaceuticals (^{11}C: 20.4 min) are attractive as all organic molecules contain carbon atoms which theoretically can be replaced by carbon-11 (48,49). The most used PET radiotracer in clinic is the glucose analogue [^{18}F]FDG that allows the visualisation of the glucose metabolism, which is high in tumour and brain compared to other tissues (50). One of the major advantages of [^{18}F]FDG is the high amount of activity that can be produced using a medical cyclotron and dedicated synthesis modules, with an average production in low-to-medium terabecquerel range, which can supply multiple clinics in the surrounding area (51). A major disadvantage with [^{18}F]FDG is the high physiological uptake in brain, making diagnosis of brain tumours with [^{18}F]FDG complicated (52). In addition, [^{18}F]FDG also accumulates in inflamed tissues, making it not a highly cancer-specific radiopharmaceutical. Furthermore, no therapeutic [^{18}F]FDG-based radiopharmaceutical is available, limiting the scope of [^{18}F]FDG in the theragnostic space.

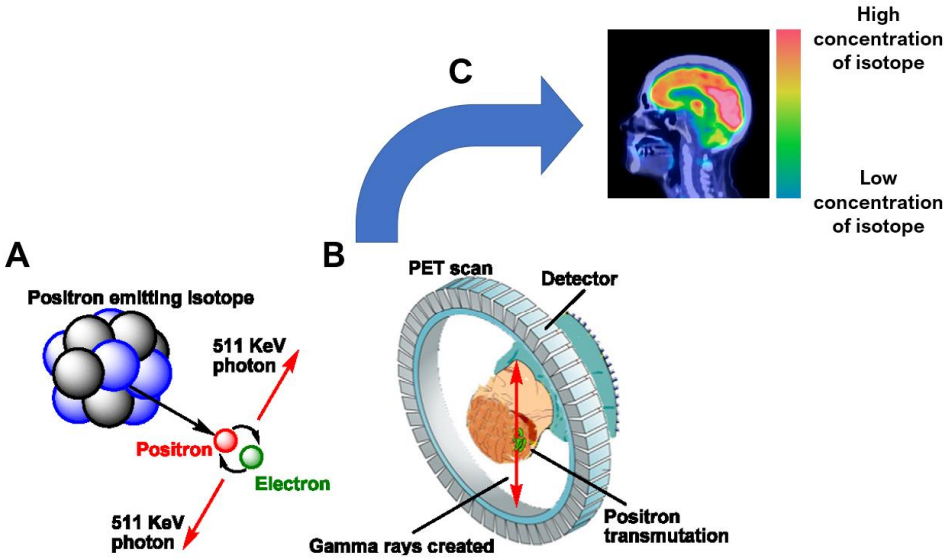


Figure 1.4. Illustration of PET detection principle. **A.** A positron emitting radioisotope emits a positron during the decay, which travels a distance from the nucleus and encounters an electron, forming a positronium which annihilates and of which the mass is converted to two near co-incident gamma rays of 511 keV in energy. **B.** The radiopharmaceutical accumulates in the target tissue and gamma rays are emitted upon decay of the PET radionuclide. These gamma rays are detected by a detector. **C.** The crossover positions of the gamma rays detected are mapped on a volumetric/projection mapping, which can be overlapped with anatomical information, collected from NMR or CT imaging. Images are used from https://innovation.ox.ac.uk/human-brain-pet-scan/ (accessed on 18 January 2023) and Z. Li *et. al.* (53).

Table 1.1. List of common PET radionuclides (39,46,49,54–56)

Radionuclide	Half-life	Production pathway	Decay	Energy ($\beta^+_{avg.}$) (MeV)	Mean positron range in water (mm)
^{15}O	2.0 min	$^{14}N(d,n)^{15}O$	β^+ (100%)	0.735	3.0
^{13}N	9.97 min	$^{16}O(p,\alpha)^{13}N$	β^+ (100%)	0.491	1.8
^{11}C	20.4 min	$^{14}N(p,\alpha)^{11}C$	β^+ (100%)	0.385	1.2
^{68}Ga	67.6 min	$^{68}Ge/^{68}Ga$-generator	β^+ (87%) EC (8.9%)	0.836	3.5
^{18}F	109.8 min	$^{18}O(p,n)^{18}F$	β^+ (97%) EC (3%)	0.249	0.6
^{64}Cu	12.7 h	$^{64}Ni(p,n)^{64}Cu$	β^+ (17.5%) β^- (38.5%) EC (43.6%)	0.278	0.7
^{89}Zr	3.3 d	$^{89}Y(p,n)^{89}Zr$	β^+ (22.7%) EC (76.2%)	0.395	1.3

SPECT radionuclides

Unlike the radioisotopes used in PET applications, SPECT radioisotopes emit single emission X-rays or γ-rays, upon electron capture (EC) decay or isomeric transition (IT) (56). Except for ^{123}I, most SPECT radionuclides used are metal or metal-like isotopes. A list of commonly used radionuclides for SPECT applications is provided **Table 1.2**. Unlike PET, SPECT cameras record single-emission events from one projection angle, and images from different projection angles, which are combined and reconstructed to obtain a tomographic image. The random angular emission of these γ-rays complicates the determination of the position of the source of the decay. To overcome this, only collimated (filtered) γ-rays that are emitted in a perpendicular direction relative to the detector plane are detected, resulting in low sensitivity. Low-energy γ-rays (50−250 keV) are ideal for SPECT since they are easily collimated and can efficiently be detected by SPECT detectors. A graphical illustration of the general principle of SPECT is provided in **Figure 1.5**. The most clinically used SPECT radiopharmaceuticals are ^{99m}Tc based (29). This is largely due to the availability of the radionuclide through an easily transportable ^{99}Mo/^{99m}Tc generator. The chemistry of technetium has been well investigated and reported, with many of these radiopharmaceuticals easily prepared with ^{99m}Tc-based labelling kits (49). These kits are generally prepared in authorised manufacturing facilities to conform to safety regulations for the intended ^{99m}Tc product. In general, a cold kit contains 1) a ligand to complex the ^{99m}Tc; 2) a reducing agent to reduce the ^{99m}Tc from +VII (TcO_4^-) to a lower oxidation number, generally $SnCl_2$; 3) buffer to adjust the pH to suit the labelling conditions; and 4) additional agents for stabilisation of the Sn^{2+}. In addition, kits are prepared in a freeze-dried form, to allow for fast dissolution of Sn^{2+} and ligand when $^{99m}TcO_4$ is introduced. Lyophilized kits can be transported at room temperature, which is advantageous for clinics where cold transports are difficult.

Table 1.2. List of common SPECT radionuclides (39,56,57).

Radionuclide	Half-life	Production pathway	Decay	Energy (γ_{max}) (keV)	Decay product
^{99m}Tc	6.06 h	^{99}Mo/^{99m}Tc generator	IT (100%)	142.7	^{99}Tc (unstable)
^{123}I	13.22 h	Cyclotron via ^{124}Xe	EC (100%)	159.0	^{123}Te (stable)
^{111}In	2.83 d	^{111}Cd(p,n)^{111}In	EC (100%)	245	^{111}Cd (stable)
^{67}Ga	3.25 d	^{67}Zn(p,n)^{67}Ga	EC (100%)	300.2	^{67}Zn (stable)

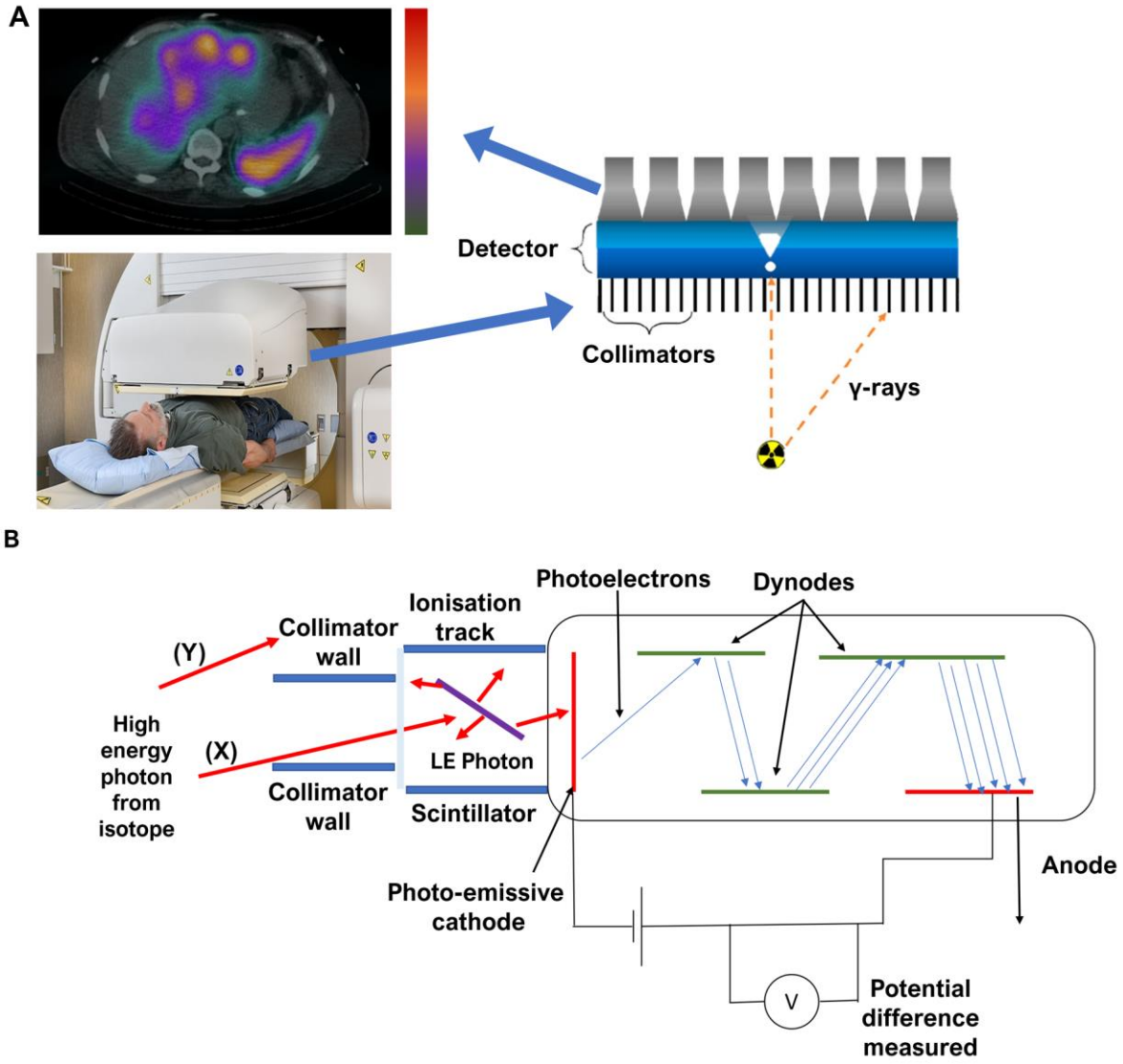


Figure 1.5. Illustration of a SPECT system and the photomultiplier tube to convert a gamma signal to voltage signal. **A.** A gamma emitting source is injected into the patient, the gamma rays pass through a collimator to filter out non-perpendicular gamma rays. The data is reconstructed to obtain a volumetric/projection image, which can be overlapped with an anatomical image of the region of interest. Images are used from https://www.mayoclinic.org, Z. Li *et. Al.,* P. Gawne *et. Al.* and M. Pericleous (53,58,59)**. B.** High energy photons are emitted from the radioisotope. Because of the collimator, only photons aligned with the collimator can enter the scintillating crystal (Y), whereas those outside of the correct alignment are absorbed (X). Inside the scintillating crystal, the energy of the gamma ray will produce ionisations resulting in high energy electrons that in turn promote electrons to a higher energy level producing light (scintillation) when they fall back to their ground state. The light energy results in ejection of electrons from the Photo-emissive cathode that are accelerated towards a dynode, where the number of electrons is amplified in proportion to the potential difference across the dynode. Finally, the cloud of amplified electrons is detected at the anode, which generates a voltage pulse. The amplitude of this pulse is proportional to the energy of the initial gamma ray.

1.2.1.2 Therapeutic radionuclides and applications

Therapeutic radionuclides primarily induce cytotoxic effects through irreversible processes such as DNA damage or/and chromosome aberrations (39). In addition, the primary damage caused can lead to secondary effects which also causes cell death. These cytotoxic effects can be 1) a direct effect of ionising radiation, 2) an indirect effect of irradiation through reactive oxygen species (ROS) formation, or 3) an immune response mediated effect (abscopal effect) (39,60,61). Radionuclides for therapy can be divided into three types: 1) beta (β^-, electrons) particles, 2) alpha (α, He^{2+}) particles, or 3) low-energy cascading electrons (conversion or Auger electrons). It is important to note that for β^- and A/CE, a high oxygen concentration is required for maximum efficiency, as one of the chemical effects occurs via reactive oxygen species (62). Therefore, in tumours that are hypoxic, water molecules from tumour environment and surrounding environments undergo radiolysis to form in the presence of O_2 the ROS needed for effective treatment (62,63). Additionally, once the treatment is administered, increases in active T-cells are also observed, which increases the likelihood of disease regression, which was observed in many cancers (64). The exact mechanism is not fully understood, but the current data suggests that release of DAMP molecules post cell death and stimulation of cGAMP molecules synergically activate T-cells which are responsible for the abscopal treatment (65). A short list of therapeutic radionuclides and their decay pathway is provided in **Table 1.3**. The ability of an emitted particle to cause damage to DNA is dependent on the linear energy transfer (LET) of the particle. This is defined as the amount of the energy deposited per unit length, commonly expressed as keV/μm (56). The range in tissue is dependent on the LET, as well as the kinetic energy of the emitted particle. A diagram depicting the average range of the particle is provided in **Figure 1.6**.

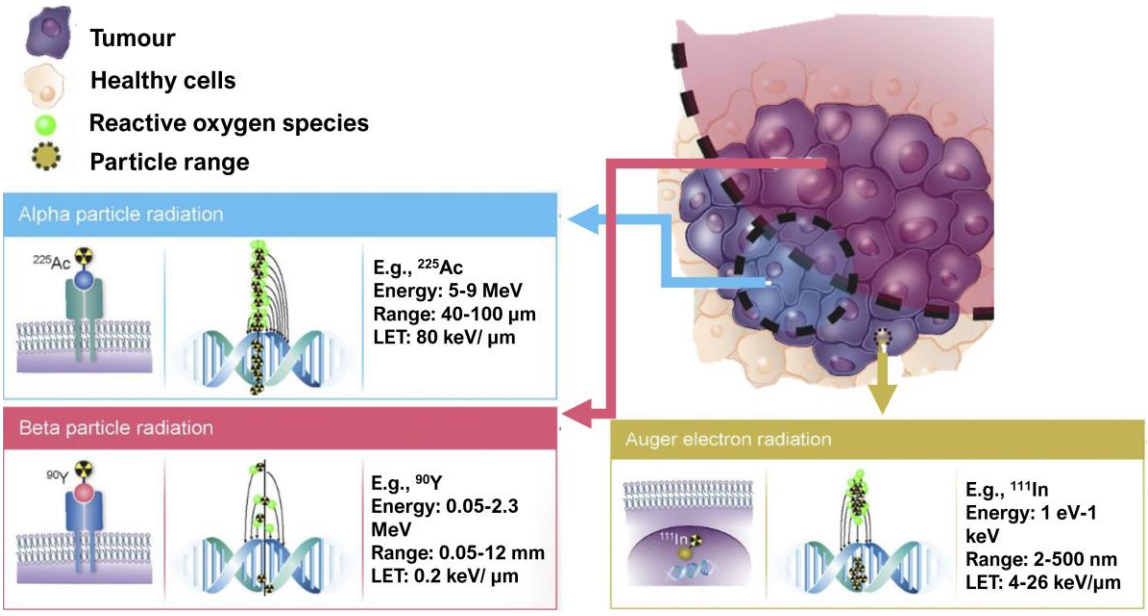


Figure 1.6. Graphical illustration of particle range for each of the therapeutic decay modes. Illustration was taken from S. Poty *et. al.* and modified for this thesis (66).

Table 1.3. Common radionuclides used in radiotherapy (only therapeutic decays shown) (35,39,56,66)

Radionuclide	Half-life	Production	Therapeutic Decay	Decay product	Energy (mean)
^{213}Bi	45.59 min	^{225}Ac/^{213}Bi generator	α β$^-$	^{209}Tl (unstable) ^{213}Po	E_α = 8.3 MeV E_β = 0.42 MeV
^{131}I	8.02 d	^{130}Te(n,γ)^{131m}Te^{131g}Te decaying to ^{131}I Decay product of ^{235}U	β$^-$	^{131}Xe (stable)	192 keV
^{223}Ra	11.43 d	Extraction from ^{231}Pa decay	α	^{219}Rn (unstable)	5.7 MeV
^{67}Cu	2.57 d	^{68}Zn(γ,p)^{67}Cu	β$^-$	^{67}Zn (stable)	141 keV
^{90}Y	2.67 d	^{90}Zr(n,p)^{90}Y	β$^-$	^{90}Zr (stable)	0.93 MeV
^{111}In	2.80 d	^{111}Cd(p,n)^{111}In	A/CE	^{111}Cd (stable)	2-4 keV
^{177}Lu	6.64 d	^{176}Lu(n,γ)^{177}Lu ^{176}Yb(n,γ)^{177}Yb decay to ^{177}Lu	β$^-$	^{177}Hf (stable)	133 keV
^{161}Tb	6.95 d	^{160}Gd(n,γ)^{161}Gd decay to^{161}Tb	β$^-$ A/CE	^{161}Dy (stable)	E_β =197 keV E_{e^-} = 3 keV
^{225}Ac	9.92 d	^{229}Th/^{225}Ac generator Spallation from ^{223}Th	α	^{221}Fr (unstable)	6.9 MeV

β$^-$-particles (electrons) can have a broad energy range, between 0.1−2.2 MeV with relatively low LET, in the range of 0.2 keV/μm. Because of the low LET and high energy, neighbouring cells often experience beta energy deposition (**Figure 1.6**), with approximately 1-2 keV per unit cell length. For example, the maximum beta energy of ^{177}Lu is 490 keV, which equates to a maximum tissue penetration of 2 mm, corresponding to 300-500 cells. This could be beneficial for large, heterogeneous tumours (experience radiation from neighbouring cells which the β⁻emitting radionuclide is bound to, known as the *crossfire effect*) but can lead to collateral damage to healthy cells. Therefore, low-energy β$^-$−emitters, with limited tissue penetration, have been favoured for therapeutic applications. Iodine-131 was the first β$^-$-radionuclide which showed significant promise for beta therapy. In more recent events, two lutetium-177 based radiopharmaceuticals, [^{177}Lu]Lu-DOTA-TATE (67) and [^{177}Lu]Lu-PSMA-617 (68) have had successful phase 3 clinical trials (NETTER-1 for [^{177}Lu]Lu-DOTA-TATE (NCT01578239)(69), VISION for [^{177}Lu]Lu-PSMA-617 (NCT03511664)(70)), with both radiopharmaceuticals being FDA and EMA approved, and commercially available as Lutathera® and Pluvicto®, respectively. The latter, Pluvicto®, is used in combination with a ^{68}Ga derivative for accurate patient follow-up post treatment (**Figure 1.7**). Pluvicto® has become one of the gold standards in beta therapy, showing highly effective tumour reduction with minimal side effects after treatment (28).

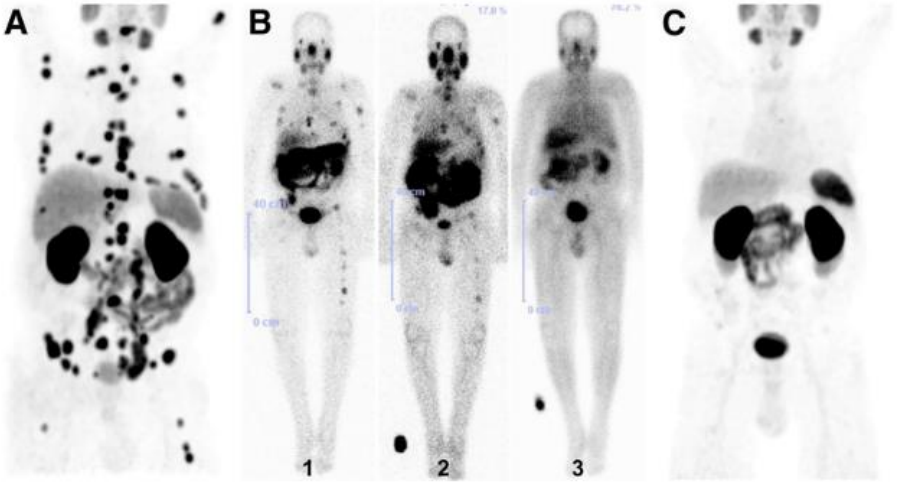


Figure 1.7. PET/CT scan of a patient with progressive bone and lymph node metastases, using [^{68}Ga]Ga-PSMA-617 before (A) and after (C) treatment cycles with [^{177}Lu]Lu-PSMA-617. Each treatment of [^{177}Lu]Lu-PSMA-617 was imaged using scintigraphy to show the efficacy of the treatment after each treatment cycle with [^{177}Lu]Lu-PSMA-617 (B) (28).

α-particles combine a high energy (5−8 MeV) with a short tissue range (40-100 μm), resulting in extremely high LET (~80 keV/μm) values. The high LET of α-particles leads to a large number of double-stranded DNA breaks, which is highly advantageous for cancer therapy. Availability of these radionuclides is scarce, with only a handful of laboratories or research centres having access to clinically relevant activities. Actinium (^{225}Ac) and radium (^{223}Ra) have shown promise in clinical studies, with the latter being used regularly in clinics to treat bone metastases. [^{225}Ac]Ac-PSMA-617 has also been instrumental in paving the path for targeted alpha therapy (TAT). [^{225}Ac]Ac-PSMA-617 has shown promising results in patients suffering from metastatic castration-resistant prostate cancer (mCRPC) (71). Feuerecker *et. al.* investigated the therapeutic effect of [^{225}Ac]Ac-PSMA-617 against mCRPC patients who show resistance to Pluvicto® therapy. In patients without liver metastases, 48% patient survival was observed 5-10 months after treatment. Unfortunately, off-target radiation of the TAT radiopharmaceutical can also be a costly detriment. In the same patient, off-target radiation of the [^{225}Ac]Ac-PSMA-617 to the salivary glands was observed causing severe xerostomia (72). In neuroendocrine cancers, a study conducted using low activity amounts of [^{225}Ac]Ac-DOTATOC resulted in successful eradication of somatostatin receptor expressing metastases in a patient (72). The administered activity was 100-fold less than the standard β⁻therapy dose, showing the potency of TAT. This showcases the dual nature of alpha emitters; highly potent at cancer therapy, but off-target damage can be a dose limiting factor.

Conversion or Auger electrons are low-energy electrons emitted as a downstream result of a transfer of energy to electrons (35). Auger electrons are electrons ejected from the outermost shell by interaction

with X-rays emitted when electrons move from a higher to a lower energy level e.g. after electron capture or internal conversion (**Figure 1.8, B**). This is different from an internal conversion electron, where the interaction of a gamma ray emitted from the nucleus results in the ejection of an inner shell electron from its orbital (**Figure 1.8, C**). Both conversion and Auger electrons deposit a high LET (4−26 keV/μm) over a substantially small range (2-500 nm) (**Figure 1.6**). Because of the short range, minimal crossfire effect or collateral damage is observed, with almost all the energy deposited in the cell the radiopharmaceutical is bound to. Initially it was believed Auger radiopharmaceuticals needed to internalise to be effective, but recent reports by Müller *et. al.* using ^{161}Tb-labelled non-internalising somatostatin receptor antagonists strongly suggests interactions at the cell membrane also has great cytotoxic properties (73). However, only few reports of this phenomenon are available, therefore additional studies are needed to fully understand the radiotoxicity mechanisms.

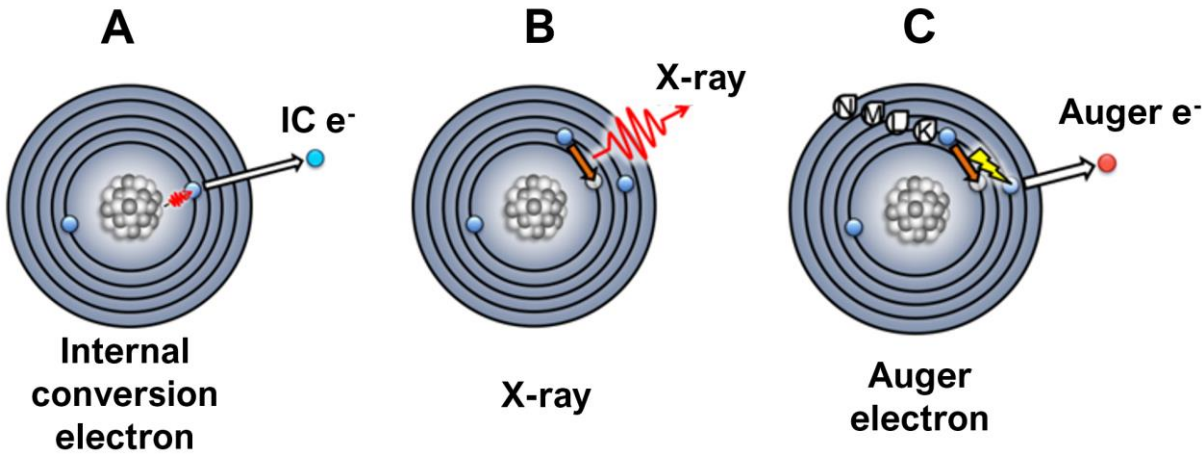


Figure 1.8. Diagram depicting the difference between X-ray, Auger electron and internal conversion electrons. Image taken from A. Ku *et. al.*(35). **A.** Excess energy in the core of the nucleus during decay can be transferred to the lowest energy shell electron, which expels the electron. This electron is referred to as an internal conversion electron. **B.** An electron transitions from a higher energy level to a vacant site in a lower energy level, resulting from electron capture (A). The difference in binding energies from the two energy levels is emitted in the form of an x-ray. **C.** The energy from the X-ray can be transferred to an electron in lower energy level, which expels the electron. This electron is referred to as an Auger electron.

1.2.2 Attaching radionuclide to a carrier molecule

In most cases, radionuclides are guided to their targets by means of a carrier molecule. In this case, it is imperative that the radionuclide has a chemically and biologically stable binding to the carrier molecule to minimise off-target accumulation of the radionuclide. In purely organic compounds, and rarely in coordination/organometallic/inorganic molecules, the radionuclide is attached directly to the carrier molecule by a covalent bond. A more common feature of radiopharmaceutical design is to incorporate linking groups between the radionuclide and carrier molecule. Linking groups are important

components of radiopharmaceuticals as they serve to secure the radionuclide to the carrier. In most cases, radiopharmaceuticals require a stable assembly of the radionuclide to the carrier. In this section, we highlight a few methods employed in current radiopharmaceuticals.

1.2.2.1 Direct bonding to carriers

An extensive library of reactions and stability constants are known for σ-bond and π-bond formation, which can be utilised in radiopharmaceutical design process. For example, ^{11}C can be introduced into a small molecule starting from $[^{11}C]CH_4$ or $[^{11}C]CO_2$ obtained in a cyclotron to form esters, aldehyde, ketones, amide or urea structures, without compromising the effectiveness of the carrier, as its chemical structure is not affected by substitution of a carbon-12 by a carbon-11 atom (74). An array of synthetic building blocks of ^{11}C can produced from these two molecules which can be used in various known, and well-researched reactions. A list of these building blocks is provided in **Figure 1.9**. Similarly, ^{18}F can be stably introduced through fluorination, cross-coupling, nucleophilic substitution or surface-activated metathesis (74). Radiopharmaceuticals such as $[^{18}F]$FDG are synthesised by nucleophilic substitution with $[^{18}F]F^-$ (75).

A disadvantage of the application of covalent binding techniques Is the non-quantitative yield, the use of organic solvents, the formation of side products and the presence of starting materials, which need to be removed prior to administration of the radiopharmaceutical. This purification step increases total processing time, which can be a concern when using a radionuclide with a short half-life. Furthermore, reactants and products may be chemically very similar, often requiring separation techniques such as high-performance liquid chromatography (HPLC) for the isolation of the desired radiolabelled compound. Direct chemical bonding to carrier molecules is largely limited to group 14-17 elements (C, S, N, O, P, F, I etc.), as σ-bonds with other elements are easily cleaved *in vivo* conditions, which can lead to leaching of the radionuclide.

1.2.2.2 Multidentate ligand systems for radiometals

Multidentate ligand systems (more than one donor atom), also called chelators, dominate the metal-based radiopharmaceutical space. Ligand systems often bind the radiometal, in addition to being coupled to the carrier (small organic frameworks, antibodies, etc.), and are called bifunctional chelators. These bifunctional chelators are often pre-coupled to the carrier by random or site-specific conjugation methods on amino acids (e.g. lysine, cysteine, etc.) that are present in the carrier molecule (76,77) using highly reactive groups such as esters, iso(thio)cyanates and maleimides (78).

Also, click reaction type systems like copper-assisted and inverse electron demand Diels-Alder reaction have been used for site specific conjugating of ligands to carriers (79,80). In addition to forming the metal-ligand bond, it is imperative that the ligand system has no effect on the overall binding potential of the carrier. The ligand system needs to satisfy the requirements of the radiometal to be chelated,

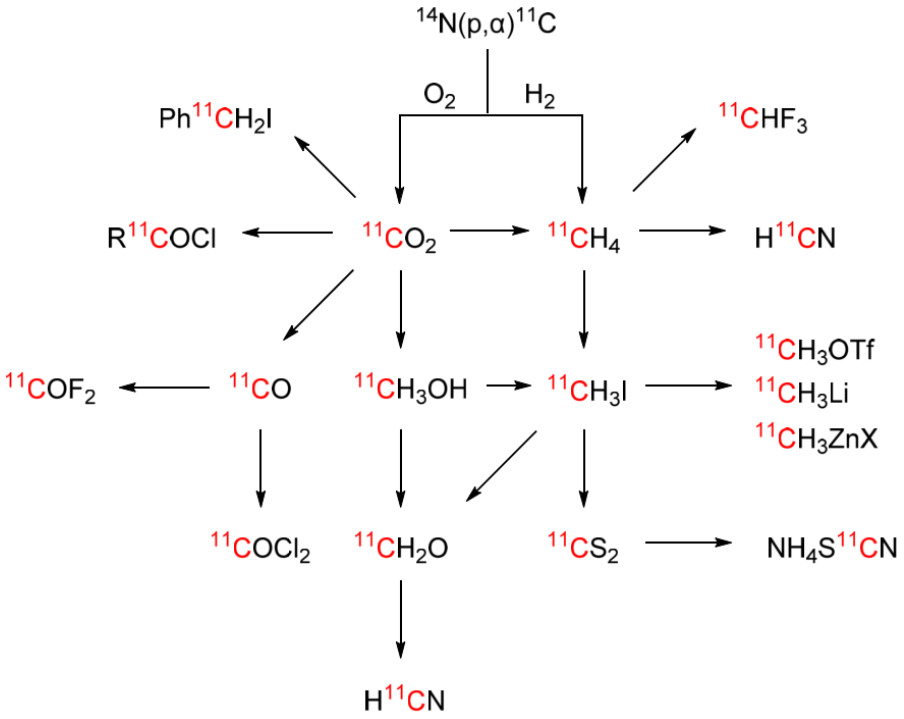


Figure 1.9. Various synthetic building blocks of ^{11}C starting from $[^{11}C]CH_4$ or $[^{11}C]CO_2$. Diagram taken from Pees *et. al.*(81)

namely donor preference (hard-soft acid-base principle), coordination number, geometry and pH dependency. Moreover, the rate of formation of the metal-ligand system is important since long reaction times could negatively impact the carrier. Furthermore, long reaction times could lead to loss of activity due to decay, requiring much larger activities to perform radiolabelling to obtain the needed amount, increasing likeliness of radiolysis products. Finally, the *in vivo* thermodynamic stability determines if a ligand system is suitable for a certain radiometal with the overall goal to retain the radiometal to the carrier molecule. There are two main types of ligand systems used with radiometals: cyclic, and acyclic.

Cyclic ligand systems

Dodecane tetraacetic acid (2,2′,2″,2‴-(1,4,7,10-tetraazacyclododecane-1,4,7,10-tetrayl)tetraacetic acid, DOTA) is the chosen framework for a variety of hard-acid metals such as lutetium, terbium, yttrium, gallium and indium (56). It is used in various clinical radiopharmaceuticals, namely $[^{177}Lu]$Lu-DOTA-TATE and $[^{68}Ga]$Ga-DOTA-TATE, owing to the great *in vivo* stability of the radiometal complex (67,82). DOTA is known to form highly stable chelates, with the hard oxygen atoms forming strong bonds with the metal, and the softer nitrogen atoms stabilising the metal centre (coordination number: 6-8). In addition, the rigid nitrogen cyclen core adds to make the final complex less susceptible to metal leaching, and prevent transchelation to other biological substances such as polyamines or

metalloenzymes (83). Variations to the DOTA framework have been investigated, with additional binding tethers added to promote faster kinetics, as observed in DOTA-GA for hard acids and DO4S (sulphur atoms replace nitrogen atoms in DOTA) for softer radiometals. Smaller cyclic ring cores, as in 1,4,7-triazacyclononane-1,4,7-triacetic acid (NOTA), have successfully been used for smaller elements, such as gallium. Larger radionuclides, such as actinides, which prefer more oxygen donor atoms, bind stronger to a macropa type system (84), which has 6 oxygen donor groups to bind to the radionuclide, with two stabilising nitrogen groups. This arrangement of donor atoms made it possible for labelling at significantly lower temperatures than the DOTA-type systems (85). A list of bifunctional chelators with a cyclic multidentate ligands, with arrows indicating sites often used to form bonds with carriers, is provided in **Figure 1.10**.

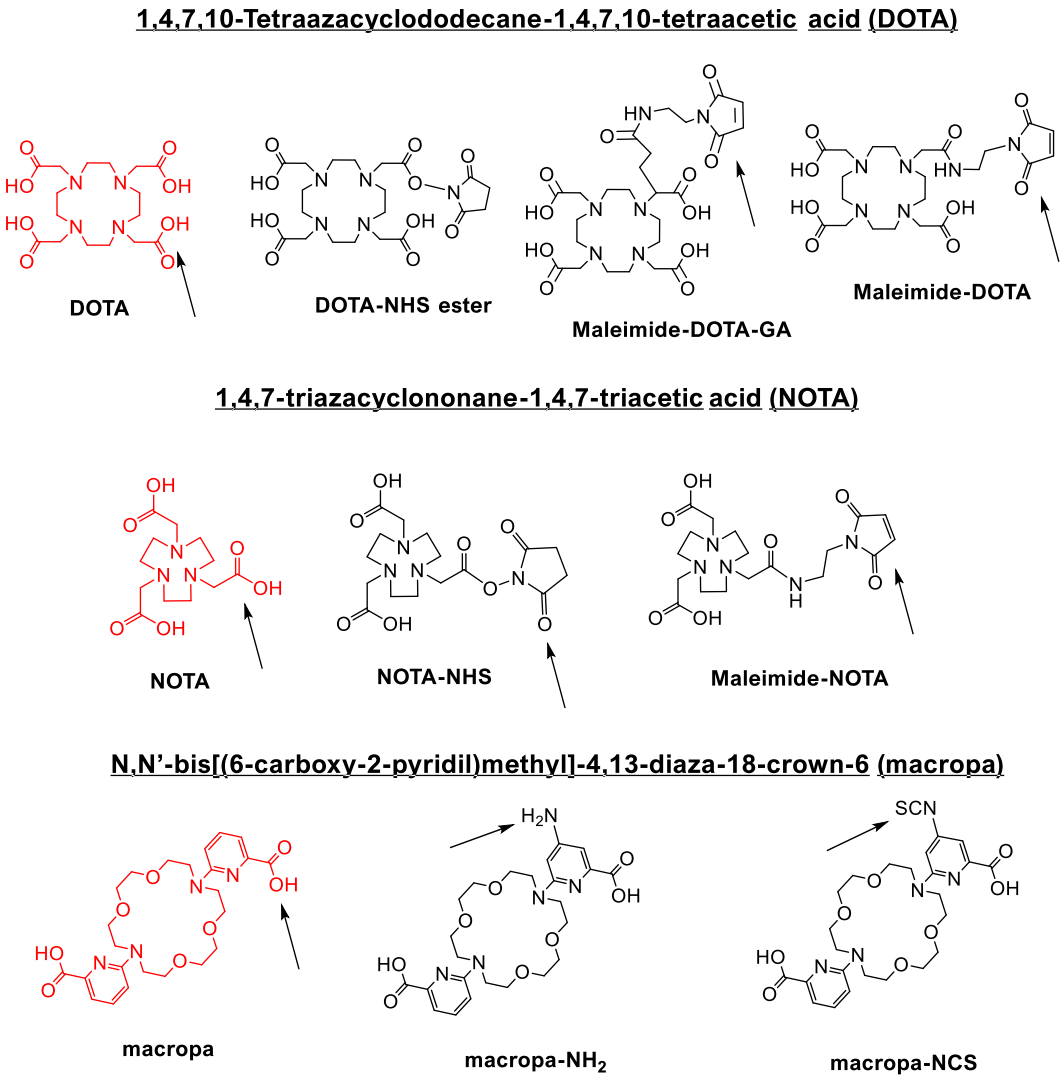


Figure 1.10. Common cyclic ligand systems and there binding moiety to carriers (78). Base ligand system is displayed in red. All ligands shown are commercially available at the time of this report.

Acyclic ligand systems

Diethylenetriaminepentaacetic acid (DTPA) (**Figure 1.11**) was one of the first acyclic systems to be used to coordinate radiometals. Many DTPA-based radiopharmaceuticals, such as [^{111}In]In-pentetreotide for the imaging of neuroendocrine tumours, have been developed and approved for clinical use (86,87). The DTPA ligand system is observed to have extremely fast reaction kinetics, but poor metal-ligand stability has been observed with radiolanthanides (78). Improvements to the stability of the base framework was investigated by incorporating a more rigid cyclohexane backbone (**Figure 1.11**, **CHX-A``-DTPA**) (88). However, when radiolabelling with lanthanides, such as bismuth radionuclides, the *in vivo* stability was found to be inferior to that of cyclic-ligand complexes (89).

A new series of compounds containing picolinic acid moieties have been extensively investigated by Orvig *et. al.,* which showed promise in addressing the stability problems associated with acyclic frameworks (78,90,91). H_2dedpa and H_2azapa (**Figure 1.11**) were the first chelators in this class of compounds, and had fast reaction kinetics with gallium ($^{67/68}$Ga) and yttrium ($^{86/90}$Y) at room temperature, as well as great *in vivo* stability, similar to DOTA (90,91). Furthermore, the picolinic acids were also tested with larger atoms, such as lutetium, which showed the versatility of the ligand to multiple classes of elements. To further increase the stability for more acidic metals, additional oxygen atoms were added to the ligand system, with great success. H_4octapa, a derivative of H_2dedpa with two additional carboxylic acids, was evaluated for labelling of ^{111}In and ^{177}Lu, resulting in quantitative conversions (>95%) at room temperature, and high *in vitro* stability. Unfortunately, as with most (N_x,O_y) ligand systems, difficult purification and low synthesis yields of the ligands are often the largest concern for commercial implementation. Another ligand that has been used for transition metal radionuclides, such as ^{89}Zr and $^{64/67}$Cu, has been Desferrioxamine B (DFO) and oxo-DFO*, a DFO derivative with extended *N*-hydroxyacetamide chain (**Figure 1.11**). In addition, gallium has shown to be efficiently chelated by the DFO derivatives. DFO/DFO* has shown superior binding kinetics with ^{89}Zr compared to DTPA, with >99% of metal chelated with the DFO framework after 1 hour and <0.1% with DTPA after the same time. Currently, no clinically approved radiopharmaceuticals use DFO as a chelator, however many ^{89}Zr-radiopharmaceuticals, such as ^{89}Zr-DFO-TLX250 (92), are currently in clinical trials.

Hybrid ligand systems

Hybrid systems, containing both cyclic and acyclic ligands, have also been investigated to incorporate the fast kinetics of acyclic ligands and thermodynamic stability of cyclic systems. 3p-*C*-DEPA and 3p-*C*-NETA (frameworks which contain DOTA or NOTA, respectively, with an acyclic arm) (**Figure 1.12**) have shown promise in binding a variety of metal/metal-like radionuclides used in the radionuclide space (83,87,93). In a recent study by Ahenkorah *et. al.*, 3p-C-NETA was investigated for radiolabelling with a series of radionuclides, and stability of the radiometal complexes was evaluated (94).This ligand provided high radiochemical conversions (> 95%) at mild temperatures (< 55 °C) with ^{177}Lu, ^{213}Bi, ^{67}Cu, and ^{161}Tb but lower radiochemical yields were observed for aluminium fluoride ([^{18}F]AlF^{2+}) and ^{68}Ga.

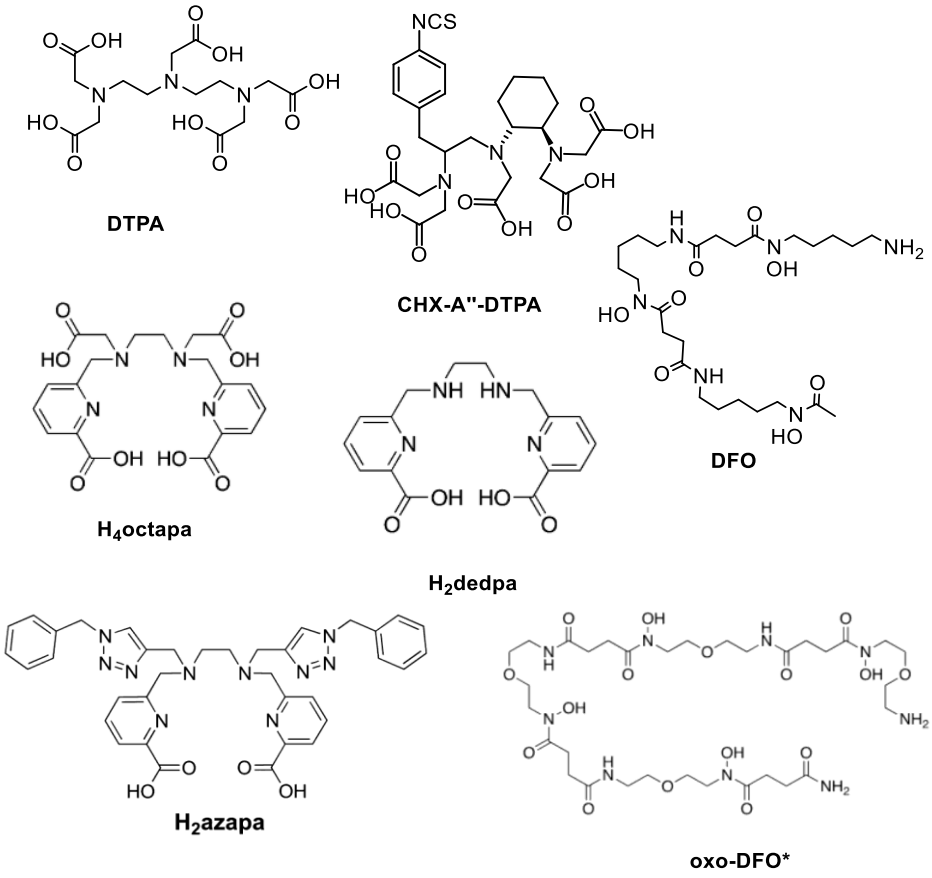


Figure 1.11. Common acyclic ligand systems used in radiopharmaceutical design.

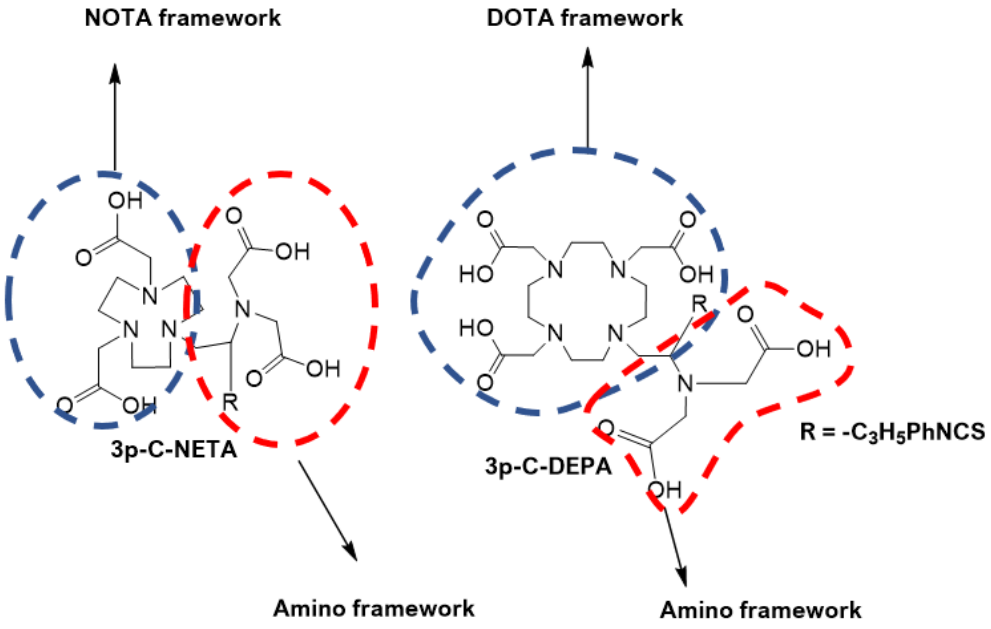


Figure 1.12. 3p-*C*-NETA and 3p-*C*-DEPA. The cyclic framework (blue) of NOTA and DOTA, with an additional amine support (nitrogen from cyclic framework and *N,N*'-methylcarboxylic acid) which can bend to form additional M-O or M-N bonds.

Additionally, the obtained complexes remained stable (> 95%) *in vitro* for at least 24 hours. Hybrid chelator systems blend the kinetics and thermodynamics of cyclic and acyclic systems, respectively, and show promising characteristics with various radiometals.

1.2.3 Carriers used in radiopharmaceuticals

The carrier molecule plays a vital role in the pharmacokinetics of the radiopharmaceutical. For a carrier molecule to be suitable for TRNT, it needs to bind with a high affinity and selectivity for the molecular target (e.g. antigens) expressed on tumour cells. In cancer, the expression of many of these molecular targets are upregulated, which increases the likelihood of selective binding to cancer cells vs. healthy tissue. The ideal case is where the biomarker is present only in the cancer cells to avoid off-target binding and potential adverse effects (68,95,96). Thus, high selectivity and affinity are crucial elements to maximise the target tumour accumulation with only limited uptake in healthy tissues. For both imaging and therapy, a fast-achieving higher tumour-to-background image contrast is essential (39,56). High selectivity is crucial so that a minimal radiation dose is absorbed by healthy cells, as the latter potentially causes harmful long-term effects (97). This off-target radiation dose is a major concern for therapeutic radionuclides. Off-target radiation is also largely caused by normal physiologic distribution and clearance of the radiopharmaceutical, and this might limit the overall dose that can be administered to the patient (98). In this section, we discuss the types of carriers commonly used for radiopharmaceuticals, and their (dis)advantages.

1.2.3.1 Small-molecule radiopharmaceuticals

Small molecules (typically under 500 Da) have been a staple in the pharmaceutical field for decades. They disturb biological interactions by forming complexes with their targets (97). Small organics/inorganic molecules have low molecular weight, fast circulation throughout the body, can permeate cells easier, and are excreted relatively quickly. In addition, their relative small size and ease of their chemical modification to a more lipophilic character can make it possible to overcome biological barriers, such as the blood-brain barrier (74,97), which is notoriously difficult to pass through by larger or hydrophilic molecules. This is achieved by interaction with extracellular or intracellular proteins (receptors, enzymes, transporters, etc.) on the periphery or in the central nervous system/brain (97). Once a small molecule carrier has been developed, a synthetic plan to radiolabel the molecule can be made.

There are three types of small molecules used for radiopharmaceuticals: 1) biologically-derived molecules from rational drug design by phenotype screening, 2) target-based drug discovery by target validation or computational docking experiments, or 3) extracted from a natural resource after drug-target identification, and modified with a radionuclide (99). An example of the first type is metaiodobenzylguanidine (mIBG), a noradrenaline analogue which is taken up by an active mechanism

into neuroendocrine cells, which is labelled with ^{123}I or ^{131}I for SPECT imaging or therapy, respectively (100).

Radioisotopes are often introduced into small organics through radioisotopes of hydrogen, carbon, or halogens, while remaining chemically identical to preserve the same pharmacokinetic profile (53,81,99). In metal-based small organics, this is difficult to achieve, as ligand systems often cause a significant change in the biodistribution and pharmacokinetic profile (101). However, in recent years, there has been an emergence of highly specific carries such as prostate specific membrane antigen (PSMA) and fibroblast activated protein inhibitor (FAPI) derivatives (61,96), which can easily be modified with radiometals and ligand systems without a significant compromise to the biodistribution and pharmacokinetic profile.

1.2.3.2 Peptide and pseudo-peptide based radiopharmaceuticals

Peptides are one of the principal elements of all known living systems (102,103). These robust structures are responsible for many biological functions such cell signalling and regulation of cell growth (103). Peptides consist of 2-25 amino acids and are considerably smaller than proteins (104). Because of their small size, peptides are often observed to have fast pharmacokinetics *in vivo*, with clearance via the renal tract (102,103,105,106). This means a greater sensitivity for imaging as a high target-to-blood background ratio is obtained after a short time post injection. The overexpression and upregulation of peptide-specific receptors in cancers make peptide receptor radionuclide therapy (PRRT) an attractive concept. The main excretion pathway of peptides is through glomerular filtration in the kidneys, which may be followed by partial tubular reabsorption (98). A potential mechanism of this tubular reuptake is through megalin and/or cubulin interaction (transmembrane scavengers-receptors) (98). This results in accumulation in the kidneys, potentially nephrotoxic when used in radionuclide therapy (107).

Radiolabelled peptides used in medicine are often modified structures of naturally occurring peptides (98,102). In recent years, somatostatin analogues, such as [^{111}In]In-DTPA-octreotide (35,86), [^{68}Ga]Ga-DOTA-TOC (67,102) and [^{177}Lu]Lu-DOTA-TATE (**Figure 1.13**)(67,108), were developed for the diagnosis and treatment of neuroendocrine tumours, respectively. The latter was FDA and EMA approved for the treatment of neuroendocrine cancer (67), which further provided testimony of peptides as useful radionuclide carriers.

Another well-known example of PRRT uses radiopharmaceuticals binding to PSMA. PSMA is a type II metalloprotease and a useful clinical biomarker of prostate cancer (72,96). Its expression is upregulated with androgen deprivation and correlates with the aggressiveness of the cancer (96). Because of its high expression in prostate-related cancers, many drug delivery reagents with PSMA (pseudo)peptides (pharmacophore consisting of glutamic acid and lysine, with a urea bond between the two)(109) have been developed. [^{177}Lu]Lu-PSMA-617, has been approved in December 2022 by the EMA for treatment

of metastatic castration-resistant prostate cancer after a successful phase III clinical trial (VISION III, NCNCT03511664)(70).

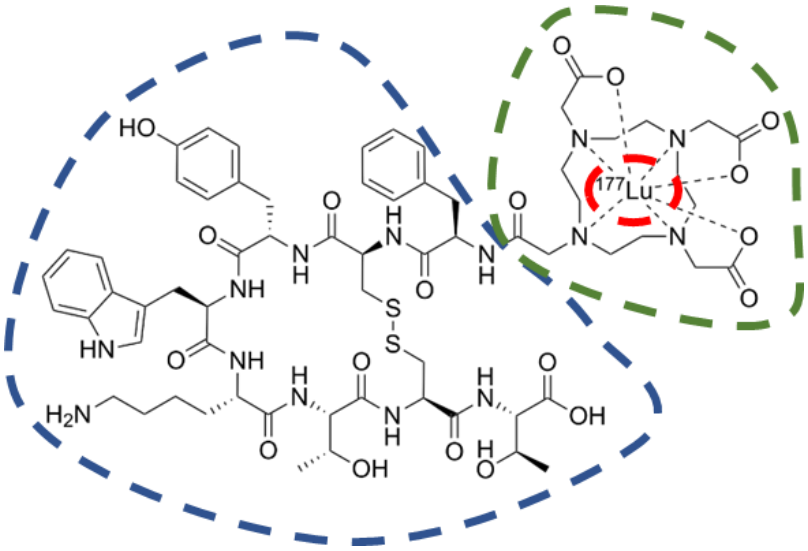


Figure 1.13. Structure of [^{177}Lu]Lu-DOTA-TATE. The carrier molecule, the somatostatin receptor targeting group (blue) is attached to a DOTA chelator molecule (green), with a ^{177}Lu radionuclide (red).

1.2.3.3 Antibody and antibody-fragments as carriers

Antibodies (Abs) are immune-response proteins produced by the immune system in response to foreign substances called antigens. Abs can be produced in larger quantities in laboratories to produce monoclonal antibodies (mAbs)(110). Approximately 30 mAbs have been approved for the treatment of cancer, with >80 still in clinical trials (111–113). Antibodies are highly selective for their target antigens, making them highly efficient for targeted therapies. Over the last two decades, antibodies have become an important group of biologicals for highly specific targeted therapies (77,102). Antibody treatments have also been effective in CNS diseases, such as Alzheimer's disease (AD), where patients are treated with aducanumab, the only anti-amyloid treatment approved for AD (114). Due to their high selectivity and affinity, antibodies have also proven to be good carrier molecules for radiopharmaceuticals. Radiopharmaceuticals, such as [^{89}Zr]Zr-APOMAB®, have been used for imaging of treatment response after chemotherapy (115). This is achieved by binding to a Lupus associated/Sjögren Syndrome-B antigen, which is overexpressed in most tumours and only becomes available for binding once the tumour cell dies (115). Drugs such as [^{90}Y]Y-ibritumomab tiuxetan (Zevalin) to treat B-cell Non-Hodgkin's lymphoma (116) have further cemented the use of mAbs in medicine (112).

Because of the large size of the antibody and interaction with proteins found in blood, such as albumin, blood clearance is slow, with a plasma half-life of several days to weeks (117). For radiolabelled

antibodies, a post administration waiting time of several days is required to obtain a sufficiently high tumour-to-background ratio for imaging purposes (115), requiring radionuclides with a relatively long physical half-life. For example, radionuclides which still a have reasonable fraction of activity after 10 days such as ^{111}In (half-life 2.8 days) or ^{89}Zr (half-life 3.3 days) are perfectly suited for antibody based radiotracers (118)).

For radionuclide therapy, highly target-specific uptake, without off target radiotoxicity (as observed with radiopeptides) is required. Anti-CD138 monoclonal antibodies, labelled with ^{111}In for diagnosis and ^{213}Bi, ^{177}Lu or ^{225}Ac for radionuclide therapy, have shown promise in preclinical models for multiple myeloma (119,120). Though not many antibody-based radiopharmaceuticals are commercially available, many are still in active clinical trials, such as JNJ-69086420, an [^{225}Ac]Ac-labelled antibody, which targets human Kallikrein-2 for advanced prostate cancer (NCT04644770). A list of some antibody-based therapeutic radiopharmaceuticals is provided in **Table 1. 4**.

The long circulation time of antibodies can also be a concern for clinical work. The repetitive long-term exposure of ionising radiation through treatments could lead to genetic mutations, which can bring forth new diseases. This can be overcome with multiple treatments with a lower radiation dose, which has been shown to be an effective strategy in a few institutions already, with a high percentage of patients in complete cancer remission following this low-dose radiation therapy (121,122). In addition, antigen-resistance and bone marrow toxicity are major concerns for the treatment strategy (123,124). Moreover, logistic and social concerns (multiple clinical visits, limited family and personnel contact, etc.) also play a role advocating for and against radiolabelled antibody treatments. One way to overcome these concerns is to use a pre-targeting approach, where a bio-orthogonal group is attached to an antibody (125–128). This non-radioactive antibody is injected and allowed to circulate to maximise tumour accumulation. A radioactive ligand is injected and reacts with the bio-orthogonal group, with the non-reacted ligand quickly excreted, resulting in a highly specific dose to the tumour. One of the most common bio-orthogonal groups used are tetrazines reacting with trans-cyclooctene (TCO) via an inverse electron demand Diels-Alder (IEDDA) (80,126,129–131).

Additionally, smaller antibody fragments (**Figure 1.14**) have been used as carrier molecules for radiopharmaceuticals, as they have a shorter biological half-life with the same selectivity for the targets (49,117,132–134). Nanobodies, v_HH, are heavy-chain only binding fragments of *Camelid* immunoglobins (134). Their size (13-16 kDa) is ideal for fast delivery and permeability to enter the tumour relatively quick (134). Preclinical studies have shown fast kinetics, with clearance via the kidneys (135). Low tumour uptake was however observed, which was postulated to be a consequence of fast excretion of the labelled nanobody (72.4% of v_HH excreted 1.5 hour post injection) (135). This effect is similar to peptide-based treatments, which are excreted via the kidneys rapidly after injection. To increase plasma half-life and tumour concentration, groups that bind to plasma proteins such as albumin (136,137) can be incorporated. This technique might be favourable for therapeutic applications, as it increases the

extent of uptake in the tumour. Conversely, this is unfavoured in diagnostic applications as it likely results in an increased time period that is required between injection and imaging.

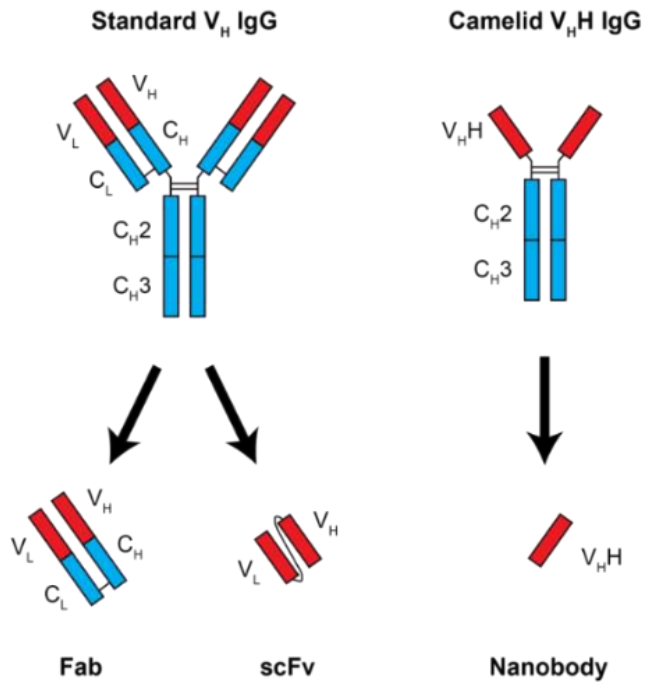


Figure 1.14. Antibody (IgG, immunoglobins), fragment antigen binding (Fab), single-chain fragment variable (scFv) and nanobody (V_HH) structures. Image taken from https://www.ncdir.org/resources/nanobodies/

Table 1.4. A list of some commercially available therapeutic radiopharmaceuticals and therapeutic radiopharmaceuticals in clinical trials in US or EU. Table taken and modified from Sgouros *et. al.* (138) and updated from www.clinicaltrials.gov.

Radiopharmaceutical	Carrier molecule	Distributor / Company	Cancer type	Properties	Development phase (2023)	NCT number
[^{153}Sm]Sm-lexidronam	Small molecule (phosphonate)	Lantheus	Cancer bone pain	Binding to hydroxyapatite matrix (bone)	Commercially available	–
[^{177}Lu]Lu-labelled DOTATATE	Peptide	Novartis/AAA	Neuroendocrine tumours	SSR-mediated binding	Commercially available	–
[^{131}I]MIBG	Small molecule	Progenics	Adrenergic receptor+ tumours	Active uptake mechanism via the adrenaline transporter	Commercially available	–
^{131}I-labelled CD45	Antibody	Actinium Pharmaceuticals	Bone marrow transplant preparation	^{131}I-based antibody targeting CD45+ cells	Phase III; not recruiting	NCT02665065
[^{177}Lu]Lu-DOTA-PSMA-617 (Pluvicto)	Pseudopeptide	Novartis/Endocyte	Prostate cancer, tumour neovasculature	PSMA-mediated binding	Commercially available	–
[^{177}Lu]Lu-labelled NeoBOMB1	Peptide	Novartis/AAA	GRPR+ tumours	GRPR binding	Phase II; terminated Phase I/II; completed	NCT03724253 NCT02931929
[^{177}Lu]Lu- OPS201	Peptide	Ipsen	Neuroendocrine tumours	SSR-mediated	Phase I/II; terminated	NCT02592707
[^{177}Lu]Lu -labelled PSMA-R2	Peptide	Novartis/AAA	Prostate cancer, tumour neovasculature	PSMA-mediated	Phase II; terminated	NCT03490838
[^{225}Ac]Ac-lintuzumab	Antibody	Actinium Pharmaceuticals	Multiple myeloma	CD38 antibody α-targeting	Phase I; terminated	NCT02998047
[^{227}Th]Th-labelled MSLN-TTCa	Antibody	Bayer	Mesothelin+ tumours	Anti-mesothelin–α-emitter immunoconjugate	Phase I; completed	NCT03507452
[^{227}Th]Th-labelled MSLN-TTCa	Antibody	Bayer	Mesothelin+ tumours	Anti-mesothelin–α-emitter immunoconjugate	Phase I; completed	NCT03507452
[^{227}Th]Th-labelled PSMA-TTCa	Antibody	Bayer	Prostate, tumour neovasculature	PSMA-targeting α-emitter immunoconjugate; PSMA+ prostate cancer targeting	Phase I; recruiting	NCT03724747

(**Table 1.4** continued)

Radiopharmaceutical	Carrier molecule	Distributor / Company	Cancer type	Properties	Development phase (2023)	NCT number
[^{227}Th]Th-CD22-TTCa	Antibody	Bayer	Lymphoma	Anti-CD22–α-emitter immunoconjugate; CD22+ tumours (lymphoma)	Phase I; completed	NCT02581878
[^{131}I]CLR131	Small molecule	Cellectar	Paediatric cancer, head and neck cancer, multiple myeloma, leukaemia, lymphoma	^{131}I-labelled phospholipid ether analogue targeting cancer cell-specific lipid raft microdomains	Phase I; recruiting Phase I; active Phase II; recruiting	NCT03478462 NCT04105543 NCT02952508
[^{131}I]CLR1404	Small molecule	Cellectar	Non-responsive solid tumour, multiple myeloma	^{131}I-labelled phospholipid ether analogue targeting cancer cell-specific lipid raft microdomains	Phase I; completed Phase I; completed	NCT02278315 NCT01495663
[^{225}Ac]Ac-FPI-1434	Antibody	J&J/Fusion Pharma	NSCLC, pan-cancer target	Insulin growth factor	Phase II; recruiting	NCT03746431
[^{153}Sm]Sm-CycloSam	Small molecule	Oncolix/Isotherapeutics	Osteosarcoma	Binding to hydroxyapatite matrix (bone)	Phase I; withdrawn	NCT03612466
[^{212}Pb]Pb-DOTAMTATE (AlphaMedix™)	Peptide	OranoMed/Radiomedix	SSR+ tumours	SSR-mediated binding	Phase I; active, recruiting	NCT03466216
^{223}RaCl$_2$ (Xofigo®)	Element only	Bayer AG	Bone cancer, prostatic neoplasm	Binding to hydroxyapatite matrix (bone)	Commercially available	-
[^{131}I]NaI (Hicon®)	Element only	Jubilant Radiopharma	Hypothyroidism, carcinoma in thyroid	Captured in thyroid during hormone production	Commercially available	-

1.3 Theragnostic Approach

As previously discussed, radionuclide therapy has shown great potential in treating various cancers. However, poor patient selection can result in a clinical trial that fails to identify the true therapeutic potential of the radiopharmaceutical. Additionally, a too low, and therefore, ineffective dose can result in a lack of response, whereas a too high dose may result in radiotoxicity to healthy tissue. Therefore, the past years the focus of the field shifted more towards theragnostics. Theragnostic (**thera**py + dia**gnostic**) refers to a set of radiopharmaceuticals, where a diagnostic radiopharmaceutical is combined with a therapeutic agent.

This concept was best demonstrated with radioiodine, which was used in the diagnosis and therapy of thyroid disease (139). Combining a diagnostic agent with a therapeutic agent allows: 1) to determine localisation of cancer or predict the behaviour of the therapeutic agent with similar biochemical properties; 2) to examine its biodistribution as predictive of therapeutic success (selection of the patient) or identify potential off-target (adverse) effects of the therapeutic agent; 3) predict tumour dosimetry to maximise therapeutic efficacy; and 4) to monitor the response to treatment.

Often, the same carrier molecule is radiolabelled with an imaging radioisotope for diagnostic purposes or a therapeutic radioisotope when the therapy is administered. Each therapeutic radionuclide is often paired up with a diagnostic radionuclide with similar chemical properties, so called theragnostic radionuclide pairs. A small list of theragnostic pairs used in clinic is provided in **Table 1.5**. An overview of the different pairing options is discussed below.

Table 1.5. A few theragnostic radiopharmaceutical pairs in clinic (140).

Clinical indication	**Diagnostic agent**	**Therapeutic agent**
Hyperthyroidism or thyroid cancer	^{123}I-iodide	^{131}I-iodide
Adrenergic tumours	^{123}I-MIBG	^{131}I-MIBG
Bone metastases from prostate cancer	[^{99m}Tc]Tc-MDP	$^{223}RaCl_2$
Non-Hodgkins lymphoma	^{111}In-ibritumomab	[^{90}Y]Y-ibritumomab
Neuroendocrine tumours	[^{68}Ga]Ga-DOTATATE	[^{177}Lu]Lu-DOTATATE
Prostate cancer	[^{68}Ga]Ga-PSMA-11	[^{177}Lu]Lu-PSMA-617

1.3.1 Homonuclear pairs

Homonuclear pairs are "*same-element radioisotope pairs*" in which the imaging and therapeutic radionuclides belongs to the isotopes from the same element. The advantage of using these pairs is that the same element is used, and therefore the corresponding radiopharmaceuticals will have identical chemical and pharmacokinetic properties. Unfortunately, very few homonuclear pairs exist which are compatible with application in nuclear medicine. In addition, large differences in physical half-life can be a complicating factor in the translation between diagnostic and therapeutic applications, which can be a radiopharmaceutical design concern. For example, using ^{123}I (half-life 13.2 hours) with an antibody fragment with slow dissociation (tumour half-life 4 days) from the target antigen would not allow to predict the half-life of the radiopharmaceutical in the tumour. This may result in an inaccurate prediction of the therapeutic dose when ^{131}I is used and potentially a too early release of a patient, who could contaminate accessible areas. The most successful homonuclear pair in theragnostics has been the diagnosis and treatment of hyperthyroidism or thyroid cancer with radioiodine. Yttrium-based theragnostic pairs have also shown promise in accurately estimating dosimetry. $^{86/90}$Y-radiolabelled compounds have shown promise as a homonuclear theragnostic pair. In a study by Helisch *et. al.,* dose estimation of the therapeutic efficacy of [^{90}Y]Y-DOTA-Phe^{1}-Tyr^{3}-octreotide using [^{86}Y]Y-DOTA-Phe^{1}-Tyr^{3}-octreotide and ^{111}In-labelled compound was performed (141). Successful dose estimation could be performed in patients without hepatomegaly (enlarged livers show increased uptake of radiopharmaceutical, limiting distribution of radiopharmaceutical). Though it must be noted that no clinical evidence suggests calculations based of diagnostic scans has a benefit over traditional calculations (patient weight, etc.)(142,143). Other homonuclear pairs that have been explored are $^{43/44}$Sc–^{47}Sc, ^{64}Cu–^{67}Cu, and ^{124}I–^{131}I (78,144).

1.3.2 Heteronuclear pairs

Heteronuclear pairs are "*different-element pairs*" in which the imaging and therapeutic radionuclides belong to different chemical elements and are both used to label the same pharmaceutical. For example, [^{68}Ga]Ga-DOTA-TATE and [^{177}Lu]Lu-DOTA-TATE have been used in the treatment and follow-up of neuroendocrine tumours. Different elements may require different labelling methods to label the same pharmaceutical. The *in vitro* affinity and/or *in vivo* pharmacokinetics of the theragnostic pairs is however not always identical. An example of this is the chemokine receptor 4 (CXCR4) theragnostic pair of PentixaFor (^{68}Ga) and PentixaTher (^{177}Lu) (105). The addition of an iodo-moiety in the PentixaTher was necessary to preserve affinity for the target (compared to PentixaFor) but which increases the log*P* resulting in increased liver uptake. This change is often a concern that needs addressing when using heteronuclear pairings. However, a larger range of heteronuclear pairs than homonuclear pairs are available to use in theragnostics, making these sets of radioisotopes more feasible to implement.

1.3.3 Terbium Radionuclides for Medical Applications

A chemical element that is rapidly emerging in the theragnostic field is terbium. (145). Four radioisotopes of terbium have been identified as promising for nuclear medicine applications: ^{152}Tb and ^{155}Tb (**Table 1.6**) can be used diagnostically in PET and SPECT, respectively and ^{149}Tb and ^{161}Tb (**Table 1.6**) can be used in targeted alpha (α), and a combination of beta (β^-) and A/CE therapy, respectively (145). Unlike with $^{43/44}$Sc–^{47}Sc, ^{64}Cu–^{67}Cu, ^{86}Y–^{90}Y, and ^{124}I–^{131}I, the terbium series can access both image modalities, as well as all three radionuclide therapy profiles.

Table 1.6. Decay and production properties of the terbium isotopes of interest (146). Half-life of radionuclides was taken from https://www.prismap.eu/ (accessed on 7 July 2023)

Isotope	Half-life	Decay mode	$E_{avg.}$ (MeV)	Production route
^{149}Tb	4.11 h	α (16.7%) β^+ (7.1%) EC (76.2%)	E(α) = 3.97 E(β^+) = 0.73 E(γ) = 0.66	Spallation reaction (Ta target), mass separated
^{152}Tb	17.52 h	β^+ (20.3%) EC (79.7%)	E(β^+) = 1.14 E(γ) = 0.34	Spallation reaction (Ta target), mass separated
^{155}Tb	5.32 d	EC (100%)	E(γ) = 0.175	Spallation reaction (Ta target), mass separated
^{161}Tb	6.95 d	β^- (100%) γ (17%)	E(β^-) = 0.197 E(γ) = 0.037	Nuclear reactor ^{160}Gd(n, γ)^{161}Gd → ^{161}Tb

1.3.3.1 Terbium chemistry

Terbium is a rare earth metal, discovered in the mid-1800s in a Swedish mine, in the mineral crystal gadolinite, locally referred to as yttria (147). Extraction of the rare metal was done by precipitation of each metal within the gadolinite crystal using ammonium hydroxide, forming insoluble terbium hydroxide ($Tb(OH)_3$) (147). Like many of the lanthanide series of elements, terbium is found in both the Tb(III) and Tb(IV) oxidation numbers. The stability of Tb(IV) is poor for pH < 13, and it readily reduces to Tb(III) (148,149).

With Tb(IV) being insoluble in water, aqueous chemistry with terbium only exists with Tb(III). Terbium, like gadolinium, dysprosium, ytterbium and erbium, is a strong Lewis acid, with a strong affinity for oxygen and phosphorus atoms (148,150,151). Furthermore, nitrogen atoms have shown to bind terbium weakly, similar to other elements in the lanthanide series. As with most metallic ions, terbium readily forms salts with chlorides, nitrates and hydroxides, with the latter being insoluble in water. These salts readily undergo decomposition in high temperatures in water. Haeseler *et. al.* showed a thermal decomposition of $TbCl_3{\cdot}6H_2O$ in water, which only required 65°C to start displacing aqua molecules in the solvent sphere (152,153). Increasing the temperature results in further loss of the aqua ligands and

the formation of a highly stable TbOCl, an irreversible product (152,153). Like many rare earth metals, terbium forms terbium oxide clusters with a general formula of Tb_nO_{2n-2m}, (n = 7, 9, 11, 12, 16, 19, 24, 29, 39, 40, 48, 62, and 88; m = 1, 2, 3, 4, 6, and 8), with a coordination number of 8-9 (150,154). These oxide clusters have been used in various biomedical fields, such as imaging, where stability of metal complexes is a concern (150,151). In addition, terbium has been incorporated in metal-organic frameworks, which amplify the natural fluorescence and magnetic properties of terbium (151,155–158). Compared to organic-only based fluorescent dyes, terbium(III) luminescent compounds have longer emitting lifetimes and sharper emission profiles. As a consequence, short-lived autofluorescence, scattering light, or photobleaching interference can easily be resolved, resulting in more accurate quantification (159). However, these effects are largely due to the organic ligand structure, which absorbs light upon excitation and transfers the energy to the terbium(III), commonly referred to as the "antenna effect", which is well-demonstrated with graphene quantum dot ligands by S. Wang *et al*. (160)

1.3.3.2 Terbium radionuclides for medicinal applications

[^{161}Tb]$TbCl_3$ is produced by neutron bombardment of a ^{160}Gd precursor, with high isolated specific activity (>4 TBq/mg) (83,161). It decays via β^--emissions, making it suitable for β⁻therapy (**Figure 1.15**). In addition, the co-emission of gamma rays (Eγ = 49 keV, I = 17.0%; Eγ = 75 keV, I = 10.2%), allows for SPECT imaging, as illustrated with the first-in-human study of [^{161}Tb]Tb-DOTATOC (162). Because the Eγ = 75 keV is close to the lead scatter gamma peak, it is often difficult to quantify the activity of ^{161}Tb. Because of its similar decay process and physical half-life, ^{161}Tb is often considered a promising alternative for ^{177}Lu (β^--emitter, $t_{1/2}$ = 6.7 days, $E_{\beta^-,avg}$ = 0.134 MeV) (163). Often in pre-clinical experiments, ^{161}Tb-labelled compounds have shown increased potency in tumour reduction and longevity of tumour-bearing mice over ^{177}Lu-labelled compounds (163). Comparative studies performed by Müller *et. al.* showed increased potency when comparing the therapeutic potential of [^{161}Tb]Tb-cm09 to [^{177}Lu]Lu-cm09 when treating KB (human cervical carcinoma) and IGROV-1 (human ovarian carcinoma) cancer cells, both *in vitro* and *in vivo* (106). In another comparative study using PSMA derivatives, increased survival of prostate cancer tumour-bearing mice was observed when treated with the same activity amount [^{161}Tb]Tb-DOTA-PSMA-617 compared to [^{177}Lu]Lu-DOTA-PSMA-617 (146). Additionally, a clinical case study have also shown [^{161}Tb]Tb-PSMA-617 to reduce cancer related antigens by 53% four weeks post treatment to cancers which no longer show effect to ^{177}Lu (164,165). It has been hypothesised that the added potency/efficacy of ^{161}Tb is due to co-emissions of ~2 Auger electrons (E_{e^-} = 5.1 keV per decay) and ~5 conversion electrons (E_{e^-} = 39.3 keV per decay). These are high linear energy transfer electrons, which can cause radiotoxicity within very short range. Therefore, the therapeutic potential of ^{161}Tb is expected to be maximal when the radioisotope is close to the cell membrane or internalised. Currently, ^{161}Tb is the only radioisotope in the terbium series which is produced routinely in high yields for research.

A promising radionuclide for TAT, ^{149}Tb can decay by high α-energy decay (E_{avg} = 3.97 MeV, 16.7%), β^+ (E_{avg} = 0.71 MeV, 7.3%) or EC decay (E_{avg} = 0.66 MeV, 76.2%) (**Figure 1.15**). This allows for dynamic treatment and follow-up PET imaging with the same radionuclide. An α tissue range of 25–28 μm and LET value of 140–142 keV/μm is ideal for TAT. A major concern with ^{149}Tb is the complexity of the production of clinically relevant amounts of activity. Currently, ^{149}Tb is produced by spallation reactions with a tantalum target,

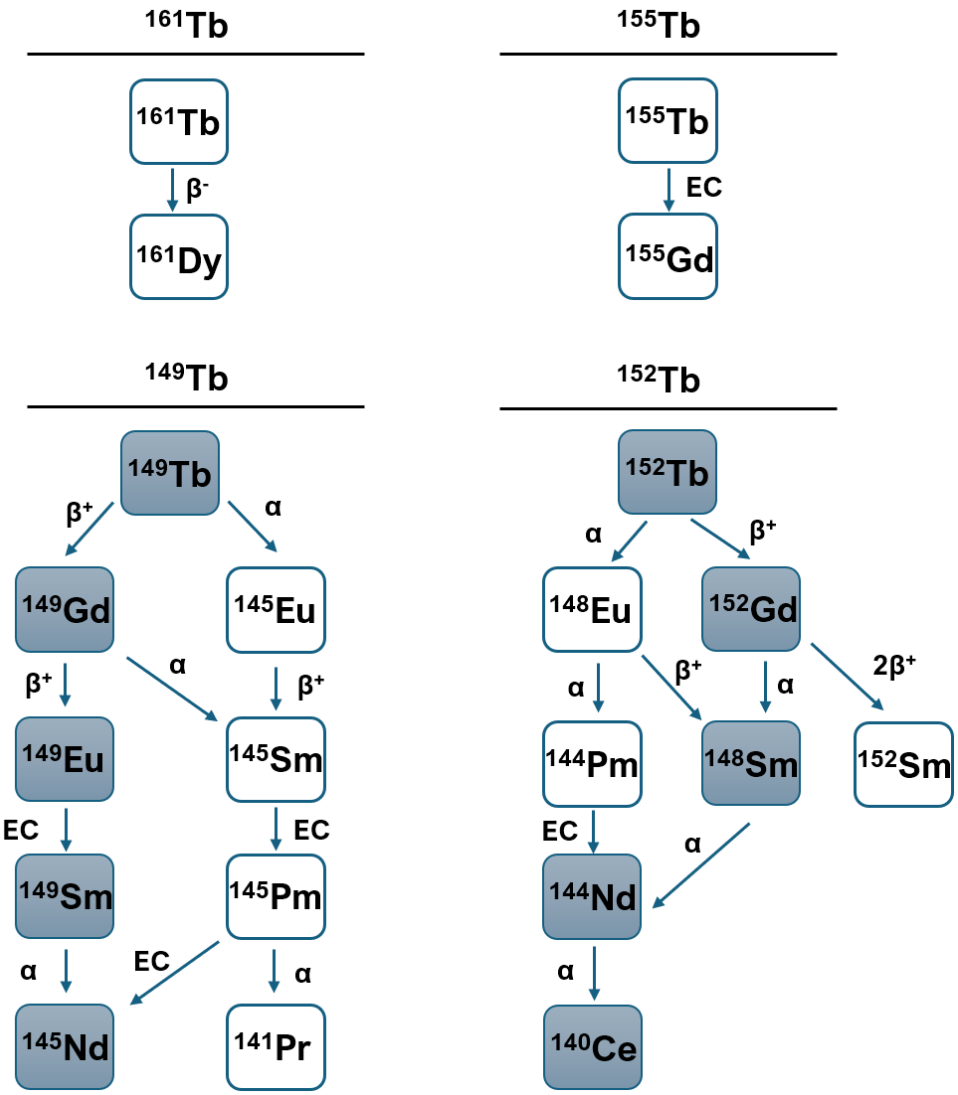


Figure 1.15. Decay schemes for ^{161}Tb, ^{155}Tb, ^{152}Tb and ^{149}Tb. For ^{149}Tb and ^{152}Tb, the highest probable decay pathway is shaded. Information extracted from www.periodictable.com (accessed 17 May 2024) and www-nds.iaea.org (accessed 17 May 2024).

with a low production yield. Rahman *et. al.* investigated the proton beam energy required to produce the radionuclide in high yields and found a proton energy in excess of 75 MeV is required for maximum production yields (703 GBq/mA.h) (161). However, the short half-life can be a logistical concern for

^{149}Tb-radiopharmaceuticals. In addition, the high radiation dose from daughter radionuclides can be of concern.

^{152}Tb decays via positron emission (20%), with an average β^+ energy of 1.14 MeV. Alternatively, it decays via electron capture (80%), with the most abundant γ energy of 344.3 keV (63.5%) (**Figure 1.15**). It is produced by heavy ion or proton spallation reactions, followed by mass separation (166,167). Due to low yields from the production, very few studies have been performed with ^{152}Tb. Of the studies performed, an in-human study using the aforementioned PSMA-617 showed great image resolution. Though only 140 MBq was injected, PET/CT scans was still visually satisfying (167). Unfortunately, like ^{149}Tb, the main concern is production, with <1% of the ^{155}Tb extracted from mass separation.

^{155}Tb undergoes electron capture, yielding 3 distinct γ-energies, with the most abundant being 105 keV (25%) (**Figure 1.15**). These energies fall within the ideal low-energy SPECT energies. [^{155}Tb]$TbCl_3$ is produced in upwards of ~300 MBq from spallation targets, which are then purified using an offline mass separation (168). This technique involves passing ions through a magnetic field, changing the direction of the particle. This degree of change is related to the mass/charge of the particle.^{155}Tb is produced in the same Ta spallation target as ^{149}Tb and ^{152}Tb, with mass 155 separation and collection. It is reported that $^{139}Ce^{16}O$ is also collected, and has to first be removed chemically (169).

Though terbium has four radionuclides which can access all avenues of the theragnostic space, the main concern is the production of relevant amounts of activity of these isotopes. Much research is currently going into different production pathways, such as using light charge particle activation and heavy ion activation (145). At this stage, only the production of ^{161}Tb is feasible for clinical and commercial use, with ^{155}Tb production yields steadily increasing. Although the other terbium radionuclides are currently not for the present, the terbium series is a very promising homonuclear theragnostic pair for the future.

1.4 References

1. Siegel RL, Miller KD, Fuchs HE, Jemal A. Cancer statistics, 2022. *CA Cancer J Clin* (2022) **72**:7–33. doi:10.3322/caac.21708

2. CRUK. Types of cancer. *Cancer Res UK* (2022)1. Available at: https://www.cancerresearchuk.org/what-is-cancer/how-cancer-starts/types-of-cancer#main [Accessed January 22, 2023]

3. Dagogo-Jack I, Shaw AT. Tumour heterogeneity and resistance to cancer therapies. *Nat Rev Clin Oncol* (2018) **15**:81–94. doi:10.1038/nrclinonc.2017.166

4. Parakh S, Lee ST, Gan HK, Scott AM. Radiolabeled Antibodies for Cancer Imaging and Therapy. *Cancers (Basel)* (2022) **14**:1–23. doi:10.3390/cancers14061454

5. Dalmartello M, La Vecchia C, Bertuccio P, Boffetta P, Levi F, Negri E, Malvezzi M. European cancer mortality predictions for the year 2022 with focus on ovarian cancer. *Ann Oncol* (2022) **33**:330–339. doi:10.1016/j.annonc.2021.12.007

6. Vasan N, Baselga J, Hyman DM. A view on drug resistance in cancer. *Nature* (2019) **575**:299–309. doi:10.1038/s41586-019-1730-1

7. Arruebo M, Vilaboa N, Sáez-Gutierrez B, Lambea J, Tres A, Valladares M, González-Fernández Á. Assessment of the evolution of cancer treatment therapies. *Cancers (Basel)* (2011) **3**:3279–3330. doi:10.3390/cancers3033279

8. NIH. Types of Cancer Treatment. *Natl Cancer Inst* (2023)1. Available at: https://www.cancer.gov/about-cancer/treatment/types [Accessed January 22, 2023]

9. CRUK. Treatment for cancer. *Cancer Res UK* (2023) Available at: https://www.cancerresearchuk.org/about-cancer/treatment [Accessed January 22, 2023]

10. ACS. Treating Liver Cancer. *Am Cancer Soc* (2023) Available at: https://www.cancer.org/cancer/types/liver-cancer/treating.html [Accessed January 22, 2023]

11. Milkovic L, Gasparovic AC, Cindric M, Mouthuy PA, Zarkovic N. Short overview of ROS as cell function regulators and their implications in therapy concepts. *Cells* (2019) **8**:1–14. doi:10.3390/cells8080793

12. Rosenberg B, VanCamp L, Trosko JE, Mansour VH. Platinum compounds: A new class of potent antitumour agents [24]. *Nature* (1969) **222**:385–386. doi:10.1038/222385a0

13. Schroeder A, Heller DA, Winslow MM, Dahlman JE, Pratt GW, Langer R, Jacks T, Anderson

DG. Treating metastatic cancer with nanotechnology. *Nat Rev Cancer* (2012) **12**:39–50. doi:10.1038/nrc3180

14. Bhandari PR. Recent advances in pharmacotherapy of chemotherapy-induced nausea and vomiting. *J Adv Pharm Technol Res* (2012) **3**:202–209. doi:10.4103/2231-4040.104710

15. Medici S, Peana M, Nurchi VM, Lachowicz JI, Crisponi G, Zoroddu MA. Noble metals in medicine: Latest advances. *Coord Chem Rev* (2015) **284**:329–350. doi:10.1016/j.ccr.2014.08.002

16. Pucci C, Martinelli C, Ciofani G. Innovative approaches for cancer treatment: Current perspectives and new challenges. *Ecancermedicalscience* (2019) **13**:1–26. doi:10.3332/ecancer.2019.961

17. Bailly C, Vidal A, Bonnemaire C, Kraeber-Bodéré F, Chérel M, Pallardy A, Rousseau C, Garcion E, Lacoeuille F, Hindré F, et al. Potential for Nuclear Medicine Therapy for Glioblastoma Treatment. *Front Pharmacol* (2019) **10**:1–9. doi:10.3389/fphar.2019.00772

18. Postow MA, Sidlow R, Hellmann MD. Immune-Related Adverse Events Associated with Immune Checkpoint Blockade. *N Engl J Med* (2018) **378**:158–168. doi:10.1056/nejmra1703481

19. Pouget JP, Navarro-Teulon I, Bardiès M, Chouin N, Cartron G, Pèlegrin A, Azria D. Clinical radioimmunotherapy-the role of radiobiology. *Nat Rev Clin Oncol* (2011) **8**:720–734. doi:10.1038/nrclinonc.2011.160

20. Ling X, Cutler CS, Anderson CJ. *The Radiopharmaceutical Chemistry of the Radioisotopes of Copper*. Cham: Springer International Publishing (2019). doi:10.1007/978-3-319-98947-1_19

21. Hurwitz MD, Halabi S, Archer L, McGinnis LS, Kuettel MR, Dibiase SJ, Small EJ. Combination external beam radiation and brachytherapy boost with androgen deprivation for treatment of intermediate-risk prostate cancer: Long-term results of CALGB 99809. *Cancer* (2011) **117**:5579–5588. doi:10.1002/cncr.26203

22. Pompos A, Durante M, Choy H. Heavy Ions in Cancer Therapy. *JAMA Oncol* (2016) **2**:1539–1540. doi:10.1001/jamaoncol.2016.2646

23. Rocha PHP, Reali RM, Decnop M, Souza SA, Teixeira LAB, Lucas Júnior A, Sarpi MO, Cintra MB, Pinho MC, Garcia MRT. Adverse Radiation Therapy Effects in the Treatment of Head and Neck Tumors. *Radiographics* (2022) **42**:806–821. doi:10.1148/rg.210150

24. Desouky O, Ding N, Zhou G. Targeted and non-targeted effects of ionizing radiation. *J Radiat Res Appl Sci* (2015) **8**:247–254. doi:10.1016/j.jrras.2015.03.003

25. Jowanaridhi B, Sriwiang W. Radiolabeling efficiency and stability study on Lutetium-177 labeled bombesin peptide. *J Phys Conf Ser* (2019) **1380**: doi:10.1088/1742-6596/1380/1/012020

26. Umbricht CA, Köster U, Bernhardt P, Gracheva N, Johnston K, Schibli R, van der Meulen NP, Müller C. Alpha-PET for Prostate Cancer: Preclinical investigation using ^{149}Tb-PSMA-617. *Sci Rep* (2019) **9**:1–10. doi:10.1038/s41598-019-54150-w

27. Müller C, Domnanich KA, Umbricht CA, Van Der Meulen NP. Scandium and terbium radionuclides for radiotheranostics: Current state of development towards clinical application. *Br J Radiol* (2018) **91**: doi:10.1259/bjr.20180074

28. Mishiro K, Hanaoka H, Yamaguchi A, Ogawa K. Radiotheranostics with radiolanthanides: Design, development strategies, and medical applications. *Coord Chem Rev* (2019) **383**:104–131. doi:10.1016/j.ccr.2018.12.005

29. Duatti A. Review on ^{99m}Tc radiopharmaceuticals with emphasis on new advancements. *Nucl Med Biol* (2021) **92**:202–216. doi:10.1016/j.nucmedbio.2020.05.005

30. Phelps ME. Positron emission tomography provides molecular imaging of biological processes. *Proc Natl Acad Sci U S A* (2000) **97**:9226–9233. doi:10.1073/pnas.97.16.9226

31. Ametamey SM, Honer M, Schubiger PA. Molecular imaging with PET. *Chem Rev* (2008) **108**:1501–1516. doi:10.1021/cr0782426

32. Willmann JK, Bruggen N Van, Dinkelborg LM, van Bruggen N, Dinkelborg LM, Gambhir SS. Molecular imaging in drug development. *Nat Rev Drug Discov* (2008) **7**:591–607. doi:10.1038/nrd2290

33. Boros E, Holland JP. Chemical aspects of metal ion chelation in the synthesis and application antibody-based radiotracers. *J Label Compd Radiopharm* (2018) **61**:652–671. doi:10.1002/jlcr.3590

34. Pereira E, Do Quental L, Palma E, Oliveira MC, Mendes F, Raposinho P, Correia I, Lavrado J, Di Maria S, Belchior A, et al. Evaluation of Acridine Orange Derivatives as DNA-Targeted Radiopharmaceuticals for Auger Therapy: Influence of the Radionuclide and Distance to DNA. *Sci Rep* (2017) **7**:1–16. doi:10.1038/srep42544

35. Ku A, Facca VJ, Cai Z, Reilly RM. Auger electrons for cancer therapy – a review. *EJNMMI Radiopharm Chem* (2019) **4**: doi:10.1186/s41181-019-0075-2

36. Ahenkorah S, Cassells I, Deroose CM, Cardinaels T, Burgoyne AR, Bormans G, Ooms M,

Cleeren F. Bismuth-213 for targeted radionuclide therapy: From atom to bedside. *Pharmaceutics* (2021) **13**:1–25. doi:10.3390/pharmaceutics13050599

37. Beierwaltes WH. The treatment of hyperthyroidism with iodine-131. *Semin Nucl Med* (1978) **8**:95–103. doi:10.1016/S0001-2998(78)80010-5

38. Ballinger JR. Theranostics and precision medicine special feature: Review Article Theranostic radiopharmaceuticals: established agents in current use. *Br J Radiol* (2018) **91**:20170969. Available at: http://europepmc.org/backend/ptpmcrender.fcgi?accid=PMC6475961&blobtype=pdf

39. Boros E, Packard AB. Radioactive Transition Metals for Imaging and Therapy. *Chem Rev* (2019) **119**:870–901. doi:10.1021/acs.chemrev.8b00281

40. Augusto RM dos S, Buehler L, Lawson Z, Marzari S, Stachura M, Stora T. CERN-MEDICIS (medical isotopes collected from ISOLDE): A new facility. *Appl Sci* (2014) **4**:265–281. doi:10.3390/app4020265

41. Blower PJ. A nuclear chocolate box: The periodic table of nuclear medicine. *Dalt Trans* (2015) **44**:4819–4844. doi:10.1039/c4dt02846e

42. Ljungberg M, Pretorius PH. SPECT/CT: an update on technological developments and clinical applications. *Br J Radiol* (2018) **91**:20160402. doi:10.1259/bjr.20160402

43. Tomasi G, Nabulsi N, Zheng M-Q, Weinzimmer D, Ropchan J, Blumberg L, Brown-Proctor C, Ding Y-S, Carson RE, Huang Y. Determination of In Vivo B max and K d for 11 C-GR103545, an Agonist PET Tracer for κ-Opioid Receptors: A Study in Nonhuman Primates. *J Nucl Med* (2013) **54**:600–608. doi:10.2967/jnumed.112.112672

44. Farde L, Halldin C, Stone-Elander S, Sedvall G. PET analysis of human dopamine receptor subtypes using ^{11}C-SCH 23390 and 11C-raclopride. *Psychopharmacology (Berl)* (1987) **92**:278–284. doi:10.1007/BF00210831

45. Farde L, Hall H, Ehrin E, Sedvall G. Quantitative analysis of D2 dopamie receptor binding in the living human brain by PET. *Science (80-)* (1986) **231**:258–261. doi:10.1126/science.2867601

46. Levin CS, Hoffman EJ. Calculation of positron range and its effect on the fundamental limit of positron emission tomography system spatial resolution. *Phys Med Biol* (1999) **44**:781–799. doi:10.1088/0031-9155/44/3/019

47. Talip Z, Favaretto C, Geistlich S, Van Der Meulen NP. A step-by-step guide for the novel radiometal production for medical applications: Case studies with ^{68}Ga, ^{44}Sc, ^{177}Lu and ^{161}Tb.

Molecules (2020) **25**: doi:10.3390/molecules25040966

48. Serdons K, Verbruggen A, Bormans GM. Developing new molecular imaging probes for PET. *Methods* (2009) **48**:104–111. doi:10.1016/j.ymeth.2009.03.010

49. Vermeulen K, Vandamme M, Bormans G, Cleeren F. Design and Challenges of Radiopharmaceuticals. *Semin Nucl Med* (2019) **49**:339–356. doi:10.1053/j.semnuclmed.2019.07.001

50. Srinivasan S, Crandall JP, Gajwani P, Sgouros G, Mena E, Lodge MA, Wahl RL. Human radiation dosimetry for orally and intravenously administered ^{18}F-FDG. *J Nucl Med* (2020) **61**:613–619. doi:10.2967/jnumed.119.233288

51. Sowa AR, Jackson IM, Desmond TJ, Alicea J, Mufarreh AJ, Pham JM, Stauff J, Winton WP, Fawaz M V., Henderson BD, et al. Futureproofing [^{18}F]Fludeoxyglucose manufacture at an Academic Medical Center. *EJNMMI Radiopharm Chem* (2018) **3**:1–12. doi:10.1186/s41181-018-0048-x

52. Brown RKJ, Bohnen NI, Wong KK, Minoshima S, Frey KA. Brain PET in suspected dementia: Patterns of altered FDG metabolism. *Radiographics* (2014) **34**:684–701. doi:10.1148/rg.343135065

53. Li Z, Conti PS. Radiopharmaceutical chemistry for positron emission tomography. *Adv Drug Deliv Rev* (2010) **62**:1031–1051. doi:10.1016/j.addr.2010.09.007

54. Horitsugi G, Watabe T, Kanai Y, Ikeda H, Kato H, Naka S, Ishibashi M, Matsunaga K, Isohashi K, Shimosegawa E, et al. Oxygen-15 labeled CO_2, O_2, and CO PET in small animals: evaluation using a 3D-mode microPET scanner and impact of reconstruction algorithms. *EJNMMI Res* (2017) **7**: doi:10.1186/s13550-017-0335-7

55. Deng X, Rong J, Wang L, Vasdev N, Zhang L, Josephson L, Liang SH. Chemistry for Positron Emission Tomography: Recent Advances in ^{11}C-, ^{18} F-, ^{13} N-, and ^{15} O-Labeling Reactions. *Angew Chemie - Int Ed* (2019) **58**:2580–2605. doi:10.1002/anie.201805501

56. Kostelnik TI, Orvig C. Radioactive Main Group and Rare Earth Metals for Imaging and Therapy. *Chem Rev* (2019) **119**:902–956. doi:10.1021/acs.chemrev.8b00294

57. Phowira J, Coffey KL, Bartholomew PH, Vennart N, Moreira M, Emerson H, Kennedy D, Weaver JU. Radioactive Iodine for the Treatment of Subclinical Thyrotoxicosis Grade 1 and 2: Outcome of up to 18-Year Follow Up. *Front Endocrinol (Lausanne)* (2022) **13**:1–9. doi:10.3389/fendo.2022.843857

58. Gawne PJ, Man F, Blower PJ, De Rosales RTM, Rosales RTM De. Direct Cell Radiolabeling for in Vivo Cell Tracking with PET and SPECT Imaging. *Chem Rev* (2022) **122**:10266–10318. doi:10.1021/acs.chemrev.1c00767

59. Pericleous M, Toumpanakis C, Lumgair H, Caplin ME, Morgan-Rowe L, Clark I, Luong TV. Gastric mixed adenoneuroendocrine carcinoma with a trilineage cell differentiation: Case report and review of the literature. *Case Rep Oncol* (2012) **5**:313–319. doi:10.1159/000339611

60. Hu ZI, McArthur HL, Ho AY. The Abscopal Effect of Radiation Therapy: What Is It and How Can We Use It in Breast Cancer? *Curr Breast Cancer Rep* (2017) **9**:45–51. doi:10.1007/s12609-017-0234-y

61. Imlimthan S, Moon ES, Rathke H, Afshar-Oromieh A, Rösch F, Rominger A, Gourni E. New frontiers in cancer imaging and therapy based on radiolabeled fibroblast activation protein inhibitors: A rational review and current progress. *Pharmaceuticals* (2021) **14**:1023. doi:10.3390/PH14101023

62. Nuszkiewicz J, Woźniak A, Szewczyk-Golec K. Ionizing Radiation as a Source of Oxidative Stress—The Protective Role of Melatonin and Vitamin D. *Int J Mol Sci* (2020) **21**:5804. doi:10.3390/ijms21165804

63. Chen Z, Han F, Du Y, Shi H, Zhou W. Hypoxic microenvironment in cancer: molecular mechanisms and therapeutic interventions. *Signal Transduct Target Ther* (2023) **8**:70. doi:10.1038/s41392-023-01332-8

64. Hatten SJ, Lehrer EJ, Liao J, Sha CM, Trifiletti DM, Siva S, McBride SM, Palma D, Holder SL, Zaorsky NG. A Patient-Level Data Meta-analysis of the Abscopal Effect. *Adv Radiat Oncol* (2022) **7**:100909. doi:10.1016/j.adro.2022.100909

65. Janopaul-Naylor JR, Shen Y, Qian DC, Buchwald ZS. The Abscopal Effect: A Review of Pre-Clinical and Clinical Advances. *Int J Mol Sci* (2021) **22**:11061. doi:10.3390/ijms222011061

66. Poty S, Francesconi LC, McDevitt MR, Morris MJ, Lewis JS. α-Emitters for Radiotherapy: From Basic Radiochemistry to Clinical Studies—Part 1. *J Nucl Med* (2018) **59**:878–884. doi:10.2967/jnumed.116.186338

67. Hennrich U, Kopka K. Lutathera®: The first FDA-and EMA-approved radiopharmaceutical for peptide receptor radionuclide therapy. *Pharmaceuticals* (2019) **12**: doi:10.3390/ph12030114

68. Farolfi A, Calderoni L, Mattana F, Mei R, Telo S, Fanti S, Castellucci P. Current and Emerging Clinical Applications of PSMA PET Diagnostic Imaging for Prostate Cancer. *J Nucl Med* (2021) **62**:596–604. doi:10.2967/jnumed.120.257238

69. Strosberg J, El-Haddad G, Wolin E, Hendifar A, Yao J, Chasen B, Mittra E, Kunz PL, Kulke MH, Jacene H, et al. Phase 3 Trial of ^{177} Lu-Dotatate for Midgut Neuroendocrine Tumors. *N Engl J Med* (2017) **376**:125–135. doi:10.1056/nejmoa1607427

70. Sartor O, Herrmann K. Prostate Cancer Treatment: ^{177}Lu-PSMA-617 Considerations, Concepts, and Limitations. *J Nucl Med* (2022) **63**:823–829. doi:10.2967/jnumed.121.262413

71. Feuerecker B, Tauber R, Knorr K, Heck M, Beheshti A, Seidl C, Bruchertseifer F, Pickhard A, Gafita A, Kratochwil C, et al. Activity and Adverse Events of Actinium-225-PSMA-617 in Advanced Metastatic Castration-resistant Prostate Cancer After Failure of Lutetium-177-PSMA[Formula presented]. *Eur Urol* (2021) **79**:343–350. doi:10.1016/j.eururo.2020.11.013

72. Morgenstern A, Apostolidis C, Kratochwil C, Sathekge M, Krolicki L, Bruchertseifer F. An Overview of Targeted Alpha Therapy with ^{225} Actinium and 213 Bismuth . *Curr Radiopharm* (2018) **11**:200–208. doi:10.2174/1874471011666180502104524

73. Müller C, Busslinger S, Fluehmann F, Borgna F, Köster U, Zeevaart J, Grundler P, van der Meulen N, Schibli R. Cell membrane localization of terbium-161 using peptide receptor antagonists: can we profit from Auger electron emission with non-internalizing targeting agents? *Nucl Med Biol* (2022) **114**–**115**:S26. doi:10.1016/S0969-8051(22)02145-X

74. Chaturvedi S, Mishra AK. Small molecule radiopharmaceuticals - A review of current approaches. *Front Med* (2016) **3**:1–18. doi:10.3389/fmed.2016.00005

75. Jacobson O, Kiesewetter DO, Chen X. Fluorine-18 radiochemistry, labeling strategies and synthetic routes. *Bioconjug Chem* (2015) **26**:1–18. doi:10.1021/bc500475e

76. Farkaš P, Bystrický S. Chemical conjugation of biomacromolecules: A mini-review. *Chem Pap* (2010) **64**:683–695. doi:10.2478/s11696-010-0057-z

77. Fay R, Holland JP. The impact of emerging bioconjugation chemistries on radiopharmaceuticals. *J Nucl Med* (2019) **60**:587–591. doi:10.2967/jnumed.118.220806

78. Price EW, Orvig C. Matching chelators to radiometals for radiopharmaceuticals. *Chem Soc Rev* (2014) **43**:260–290. doi:10.1039/c3cs60304k

79. Zhang J, Shukla V, Boger DL. Inverse Electron Demand Diels-Alder Reactions of Heterocyclic Azadienes, 1-Aza-1,3-Butadienes, Cyclopropenone Ketals, and Related Systems. A Retrospective. *J Org Chem* (2019) **84**:9397–9445. doi:10.1021/acs.joc.9b00834

80. Sarrett SM, Keinänen O, Dayts EJ, Dewaele-Le Roi G, Rodriguez C, Carnazza KE, Zeglis BM. Inverse electron demand Diels–Alder click chemistry for pretargeted PET imaging and

radioimmunotherapy. *Nat Protoc* (2021) **16**:3348–3381. doi:10.1038/s41596-021-00540-2

81. Pees A, Chassé M, Lindberg A, Vasdev N. Recent Developments in Carbon-11 Chemistry and Applications for First-In-Human PET Studies. *Molecules* (2023) **28**:931. doi:10.3390/molecules28030931

82. Pauwels E, Cleeren F, Tshibangu T, Koole M, Serdons K, Dekervel J, Van Cutsem E, Verslype C, Van Laere K, Bormans G, et al. [^{18}F]AlF-NOTA-octreotide PET imaging: biodistribution, dosimetry and first comparison with [^{68}Ga]Ga-DOTATATE in neuroendocrine tumour patients. *Eur J Nucl Med Mol Imaging* (2020) **47**:3033–3046. doi:10.1007/s00259-020-04918-4

83. Cassells I, Ahenkorah S, Burgoyne AR, Van de Voorde M, Deroose CM, Cardinaels T, Bormans G, Ooms M, Cleeren F. Radiolabeling of Human Serum Albumin With Terbium-161 Using Mild Conditions and Evaluation of in vivo Stability. *Front Med* (2021) **8**:1–12. doi:10.3389/fmed.2021.675122

84. Thiele NA, Brown V, Kelly JM, Amor-coarasa A, Jermilova U, Macmillan SN, Nikolopoulou A, Ponnala S, Ramogida CF, Robertson AKH, et al. Communications Radiopharmaceuticals Hot Paper An Eighteen-Membered Macrocyclic Ligand for Actinium-225 Targeted Alpha Therapy. (2017)14712–14717. doi:10.1002/anie.201709532

85. Thiele NA, Brown V, Kelly JM, Amor-Coarasa A, Jermilova U, MacMillan SN, Nikolopoulou A, Ponnala S, Ramogida CF, Robertson AKHH, et al. An Eighteen-Membered Macrocyclic Ligand for Actinium-225 Targeted Alpha Therapy. *Angew Chemie - Int Ed* (2017) **56**:14712–14717. doi:10.1002/anie.201709532

86. de Jong M, Rolleman EJ, Bernard BF, Visser TJ, Bakker WH, Breeman WA, Krenning EP. Inhibition of renal uptake of indium-111-DTPA-octreotide in vivo. *J Nucl Med* (1996) **37**:1388–92. Available at: http://www.ncbi.nlm.nih.gov/pubmed/8708781

87. Chong HS, Sun X, Chen Y, Sin I, Kang CS, Lewis MR, Liu D, Ruthengael VC, Zhong Y, Wu N, et al. Synthesis and comparative biological evaluation of bifunctional ligands for radiotherapy applications of ^{90}Y and ^{177}Lu. *Bioorganic Med Chem* (2015) **23**:1169–1178. doi:10.1016/j.bmc.2014.12.035

88. Abbas Rizvi SM, Song E, Raja C, Beretov J, Morgenstern A, Apostolidis C, Russell PJ, Kearsley JH, Abbas K, Allen BJ. Preparation and testing of bevacizumab radioimmunoconjugates with bismuth-213 and bismuth-205/bismuth-206. *Cancer Biol Ther* (2008) **7**:1547–1554. doi:10.4161/cbt.7.10.6538

89. Dadwal M, Kang CS, Song HA, Sun X, Dai A, Baidoo KE, Brechbiel MW, Chong H-S. Synthesis

and evaluation of a bifunctional chelate for development of Bi(III)-labeled radioimmunoconjugates. *Bioorg Med Chem Lett* (2011) **21**:7513–7515. doi:10.1016/j.bmcl.2011.06.107

90. Price EW, Cawthray JF, Adam MJ, Orvig C. Modular syntheses of H_4octapa and H_2dedpa, and yttrium coordination chemistry relevant to $^{86}Y/^{90}Y$ radiopharmaceuticals. *J Chem Soc Dalt Trans* (2014) **43**:7176–7190. doi:10.1039/c4dt00239c

91. Bailey GA, Price EW, Zeglis BM, Ferreira CL, Boros E, Lacasse MJ, Patrick BO, Lewis JS, Adam MJ, Orvig C. H_2azapa: A versatile acyclic multifunctional chelator for ^{67}Ga, ^{64}Cu, ^{111}In, and ^{177}Lu. *Inorg Chem* (2012) **51**:12575–12589. doi:10.1021/ic302225z

92. Al-Zubaidi M, Viswambaram P, McCombie S, Liow E, Lenzo N, Ferguson T, Redfern AD, Gauci R, Hayne D. ^{89} Zirconium-labelled girentuximab (^{89} Zr-TLX250) PET in Urothelial Cancer Patients (ZiPUP): Protocol for a phase i trial of a novel staging modality for urothelial carcinoma. *BMJ Open* (2022) **12**:1–5. doi:10.1136/bmjopen-2021-060478

93. Kang CS, Sun X, Jia F, Song HA, Chen Y, Lewis M, Chong HS. Synthesis and preclinical evaluation of bifunctional ligands for improved chelation chemistry of ^{90}Y and ^{177}Lu for targeted radioimmunotherapy. *Bioconjug Chem* (2012) **23**:1775–1782. doi:10.1021/bc200696b

94. Ahenkorah S, Murce E, Cawthorne C, Ketchemen JP, Deroose CM, Cardinaels T, Seimbille Y, Fonge H, Gsell W, Bormans G, et al. 3p-C-NETA: A versatile and effective chelator for development of Al^{18}F-labeled and therapeutic radiopharmaceuticals. *Theranostics* (2022) **12**:5971–5985. doi:10.7150/thno.75336

95. Tiernan JP, Perry SL, Verghese ET, West NP, Yeluri S, Jayne DG, Hughes TA. Carcinoembryonic antigen is the preferred biomarker for in vivo colorectal cancer targeting. *Br J Cancer* (2013) **108**:662–667. doi:10.1038/bjc.2012.605

96. Chang SS. Overview of prostate-specific membrane antigen. *Rev Urol* (2004) **6 Suppl 10**:S13-8. Available at: http://www.ncbi.nlm.nih.gov/pubmed/16985927%0Ahttp://www.pubmedcentral.nih.gov/articlerender.fcgi?artid=PMC1472940

97. Gee AD, Bongarzone S, Wilson AA. Small Molecules as Radiopharmaceutical Vectors. *Radiopharm Chem* (2019) **4**:119–136. doi:10.1007/978-3-319-98947-1_7

98. Gotthardt M, Van Eerd-Vismale J, Oyen WJG, De Jong M, Zhang H, Rolleman E, Maecke HR, Béhé M, Boerman O. Indication for different mechanisms of kidney uptake of radiolabeled peptides. *J Nucl Med* (2007) **48**:596–601. doi:10.2967/jnumed.106.036020

99. Li Q, Kang C. Mechanisms of action for small molecules revealed by structural biology in drug discovery. *Int J Mol Sci* (2020) **21**:1–18. doi:10.3390/ijms21155262

100. Agrawal A, Rangarajan V, Shah S, Puranik A, Purandare N. MIBG (Metaiodobenzylguanidine) Theranostics in pediatric and adult malignancies. *Br J Radiol* (2018) **91**: doi:10.1259/bjr.20180103

101. Zhao Z, Ukidve A, Kim J, Mitragotri S. Targeting Strategies for Tissue-Specific Drug Delivery. *Cell* (2020) **181**:151–167. doi:10.1016/j.cell.2020.02.001

102. Kręcisz P, Czarnecka K, Królicki L, Mikiciuk-Olasik E, Szymański P. Radiolabeled Peptides and Antibodies in Medicine. *Bioconjug Chem* (2021) **32**:25–42. doi:10.1021/acs.bioconjchem.0c00617

103. Apostolopoulos V, Bojarska J, Chai TT, Elnagdy S, Kaczmarek K, Matsoukas J, New R, Parang K, Lopez OP, Parhiz H, et al. A global review on short peptides: Frontiers and perspectives. *Molecules* (2021) **26**: doi:10.3390/molecules26020430

104. Commission IJ, Nomenclature B. Nomenclature and Symbolism for Amino Acids and Peptides: Recommendations 1983. *Eur J Biochem* (1984) **138**:9–37. doi:10.1111/j.1432-1033.1984.tb07877.x

105. Osl T, Schmidt A, Schwaiger M, Schottelius M, Wester HJ. A new class of pentixa for and pentixa ther-based theranostic agents with enhanced CXCR4-targeting efficiency. *Theranostics* (2020) **10**:8264–8280. doi:10.7150/thno.45537

106. Müller C, Fischer E, Behe M, Köster U, Dorrer H, Reber J, Haller S, Cohrs S, Blanc A, Grünberg J, et al. Future prospects for SPECT imaging using the radiolanthanide terbium-155 - production and preclinical evaluation in tumor-bearing mice. *Nucl Med Biol* (2014) **41**:58–65. doi:10.1016/j.nucmedbio.2013.11.002

107. Klaus R, Niyazi M, Lange-Sperandio B. Radiation-induced kidney toxicity: molecular and cellular pathogenesis. *Radiat Oncol* (2021) **16**:1–11. doi:10.1186/s13014-021-01764-y

108. Severi S, Sansovini M, Ianniello A, Bodei L, Nicolini S, Ibrahim T, Di Iorio V, D'Errico V, Caroli P, Monti M, et al. Feasibility and utility of re-treatment with ^{177}Lu-DOTATATE in GEP-NENs relapsed after treatment with ^{90}Y-DOTATOC. *Eur J Nucl Med Mol Imaging* (2015) **42**:1955–1963. doi:10.1007/s00259-015-3105-7

109. Kumar KSA, Mathur A. A convenient total synthesis of PSMA-617: A prostate specific membrane antigen (PSMA) ligand for prostate cancer endotherapeutic applications. *Eur J Med Chem Reports* (2022) **6**:100084. doi:10.1016/j.ejmcr.2022.100084

110. Köhler, G., Milstein C. Cultivos continuos de células fusionadas que secretan anticuerpos de especificidad predefinida. *Nature* (1975) **256**:495–497. Available at: http://www.nature.com/articles/256495a0%0Apapers3://publication/doi/10.1038/256495a0

111. Lu RM, Hwang YC, Liu IJ, Lee CC, Tsai HZ, Li HJ, Wu HC. Development of therapeutic antibodies for the treatment of diseases. *J Biomed Sci* (2020) **27**:1–30. doi:10.1186/s12929-019-0592-z

112. Lin M, Paolillo V, Le DB, Macapinlac H, Ravizzini GC. Monoclonal antibody based radiopharmaceuticals for imaging and therapy. *Curr Probl Cancer* (2021) **45**:100796. doi:10.1016/j.currproblcancer.2021.100796

113. Zhao P, Zhang Y, Li W, Jeanty C, Xiang G, Dong Y. Recent advances of antibody drug conjugates for clinical applications. *Acta Pharm Sin B* (2020) **10**:1589–1600. doi:10.1016/j.apsb.2020.04.012

114. Bateman RJ, Cummings J, Schobel S, Salloway S, Vellas B, Boada M, Black SE, Blennow K, Fontoura P, Klein G, et al. Gantenerumab: an anti-amyloid monoclonal antibody with potential disease-modifying effects in early Alzheimer's disease. *Alzheimer's Res Ther* (2022) **14**:1–17. doi:10.1186/s13195-022-01110-8

115. Liapis V, Tieu W, Rudd SE, Donnelly PS, Wittwer NL, Brown MP, Staudacher AH. Improved non-invasive positron emission tomographic imaging of chemotherapy-induced tumor cell death using Zirconium-89-labeled APOMAB®. *EJNMMI Radiopharm Chem* (2020) **5**: doi:10.1186/s41181-020-00109-6

116. Mondello P, Cuzzocrea S, Navarra M, Mian M. ^{90}Y-ibritumomab tiuxetan: A nearly forgotten opportunity. *Oncotarget* (2016) **7**:7597–7609. doi:10.18632/oncotarget.6531

117. Nguyen A, Reyes AE, Zhang M, McDonald P, Wong WLT, Damico LA, Dennis MS. The pharmacokinetics of an albumin-binding Fab (AB.Fab) can be modulated as a function of affinity for albumin. *Protein Eng Des Sel* (2006) **19**:291–297. doi:10.1093/protein/gzl011

118. Knight JC, Mosley MJ, Kersemans V, Dias GM, Allen PD, Smart S, Cornelissen B. Dual-isotope imaging allows in vivo immunohistochemistry using radiolabelled antibodies in tumours. *Nucl Med Biol* (2019) **70**:14–22. doi:10.1016/j.nucmedbio.2019.01.010

119. Fichou N, Gouard S, Maurel C, Barbet J, Ferrer L, Morgenstern A, Bruchertseifer F, Faivre-Chauvet A, Bigot-Corbel E, Davodeau F, et al. Single-dose anti-CD138 radioimmunotherapy: Bismuth-213 is more efficient than lutetium-177 for treatment of multiple myeloma in a preclinical model. *Front Med* (2015) **2**: doi:10.3389/fmed.2015.00076

120. Dawicki W, Allen KJH, Jiao R, Malo ME, Helal M, Berger MS, Ludwig DL, Dadachova E. Daratumumab-^{225}Actinium conjugate demonstrates greatly enhanced antitumor activity against experimental multiple myeloma tumors. *Oncoimmunology* (2019) **8**:1–9. doi:10.1080/2162402X.2019.1607673

121. Le Reun E, Foray N. Low-Dose Radiation Therapy (LDRT) against Cancer and Inflammatory or Degenerative Diseases: Three Parallel Stories with a Common Molecular Mechanism Involving the Nucleoshuttling of the ATM Protein? *Cancers (Basel)* (2023) **15**: doi:10.3390/cancers15051482

122. Elhammali A, Amini B, Ludmir EB, Gunther JR, Milgrom SA, Pinnix CC, Andraos T, Yoder A, Weber D, Orlowski R, et al. New paradigm for radiation in multiple myeloma: lower yet effective dose to avoid radiation toxicity. *Haematologica* (2020) **105**:E355–E357. doi:10.3324/haematol.2019.235804

123. Kapoor V, Singh AK, Lewis CD, Deore S, Hallahan DE. Exploiting Radiation Induction of Antigens in Cancer: Targeted Drug Delivery. *Int J Mol Sci* (2022) **23**: doi:10.3390/ijms23063041

124. Rudmann DG. On-target and off-target-based toxicologic effects. *Toxicol Pathol* (2013) **41**:310–314. doi:10.1177/0192623312464311

125. Jallinoja VIJ, Houghton JL. Current Landscape in Clinical Pretargeted Radioimmunoimaging and Therapy. *J Nucl Med* (2021) **62**:1200–1206. doi:10.2967/jnumed.120.260687

126. Stéen EJL, Edem PE, Nørregaard K, Jørgensen JT, Shalgunov V, Kjaer A, Herth MM. *Pretargeting in nuclear imaging and radionuclide therapy: Improving efficacy of theranostics and nanomedicines*. (2018). doi:10.1016/j.biomaterials.2018.06.021

127. Cheal SM, Chung SK, Vaughn BA, Cheung NK V., Larson SM. Pretargeting: A Path Forward for Radioimmunotherapy. *J Nucl Med* (2022) **63**:1302–1315. doi:10.2967/jnumed.121.262186

128. Bailly C, Bodet-milin C, Rousseau C, Faivre-Chauvet A, Kraeber-bodéré F, Barbet J. Pretargeting for imaging and therapy in oncological nuclear medicine. *EJNMMI Radiopharm Chem* (2017) **2**: doi:10.1186/s41181-017-0026-8

129. Liang D, Wu K, Tei R, Bumpus TW, Ye J, Baskin JM. A real-time click chemistry imaging approach reveals stimulus-specific subcellular locations of phospholipase D activity. *Proc Natl Acad Sci U S A* (2019) **116**:15453–15462. doi:10.1073/pnas.1903949116

130. Billaud EMF, Shahbazali E, Ahamed M, Cleeren F, Noël T, Koole M, Verbruggen A, Hessel V, Bormans G. Micro-flow photosynthesis of new dienophiles for inverse-electron-demand Diels-

Alder reactions. Potential applications for pretargeted in vivo PET imaging. *Chem Sci* (2017) **8**:1251–1258. doi:10.1039/c6sc02933g

131. D'Onofrio A, Silva F, Gano L, Karczmarczyk U, Mikołajczak R, Garnuszek P, Paulo A. Clickable Radiocomplexes With Trivalent Radiometals for Cancer Theranostics: In vitro and in vivo Studies. *Front Med* (2021) **8**:1–9. doi:10.3389/fmed.2021.647379

132. Garousi J, Orlova A, Frejd FY, Tolmachev V. Imaging using radiolabelled targeted proteins: radioimmunodetection and beyond. *EJNMMI Radiopharm Chem* (2020) **5**: doi:10.1186/s41181-020-00094-w

133. Vaneycken I, D'huyvetter M, Hernot S, de Vos J, Xavier C, Devoogdt N, Caveliers V, Lahoutte T. Immuno-imaging using nanobodies. *Curr Opin Biotechnol* (2011) **22**:877–881. doi:10.1016/j.copbio.2011.06.009

134. Kijanka M, Dorresteijn B, Oliveira S, Van Bergen En Henegouwen PMP. Nanobody-based cancer therapy of solid tumors. *Nanomedicine* (2015) **10**:161–174. doi:10.2217/nnm.14.178

135. Tchouate Gainkam LO, Caveliers V, Devoogdt N, Vanhove C, Xavier C, Boerman O, Muyldermans S, Bossuyt A, Lahoutte T. Localization, mechanism and reduction of renal retention of technetium-99m labeled epidermal growth factor receptor-specific nanobody in mice. *Contrast Media Mol Imaging* (2011) **6**:85–92. doi:10.1002/cmmi.408

136. Guizado TRC. Analysis of the structure and dynamics of human serum albumin. *J Mol Model* (2014) **20**: doi:10.1007/s00894-014-2450-y

137. Hambach J, Fumey W, Stähler T, Gebhardt AJ, Adam G, Weisel K, Koch-Nolte F, Bannas P. Half-Life Extended Nanobody-Based CD38-Specific Bispecific Killercell Engagers Induce Killing of Multiple Myeloma Cells. *Front Immunol* (2022) **13**:1–12. doi:10.3389/fimmu.2022.838406

138. Sgouros G, Bodei L, McDevitt MR, Nedrow JR. Radiopharmaceutical therapy in cancer: clinical advances and challenges. *Nat Rev Drug Discov* (2020) **19**:589–608. doi:10.1038/s41573-020-0073-9

139. Bizhanova A, Kopp P. Minireview: The sodium-iodide symporter NIS and pendrin in iodide homeostasis of the thyroid. *Endocrinology* (2009) **150**:1084–1090. doi:10.1210/en.2008-1437

140. Marin JFG, Nunes RF, Coutinho AM, Zaniboni EC, Costa LB, Barbosa FG, Queiroz MA, Cerri GG, Buchpiguel CA. Theranostics in nuclear medicine: Emerging and re-emerging integrated imaging and therapies in the era of precision oncology. *Radiographics* (2020) **40**:1715–1740. doi:10.1148/rg.2020200021

141. Helisch A, Fórster GJ, Reber H, Buchholz HG, Arnold R, Göke B, Weber MM, Wiedenmann B, Pauwels S, Haus U, et al. Pre-therapeutic dosimetry and biodistribution of ^{86}Y-DOTA- Phe1-Tyr3-octreotide versus ^{111}In-pentetreotide in patients with advanced neuroendocrine tumours. *Eur J Nucl Med Mol Imaging* (2004) **31**:1386–1392. doi:10.1007/s00259-004-1561-6

142. Meiboom MF, Hoffmann W, Weitmann K, von Boetticher H. Tables for effective dose assessment from diagnostic radiology (period 1946–1995) in epidemiologic studies. *PLoS One* (2021) **16**:1–16. doi:10.1371/journal.pone.0248987

143. Ahmed NA. Typical effective dose values from diagnostic and interventional radiology. *Appl Radiat Isot* (2023) **192**:110611. doi:10.1016/j.apradiso.2022.110611

144. Qaim SM, Scholten B, Neumaier B. New developments in the production of theranostic pairs of radionuclides. *J Radioanal Nucl Chem* (2018) **318**:1493–1509. doi:10.1007/s10967-018-6238-x

145. Naskar N, Lahiri S. Theranostic Terbium Radioisotopes: Challenges in Production for Clinical Application. *Front Med* (2021) **8**:1–11. doi:10.3389/fmed.2021.675014

146. Müller C, Umbricht CA, Gracheva N, Tschan VJ, Pellegrini G, Bernhardt P, Zeevaart JR, Köster U, Schibli R, van der Meulen NP. Terbium-161 for PSMA-targeted radionuclide therapy of prostate cancer. *Eur J Nucl Med Mol Imaging* (2019) **46**:1919–1930. doi:10.1007/s00259-019-04345-0

147. Marshall JL, Marshall VR. Rediscovery of the elements: Ytterby Gruva (Ytterby Mine). *J Chem Educ* (2001) **78**:1343. doi:10.1021/ed078p1343

148. Li X, Dong W, Qi Y, Wang D, Yang R. Studies on the stabilization of terbium(IV) in aqueous tetrametaphosphate solution. *Polyhedron* (1991) **10**:1479–1483. doi:10.1016/S0277-5387(00)86069-6

149. Ozge M, Geboes B, Hecke K Van, Binnemans K, Cardinaels T. Electrochemical oxidation of terbium (III) in aqueous media : influence of supporting electrolyte on oxidation potential and stability.0–3.

150. Wagner AT, Roesky PW. Rare-Earth Metal Oxo/Hydroxo Clusters – Synthesis, Structures, and Applications. *Eur J Inorg Chem* (2016) **2016**:782–791. doi:10.1002/ejic.201501281

151. Wang YW, Liu SB, Yang YL, Wang PZ, Zhang AJ, Peng Y. A terbium(III)-complex-based on-off fluorescent chemosensor for phosphate anions in aqueous solution and its application in molecular logic gates. *ACS Appl Mater Interfaces* (2015) **7**:4415–4422. doi:10.1021/am5089346

152. Haeseler G, Matthes F. Über den thermischen Abbau der Chloridhydrate der Elemente der Seltenen Erden. *J Less Common Met* (1965) **9**:133–151. doi:10.1016/0022-5088(65)90090-1

153. Wendlandt WW. The thermal decomposition of the heavier rare earth metal chloride hydrates. *J Inorg Nucl Chem* (1959) **9**:136–139. doi:10.1016/0022-1902(59)80072-5

154. Masui T, Isota S, Tamura S, Imanaka N. Electrochemical Single-Crystal Growth of Nonstoichiometric Terbium Oxide. *Cryst Growth Des* (2008) **8**:1035–1038. doi:10.1021/cg070178y

155. Wang H-M, Yang Y-Y, Zeng C-H, Chu T-S, Zhu Y-M, Ng SW. A highly luminescent terbium-organic framework for reversible detection of mercury ions in aqueous solution. *Photochem Photobiol Sci* (2013) **12**:1700–1706. doi:10.1039/c3pp50105a

156. Wei JH, Yi JW, Han M Le, Li B, Liu S, Wu YP, Ma LF, Li DS. A Water-Stable Terbium(III)–Organic Framework as a Chemosensor for Inorganic Ions, Nitro-Containing Compounds and Antibiotics in Aqueous Solutions. *Chem - An Asian J* (2019) **14**:3694–3701. doi:10.1002/asia.201900706

157. Ye Z, Xiao Y, Song B, Yuan J. Design and synthesis of a new terbium complex-based luminescent probe for time-resolved luminescence sensing of zinc ions. *J Fluoresc* (2014) **24**:1537–1544. doi:10.1007/s10895-014-1442-8

158. Kegl, Košak, Lobnik, Ban. Terbium Ion Adsorption from Aqueous Solution by Using Magnetic γFe_2O_3-NH_4OH@SiO_2 Nanoparticles Functionalized with Amino Groups. *Materials (Basel)* (2019) **12**:1294. doi:10.3390/ma12081294

159. Yuan J, Wang G. Lanthanide complex-based fluorescence label for time-resolved fluorescence bioassay. *J Fluoresc* (2005) **15**:559–568. doi:10.1007/s10895-005-2829-3

160. Wang S, Chu X, Xiang X, Cao Y. Highly selective antenna effect of graphene quantum dots (GQDs): A new fluorescent sensitizer for rare earth element terbium in aqueous media. *Talanta* (2020) **209**:120504. doi:10.1016/j.talanta.2019.120504

161. Rahman AKMR, Awal A. Production of ^{149}Tb, ^{152}Tb, ^{155}Tb and ^{161}Tb from gadolinium using different light-particle beams. *J Radioanal Nucl Chem* (2020) **323**:731–740. doi:10.1007/s10967-019-06973-0

162. Baum RP, Singh A, Kulkarni HR, Bernhardt P, Rydén T, Schuchardt C, Gracheva N, Grundler P V., Köster U, Müller D, et al. First-in-human application of terbium-161: A feasibility study using ^{161}Tb-DOTATOC. *J Nucl Med* (2021) **62**:1391–1397. doi:10.2967/jnumed.120.258376

163. Müller C, Reber J, Haller S, Dorrer H, Bernhardt P, Zhernosekov K, Türler A, Schibli R. Direct in vitro and in vivo comparison of ^{161}Tb and ^{177}Lu using a tumour-targeting folate conjugate. *Eur J Nucl Med Mol Imaging* (2014) **41**:476–485. doi:10.1007/s00259-013-2563-z

164. Rosar F, Maus S, Schaefer-Schuler A, Burgard C, Khreish F, Ezziddin S. New Horizons in Radioligand Therapy. *Clin Nucl Med* (2023) **48**:433–434. doi:10.1097/RLU.0000000000004589

165. Al-Ibraheem A, Scott AM. ^{161}Tb-PSMA Unleashed: a Promising New Player in the Theranostics of Prostate Cancer. *Nucl Med Mol Imaging (2010)* (2023) **57**:168–171. doi:10.1007/s13139-023-00804-7

166. Allen BJ, Goozee G, Sarkar S, Beyer G, Morel C, Byrne AP. Production of terbium-152 by heavy ion reactions and proton induced spallation. *Appl Radiat Isot* (2001) **54**:53–58. doi:10.1016/S0969-8043(00)00164-0

167. Müller C, Singh A, Umbricht CA, Kulkarni HR, Johnston K, Benešová M, Senftleben S, Müller D, Vermeulen C, Schibli R, et al. Preclinical investigations and first-in-human application of ^{152}Tb-PSMA-617 for PET/CT imaging of prostate cancer. *EJNMMI Res* (2019) **9**:1–10. doi:10.1186/s13550-019-0538-1

168. Wharton L, McNeil SW, Merkens H, Yuan Z, Van de Voorde M, Engudar G, Ingham A, Koniar H, Rodríguez-Rodríguez C, Radchenko V, et al. Preclinical Evaluation of [$^{155/161}$Tb]Tb-Crown-TATE—A Novel SPECT Imaging Theranostic Agent Targeting Neuroendocrine Tumours. *Molecules* (2023) **28**:3155. doi:10.3390/molecules28073155

169. Webster B, Ivanov P, Russell B, Collins S, Stora T, Ramos JP, Köster U, Robinson AP, Read D. Chemical Purification of Terbium-155 from Pseudo-Isobaric Impurities in a Mass Separated Source Produced at CERN. *Sci Rep* (2019) **9**:1–9. doi:10.1038/s41598-019-47463-3

Objectives

Nuclear medicine significantly contributes to all stages of cancer patient care, including early detection, diagnosis, therapy monitoring and treatment. In **t**argeted **r**adio**n**uclide **t**herapy (TRNT), the therapeutic radiopharmaceutical is distributed within the body by the vascular system and allows targeted irradiation of a primary tumour and all its metastases. The radiolanthanide terbium-161 (^{161}Tb) has gathered increasing interest from the nuclear medicine society in recent years, due to its favourable properties for medical applications. Since the initial published reports of Lehenberger *et al.* (1), positive advances towards the production yields of terbium-161 have been made. Tb-radiopharmaceuticals can be used in a true theragnostic approach with diagnostic terbium isotopes such as ^{152}Tb and ^{155}Tb, which can be used for positron emission tomography (PET) and single photon emission computed tomography (SPECT) applications, respectively. A list of terbium isotopes which are currently researched for nuclear medicine applications is provided in **Table 1**.

Table 1. List of medical interesting terbium isotopes. Half-life of radionuclides was taken from https://www.prismap.eu/ (accessed on 14 July 2023).

Isotope	Half-life	Application
^{149}Tb	4.12 h	Therapy (TAT) Diagnostic (PET)
^{152}Tb	17.52 h	Diagnostic (PET)
^{155}Tb	5.32 d	Diagnostic (SPECT)
^{161}Tb	6.95 d	Therapy (TRNT) Diagnostic (SPECT)

Antibodies and antibody fragments show high affinity and selectivity for their corresponding antigen targets, making them interesting carrier molecules for development of novel and highly target-specific radiopharmaceuticals (2,3). However, antibody and antibody fragments are proteins that can be unstable under various non-physiological conditions, such as high temperatures, which cause denaturing of the carrier.

Current methods used for radiolabelling with terbium, and in general *f*-block elements, require high temperatures, which are not compatible with heat-sensitive carriers (3). Therefore, it is imperative to develop radiolabelling methods that use mild conditions to safeguard the integrity of the protein-based carrier molecules. For terbium, a mild direct radiolabelling protocol compatible with biological carrier molecules has yet to be established.

In addition to the carrier affinity and specificity for the molecular target, it is important to match the physical half-life of the therapeutic radionuclide with the biological half-life and tumour retention of the carrier to achieve maximum selectivity of the radiation dose delivered to the tumour versus healthy tissue.

Finally, ^{161}Tb also emits both conversion and Auger electrons (short range electrons with high linear energy transfer), which has shown promise to target the radiation dose at a sub-cellular level.

Based on the concerns of terbium-radiolabelling methods outlined above and the potential of ^{161}Tb as a therapeutic radionuclide, we have designed and carried out a project which aims to:

1) Develop an efficient terbium radiolabelling method compatible with heat-sensitive biomolecules (**Chapter 2**).

2) Develop and pre-clinically evaluate a half-life extended anti-c-Met v_HH using both ^{155}Tb and ^{161}Tb as radionuclides (**Chapter 3**).

3) Investigate the potency of the conversion and Auger electrons emitted by ^{161}Tb-labelled probes when targeting mitochondria in prostate cancer cells (**Chapter 4**).

References

1. Lehenberger S, Barkhausen C, Cohrs S, Fischer E, Grünberg J, Hohn A, Köster U, Schibli R, Türler A, Zhernosekov K. The low-energy β - and electron emitter ^{161}Tb as an alternative to ^{177}Lu for targeted radionuclide therapy. *Nucl Med Biol* (2011) **38**:917–924. doi:10.1016/j.nucmedbio.2011.02.007

2. Bannas P, Hambach J, Koch-Nolte F. Nanobodies and nanobody-based human heavy chain antibodies as antitumor therapeutics. *Front Immunol* (2017) **8**:1–13. doi:10.3389/fimmu.2017.01603

3. Boros E, Holland JP. Chemical aspects of metal ion chelation in the synthesis and application antibody-based radiotracers. *J Label Compd Radiopharm* (2018) **61**:652–671. doi:10.1002/jlcr.3590

Chapter 2: Radiolabelling of human serum albumin with terbium-161 using mild conditions and evaluation of *in vivo* stability

Irwin Cassells[1,2], Stephen Ahenkorah[1,2], Andrew R. Burgoyne[2], Michiel Van de Voorde[2], Christophe M. Deroose[3], Thomas Cardinaels[2,4], Guy Bormans[1], Maarten Ooms[2*] and Frederik Cleeren[1*]

[1] Radiopharmaceutical Research, Department of Pharmacy and Pharmacology, KU Leuven, Leuven, Belgium, [2] Institute for Nuclear Materials Science, Belgian Nuclear Research Centre (SCK CEN), Mol, Belgium, [3] Nuclear Medicine, University Hospital Leuven & Nuclear Medicine and Molecular Imaging, Department of Imaging and Pathology, KU Leuven, Leuven, Belgium, [4] Department of Chemistry, KU Leuven, Leuven, Belgium

* Correspondence:
Maarten Ooms, maarten.ooms@sckcen.be
Frederik Cleeren, frederik.cleeren@kuleuven.be

The work describe below has been compiled and published: I. Cassells, S. Ahenkorah, A. R. Burgoyne, M. Van De Voorde, C. M. Deroose, T. Cardinaels, G. Bormans, M. Ooms and F. Cleeren, Front. Med., 2021, 8, 675122, https://doi.org/10.3389/fmed.2021.675122

2.1 Introduction

Terbium is an emerging theragnostic element that has four medically relevant radioisotopes (^{149}Tb, ^{152}Tb, ^{155}Tb and ^{161}Tb) (1). For instance, ^{152}Tb (β^+ emitter, $t_{1/2}$ = 17.5 hours, $E\beta^+_{average}$ = 1.140 MeV) and ^{155}Tb (EC γ emitter, $t_{1/2}$ = 5.32 days, Eγ = 0.105 MeV) can be used in diagnostic applications, such as positron emission tomography (PET) and single photon emission computed tomography (SPECT), respectively (1,2). ^{149}Tb (α emitter, $t_{1/2}$ = 4.12 hours, Eα = 3.97 MeV) and ^{161}Tb (β^- emitter, $t_{1/2}$ = 6.90 days, $E\beta^-_{average}$ = 0.154 MeV) on the other hand can be applied in targeted alpha (α) and beta (β) therapy, respectively (3–5). Once radiolabelling is optimised for a single radionuclide, the same protocol can be used to incorporate other terbium isotopes.

Because of its similar decay process and physical half-life, ^{161}Tb is often considered a promising alternative for ^{177}Lu (β^- emitter, $t_{1/2}$ = 6.7 days, $E\beta^-_{average}$ = 0.134 MeV) (4,6), which has become the golden standard in beta therapy since the clinical approval of Lutathera® ([^{177}Lu]Lu-DOTATATE) for the treatment of neuroendocrine tumours (7,8). In a study by Müller *et al.* (9), a direct comparison of the therapeutic effect of the two radioisotopes was investigated. It was concluded that [^{161}Tb]Tb-cm09 had increased potency compared to [^{177}Lu]Lu-cm09 (9). In a follow-up study using a prostate specific membrane antigen (PSMA) targeting radiopharmaceutical, increased survival of prostate cancer tumour-bearing mice was observed when treated with [^{161}Tb]Tb-DOTA-PSMA-617 compared to [^{177}Lu]Lu-DOTA-PSMA-617 (3). It has been postulated that the added efficacy of ^{161}Tb is due to the additional therapeutic effect of Auger/conversion electrons (E_{e^-} = 36 keV) (3,4,9,10). In addition to the

therapeutic power of ^{161}Tb, there is co-emission of gamma radiation (Eγ = 49 keV, I = 17.0%; Eγ = 75 keV, I = 10.2%) (4), which can be used for SPECT imaging (similar to ^{177}Lu (Eγ = 113 keV, I = 6.17%, Eγ = 208 keV, I = 10.36%)) (11,12), as illustrated with the first-in-human application of [^{161}Tb]Tb-DOTATOC (13).

Radiolabelling of a vector molecule with a terbium isotope is accomplished through specific bifunctional chelating agents (1). These bifunctional agents are often coupled in a non-site-specific manner to biological vector molecules through reactions with free lysine (e.g. using bifunctional chelators containing activated esters or isothiocyanate groups) or coupled site-specifically on cysteine groups (e.g. using thiol-maleimide chemistry) (14). Chelating agents, such as the macrocyclic 1,4,7,10-tetraazacyclododecane-1,4,7,10-tetraacetic acid (DOTA) and acyclic diethylene-triamine-pentaacetic acid (DTPA) type ligands exhibit high affinity for lanthanides and have been used extensively for decades by the radiopharmaceutical community (2,15–17). Ideally, to allow radiolabelling of heat-sensitive vector molecules, ligands should combine the stable nature of the DOTA-metal bond and the fast reaction kinetics of DTPA chelators (18). In recent years, ligands such as [4-[2-(bis-carboxymethyl-amino)-ethyl]-7-carboxymethyl-[1,4,7]triazonan-1-yl]-acetic acid (NETA) have recently also received attention, as they have a hybrid structure in between the flexible DTPA framework and rigid DOTA core (19,20).

Up until now, most terbium-labelling reactions were reported with ligands and peptides which are compatible with high radiolabelling temperatures (3,9). Biomolecule-based radionuclide therapies, e.g. using trastuzumab for cancers with overexpression of human epidermal growth factor receptor-2 (HER-2), have paved the way for a more targeted approach to theragnostic (21). Radiolabelling with terbium, and most of the other f-block elements, were performed at temperatures (>90°C), well exceeding the temperatures compatible with heat-sensitive biomolecules such as monoclonal antibodies and antibody fragments (22). In this study, we developed a mild radiolabelling protocol (reaction temperature of 40°C in an aqueous buffer), with a series of commonly used bifunctional ligands (**Figure 2.1**). We then used human serum albumin (HSA, 66.5 kDa) as a model protein to assess the *in vitro* and *in vivo* stability of the corresponding ^{161}Tb-labeled HSA conjugates. The high solubility, stability and plasma half-life of approximately 16-18 h make HSA the ideal vector to evaluate the stability of the ^{161}Tb-chelates *in vivo.*

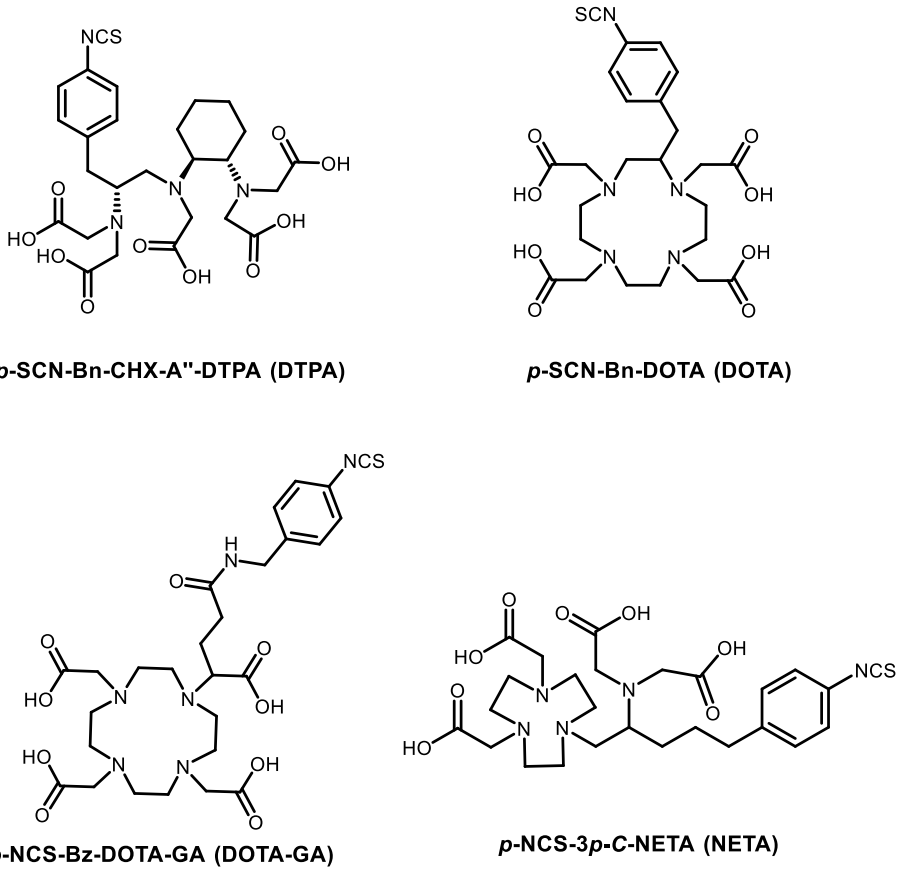


Figure 2.1. Chemical structure of bifunctional chelators used in this study.

2.2 Material and Methods

2.2.1 Materials

Reagents, unless specified otherwise, were purchased from Sigma-Aldrich (Bornem, Belgium) and used without further purification. Solvents were purchased from VWR (Leuven, Belgium) or Sigma-Aldrich, and used without further purification. *p*-SCN-Bn-CHX-A´´-DTPA (**DTPA**) and *p*-SCN-Bn-DOTA (**DOTA**) were purchased from Macrocyclics, Inc. (Texas, USA), and *p*-NCS-Bz-DOTA-GA (**DOTA-GA**) was purchased from CheMatech (Dijon, France), and used without further purification. 3*p*-C-NETA-NCS (**NETA**) was synthesised and characterised according to literature methods (19). All radiolabelling buffers were stirred with chelex (Chelex 100 sodium form (50-100 mesh, Sigma Aldrich)), to remove trace metals, for 15 minutes and then filtered to remove the chelex beads. All solutions were degassed and filtered before use.

2.2.2 Animals

Healthy albino Naval Medical Research Institute (NMRI) mice (age: 6-8 weeks, Envigo, Gannat, France) were housed in individually ventilated cages (IVC) in a regulated environment (22 ºC, humidity, 12h day/night cycle), with food and water. Animal experiments were conducted according to the Belgian code of practice and use of animal experiments were approved by the ethical committee for animal care from KU Leuven.

2.2.3 Instrumentation and Characterisation

Mass spectra were recorded on an ultra-high-resolution time-of-flight mass spectrometer with electrospray ionisation (ESI) (Bruker MaXis Impact, Bremen, Germany), coupled to a Dionex Ultimate 3000 UPLC System (Thermo Fisher Scientific, USA). Quantification of protein concentration was determined using a microvolume UV-Vis spectrophotometer (NanoDrop One, Thermo Fisher Scientific). Quality assurance of the derivatised HSA constructs and ^{161}Tb-HSA constructs were carried out with size-exclusion chromatography (SEC) using a Superdex 200 10/300 GL column (GE Healthcare Bio-Science AB, Uppsala, Sweden), eluted with a sodium phosphate buffer (0.15 M sodium chloride, 0.01 M phosphate, pH 7.4, Thermo Fisher) at a flow rate of 0.75 mL/min. The column effluent was passed through a UV detector (2998 PDA detector, Waters) in series with a 3-inch NaI(Tl) radioactivity detector. Gamma counting was performed on a Wizard^2 3470 (crystal: NaI(Tl), 50 mm in height, 32 mm in diameter, dead time 2.5 µs; Perkin Elmer, Germany), with a detection profile referenced for ^{161}Tb decay (4). Counts were corrected for background radiation, physical decay and counter dead time.

2.2.4 Production of [^{161}Tb]TbCl$_3$

[^{161}Tb]TbCl$_3$ was produced using a method adapted from literature (4). In brief, enriched $^{160}Gd_2O_3$ (1.0 mg , 98.2 %, Isoflex USA) was loaded as a nitrate salt into a quartz ampoule and sealed. The ampoule was sealed inside an aluminium capsule and was irradiated for 10 days in the BR2 Reactor at the Belgian Nuclear Research Centre (SCK CEN) at a thermal neutron flux of 3.0 x 10^{14} n/cm^2/s. Following the irradiation and subsequent cooling for 5 days, the irradiated material was dissolved in trace metal water. High-pressure ion chromatography (HPIC, Shimadzu), with a strong cation exchange column (ø: 6 mm, l: 50 mm, Shodex IC R-621), was used to separate the [^{161}Tb] from the [^{160}Gd] target matrix by elution with α-hydroxyisobutyric acid, with ammonium hydroxide (trace-metal grade) (added to adjust to pH 4.5). The collected fractions containing [^{161}Tb] were combined and concentrated by loading them onto a column packed with extraction resin (ø: 2.1 mm, l: 30 mm, LN3, TrisKem International) and eluted with 50 mM hydrochloric acid (trace-metal free). The isolated solutions of [^{161}Tb]TbCl$_3$ had a radionuclidical purity of 99.998% (determined by gamma spectroscopy), a concentration of ~ 0.99 MBq/µL, and specific activity of ~ 3.6 TBq/mg.

2.2.5 Human serum albumin (HSA) ligand constructs

A five-molar excess of bifunctional ligand (3 µmol) in 200 µl of a sodium bicarbonate solution (0.05 M, pH 8.5, 1.5 % DMSO) was added dropwise to a stirring solution of human serum albumin (400 µL, 0.6 µmol, CAF-DCF, Brussels, Belgium) in sodium bicarbonate (0.05 M, pH 8.5) in a LoBind vial (Eppendorf, Aarschot, Belgium). The mixture was then stirred for 2 hours at room temperature and the conjugate was purified using a size exclusion chromatography cartridge (PD-10 column, GE Healthcare Bio-Science AB, Uppsala, Sweden) eluted with sodium acetate buffer (0.1 M, pH 4.7). The concentration of the HSA-ligand construct in the final reaction product was determined using spectrophotometry at 280 nm (NanoDrop® One, Thermo Fisher Scientific), with ε = 35700 L/mol/cm and M = 66477 g/mol. The purified product was analysed using SEC using the method described above. UV detection of the eluate was performed at 280 nm. The number of chelators per protein was estimated by ESI-TOF-HRMS analysis considering the most abundant peak. The system was equipped with a Waters Acquity UPLC BEH C18 column (1.7 µm 2.1 X 50 mm, Waters, Milford, USA) using a gradient at a flowrate of 0.6 mL/min with mobile phase A: H_2O, 0.1% HCOOH and mobile phase B: acetonitrile, 0.1 % HCOOH. The column was heated at 40°C. The elution gradient was: 0-2 min: 95% A; 2-8 min: from 95 % A to 5 % A; 8-10 min: 5 % A; 10-12 min.: from 5 % A to 95 % A. Calculated molecular ion mass values were obtained using Compass Isotope Pattern (version 3.2, Bruker) software. **HSA-DTPA**:. ESI-MS *m/z* (decon.) calculated for HSA [66477.96] + $C_{52}H_{68}N_8O_{20}S_2 \cdot H_6Cl_6$ [1296.33]: 67 852.22. Found: 67 852.20 (81.9 %). **HSA-DOTA**: ESI-MS *m/z* (decon.) calculated for HSA [66477.96] + $C_{48}H_{66}N_{10}O_{16}S_2 \cdot H_3Cl_3$ [1210.34]: 67 688.30. Found: 67 687.74 (31.4 %). **HSA-DOTA-GA**: ESI-MS *m/z* (decon.) calculated for HSA [66485.42] + $C_{54}H_{76}N_{12}O_{18}S_2 \cdot C_2H_4O_4$ [1336.50]: 67 821.91. Found: 67 821.87 (95.2 %). **HSA-NETA**: ESI-MS *m/z* (decon.) calculated for HSA [66457.96] + $C_{52}H_{74}N_{10}O_{16}S_2 \cdot C_2O_5H_6$ [1268.49]: 67 726.46. Found: 67 726.63 (80.1 %).

2.2.6 Radiolabelling studies with [^{161}Tb]$TbCl_3$

Optimisation of radiolabelling conditions: [^{161}Tb]$TbCl_3$ (0.2 MBq, 10 µL, 50 mM HCl) was added to 90 µL of a solution with different quantities of the ligand (**DTPA**, **DOTA**, **DOTA-GA** or **NETA**, 0.1-1.0 nmol) in sodium acetate buffer (0.1M, pH 4.7, chelex treated) and reacted in a glass vial for 60 minutes at 25 or 40 °C (n=3). The radiochemical yield of each reaction mixture was determined by instant thin-layer liquid chromatography (iTLC-SG, Varian, Diegem, Belgium). iTLC-SG papers were developed in an elution chamber using acetonitrile/water (75/25). The distribution of activity on the iTLC chromatograms was quantified using phosphor storage autoradiography (super-resolution screen, Perkin Elmer, Waltham, USA processed in a Cyclone Plus system (Perkin Elmer) and analysed using Optiquant software (Perkin Elmer)).

Radiolabelling HSA-constructs: Purified HSA-constructs were labelled using 10 µM of the HSA-conjugate (90 µL) with [^{161}Tb]$TbCl_3$ (0.2 MBq, 10 µL, 50mM HCl) at 40 ºC for 60 minutes (n=3).

Radiochemical yields were determined by iTLC-SG, eluted with sodium citrate buffer (0.1 M, pH 5.8). Radiolabelled HSA-constructs were additionally analysed by radio-SEC using the method described above.

2.2.7 *In vitro* stability studies

Stability of ligand complexes in phosphate buffered saline pH 7.4: The radiolabelled ligands were purified using a C18 Plus SEP-PAK cartridge (Waters, Antwerp, Belgium) by loading the reaction mixture, rinsing with water (5 mL) to remove unreacted [^{161}Tb]$TbCl_3$, and eluting the purified complex with abs. ethanol (0.5 mL). 80 µL of the ethanolic solution was added to 720 µL of sodium phosphate buffer (0.15 M sodium chloride, 0.01 M phosphate, pH 7.4, Thermo Fisher) and incubated at 37 °C (n=3). Samples were collected at different time points (10 min, 1 hour, 4 hours, and 24 hours) and the percentage of intact ^{161}Tb-complex was determined using the same iTLC chromatography system as used above.

Stability of HSA-ligand in human serum: After radiolabelling and without purification, 50 µL of the ^{161}Tb-HSA radiolabelling solution was added to 720 µL human serum (Sigma Aldrich) and incubated at 37 °C (n=3). Samples were collected at different time points (10 min, 1 hour, 4 hours, and 24 hours) and the percentage of intact ^{161}Tb-HSA construct was determined using the same instant thin-layered liquid chromatography system as used in radiolabelling and referenced to the initial radiochemical yield. The *in vitro* stability was confirmed with the radio-SEC method described above at 1, 4 and 24 hours.

Competition studies with EDTA: After radiolabelling and without purification, 50 µL of the ^{161}Tb-HSA radiolabelling solution was added to 50 µL EDTA solution (10 mM, 0.1M PBS, pH 7.4, Sigma Aldrich) and incubated at 37 °C (n=3). Samples were collected at different time points after incubation (1 hour, 4 hours, and 24 hours) and the percentage of intact ^{161}Tb-HSA construct was determined using the same iTLC method mentioned above.

2.2.8 Biodistribution studies

Mice were anaesthetised with 2.5% isoflurane in O_2 at a flow of 1 L/min and injected with ~1 MBq of [^{161}Tb]$TbCl_3$ or ^{161}Tb-HSA construct (0.1-0.3 nmoles) via a tail vein. Animals were sacrificed by decapitation at 10 min, 1 hour, 4 hours, 24 hours, or 7 days post injection (n = 3 animals per time point). Blood and organs were collected in tubes, weighed, and radioactivity was determined using an automated gamma counter as described above. Results are presented as standardised uptake values (SUV; determined using SUV = (MBq_{tissue}/g_{tissue}) / ($MBq_{injected}/g_{mouse}$). For calculation of percentage

injected dose (%ID) in blood, bone and muscle, masses were assumed to be 7%, 12% and 40% of mouse body weight, respectively (23,24). Blood data points ($\%ID_{calculated}$) were fitted to a standard half-life equation (least-squares regression analysis), $\%ID_{calc} = A \cdot 0.5^{k\Delta t}$, where A = constant, Δt = hours after injection (h), and k = 1 / plasma half-life (h^{-1}).

2.2.9 Statistical analysis

Quantitative data are expressed as mean ± SD unless stated otherwise. Means were compared using a mixed model ANOVA analysis in GraphPad Prism 9.1.2. Values were determined to be statistically significant for *p*-values less than the threshold value of 0.05.

2.3 Results

2.3.1 Optimisation of radiolabelling conditions for low temperature labelling

Radiolabelling efficiency of all ligands (**DTPA**, **DOTA**, **DOTA-GA**, **NETA**) was evaluated using four different ligand concentrations (0.1, 1, 5 and 10 µM) at 25 °C and 40 °C after 60 minutes reaction time. Results of the radiolabelling can be found in **Figure 2.2A** and **2.2B**. Radiolabelling with **DTPA** resulted in >98% radiolabelling efficiency at all tested concentrations, even at 25 °C. All other ligands required a temperature of 40 °C to efficiently (>90%) chelate the terbium(III) ion. Radiolabelling using **NETA** at 40 °C resulted in quantitative yields in all investigated ligand concentrations (labelling efficiency > 97%). Both **DOTA** and **DOTA-GA** required higher concentrations to allow sufficient radiolabelling efficiency.

2.3.2 *In vitro* stability of radiolabelled ligands

Metal-ligand *in vitro* stability was determined in phosphate buffered saline (PBS, pH 7.4) at 37 °C and analysed over 24 hours (**Figure 2.3**). The amount of ^{161}Tb bound to the ligand was referenced to the initial radiochemical purity. For **DTPA**, **DOTA** and **NETA** ligand systems, >95% of the metal was still chelated to the ligand after 24 hours. The **DOTA-GA** ligand was observed to have retained only 92.1 ± 6.8 % of the initial radiochemical purity over the same period.

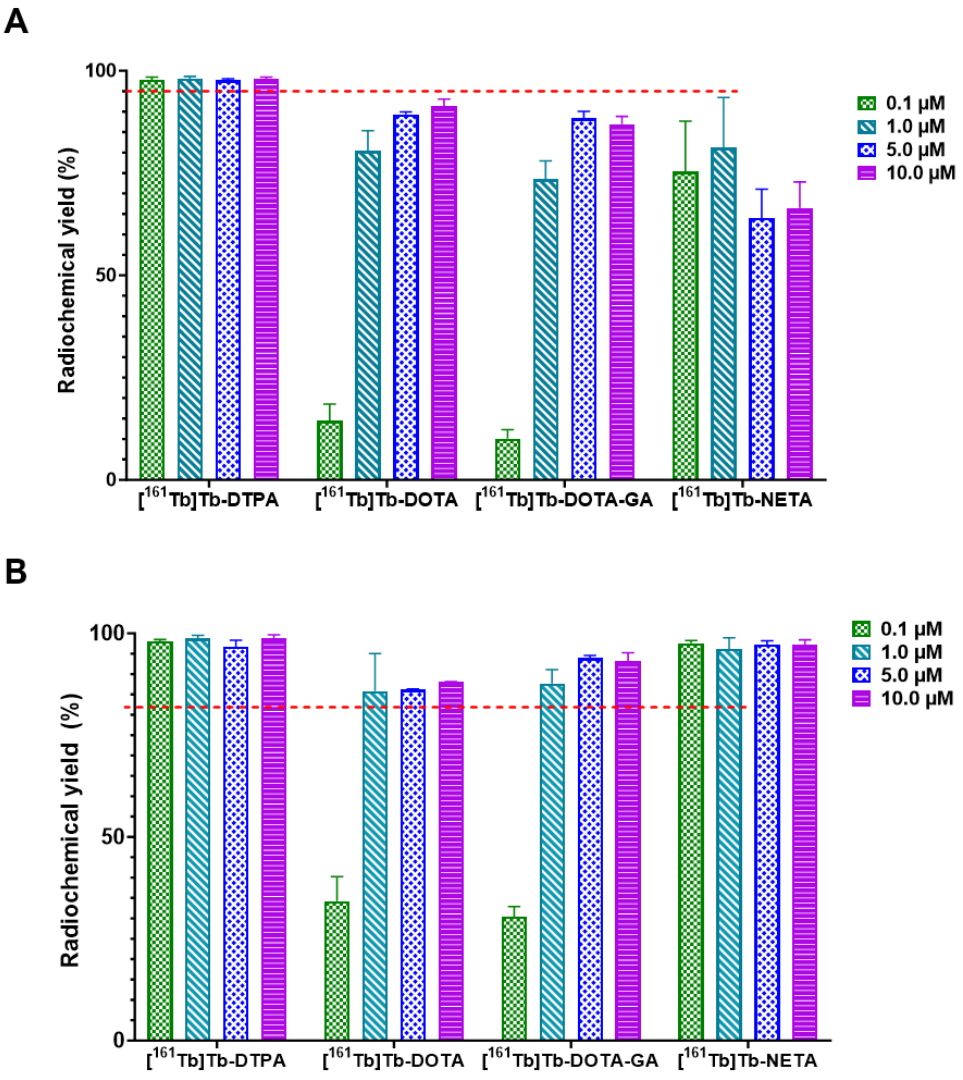


Figure 2.2. Radiochemical yields of [^{161}Tb]Tb-**L** (where **L** = **DTPA**, **DOTA**, **DOTA-GA** or **NETA**) at 25 °C **(A)** and 40 ºC **(B)** after 60 minutes. Red line is inserted to indicated quantitative yield (95%).

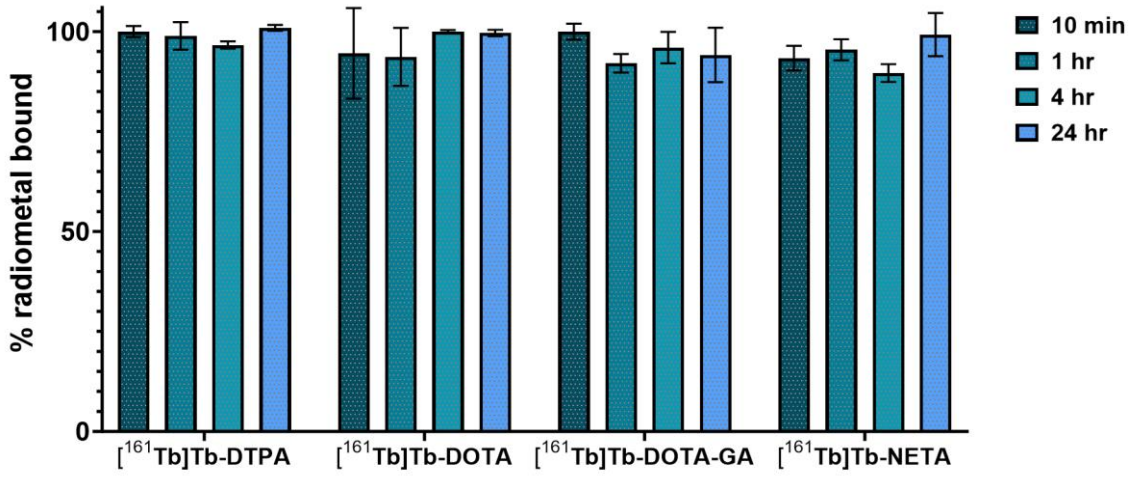


Figure 2.3. *In vitro* stability of ^{161}Tb-radiolabeled complexes in PBS at 37 °C.

2.3.3 Synthesis, radiolabelling and *in vitro* stability of human serum albumin conjugates.

DTPA, **DOTA**, **DOTA-GA** or **NETA** was reacted with HSA in a 5:1 molar excess. HSA-constructs were purified using a size exclusion cartridge and analysed using HPLC-SEC. Unconjugated human serum albumin was found to be retained in the size exclusion column for 19 minutes and HSA-chelator constructs eluted at the same retention time (**Figure S1-S6**). Constructs were analysed using mass spectrometry to determine the number of ligands attached to the HSA protein. An increase of 1000-1300 Da was observed for each conjugate, indicating an average number of two chelators per albumin molecule. The mass spectra data is summarised in **Table 2.1**.

Table 2.1. Mass spectrum data of HSA and compounds L-HSA.

Compound	Mass found (kDa)	Chelators per albumin
HSA	66.478	N/A
HSA-DTPA	67.852	~2
HSA-DOTA	67.688	~2
HSA-DOTA-GA	67.821	~2
HSA-NETA	67.726	~2

HSA-conjugates and unconjugated HSA were radiolabelled at a concentration of 10 μM with [^{161}Tb]$TbCl_3$ at 40 ºC to ensure maximum radiochemical yield. HSA (not conjugated to any chelator) only coordinated 6.0 ± 1.2% of the [^{161}Tb]$TbCl_3$ in the reaction mixture. The investigated conjugates were all labelled with quantitative yields (> 98%) (**Table S1**) as determined with iTLC and radio-SEC-HPLC (**Figure S3-S6**). The radiolabelled constructs (without further purification) were added to human serum and incubated at 37ºC for 24 hours. [^{161}Tb]Tb-**DOTA**-HSA, [^{161}Tb]Tb-**DOTA-GA**-HSA and [^{161}Tb]Tb-**NETA**-HSA remained intact (> 93%) for at least 24 hours. In contrast, only 87.5 ± 2.6 % of radiometal remained coordinated to [^{161}Tb]Tb-**DTPA**-HSA after 24 hours (**Figure 2.4**). Radio-SEC-HPLC chromatograms of ^{161}Tb-labelled HSA conjugates are provided in the supporting information (**Figure S7-S10**). To assess the susceptibility of trans-chelation, the labelled HSA-conjugates were incubated with 1000-fold excess of EDTA (**Figure S11**). As observed in the previous study, ^{161}Tb leached from the **DTPA**-HSA ligand system, with only 64.4 ± 0.9 of the initial ^{161}Tb remained bound to HSA after 24 hours at 37 °C. For the other conjugates, > 90% of the initial fraction of the radiometal remained bound to HSA after 24 hours.

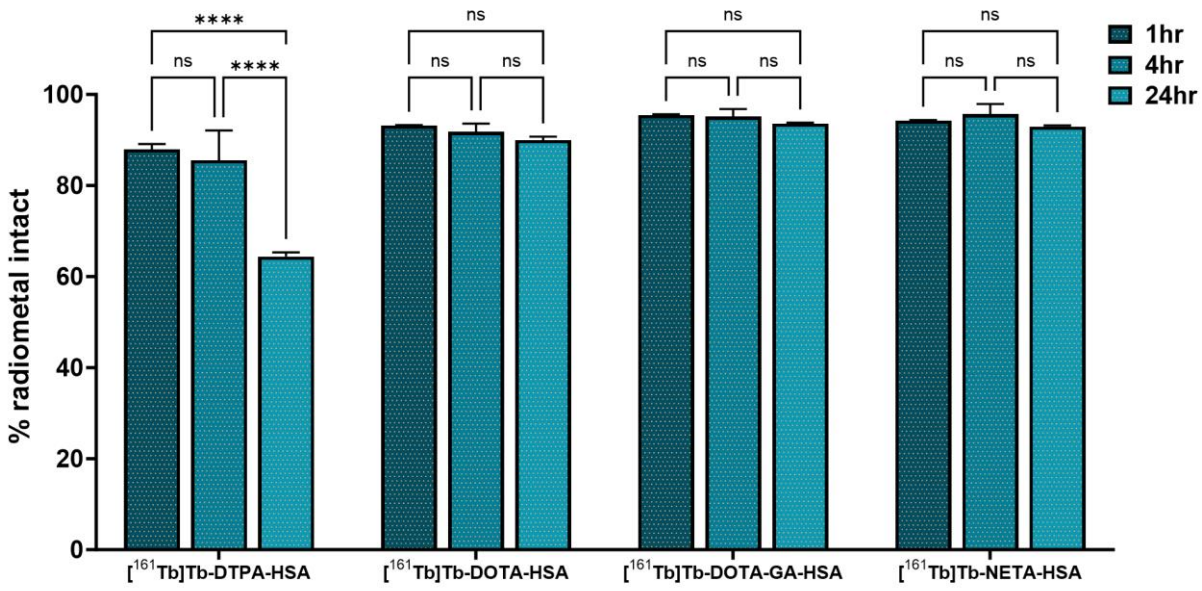


Figure 2.4. *In vitro* stability of ^{161}Tb-radiolabeled HSA-complexes in human serum at 37 °C. Significant values are expressed as $P <$ * = 0.05, ** = 0.01, *** = 0.001, **** = 0.0001.

2.3.4 *Ex vivo* biodistribution of [^{161}Tb]$TbCl_3$ and ^{161}Tb-labeled HSA-conjugates.

HSA-conjugates were labelled with [^{161}Tb]$TbCl_3$ and injected into mice intravenously (tail vein). Additionally, [^{161}Tb]$TbCl_3$ (PBS, pH 7.4) was injected in a control group to identify the organs in which ^{161}Tb accumulates in case it leaches from the complex. Unconjugated [^{161}Tb]$TbCl_3$ showed high accumulation in bone and liver (**Figure 2.5, Table 2.2, Table S4-S6).** Four hours after injection of [^{161}Tb]$TbCl_3$, a SUV of 5.0 ± 0.5 (60.2 ± 6.4 % ID) and 4.1 ± 0.4 (23.8 ± 2.5 % ID) was observed for bone and liver, respectively. A bone-to-blood ratio of 4.8 ± 3.8 was observed already after 1 hour post injection (p.i.) and this value further increased reaching a bone-to-blood ratio of 39.3 ± 13.0 after 4 hours p.i. (**Table S2**). The half-life of the free [^{161}Tb]$TbCl_3$ in blood was about 0.4 hours (**Figure S17**). As could be expected, the HSA constructs did not show any specific accumulation in any target tissue. No significant bone uptake of activity was observed for the [^{161}Tb]Tb-**DOTA**-HSA, [^{161}Tb]Tb-**NETA**-HSA, and [^{161}Tb]Tb-**DOTA-GA**-HSA conjugates (**Figure 2.6A-D**, **Table 2.2**). In contrast, in the mice injected with [^{161}Tb]Tb-**DTPA**-HSA, increasing bone uptake was observed (SUV: 0.8 ± 0.3 and 1.1 ± 0.3 at 24 h and 7 days p.i., respectively) in function of time (**Table 2.2**), suggesting *in vivo* dissociation and absorption of free ^{161}Tb in bone. The blood half-life of the HSA constructs was significantly longer than for [^{161}Tb]$TbCl_3$ (8-15 hours, **Figure S17-S21**). Standardised uptake value graphs are provided in **Figure 2.6**, with % injected activity diagrams provided in **Figure S12-S16**. %ID, %ID/g and SUV values are presented in **Table S4-S18**.

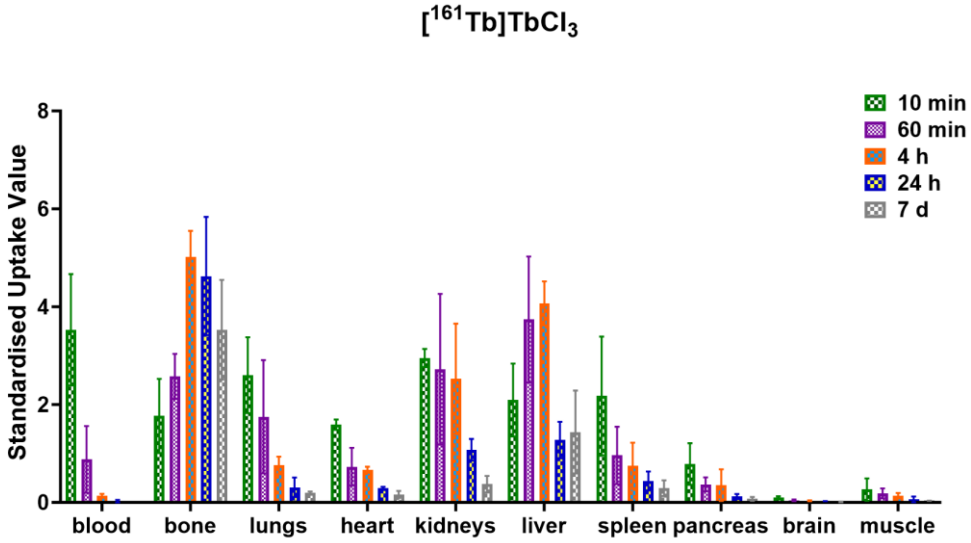


Figure 2.5. Biodistribution of [^{161}Tb]$TbCl_3$ expressed in standardised uptake values per organ.

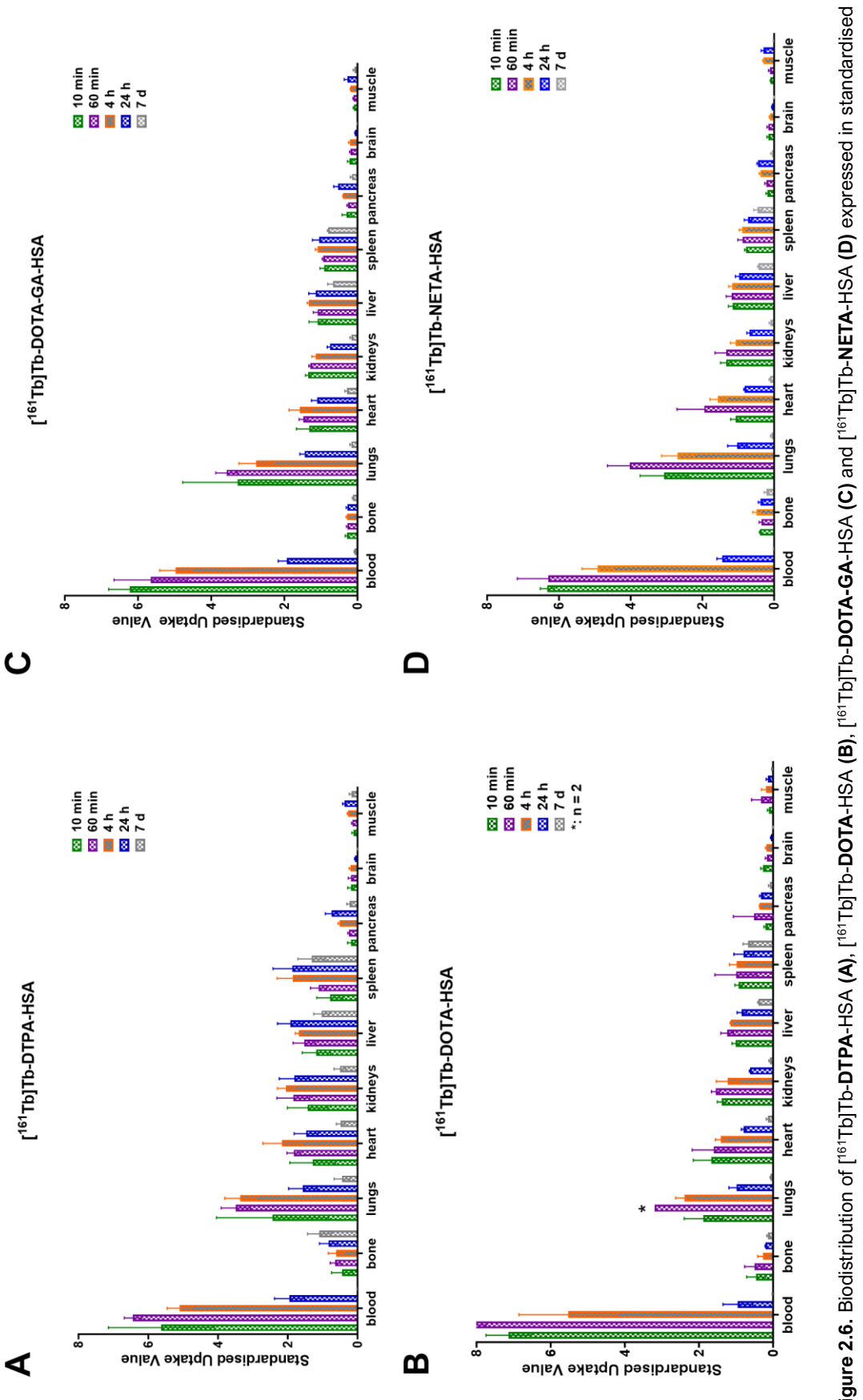


Figure 2.6. Biodistribution of [^{161}Tb]Tb-**DTPA**-HSA **(A)**, [^{161}Tb]Tb-**DOTA**-HSA **(B)**, [^{161}Tb]Tb-**DOTA-GA**-HSA **(C)** and [^{161}Tb]Tb-**NETA**-HSA **(D)** expressed in standardised uptake values per organ.

Table 2.2: SUV values of bone uptake in healthy mice.

	[^{161}Tb]TbCl$_3$	[^{161}Tb]Tb - **DTPA**-HSA	[^{161}Tb]Tb - **DOTA**-HSA	[^{161}Tb]Tb - **DOTA-GA**-HSA	[^{161}Tb]Tb - **NETA**-HSA
10 min	1.77 ± 0.76	0.44 ± 0.30	0.46 ± 0.25	0.29 ± 0.05	0.39 ± 0.02
1 hr	2.58 ± 0.46	0.64 ± 0.15	0.50 ± 0.26	0.28 ± 0.02	0.35 ± 0.07
4 hrs	5.02 ± 0.53	0.62 ± 0.22	0.27 ± 0.15	0.29 ± 0.02	0.49 ± 0.11
24 hrs	4.63 ± 1.21	0.83 ± 0.26	0.20 ± 0.01	0.28 ± 0.03	0.38 ± 0.06
7 d	3.53 ± 1.02	1.1 ± 0.34	0.13 ± 0.04	0.12 ± 0.02	0.21 ± 0.06

2.4 Discussion

In this study, we aimed to develop techniques that allow radiolabelling of heat sensitive biomolecules with ^{161}Tb. A series of ligands were preselected based on their lanthanide chelating capacity reported in literature (20,25,26). For each ligand, we evaluated the effect of ligand concentration and temperature on radiolabelling yields. Finally, stability of the different ligand complexes was evaluated *in vitro* and *in vivo*.

Coordination of terbium is pH sensitive, as too low pH blocks carboxyl coordination, which is the main coordinating moiety of the ligands of interest (**Table S3)**. In aqueous terbium solutions, hydrolysis (formation of $Tb(H_2O)_x(OH)_y$ species) will occur at increased pH (pH ~ 6-7.6) (3,10,12,27–29). Hydrolysis will dramatically reduce or prevent the overall formation of Tb-ligand complex, which might be mitigated by increasing the temperature during radiolabelling. We selected low pH conditions (sodium acetate buffer (0.1 M, pH 4.7)) to prevent hydrolysis and enable low-temperature chelation of Tb. When radiolabelling the **DTPA** ligand, quantitative radiochemical yields (>98%) were observed for all conditions investigated. Incubating the reaction mixture at 25 °C was enough to obtain quantitative yields, even at low ligand concentrations (**Figure 2.2A**). This can be attributed to the flexible nature of the linear DTPA framework which makes chelating the terbium(III) ion easier (1). At 25 ºC, radiochemical yields of **DOTA** and **DOTA-GA** were lower, with a maximum radiochemical yield of 91% (10 µM). This could be expected in view of the more rigid tetraaza ring of the latter two ligand structures. Increasing the temperature to 40 ºC yielded no change in the maximum yields obtained for higher concentrations of **DOTA** and **DOTA-GA** but allowed for better radiochemical yields in the low concentrations tested (**Figure 2.2B**). Finally, for **NETA**, a mean radiochemical yield of ~60% was observed at 25 ºC but quantitative yields (> 95%), comparable to **DTPA,** were obtained at 40 ºC. The hybrid nature of the **NETA** framework could explain the radiochemical yields similar to **DOTA** and **DOTA-GA** at 25 ºC. Slightly increasing the temperature however seems to provide enough energy to allow terbium(III) to be incorporated more efficiently into the chelator binding pocket.

The stability of the ^{161}Tb-ligand bond was evaluated in a phosphate buffered saline solution (pH 7.4) at 37 ºC during a time period of 24 hours using instant thin-layer chromatography (**Figure 2.3**). At the end of the study, > 95% (relative to the initial radiochemical purity) of the metal remained intact for complexes with **DTPA**, **DOTA** and **NETA**. The complex with **DOTA-GA** was found to be the least stable, with 92.1 ± 6.8 % of the initially chelated metal intact after 24 hours.

After optimising the radiolabelling conditions, we used these optimised conditions to radiolabel HSA conjugates, as a proof of concept. HSA is a heat sensitive molecule and is the most abundant protein in blood essential for the transport of many proteins throughout the body (30,31). It has a prolonged serum half-life (30), which also makes it advantageous for determining long-term *in vivo* stability of radiolabelled conjugates. Additionally, since HSA circulates in the blood and shows minimal physiological accumulation in tissue, it is the perfect tool to evaluate dissociation and potential accumulation of the free radiometal to other tissues. Bifunctional ligands were conjugated to HSA non-regioselectively, using lysine coupling. The ligands were reacted with HSA to afford conjugates **L**-HSA (where **L** = **DTPA**, **DOTA**, **DOTA-GA** or **NETA**), and analysed by UV-HPLC and high-resolution mass spectrometry. Only a single peak (Rt = 19 min) was recorded in the UV channel (**L**-HSA), and their retention time is identical to that of underivatised HSA (**Figure S1**, **S3-S6**). No aggregation or degradation products were observed via SEC-HPLC. Furthermore, high resolution mass spectrometry was used to estimate the number of ligands conjugated to HSA for every conjugate. Unconjugated HSA was used as a reference for calculating the number of ligand molecules that are conjugated (66477-66485 Da) to HSA. The molecular mass of all the conjugates increased by 1000-1300 Da relative to HSA, which suggests that the conjugates have an average of two ligands per HSA moiety (**Table 2.1**).

Using the optimised labelling conditions (60 minutes, 40 °C), HSA constructs **L**-HSA were radiolabelled with ^{161}Tb and the labelling reaction mixture was analysed by iTLC and radio-SEC. In addition, non-derivatised HSA was incubated with [^{161}Tb]$TbCl_3$ to determine if there is any non-chelator related binding of terbium to the protein. The ^{161}Tb-labelled conjugates ([^{161}Tb]Tb-**L**-HSA) were found to have radiochemical purity greater than 98% for all constructs. In contrast, unconjugated HSA was observed to have a radiochemical purity of only 6.0 ± 1.2%, suggesting minimal complexation of ^{161}Tb occurs in absence of a chelator (**Table S1**). RadioHPLC analysis of the HSA-constructs confirms successful coordination of ^{161}Tb to the investigated HSA conjugates (**Figure S1-S6**).

Upon incubation in human serum, a radiochemical purity above 95% was maintained for the radiolabelled HSA constructs [^{161}Tb]Tb-**DOTA**-HSA, [^{161}Tb]Tb-**DOTA-GA**-HSA and [^{161}Tb]Tb-**NETA**-HSA over a 24-hour study period. [^{161}Tb]Tb-**DTPA**-HSA had a noticeable decrease in radiochemical purity after 24 hours from 98.6 ± 0.5% to 88.1 ± 1.3%. This is commonly observed with ligands bearing the DTPA chelating framework, as it is often labelled as an “easy-in-easy-out" ligand for metals (18). In a competition study with EDTA (1000x molar excess), [^{161}Tb]Tb-**DOTA**-HSA, [^{161}Tb]Tb-**DOTA-GA**-HSA and [^{161}Tb]Tb-**NETA**-HSA was observed to show minimal transchelation of ^{161}Tb, with > 90% of metal still

associated to L-HSA. In stark contrast, > 35% of ^{161}Tb transchelated from **DTPA**-HSA to EDTA (**Figure S11**). These *in vitro* results indicate that **DTPA** is a poor choice for chelation of terbium.

As described before, HSA can be used as an effective model protein to evaluate the *in vivo* stability of radiolabelled complexes (30). First, a biodistribution was performed with [^{161}Tb]$TbCl_3$ to determine its *in vivo* fate. Free [^{161}Tb]$TbCl_3$ was observed to clear from the blood within the first 24 hours (**Figure 2.5, Table S4-S6**) and high uptake and retention were observed in liver and bone, with the highest values observed at 4h p.i (SUV_{liver} = 4.1 ± 0.4 and SUV_{bone} 5.0 ± 0.5). At day 7, still high retention of radioactivity in bone and liver was observed (SUV_{liver} = 1.4 ± 0.8, SUV_{bone} = 3.5 ± 1.0), resulting in a strongly increasing bone-to-blood and bone-to-muscle ratio over the 7-day period (**Table S2**). The high accumulation of radioactivity in bone, allowed us to identify this tissue as an indicator for leaching of the radionuclide from the radiopharmaceutical *in vivo*. The biodistribution of the ^{161}Tb-labeled HSA constructs showed the expected accumulation of activity in organs with high blood content (heart, lungs, spleen, etc.). As observed with the free [^{161}Tb]$TbCl_3$, increased bone and liver uptake was observed over the entire 7-day period for [^{161}Tb]Tb-**DTPA**-HSA (**Figure 2.6A**). At 7 days post injection of [^{161}Tb]Tb-**DTPA**-HSA, a SUV_{bone} value of 1.1 ± 0.3 was observed. This is significantly higher (P < 0.001) than for the other three constructs ([^{161}Tb]Tb-**DOTA**-HSA: SUV_{bone} 0.1 ± 0.0; [^{161}Tb]Tb-**DOTA-GA**-HSA: SUV_{bone} 0.1 ± 0.0; [^{161}Tb]Tb-**NETA**-HSA: SUV_{bone} 0.2 ± 0.1), strongly suggesting that there is *in vivo* dissociation of the metal from the **DTPA**-HSA ligand (**Figure 2.6B-D**). This result, together with the *in vitro* stability data in human serum and EDTA competition study, strongly suggests **DTPA** has fast radiolabelling kinetics but does not adequately retain the radiometal after chelation. In the *in vitro* test with human serum, 10 % of the radioactivity of [^{161}Tb]Tb-**DTPA**-HSA was dissociated after 24 hours. After 24 hours *in vivo* studies showed 10 % of the injected activity in the bone (**Figure S12**), showing a good concordance between *in vitro* and *in vivo* results. No increase in retention of liver and bone activity was observed over 7 days after injection of radiolabelled constructs with **DOTA**-HSA, **DOTA-GA**-HSA and **NETA**-HSA (**Figure 2.6B-D**), suggesting high *in vivo* stability of ^{161}Tb complexes with ligands **DOTA**, **DOTA-GA** and **NETA** as compared to **DTPA**. This is an important result for further studies with radioactive terbium isotopes as the CHX-A´´-DTPA framework (**DTPA**, **Figure 2.1**) is often seen and used as a generic chelator for different radiometals (32). **DOTA**, **DOTA-GA** and **NETA** have more rigid frameworks, which can explain the more stable chelation of metals *in vivo*.

As expected, radiolabelled HSA-constructs were retained longer in blood compared to [^{161}Tb]$TbCl_3$. The blood biological half-life increased from 0.4 hours (free [^{161}Tb]$TbCl_3$, **Figure S17**) to 8-14 hours ([^{161}Tb]Tb-**DTPA**-HSA: 14.8 hours; [^{161}Tb]Tb-**DOTA**-HSA: 8.6 hours; [^{161}Tb]Tb-**DOTA-GA**-HSA: 14.2 hours; [^{161}Tb]Tb-**NETA**-HSA: 10.8 hours; **Figure S18-S21**). This minor variation in blood biological half-life of the different conjugates might be attributed to the non-regioselective coupling of ligands to HSA; potentially reacting with regions essential to biological circulating proteins (neonatal Fc receptor, etc.). Therefore, in future experiments, it is essential to make use of more site-specific targeting approaches (his-tag coupling, *sortase A*, etc.) (33-35) to avoid interfering with the binding affinity of the biomolecule.

2.5 Conclusion

This study is the first report on labelling with ^{161}Tb in mild conditions (25°C and 40°C in aqueous buffer). As a proof of concept, we successfully radiolabelled the heat-sensitive biomolecule HSA with ^{161}Tb, with high radiochemical yields. Several bifunctional ligands were evaluated for their radiolabelling properties, as well as their *in vivo* and *in vitro* stability. Of these ligands, radiolabelling with **DTPA** was highly efficient, even at room temperature. However, the **DTPA**-HSA construct showed the lowest stability, both *in vitro* and *in vivo*, leading to significant off-target bone uptake and retention. In contrast, complexes with a more rigid backbone (**DOTA**, **DOTA-GA** and **NETA**) required slightly higher radiolabelling temperatures but were found to be very stable *in vitro* and *in vivo*. These ligands have potential to be used with other vector molecules for diagnostic and therapeutic applications of the terbium radioisotope family. Research is currently ongoing to conjugate these ligands to other heat-sensitive vector molecules to allow delivery of ^{161}Tb or other terbium radioisotopes to the biological target of interest.

2.6 Ethical statement

Animal experiments were conducted according to the Belgian code of practice for the care and the use of animals, after approval from the animal ethics committee of KU Leuven (P054/2 019).

2.7 Conflict of Interest

The authors declare that the research was conducted without any conflict of interest.

2.8 Supplementary information

https://www.frontiersin.org/articles/10.3389/fmed.2021.675122/full#supplementary-material

2.9 References

1. Mishiro K, Hanaoka H, Yamaguchi A, Ogawa K. Radiotheranostics with radiolanthanides: Design, development strategies, and medical applications. *Coord Chem Rev* (2019) **383**:104–131. doi:10.1016/j.ccr.2018.12.005

2. Amoroso AJ, Fallis IA, Pope SJA. Chelating agents for radiolanthanides: Applications to imaging and therapy. *Coord Chem Rev* (2017) **340**:198–219. doi:10.1016/j.ccr.2017.01.010

3. Müller C, Umbricht CA, Gracheva N, Tschan VJ, Pellegrini G, Bernhardt P, Zeevaart JR, Köster U, Schibli R, van der Meulen NP. Terbium-161 for PSMA-targeted radionuclide therapy of prostate cancer. *Eur J Nucl Med Mol Imaging* (2019) **46**:1919–1930. doi:10.1007/s00259-019-04345-0

4. Gracheva N, Müller C, Talip Z, Heinitz S, Köster U, Zeevaart JR, Vögele A, Schibli R, Meulen NP Van Der. Production and characterization of no- carrier-added ^{161}Tb as an alternative to the therapy. *EJNMMI Radiopharm Chem* (2019) **4**:12:1–16.

5. Müller C, Vermeulen C, Köster U, Johnston K, Türler A, Schibli R, van der Meulen NP. Alpha-PET with terbium-149: evidence and perspectives for radiotheragnostics. *EJNMMI Radiopharm Chem* (2017) **1**:2–6. doi:10.1186/s41181-016-0008-2

6. Lehenberger S, Barkhausen C, Cohrs S, Fischer E, Grünberg J, Hohn A, Köster U, Schibli R, Türler A, Zhernosekov K. The low-energy β - and electron emitter ^{161}Tb as an alternative to ^{177}Lu for targeted radionuclide therapy. *Nucl Med Biol* (2011) **38**:917–924. doi:10.1016/j.nucmedbio.2011.02.007

7. Hennrich U, Kopka K. Lutathera®: The first FDA-and EMA-approved radiopharmaceutical for peptide receptor radionuclide therapy. *Pharmaceuticals* (2019) **12**:114-125 doi:10.3390/ph12030114

8. Strosberg J, El-Haddad G, Wolin E, Hendifar A, Yao J, Chasen B, Mittra E, Kunz PL, Kulke MH, Jacene H, et al. Phase 3 Trial of ^{177}Lu-Dotatate for Midgut Neuroendocrine Tumors . *N Engl J Med* (2017) **376**:125–135. doi:10.1056/nejmoa1607427

9. Müller C, Reber J, Haller S, Dorrer H, Bernhardt P, Zhernosekov K, Türler A, Schibli R. Direct *in vitro* and *in vivo* comparison of ^{161}Tb and ^{177}Lu using a tumour-targeting folate conjugate. *Eur J Nucl Med Mol Imaging* (2014) **41**:476–485. doi:10.1007/s00259-013-2563-z

10. Grünberg J, Lindenblatt D, Dorrer H, Cohrs S, Zhernosekov K, Köster U, Türler A, Fischer E, Schibli R. Anti-L1CAM radioimmunotherapy is more effective with the radiolanthanide terbium-161 compared to lutetium-177 in an ovarian cancer model. *Eur J Nucl Med Mol Imaging* (2014) **41**:1907–1915. doi:10.1007/s00259-014-2798-3

11. Marin I, Rydèn T, Van Essen M, Svensson J, Gracheva N, Köster U, Zeevaart JR, van der Meulen NP, Müller C, Bernhardt P. Establishment of a clinical SPECT/CT protocol for imaging of 161Tb. *EJNMMI Phys* (2020) **7**: 45–60. doi:10.1186/s40658-020-00314-x

12. Emmett L, Willowson K, Violet J, Shin J, Blanksby A, Lee J. Lutetium 177 PSMA radionuclide therapy for men with prostate cancer: a review of the current literature and discussion of practical aspects of therapy. *J Med Radiat Sci* (2017) **64**:52–60. doi:10.1002/jmrs.227

13. Baum RP, Singh A, Kulkarni HR, Bernhardt P, Rydén T, Schuchardt C, Gracheva N, Grundler P V, Köster U, Müller D, *et al.* First-in-Human Application of Terbium-161: A Feasibility Study Using ^{161}Tb-DOTATOC. *J Nucl Med* (2021) jnumed.120.258376. doi:10.2967/jnumed.120.258376

14. Farkaš P, Bystrický S. Chemical conjugation of biomacromolecules: A mini-review. *Chem Pap* (2010) **64**:683–695. doi:10.2478/s11696-010-0057-z

15. Chastel A, Worm DJ, Alves ID, Vimont D, Petrel M, Fernandez S, Garrigue P, Fernandez P, Hindié E, Beck-Sickinger AG, *et al.* Design, synthesis, and biological evaluation of a multifunctional neuropeptide-Y conjugate for selective nuclear delivery of radiolanthanides. *EJNMMI Res* (2020) **10**:16-27 doi:10.1186/s13550-020-0612-8

16. Blower PJ. A nuclear chocolate box: The periodic table of nuclear medicine. *Dalt Trans* (2015) **44**:4819–4844. doi:10.1039/c4dt02846e

17. Zhang WJ, Luo X, Liu YL, Shao XX, Wade JD, Bathgate RAD, Guo ZY. Site-specific DOTA/europium-labeling of recombinant human relaxin-3 for receptor-ligand interaction studies. *Amino Acids* (2012) **43**:983–992. doi:10.1007/s00726-011-1164-z

18. Hijnen NM, de Vries A, Blange R, Burdinski D, Grüll H. Synthesis and *in vivo* evaluation of ^{201}Tl(III)-DOTA complexes for applications in SPECT imaging. *Nucl Med Biol* (2011) **38**:585–592. doi:10.1016/j.nucmedbio.2010.10.009

19. Kang CS, Sun X, Jia F, Song HA, Chen Y, Lewis M, Chong HS. Synthesis and preclinical evaluation of bifunctional ligands for improved chelation chemistry of ^{90}Y and ^{177}Lu for targeted radioimmunotherapy. *Bioconjug Chem* (2012) **23**:1775–1782. doi:10.1021/bc200696b

20. Chong HS, Sun X, Chen Y, Sin I, Kang CS, Lewis MR, Liu D, Ruthengael VC, Zhong Y, Wu N, *et al.* Synthesis and comparative biological evaluation of bifunctional ligands for radiotherapy applications of ^{90}Y and ^{177}Lu. *Bioorganic Med Chem* (2015) **23**:1169–1178. doi:10.1016/j.bmc.2014.12.035

21. Obaid G, Chambrier I, Cook MJ, Russell DA. Cancer targeting with biomolecules: A comparative study of photodynamic therapy efficacy using antibody or lectin conjugated phthalocyanine-PEG gold nanoparticles. *Photochem Photobiol Sci* (2015) **14**:737–747. doi:10.1039/c4pp00312h

22. Kim TD, Ryu HJ, Cho H Il, Yang CH, Kim J. Thermal behavior of proteins: Heat-resistant proteins and their heat-induced secondary structural changes. *Biochemistry* (2000) **39**:14839–14846. doi:10.1021/bi001441y

23. Mitterhauser M, Toegel S, Wadsak W, Lanzenberger RR, Mien LK, Kuntner C, Wanek T, Eidherr H, Ettlinger DE, Viernstein H, *et al.* Pre *vivo*, *ex vivo* and *in vivo* evaluations of [^{68}Ga]-EDTMP. *Nucl Med Biol* (2007) **34**:391–397. doi:10.1016/j.nucmedbio.2007.03.002

24. Fritzberg AR, Whitney WP, Kuni CC, Klingensmith W. Biodistribution and renal excretion of ^{99m}Tc-N,N'-bis-(mercaptoacetamido) ethylenediamine. Effect of renal tubular transport inhibitors. *Int J Nucl Med Biol* (1982) **9**:79–82. doi:10.1016/0047-0740(82)90081-X

25. Knör S, Modlinger A, Poethko T, Schottelius M, Wester HJ, Kessler H. Synthesis of novel 1,4,7,10-tetraazacyclodecane-1,4,7,10-tetraacetic acid (DOTA) derivatives for chemoselective attachment to unprotected polyfunctionalized compounds. *Chem - A Eur J* (2007) **13**:6082–6090. doi:10.1002/chem.200700231

26. Brücher E, Zékány L. Aminopolycarboxylates of rare earths—VII. *J Inorg Nucl Chem* (1981) **43**:351–356. doi:10.1016/0022-1902(81)90022-1

27. Camargo MA, Neves A, Bortoluzzi AJ, Szpoganicz B, Fischer FL, Terenzi H, Serra OA, Santos VG, Vaz BG, Eberlin MN. Efficient phosphodiester hydrolysis by luminescent terbium(III) and europium(III) complexes. *Inorg Chem* (2010) **49**:6013–6025. doi:10.1021/ic100549u

28. Carpanese D, Ferro-Flores G, Ocampo-Garcia B, Santos-Cuevas C, Salvarese N, Figini M, Fracasso G, De Nardo L, Bolzati C, Rosato A, *et al.* Development of ^{177}Lu-scFvD2B as a Potential Immunotheranostic Agent for Tumors Overexpressing the Prostate Specific Membrane Antigen. *Sci Rep* (2020) **10**:1–10. doi:10.1038/s41598-020-66285-2

29. Morgenstern A, Apostolidis C, Kratochwil C, Sathekge M, Krolicki L, Bruchertseifer F. An Overview of Targeted Alpha Therapy with ^{225}Actinium and ^{213}Bismuth. *Curr Radiopharm* (2018) **11**:200–208. doi:10.2174/1874471011666180502104524

30. Guizado TRC. Analysis of the structure and dynamics of human serum albumin. *J Mol Model* (2014) **20**:2450. doi:10.1007/s00894-014-2450-y

31. Nguyen A, Reyes AE, Zhang M, McDonald P, Wong WLT, Damico LA, Dennis MS. The pharmacokinetics of an albumin-binding Fab (AB.Fab) can be modulated as a function of affinity for albumin. *Protein Eng Des Sel* (2006) **19**:291–297. doi:10.1093/protein/gzl011

32. Boros E, Holland JP. Chemical aspects of metal ion chelation in the synthesis and application antibody-based radiotracers. *J Label Compd Radiopharm* (2018) **61**:652–671. doi:10.1002/jlcr.3590

33. Li M, Cheng F, Li H, Jin W, Chen C, He W, Cheng G, Wang Q, Site-Specific and Covalent Immobilization of His-Tagged Proteins via Surface Vinyl Sulfone–Imidazole Coupling, *Langmuir* (2019) **35**:16466–16475. doi : 10.1021/acs.langmuir.9b02933

34. Kumari P, Nath Y, Murty US, Ravichandiran V, Mohan U, Sortase A Mediated Bioconjugation of Common Epitopes Decreases Biofilm Formation in *Staphylococcus aureus*, *Front. Microbiol.*(2020) **11**:1–8. doi: 10.3389/fmicb.2020.0170235. Dorta DA, Deniaud D, Mével M, Gouin SG, Tyrosine Conjugation Methods for Protein Labelling, *Chem. Eur. J.* (2020) **26**:14257–14269. doi : 10.1002/chem.202001992

Chapter 3 – Preclinical evaluation of a terbium-161 labelled half-life extended anti-c-Met Nanobody® (v_HH)

Irwin Cassells[1,2], Koen Vermeulen[1], Sunay Rodriguez Perez[1], Michiel Van de Voorde[1], Peter Casteels[3], Ben Webster[4], Charlotte Segers[1], Christopher Cawthorne[5], Peter Ivanov[4], Christophe M. Deroose[5,6], Thomas Cardinaels[7,8], Guy Bormans[2], Frederik Cleeren[2*] and Maarten Ooms[1*]

[1] Nuclear Medical applications institute, Belgian Nuclear Research Centre (SCK CEN), Mol, Belgium. [2] Radiopharmaceutical Research, Department of Pharmaceutical and Pharmacological Sciences, University of Leuven, Leuven, Belgium. [3]Large Molecule Research Innovation, Sanofi, Ghent, Belgium. [4] National Physical Laboratory, Teddington, London, England. [5] Nuclear Medicine & Molecular Imaging, Department of Imaging and Pathology, KU Leuven, Leuven, Belgium. [6] Nuclear Medicine, University Hospitals Leuven; Nuclear Medicine and Molecular Imaging, Department of Imaging and Pathology, KU Leuven; Leuven, Belgium. [7] Nuclear Energy Technology institute, Belgian Nuclear Research Centre (SCK CEN), Mol, Belgium. [8] Department of Chemistry, University of Leuven, Leuven, Belgium

**Corresponding authors*

[*Manuscript in progress for submission for publication*]

3.1 Introduction

In the last decade, the terbium radioisotope series has been gathering interest from the nuclear medicine community (1), as there are four radioisotopes (^{149}Tb, ^{152}Tb, ^{155}Tb and ^{161}Tb) interesting for nuclear medicine applications (2). Of these terbium isotopes, ^{161}Tb is often considered as the upcoming isotope for targeted radionuclide therapy. With its half-life ($t_{1/2}$ = 6.96 days), decay characteristics (β^- decay, $E\beta^-_{average}$ = 0.154 MeV) and chemical similarities, it is often compared to ^{177}Lu (β^- emitter, $t_{1/2}$ = 6.64 days, $E\beta^-_{average}$ = 0.134 MeV) (3,4). However, the therapeutic potential of ^{161}Tb might be superior to that of ^{177}Lu due to the co-emission of conversion and Auger electrons. These low energy electrons can deposit ~36 keV in a short range, which can be favourable for sub-cellular targeting. In a study by Müller *et al.* (5), a direct *in vitro* comparison of the therapeutic effect of ^{177}Lu and ^{161}Tb was investigated. Therein, they observed a greater therapeutic potency of folate compounds bearing terbium-161 compared to its lutetium-177 counterpart (5). A similar result was observed *in vivo* with prostate-specific membrane antigen (PSMA) targeting groups, whereby tumour-bearing mice treated with ^{161}Tb-labelled constructs had a greater survival rate compared to mice treated with ^{177}Lu-labelled constructs (6). Additionally, a clinical case study with a single patient that did no longer respond to ^{177}Lu treatment showed [^{161}Tb]Tb-PSMA-617 to reduce prostate specific antigens by 53% for weeks (7,8). Finally, ^{161}Tb is also interesting because of its diagnostic partners ^{155}Tb (EC γ emitter, $t_{1/2}$ = 5.32 days, $E\gamma_{average}$ = 105 keV) and ^{152}Tb (β^+ emitter, $t_{1/2}$ = 17.52 h, $E\beta^+_{average}$ = 1.14 MeV) thus allowing therapy and imaging using the same chemical element.

Current ^{161}Tb-radiopharmaceuticals consist out of vector molecules that are robust enough to handle high labelling temperatures (>80 °C). However, many promising vector molecules for nuclear medicine applications are heat-sensitive and are incompatible with the current ^{161}Tb-labelling techniques. In our previous study, we developed a radiolabelling protocol using mild conditions allowing the radiolabelling of these heat-sensitive biomolecules with [^{161}Tb]$TbCl_3$ (9). Biomolecules, predominantly antibodies, have shown clinical success, with [^{131}I]I-tositumomab, [^{90}Y]Y-ibritumomab tiuxetan and [^{131}I]I-chTNT being some of the radiopharmaceuticals paving the way for biomolecule-based radionuclide therapy application (10–13). Though antibodies have excellent affinity for the target, long *in vivo* circulation times result in low target-to-blood ratios, resulting in poor contrast (14) at short time after injection. Longer plasma circulation times result in longer exposure to potentially harmful off-target radiation. Nanobodies (v_HH, heavy-chain only variable antibody fragment) have proven to be a promising class of biomolecules in recent years, with successful applications in fields such as oncology, infection and immunology (15). These v_HH have similar specific affinity for their target antigen compared to antibodies, but at a fraction of the size (12-15 kDa vs ±150 kDa). As a result, v_HH have much faster pharmacokinetics and better tissue penetration than the parent antibody (15,16). However, too fast kinetics can also be counterproductive, as rapid excretion of the v_HH can occur, potentially resulting in limited target binding/uptake, although this is also dependent on the target expression. Ideally, a balance is needed. Therefore, the plasma half-life can be modified by introducing biological half-life extending (HLE) groups such as serum albumin binding agents (17).

In collaboration with Sanofi® Ghent, a bivalent v_HH, combining a targeting moiety against humanised mesenchymal-epithelial transition factor (c-Met; HGF ligand blocking: IC_{50} = 72 pM) with a serum albumin binding moiety (albumin binding v_HH; human serum albumin, K_D = 19 nM; mouse serum albumin , K_D = 260 nM) for enhanced plasma pharmacokinetics, was developed (**Figure 3.1**). c-Met is a member of the receptor tyrosine kinase (RTK) family of receptors responsible for migration, cell survival, angiogenesis and motility (18–21). Conventionally, c-Met is activated by hepatocyte growth factor (HGF) but can also be activated by other molecules once it heterodimerises with other surface proteins (18). Since c-Met activation is responsible for cell proliferation, migration and angiogenesis, it is often upregulated in several tumour types (20,22–24) making it a good target for cancer treatment. As a result, the v_HH targeting c-Met, together with a highly favourable pharmacokinetic profile, could be an ideal carrier for a ^{161}Tb-based radiopharmaceutical. Therefore, in this study, we aimed to use our expertise in radiolabelling of heat sensitive molecules with terbium isotopes (9) and apply it to this HLE targeting c-Met v_HH. We report the radiolabelling of the c-Met v_HH with both a therapeutic (^{161}Tb) and an imaging (^{155}Tb) isotope of terbium to create a potential potent theragnostic radiopharmaceutical pair. Radiolabelling was followed by early biological evaluation both *in vitro* and *in vivo*.

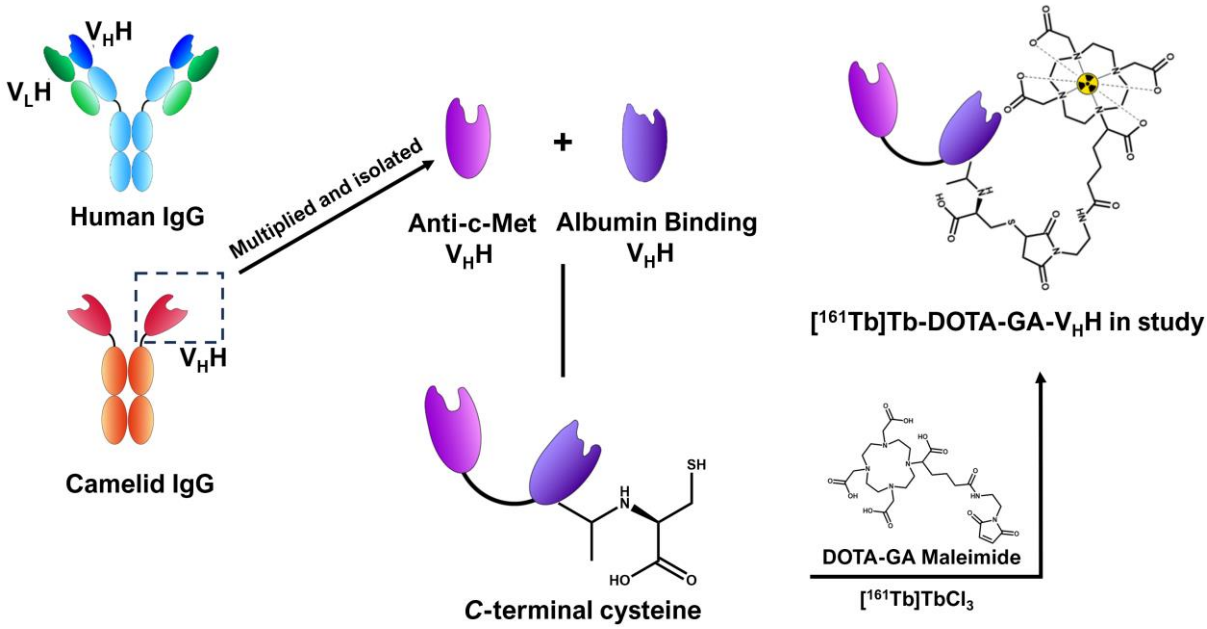


Figure 3.1. Simplified source and structure of the half-life extended v$_H$H used in this study. Terbium isotopes are complexed by a DOTA-GA moiety, which is introduced by reacting with the free thiol on the *C*-terminal cysteine using commercially-available maleimide-DOTA-GA. Images were adapted from https://www.gesundheitsindustrie-bw.de/en/article/news/nanobodies-determining-neutralising-antibodies-after-corona-infection .

3.2 Materials and Methods

3.2.1 General

All reagents and solvents were purchased from Sigma-Aldrich (Bornem, Belgium) or VWR (Leuven, Belgium), and used without further purification. Maleimide-DOTA-GA (DOTA-GA, cat. no. 1006711-09-5) was purchased from CheMatech (Dijon, France) and used without further purification. Trace metals were removed from radiolabelling buffers using Chelex 100 (sodium form, 50-100 mesh, Sigma Aldrich). Buffers were degassed and filtered before use.

The bivalent v$_H$H combining a c-Met targeting v$_H$H, together with a plasma half-life extending albumin binding v$_H$H, was provided by Sanofi Ghent. The c-Met v$_H$H is specific for human c-Met (HGF ligand blocking: IC_{50} = 72 pM) with no cross reactivity with mouse c-MET. The half-life extending albumin binding component is cross reactive with human (K_D = 19 nM), mouse (K_D = 260 nM) and calf serum albumin (K_D = 24 nM).

BxPC-3 cells (cat. no. CRL-1687, ATCC) were maintained in RPMI 1640 (ATCC (cat. no. 30-2001, Molsheim Cedex, France) or Thermo Fisher (Gibco, cat. no. A1049101, Merelbeke, Belgium)), and supplemented with 10% foetal bovine serum (FBS, Thermo Fisher, cat. no. A5256701) and 1% Penicillin-Streptomycin (Thermo Fisher, cat. no. 15140122). Cells were maintained in the afore-mentioned

medium solution, at 37ºC and 5% CO_2 and sub-cultured according to ATCC specifications without modification. Cell doubling rate (P5-P12): 50-76 h.

3.2.2 Animal Studies

All animal experiments were conducted under the Belgian code of practice and use of animal experiments and subjected to approval by an ethical committee from either KU Leuven (P054/2 019) or SCK CEN (EC MxCl 2021-169). Healthy albino Naval Medical Research Institute (NMRI) (Envigo, Gannat, France) and immunodeficient NMRI nude Foxn1$^{nu/nu}$ mice (Janvier, Saint-Berthevin, France) (age: 4-8 weeks) were housed in individually ventilated cages, in a regulated environment (22 °C, humidity 55%, 12h day/night cycle), with food and water *ad libitum*. BxPC-3 tumour models were generated by subcutaneously inoculating NMRI nude Foxn1$^{nu/nu}$ mice in the shoulder region with 1x10^6 BxPC-3 cells dispersed in Cultrex (Bio-techne, cat. no. 3432-010-01, Minneapolis, MN) (25). Tumours were left to develop for a minimum of 3 weeks (tumour size: 150-200 mm^3) before experiments were performed.

3.2.3 Instrumentation and Characterisation

Quality control of the nanobody constructs was carried out using size-exclusion chromatography (SEC) (Superdex 75 10/300 GL column, GE Healthcare Bio-Science AB, Uppsala, Sweden), eluted with sodium phosphate buffered saline (PBS solution: 0.15 M sodium chloride, 0.01 M phosphate, pH 7.4, Thermo Fisher) at a flow rate of 0.75 mL/min. The column effluent was passed through a UV (280nm) detector (2998 PDA detector, Waters, Milford, Massachusetts) in series with a 3-inch NaI(Tl) radioactivity detector. Gamma counting was performed on a Wizard^2 2470 or 3470 (crystal: NaI(Tl), 50 mm in height, 32 mm in diameter, dead time 2.5 µs; Perkin Elmer, Rodgau, Germany) with a detection profile referenced for ^{161}Tb decay (window: 40-120 keV, sample count time: 60 seconds). Counts were corrected for background radiation, physical decay and detector dead time. Mass spectrometry was performed on an Agilent 6530 Q-TOF after separation on an Agilent 1290 Infinity UHPLC system (Pedroso, Portugal), equipped with a Waters XBridge Protein UPLC BEH C4 column (5.0 µm, 10 X 50 mm, Waters, Milford, USA). Colorimetry cell-based assays were quantified using a CLARIOstar microplate reader (BMS Labtech, De Meern, Netherlands). Real-time cytotoxicity was assessed using an Incucyte zoom live-cell imaging system (Essen Bioscience, Newark-on-Trent, England).

3.2.4 Isotope production

[^{161}Tb]$TbCl_3$ was produced at SCK CEN using a modified method described in Cassells *et al.*(9). In brief, enriched $^{160}Gd_2O_3$ (1.0 mg, 98.2 %, Isoflex, San Francisco, CA) was dissolved in nitric acid (7M, 2.0 mL) and transferred into a quartz ampoule and sealed. The ampoule was sealed inside an aluminium capsule and was irradiated for 7 days in the BR2 Reactor at the Belgian Nuclear Research Centre (SCK CEN) at

a thermal neutron flux of approx. 3.0 x 10^{14} n·cm^{-2}·s^{-1}. After the ampoule was allowed to cool for 24 hours, the sample was diluted in high purity water. High-pressure ion chromatography (HPIC, Shimadzu), with a strong cation exchange column (ø: 6 mm, l: 50 mm, Shodex IC R-621), was used to separate the ^{161}Tb from unconverted ^{160}Gd target matrix by elution with α-hydroxyisobutyric acid (α-HIBA) / ammonium hydroxide (trace-metal grade, pH 4.5) solution. [^{161}Tb]Tb-(α-HIBA)$_n$ complex was converted to the chloride salt by trapping the terbium source on an extraction resin (ø: 2.1 mm, l: 30 mm, LN3, TrisKem International, Bruz, France) and elution with 50 mM hydrochloric acid (trace-metal free). [^{161}Tb]Cl_3 was obtained with a radionuclidic purity of >99.999% (determined by high resolution gamma spectroscopy).

[^{155}Tb]$TbCl_3$ was provided through the MEDICIS ProMed collaboration (9,26). Three sources of ^{155}Tb were produced at the ARRONAX cyclotron in Nantes (France) from the irradiation of natural gadolinium foil targets (*ca.* 300 mg, 25 µm thickness, 99.9% Gd purity) with 34 MeV protons (27). Before being shipped to CERN-MEDICIS for offline mass separation of the spallation material, the irradiated Gd foils were first dissolved and processed at ARRONAX using a LN resin method to reach a ^{155}Tb:Gd ratio of < 1:100 from an initial ratio of ~1:1,000,000. The solution was deposited and evaporated on a dedicated sample holder, to transfer and load the radioactive source into an empty target tantalum oven of a standard ISOLDE target and rhenium ion source unit (28). In preparation for the collection of ^{155}Tb, the extraction voltage was set to 60 kV, and the extraction electrode positioned after an acceleration gap of 60 mm from the ion source exit. This way the beam profile displays a gaussian shape of sigma = 0.8 mm at the position of the beam diagnostics before the implantation chamber. Respective resistive heating currents of 400 A (1300 °C) and 290 A (2100 °C) were applied to heat the target and the ion source and allow for preliminary optimisation steps on a stable ^{159}Tb mass marker (29). Terbium-155 was extracted from targets that were heated to 2200 °C (corresponding to a current of 750 A). Laser resonance ionisation was applied with MEDICIS's Laser Ion Source for Separator Assembly (MELISSA) with a 10 kHz pulsed system to selectively enhance the ionisation of ^{155}Tb, using a combination of a two-step resonant and a one-colour two-resonance ionisation scheme with output powers around 1 W. The mass-separated ^{155}Tb beam was implanted into a solid catcher (zinc-coated gold foil, gold thickness: 0.25 mm, purity: 99.95%, Goodfellow Cambridge Ltd. Huntingdon, UK, zinc thickness: 500 nm, by Physical Vapour Deposition (PVD) process)(30) and shipped to National Physical Laboratory (NPL, Teddington, England) for radiochemical separation.

3.2.5 Synthesis of compounds

Synthesis of v$_H$H constructs

The bivalent v$_H$H was engineered with a free cysteine at the *C*-terminus, which spontaneously forms S-S bonds with other free thiol molecules, including other v$_H$H resulting in dimers. To obtain monomeric v$_H$H (a free thiol), the partial dimer solution (0.29 µmol, based on dimer) was stirred in an aqueous solution of 10 mM DL-dithiothreitol (DTT), 10 mM HEPES and 150 mM NaCl (total volume: 1.0 mL) at room temperature for 75 minutes. The solution was purified using a desalting chromatography cartridge

(PD-10 column, GE Healthcare Bio-Science AB, Uppsala, Sweden) eluted with 10 mM HEPES and 150 mM NaCl (1.9 mL). The sample (1.0 mL) was collected in an Eppendorf tube (Protein LoBind, Eppendorf, Aarschot, Belgium) containing a five-molar excess of maleimide-DOTA-GA (3 µmol) in 100 µL of high-purity water (HPCE grade, CAS 7732-18-5, Sigma Aldrich). The solution was gently stirred at 37°C for 75 minutes. The solution was purified using a PD-10 column, and the **DOTA-GA-v_HH** was eluted with sodium acetate buffer (0.1 M, pH 4.7, chelex treated) for radiolabelling or PBS for analysis. The concentration of the construct (**DOTA-GA-v_HH**) was determined using spectrophotometry at 280 nm (NanoDrop® One, Thermo Fisher Scientific), with ε = 41 000 L/mol/cm and M = 26588 g/mol. The purified product was analysed using a Superdex 75 10/300 GL column and the aforementioned method. **DOTA-GA-v_HH**: HPLC: 14.8 min (280 nm), purity: 99.7 %, ESI-MS *m/z* (decon.) calculated for **v_HH-DOTA-GA**: 27 180.80 Da. Found: 27 180.63 Da.

Using the same method, the blocking agent (**v_HH-HPM**) was produced v_HH using the same method as described above via reacting the free thiol with *N*-(4-hydroxyphenyl)maleimide (**HPM**). HPLC analysis of this purified **v_HH-HPM** construct showed a retention time of 14.9 min (280 nm) and a purity of 99.8 %, ESI-MS *m/z* (decon.) calculated for v_HH-HPM: 26 777.17 Da. Found: 26 777.32 Da.

3.2.6 Radiolabelling

For radiolabelling, 0.4-0.8 MBq of [^{155}Tb]$TbCl_3$ or up to 90 MBq of [^{161}Tb]$TbCl_3$ (in 20 µL 50mM HCl) was added to a solution of the purified **DOTA-GA-v_HH** (3 nmol) in 0.1M sodium acetate buffer pH 4.7 (total reaction volume 300 µL). The reaction was performed by heating the mixture at 40 ºC for 60 minutes. Radiochemical conversion was determined by iTLC-SG (Agilent, cat. no. SGI0001, Leuven, Belgium), eluted with sodium citrate buffer (0.1 M, pH 5.8). Plates were cut in two, with the top part associated with non-chelated [$^{155/161}$Tb]$TbCl_3$ (R_f = 1.0) and bottom part associated with labelled conjugate (**[$^{155/161}$Tb]Tb-DOTA-GA-v_HH**, R_f = 0.0) (R_f values determined by autoradiography). The activity in each part was determined using an automatic gamma counter, and the radiochemical conversion calculated as the ratio of activity in bottom part over the total activity of the TLC strip. In addition, radiolabelling conversion **DOTA-GA-v_HH** was confirmed by radio-SEC using the method described above.

The same protocol was used to radiolabel DOTA-GA-Maleimide with ^{155}Tb or ^{161}Tb. Radiochemical conversion was determined by iTLC-SG, eluted with a 3:1 acetonitrile:water mixture. Plates were cut in two, with the bottom part was associated with non-chelated [$^{155/161}$Tb]$TbCl_3$ (R_f = 0.1) and top portion associated with labelled [$^{155/161}$Tb]Tb-DOTA-GA-Maleimide (**[^{161}Tb]Tb-DOTA-GA-Mal**, R_f = 1.0).

3.2.7 Cell binding of [^{161}Tb]Tb-DOTA-GA-v_HH

To study cell binding of **[^{161}Tb]Tb-DOTA-GA-v_HH**, BxPC-3 cells were seeded in a 24-well plate (5 x 10^4 cells per well) and allowed to attach over 48 h at 37 °C, 5% CO_2. Culture medium was replaced 60 minutes before the experiment was performed. Cells were then incubated with 1 nM (10 kBq) of

[^{161}Tb]Tb-DOTA-GA-v$_H$H at 37°C for 30, 60, 90 and 120 min. In parallel, receptor blocking was performed using the same time points after pre-treating the cells with an excess of **v$_H$H-HPM** (1 µM) 30 min before radiotracer incubation. For total receptor blocking using 0.1 µmol of **v$_H$H-HPM**, the bound activity was assessed at 60 and 120 minutes.

At the end of incubation, cell medium was removed and washed with cell culture medium (3 x 0.5 mL). Cells were detached from the well surface by incubating cells with Trypsin EDTA (0.25%, 0.5 mL, 25200072, Thermo Fisher, USA) for 30 minutes. Wells were washed with additional medium and collected (3 x 0.5 mL). Collected solutions were assessed for their radioactive content using an automatic gamma counter and counts were decay corrected to start of counting. Percentage bound was calculated using: $\%_{bound}$ = $Counts_{cells}$ / ($Counts_{cells}$ + $Counts_{medium}$). To estimate nanobody cell internalisation, cell binding was also performed at 4°C, as at this temperature internalisation is minimal. The internalisation was estimated by calculating the difference between $\%_{bound}$ at 4 and 37 °C (31). Results were normalised to 1 x 10^5 cells for comparison.

3.2.8 Cell viability and cytotoxicity screening

Cell viability after exposure to **[^{161}Tb]Tb-DOTA-GA-v$_H$H** was tested using the CellTiter 96® Aqueous One Solution Cell Proliferation Assay (Promega G3582). A total of 3000 cells per well were seeded in a 96-well plate and allowed to attach at 37 °C, 5% CO_2. Cells were treated with 0-20 MBq/mL of **[^{161}Tb]Tb-DOTA-GA-v$_H$H** (total volume 100 µL) and incubated for 4 or 24h. Following the initial treatment, cells were washed and replaced with activity-free culture medium. After 5 days incubation, 10 µL of CellTiter 96® Aqueous One Solution (which contains MTS (3-(4,5-dimethylthiazol-2-yl)-5-(3-carboxymethoxyphenyl)-2-(4-sulfophenyl)-2H-tetrazolium)) was added to the cells. After 30 minutes, the absorbance (490 nm) was determined for each well using a microplate reader and normalised to the absorbance from cell culture medium. The experiment was performed in quadruplicate. The mean cell viability was calculated by using the ratio of the absorbance of treated and untreated cells. The same assay was repeated with **[^{161}Tb]Tb-DOTA-GA-Mal**, as a control compound with no affinity for c-MET, to quantify the medium-related effects of the radioactivity present. Effective concentration (EC_{50}) was determined by non-linear regression analysis of the data using GraphPad Prism 9.1.

Cytotoxicity and the involved cell death pathways were investigated using Incucyte® Cytotox Green (cat. no. 4633, Brussels, Belgium) and Incucyte® Annexin V Red (cat. no.4641, Brussels, Belgium). For this assay, 3000 cells were seeded in a 96-well plate and treated with **[^{161}Tb]Tb-DOTA-GA-v$_H$H** or **[^{161}Tb]Tb-DOTA-GA-Mal** (0-20.0 MBq/mL, total volume: 100 µL) for 4 or 24 h. After treatment, cells were washed and incubated with medium containing Incucyte® Cytotox Green (general cell death) or Incucyte® Annexin V Red (apoptosis) for 5 days according to manufacturing protocols.

3.2.9 Clonogenic survival assay

Clonogenic survival assays were performed based on the methods described Brix *et al.*(32). Cells were seeded in a 6-well plate, at a cell density of 1.5 x 10^3 cells per well and allowed to attach over 48 h at 37 °C, 5% CO_2. Cells were treated with **[^{161}Tb]Tb-DOTA-GA-v$_H$H** or **[^{161}Tb]Tb-DOTA-GA-Mal** (0.1, 0.5, 1.0, 2.0 MBq/mL) and incubated for 4 or 24 h, in triplicate. At the end of the treatment period, cells were washed with phosphate buffered saline (3 x 3 mL) to remove all non-bound activity. Then fresh, non-radioactive cell medium was added (3 mL) and the cells were incubated for 10 days. Finally, cells were fixed by incubation with 1 mL of 0.5% crystal violet and 6% glutaraldehyde solution (CAS: 111-30-8, Merck) for 30 min. The crystal violet/glutaraldehyde solution was removed by gravity and cells were dried at room temperature in air, colonies counted (minimum of 50 cells per colony) and the plating efficiency (PE) and survival fraction (SF) was calculated (33):

$$PE(\%) = 100 \times N_{\text{colonies without treatment}} / N_{\text{cells seeded}}$$

$$SF(\%) = 100 \times N_{\text{colonies after treatment}} / (N_{\text{cells seeded}} \times PE)$$

3.2.10 *Ex vivo* biodistribution

Mice were anaesthetised with isoflurane (2.5% in O_2, 1 L/min) and intravenously injected with ~1 MBq of **[^{161}Tb]Tb-DOTA-GA-v$_H$H** (0.1-0.3 nmol, average animal weight: 35.5 ± 2.4 g). Animals were anaesthetised, then sacrificed by decapitation (healthy mice) or cardiac puncture (tumour-bearing mice) at 4 h, 24 h, or 7 d post injection (minimum n = 3 for analysis). Organs were collected in tarred tubes, weighed, and radioactivity was determined using an automated gamma counter as described above. Collected counts were converted to MBq based on a calibration factor. For the calculation of activity in blood, bone and muscle tissues were assumed to be 7%, 12% and 40% of mouse body, respectively (34). Blood activity data points (%$ID_{\text{calculated}}$) were fitted to a standard half-life equation (least-squares regression analysis), $\%ID_{calc} = A_0 \cdot 0.5^{kt}$, where A_0 = constant, t = hours after injection (h), and k = 1 / plasma half-life (h).

3.2.11 *μ*-SPECT/ CT scans

One healthy mouse was injected with 0.6 MBq of **[^{155}Tb]Tb-DOTA-GA-v$_H$H** (0.8 nmol , mouse weight = 42 g) and small animal whole-body μ-SPECT/CT imaging was performed 4 hrs post injection using Molecubes γ- and χ-cube systems (Ghent, Belgium). The SPECT scan was performed by scanning the animal for 1h after the indicated time point, with 5 min CT acquisition post scan for attenuation correction. The mouse was placed and kept under anaesthesia (2.5% isoflurane, 1 L/min O_2 as the carrier gas) prior and during image collection.

Tumour-bearing mice were injected with 24-28 MBq of **[^{161}Tb]Tb-DOTA-GA-v$_H$H** (16-21 nmol/kg, n=4) and small animal whole-body μ-SPECT/CT imaging was performed after 4 h, 24 h, 48 h and 72 h post

injection using MiLabs μ-SPECT-6 (Houten, The Netherlands). After the indicated time points, SPECT scans were performed by scanning the animals for 1.5 - 2 h, with 3 min CT acquisition post scan for attenuation correction. Mice were placed and kept under anaesthesia (2.5% isoflurane, 1 L/min O_2 as the carrier gas) prior and during image collection.

Image Reconstruction

For healthy animal scans, reconstruction and co-registration of the images was performed using the Molecubes provided manufacturer software. The reconstruction software uses the similarity-regulated ordered subsets expectation maximization (SROSEM) algorithm (35), with 10 iterations, 128 subsets and a voxel size of 0.4 mm^3. After reconstruction, SPECT images were registered to the computed tomography (CT) images and corrected for photon attenuation based on the CT data. The final voxel size after registration was 0.4 mm^3. PMOD 4.101 software (PMOD, Switzerland) was used for image analysis. SPECT data in reconstructed counts per seconds (cps) units were calibrated to activity units (kBq/cc) using a single activity Q-factor calibration (kBq/AU), calculated from a reference activity (kBq/cc) and the region of interest (AU/cc).

For tumour-bearing mice, reconstruction and co-registration of the images was performed using the Milabs provided manufacturer software. To reconstruct the SPECT images, two windows of 17% and 30% were centred on the 52 keV and 78 keV photopeaks, respectively. Scatter correction was applied using the triple energy window method automatically applied by the software. The reconstruction software uses the similarity-regulated ordered subsets expectation maximization (SROSEM) algorithm (35), with four iterations, 128 subsets and a voxel size of 0.4 mm^3. After reconstruction, SPECT images were registered to the computed tomography (CT) images and corrected for photon attenuation based on the CT data. The final voxel size after registration was 0.16 mm^3. PMOD 4.101 software (PMOD, Switzerland) was used for image analysis.

SPECT data in reconstructed counts per seconds (cps) units were calibrated to activity units (MBq/cc) using a calibration factor (CF). To determine the calibration factor, a known activity of ^{161}Tb was used to fill a 10 mL syringe which was then scanned in the SPECT-CT system. The images were reconstructed using identical settings (energy windows, voxel size, number or iterations, etc.) as in the *in vivo* study. A volume of interest (VOI) corresponding to 90% of the diameter of the syringe was used to calculate CF as the mean voxel intensity in the VOI (cps) divided by the known activity (MBq/cc). The displayed images were converted to SUV [activity concentration /(injected activity x weight of mouse)], where the activity measured from an image acquired at time t, decay corrected to t=0 (injection time) and expressed as volume concentration (e.g. MBq/mL) and injected activity is the activity at t=0 in MBq.

3.2.12 Statistical Analyses

Quantitative data are expressed as mean ± standard deviation, unless stated otherwise. Means were compared using a mixed model ANOVA analysis in GraphPad Prism 9.4.1, corrected using Sidak's or

Tukey multiple comparison test. Values were determined to be statistically significant for *p*-values less than the threshold value of 0.05.

3.3 Results and Discussion

3.3.1 Conjugation and Radiolabelling with [^{161}Tb]TbCl$_3$

Radiolabelling of the bivalent anti-c-Met, anti-albumin v_HH was performed by first coupling a DOTA-GA-maleimide bifunctional chelator to the v_HH. This commercially available chelator was chosen based on previous studies (9), where **DOTA-GA** was found to be an ideal chelator for ^{161}Tb-radiolabelling of heat-sensitive molecules. To avoid potential interference of the chelator to the antigen-binding site of the v_HH, **DOTA-GA** was conjugated to the c-Met nanobody using a site-specific coupling on a cysteine, which was engineered on the *C*-terminus of the bivalent v_HH. The free thiol group found in cysteines are known to be cross-reactive with each other resulting in dimerisation of the v_HH constructs. Since the free thiol group is crucial for site-specific radiolabelling, a reducing protocol using Cleland's reagent (dithiothreitol, DTT) was developed that successfully monomerised the v_HH to form **v_HH-SH**. Using the cleaving protocol, full conversion to the monomer was observed with a retention time of 14.2 minutes when analysed by size exclusion chromatography (**Figure 3.2**). After the S-S bridge was cleaved and DTT removed, an excess of DOTA-GA-Maleimide was added to the solution and allowed to react. The conjugated sample was analysed using size-exclusion UV chromatography. A single UV signal was observed at 14.8 minutes at 280 nm, which corresponded to the retention time of the bivalent monomeric nanobody construct (**v_HH-SH**) (**Figure 3.2**). The global recovery yield of the final product, **DOTA-GA-v_HH**, was 51.9 ± 2.0% (purity>99%, HPLC).

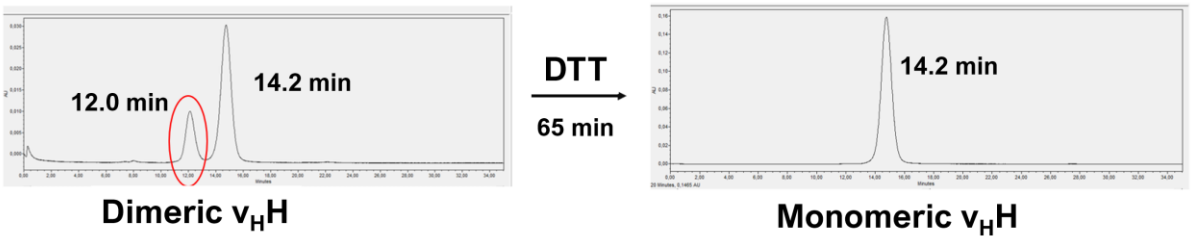


Figure 3.2: SEC-HPLC chromatogram (280 nm) of the bivalent v_HH before and after reducing with DTT.

The **DOTA-GA-v_HH** construct was subsequently used for radiolabelling with [^{155}Tb]TbCl$_3$ or [^{161}Tb]TbCl$_3$. Radiolabelling conditions were adapted from our earlier reports (9). Radiolabelling for 60 min at 37°C was highly efficient, resulting in radiochemical conversion of >99%, with a maximum molar activity of 30 MBq/nmol. Radio-SEC showed a clear separation between [^{161}Tb]TbCl$_3$ (rt = 21.1 min, spiked) and **[^{161}Tb]Tb-DOTA-GA-v_HH** (RT = 14.2 min) **(Figure 3.3).**

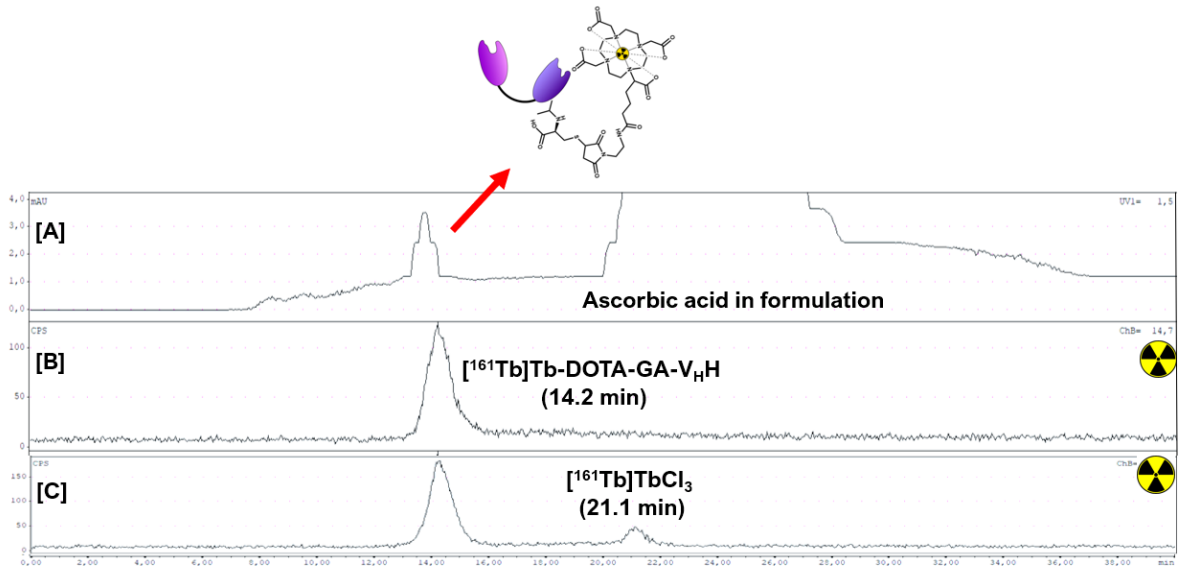


Figure 3.3: SEC-HPLC chromatogram (280 nm) of **[^{161}Tb]Tb-DOTA-GA-v_HH** in PBS with 0.5 mg/mL ascorbic acid, with **[A]** the UV chromatogram and **[B]** the radioactivity trace of the compound. **[C]** Free [^{161}Tb]$TbCl_3$ (50kBq) was co-injected with **[^{161}Tb]Tb-DOTA-GA-v_HH** to show the difference between chelated and unchelated [^{161}Tb] retention.

3.3.2 Cell binding

To assess the cell binding of **[^{161}Tb]Tb-DOTA-GA-v_HH** to c-Met, a cell binding experiment was conducted with BxPC-3 cells; a pancreatic cell line known for its upregulated c-Met expression. However, the expression in this cell line is still relatively low, as shown in work conducted by Tang *et al.*(36). Therefore, molar activity becomes crucial in cell binding, as the presence of high amounts of cold compound can result in low radionuclide readout due to self-blocking effects. Based on our molar activity and the results of Xu and co-workers (36), we expected low but measurable binding percentage of the radioconjugate. The experiment was performed at physiological conditions (37 °C, pH 7.4) to simulate and gather valuable information for potential *in vivo* translation. After 30 minutes of incubation, 5.5% ± 0.7 % of the construct was found to be associated with the cells, either bound to the cell membrane surface or internalised. Incubating for longer periods showed increased uptake of the radiolabelled construct, with 8.4% ± 0.4% of the activity associated after 60 minutes incubation, and 12.6% ± 0.2% of the activity associated after 120 minutes incubation. As expected, molar activities > 30 MBq/nmol were sufficient to have c-MET specific binding without fully occupying all binding sites. In addition, cell binding was similar to the results observed by Tang *et al.*(36).

To saturate all c-MET binding sites for the v_HH, cells were pre-incubated with the non-chelator associated variant **v_HH-HPM**. This pre-blocking step blocked ~96% of all binding of the radiolabelled construct. The data of the blocking study is presented in **Figure 3.4.** Further, c-Met binding of the **^{nat}Tb-DOTA-GA-v_HH** was determined at Sanofi Ghent by means of HGF competitive binding assays, which showed similar blocking parameters as previously studied with the unmodified v_HH (IC_{50} ~ 80 pM).

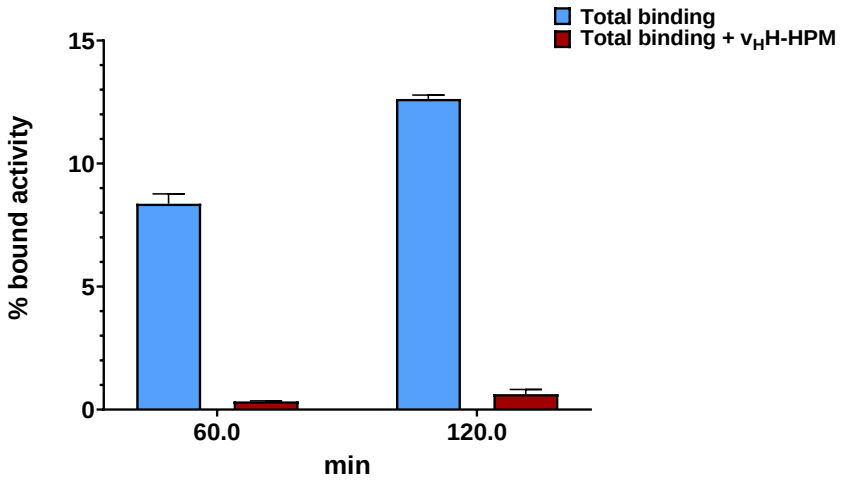


Figure 3.4: Total binding of **[^{161}Tb]Tb-DOTA-GA-v_HH** in the presence of **v_HH-HPM** (1 µM) to block c-Met receptors. The cell binding was assessed after 60 and 120 minutes.

The cell binding studies give no indication of the degree of receptor internalisation, which is an important parameter in radionuclide therapeutics, especially in low energy Auger/conversion therapy, where the therapeutic dose is deposited within ~1 cell length (37). Internalisation of the c-Met receptor is largely facilitated by Cbl E3 and Grb2 proteins, and is ineffective at low temperatures (22). Therefore, comparing the binding assay at 37°C with the cell binding assay performed at 4°C could give us some insight in the cellular internalisation of the v_HH. After 30 minutes, 3.6% ± 0.3% of the radiolabelled construct was bound to the cells at 4°C, which corresponds to ~65% of the binding at 37°C. Incubating for a longer period (up to 120 minutes) sees only 6.9% ± 0.8% of the activity bound to cells at 4°C, which corresponds to 54% of the activity associated to the cells at 37 °C. These results are in accordance to internalisation data collected by Hasenauer *et al.*, who used temperature changes to mediate internalisation of activated/phosphorylated c-Met receptor in various cell lines (38). However, due to this temperature constraint, the resulting internalisation could be an overestimation, as the low temperatures could also influence the binding kinetics (39–41). The total binding and internalisation results are provided in **Figure 3.5.**

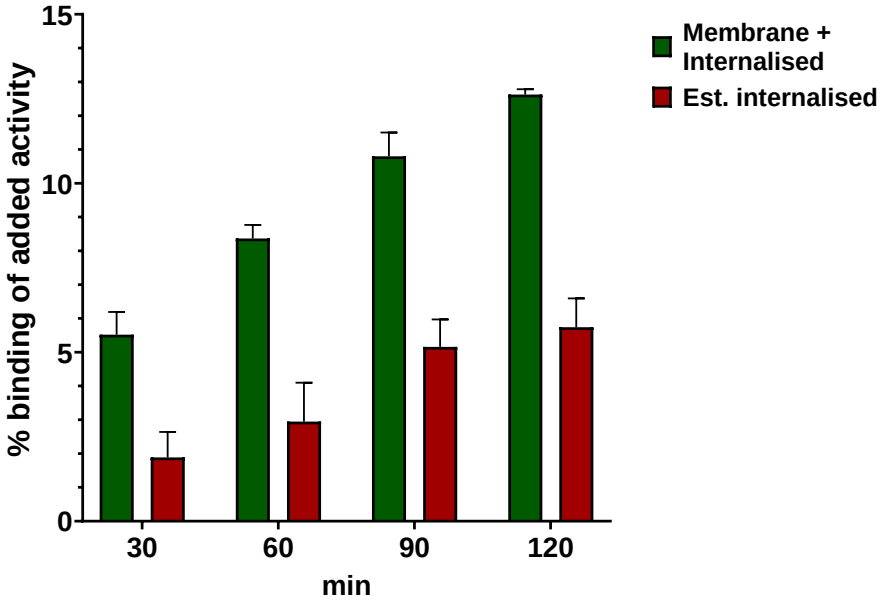


Figure 3.5: Cell binding of **[^{161}Tb]Tb-DOTA-GA-v$_H$H** to BxPC-3 cells showing the total bound activity (membrane and internalised radiolabelled construct) and estimated internalised activity (determined from the difference in total binding (37°C) and internalisation-prohibited binding (4°C)).

3.3.3 *In vitro* cell viability

In vitro cell viability after exposure of **[^{161}Tb]Tb-DOTA-GA-v$_H$H** was evaluated using an MTS assay. Exposing cells for 4 h to **[^{161}Tb]Tb-DOTA-GA-v$_H$H** resulted in an activity concentration dependent decrease of cell viability (EC_{50} = 16.4 MBq/mL). After addition of 5 MBq/mL, cell viability was already significantly lower compared to baseline cells (69% ± 11%, $P < 0.05$). At the highest concentration (20 MBq/mL), cell viability was further reduced to 38% ± 10% (**Figure 3.6A**). Exposure of cells to **[^{161}Tb]Tb-DOTA-GA-v$_H$H** for a longer period of time (24h) resulted again in an activity-dependent decrease in cell viability, with the therapeutic effect being more pronounced. For example, at the highest concentration, cell viability decreased to 12% ± 2%, with an EC_{50} of 3.4 MBq/mL. Additionally, the onset of therapeutic effects after longer exposure occurred at lower activity concentrations. Even the addition of 1.25 MBq/mL of **[^{161}Tb]Tb-DOTA-GA-v$_H$H** resulted already in a significant decrease in cell viability (70% ±12%, $P < 0.001$). These results confirm findings of many ^{161}Tb therapeutic studies, where exposure time is directly proportional to cell viability (6,42,43).

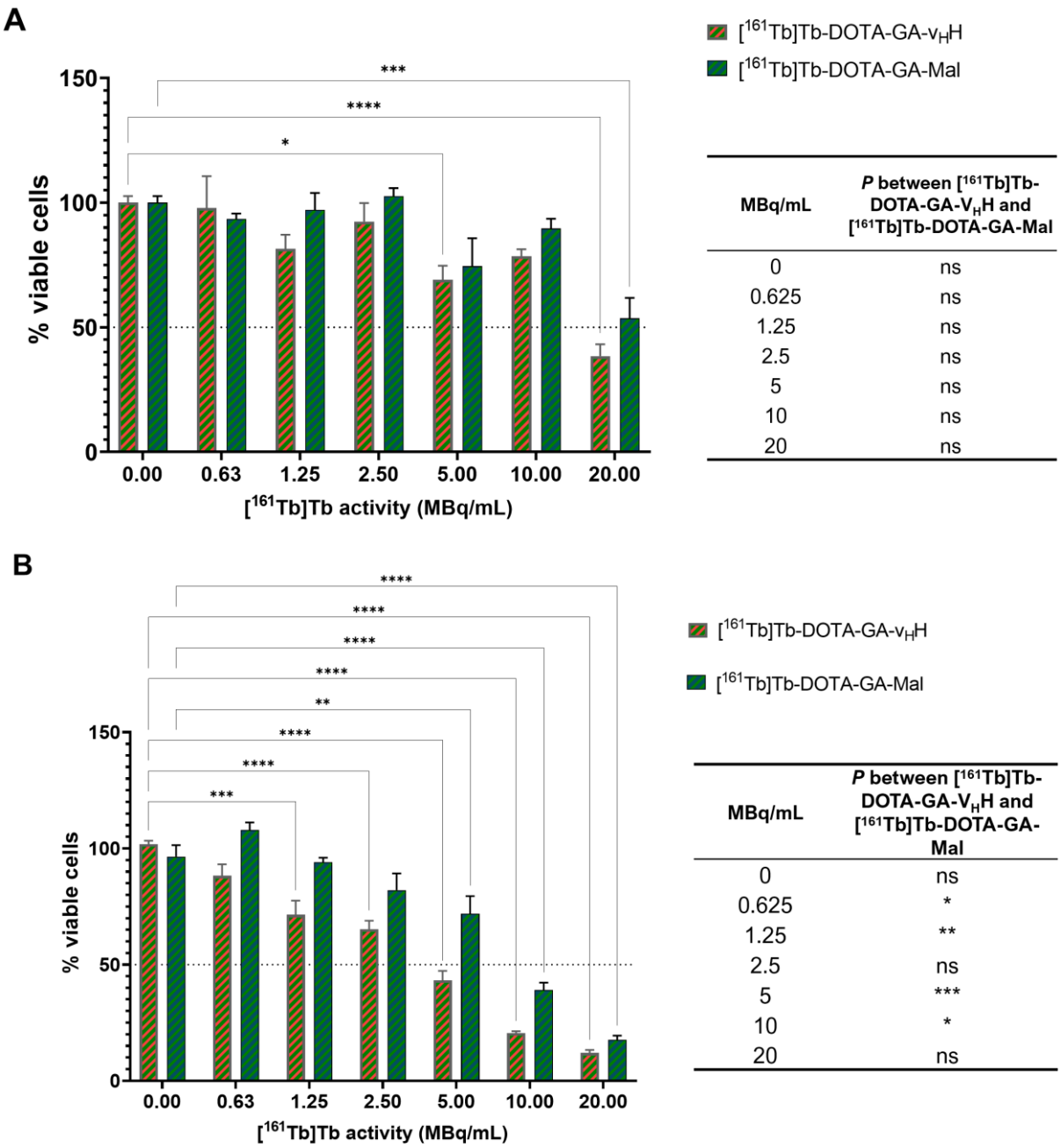
In parallel, we performed the MTS assay using the same concentrations of **[^{161}Tb]Tb-DOTA-GA-Mal**, a control compound with no affinity towards c-MET, as a surrogate for radioactive effects originating from the presence of ^{161}Tb in the cell culture medium. Moreover, the free maleimide of the maleimide-DOTA-GA may react with L-cysteine in the culture medium, limiting cell-based interactions. It is understood that reactive oxygen species are generated from ionisation of water molecules which interact with cell biomolecules killing cells (44). It is important to note that these indirect radiation effects are present in

addition to the direct radiation effects from the emission of electrons associated with the decay of ^{161}Tb. The assay also showed an activity-dependent decline in cell viability for **[^{161}Tb]Tb-DOTA-GA-Mal**. As expected, the effect generated from the non-cell bound ^{161}Tb also increased after longer exposure times as is evident from the noticeably lower viability after 24h versus 4h exposure with **[^{161}Tb]Tb-DOTA-GA-Mal** (19% ± 3%, at 20.0 MBq/mL, EC_{50} = 7.90 MBq/mL, 24h)(**Figure 3.6**). However, for **[^{161}Tb]Tb-DOTA-GA-Mal**, much higher concentrations (>5 MBq/mL, $P < 0.01$) were required to obtain statistical significant differences in viability. Although the medium bias (dose-response from non-cell bound ^{161}Tb) in this assay is significant, this difference still clearly suggests a therapeutic effect of **[^{161}Tb]Tb-DOTA-GA-v$_H$H** larger than only the medium effects on the viability. However, as the activity increases, this bias diminishes (P > 0.05), as illustrated at 20 MBq/mL (**Figure 3.6B**). A similar effect was observed in Vermeulen *et al.*, where [^{153}Sm]Sm-DTPA, a control compound with no affinity for somatostatin receptors, showed significant lower inhibitory effects compared to [^{153}Sm]Sm-DOTATATE (45).

3.3.4 Clonogenic assays

Additionally, the clonogenic potential of BxPC-3 cells was evaluated after exposure of **[^{161}Tb]Tb-DOTA-GA-v$_H$H**. ^{161}Tb has shown to deliver a large dose (~70% of all absorbed dose) to the nucleus (from outside the cell), where DNA damage is the dominant mechanism in decreasing cell viability (46). However, as our radioconjugate internalises, we expect some changes based on the intracellular distribution. We were interested in understanding the ^{161}Tb-intracellular interaction, as previous *in vitro* assays showed a clear non-cell bound killing potential of the β^- radiation. Exposing the singular cells to **[^{161}Tb]Tb-DOTA-GA-v$_H$H** for 4 h resulted in an activity concentration dependent decrease in the clonogenic potential (**Figure 3.7A**). After addition of 2 MBq/mL, a significantly reduced survival fraction was observed (46% ± 7%, P < 0.05) compared to baseline cells. Analogous to the MTS study, we also repeated the experiment using the non-targeting **[^{161}Tb]Tb-DOTA-GA-Mal** to ascertain medium related effects on the clonogenic potential. As expected, the activity in the medium did seem to affect the clonogenic potential after short exposure to **[^{161}Tb]Tb-DOTA-GA-Mal** (SF = 53% ± 9%, 2.0 MBq/mL); with no significant differences between the two compounds.

Exposure of cells to **[^{161}Tb]Tb-DOTA-GA-v$_H$H** for a longer period of time (24h, **Figure 3.7B**) did not further decrease clonogenic potential at high concentrations. At the highest concentration, we observed a survival fraction of 44% ± 6% (P < 0.001) compared to the baseline. However, we started to observe significant differences in clonogenic potential at lower concentrations. At an exposure of 1.0 MBq/mL of **[^{161}Tb]Tb-DOTA-GA-v$_H$H** we already observed a significant decrease in survival fraction (SF = 63% ± 11%, $P < 0.05$). Equally, incubating cells with **[^{161}Tb]Tb-DOTA-GA-Mal** for 24h resulted in noticeable higher effects on the clonogenic potential (SF = 72% ± 9%). As observed in the cell viability assay, **[^{161}Tb]Tb-DOTA-GA-Mal** showed statistical significant differences at higher concentrations (2.0 MBq/mL, $P < 0.01$).



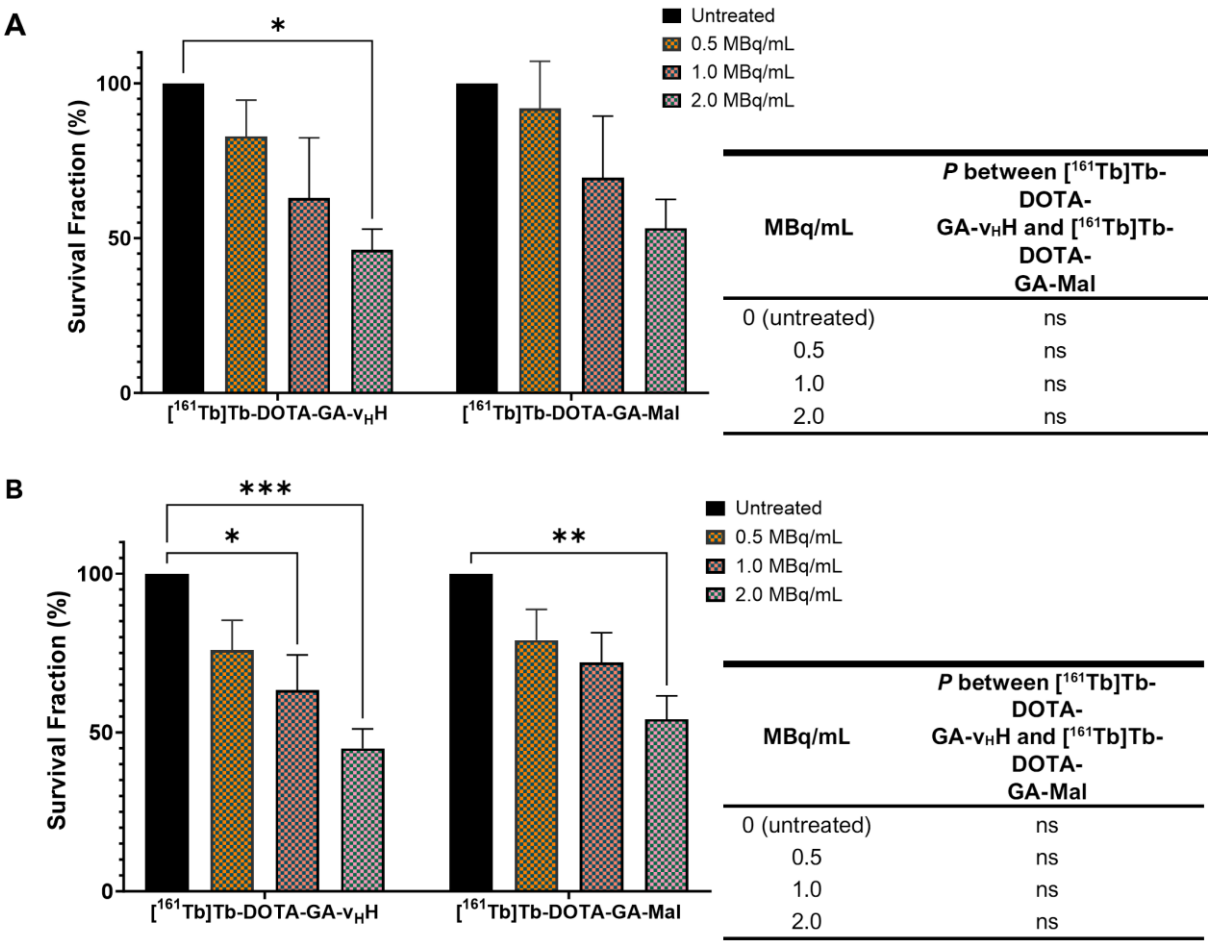
MBq/mL	*P* between [^{161}Tb]Tb-DOTA-GA-V$_H$H and [^{161}Tb]Tb-DOTA-GA-Mal
0	ns
0.625	ns
1.25	ns
2.5	ns
5	ns
10	ns
20	ns

MBq/mL	*P* between [^{161}Tb]Tb-DOTA-GA-V$_H$H and [^{161}Tb]Tb-DOTA-GA-Mal
0	ns
0.625	*
1.25	**
2.5	ns
5	***
10	*
20	ns

Figure 3.6. Cell viability of BxPC-3 cells after 4 h (**A**) or 24 h (**B**) exposure to **[^{161}Tb]Tb-DOTA-GA-v$_H$H** or **[^{161}Tb]Tb-DOTA-GA-Mal.** A table of significance values between tested compounds is provided**.** Significant values are expressed as *P* < *0.05, **0.01, ***0.001, ****0.0001 (Sidak's multiple comparison test)

Again, onset of effects on clonogenic potential was observed at lower concentrations for **[^{161}Tb]Tb-DOTA-GA-v$_H$H** as for **[^{161}Tb]Tb-DOTA-GA-Mal**. These data clearly support an activity concentration-dependent therapeutic effect **[^{161}Tb]Tb-DOTA-GA-v$_H$H** on the clonogenic potential of BxPC-3. The effects of **[^{161}Tb]Tb-DOTA-GA-Mal** further supports the notion that the effect of the ^{161}Tb source in medium is a major contributor to the effect which cannot be ignored. This result further indicates that

^{161}Tb potency is linked to both the long range β$^-$ and the Auger/conversion electrons and these effects cannot be separately studied at large activity-to-cell ratios. Cell survival as a function of activity is shown in **Figure 3.7.**



MBq/mL	*P* between [^{161}Tb]Tb-DOTA-GA-v$_H$H and [^{161}Tb]Tb-DOTA-GA-Mal
0 (untreated)	ns
0.5	ns
1.0	ns
2.0	ns

MBq/mL	*P* between [^{161}Tb]Tb-DOTA-GA-v$_H$H and [^{161}Tb]Tb-DOTA-GA-Mal
0 (untreated)	ns
0.5	ns
1.0	ns
2.0	ns

Figure 3.7. Survival fraction of BxPC-3 cells after 4 h (**A**) or 24 h (**B**) treatment of **[^{161}Tb]Tb-DOTA-GA-v$_H$H** or **[^{161}Tb]Tb-DOTA-GA-Mal.** Significance values are expressed as P < * = 0.05, ** = 0.01, *** = 0.001, **** = 0.0001.

3.3.5 *Ex vivo* biodistribution

[^{161}Tb]Tb-DOTA-GA-v$_H$H was injected into healthy mice (n = 3) to identify potential organs of high accumulation. The activity was slowly excreted from blood, with 35.82% ± 1.61% of the activity still circulating after 4 h (SUV: 1.56 ± 0.26) (**Figure 3.9**). Full washout of the activity from blood was observed after 7 days *p.i.* The predicted plasma half-life of the radiolabelled conjugate was *ca.*10 h. The plasma half-life is higher than observed for most other v$_H$H moieties reported in literature, which often have a short plasma half-life (<100 min) (15). This could however be expected as the presence of the albumin

binding **v$_H$H** significantly extended the plasma residence time. This was confirmed by incubating a small amount of mouse serum albumin with the labelled compound and analysing by SEC-HPLC confirming the binding of the bivalent **v$_H$H** to mouse serum albumin. High kidney uptake was observed (SUV_{max} = 5.84 ± 0.66, 4 h *p.i.*), a common trend for v$_H$H as these small biomolecules are often reabsorbed and retained in the proximal tubule after glomerular filtration (16). Furthermore, most of the remaining activity was distributed in the liver (SUV: 2.75 ± 0.12) and spleen (SUV: 1.63 ± 0.09) 4h post injection. Distribution in the lungs was moderate, with an initial SUV of 2.62 ±0.76 after 4h, and a steady decrease to 1.01 ±0.16 and 0.11 ±0.02 after 24h and 7d, respectively. This decrease is similar to other blood-rich organs (heart, etc) suggesting the radioconjugate does not bind to the lungs but is present in the blood contained within the lungs. Bone and liver uptake was consistently decreasing over the 7-day period from 0.61 ± 0.21 and 2.75 ± 0.12 (SUV 4 h *p.i.*) to 0.16 ± 0.03 and 0.52 ± 0.10 (SUV 7 d *p.i.*), respectively. Previously, we investigated the biodistribution of [^{161}Tb]$TbCl_3$ and found, in the same strain of mice (NMRI), terbium accumulation in bone and liver (9). The lack of accumulation in these organs, indicates that terbium is strongly bound to the DOTA-GA core *in vivo*. The standardised uptake values over the 7 days are shown in **Figure 3.8**

In tumour-bearing mice (n = 4), a similar pharmacokinetic profile was observed. An apparent slower clearance of the radioconjugate from blood was observed, with an estimated blood plasma half-life of ~23 h, as opposed to ~ 9 h in the healthy mice. A higher concentration of the radioconjugate was observed in the liver and kidney as compared to healthy mice 4 h *p.i.* (liver: SUV: 6.27 ± 1.60; kidney: SUV: 9.69 ± 0.71) (**Figure 3.9**). Genetic differences in the mice used for the comparative biodistributions could explain the large difference in uptake. However, further studies into the true reason for the high liver uptake needs to be explored. The dissociation of the radioconjugate from the liver into the blood stream could explain the large disparity in the blood plasma half-life between healthy and tumour-bearing mice. Additionally, high concentration of the radioconjugate was present in the lungs 4h p.i. (SUV: 1.91 ±1.08), similar to the distribution in healthy mice. **[^{161}Tb]Tb-DOTA-GA-v$_H$H** showed rapid accumulation in tumour during the first 24h, with a SUV of 3.46 ± 2.16 after 4 h increasing to 6.65 ± 2.81 after 24 h. This tumour uptake profile shows fast accumulation which is preferred for low adverse effects, and slow dissociation for maximal accumulation and prolonged radiation exposure to the tumour. Tumour-to-blood ratios also indicate a fast transfer of the compound from blood to the tumour (mean ± standard deviation; 4h: 2.84 ± 0.94, 24h: 3.65 ± 0.44, 7d: 88.74 ± 0.63). This was similar to uptake in BxPC-3 tumour-bearing mice using c-Met targeting peptides YQ-M3-MPA and GE137-MPA by Tang *et. al.* (36). No increasing bone uptake, a known target for free [^{161}Tb]$TbCl_3$, was observed (**Figure 3.9**), (9). In addition, tumour-to-kidney ratios strongly suggest that a greater amount of radiation dose is received at the tumour site, rather than at the kidneys (4h: 0.36 ± 0.63, 24h: 1.39 ± 0.46, 7d: 5.14 ± 0.63). For translation to humans, this is an important factor as nephrotoxicity is one of the limiting factors for radionuclide therapy with smaller antibody fragments. The standardised uptake values over the 7 days are shown in **Figure 3.9.**

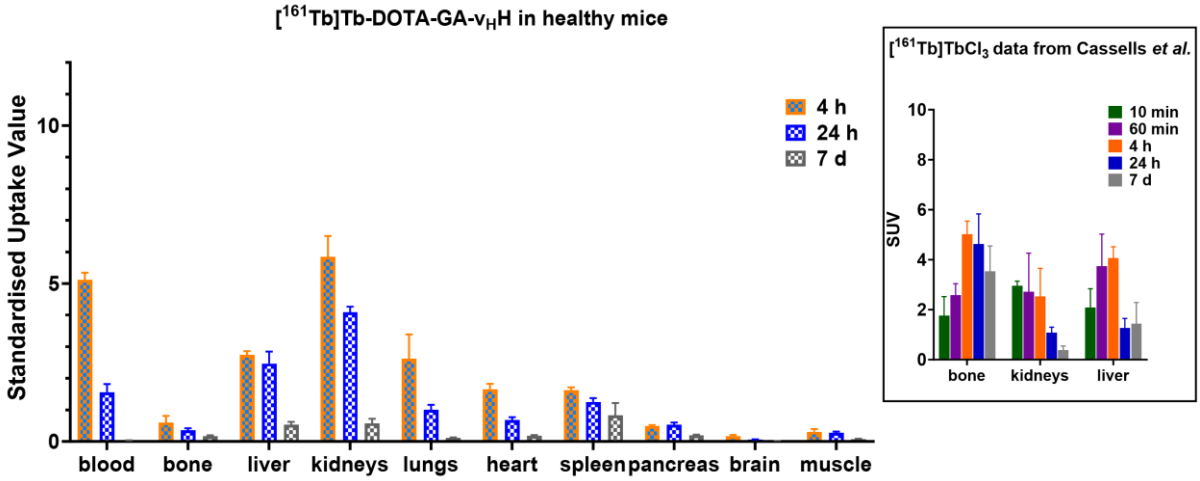


Figure 3.8. Standardised uptake values of **[^{161}Tb]Tb-DOTA-GA-v$_H$H** in healthy mice. Uncomplexed **[^{161}Tb]TbCl$_3$** is provided for reference (9).

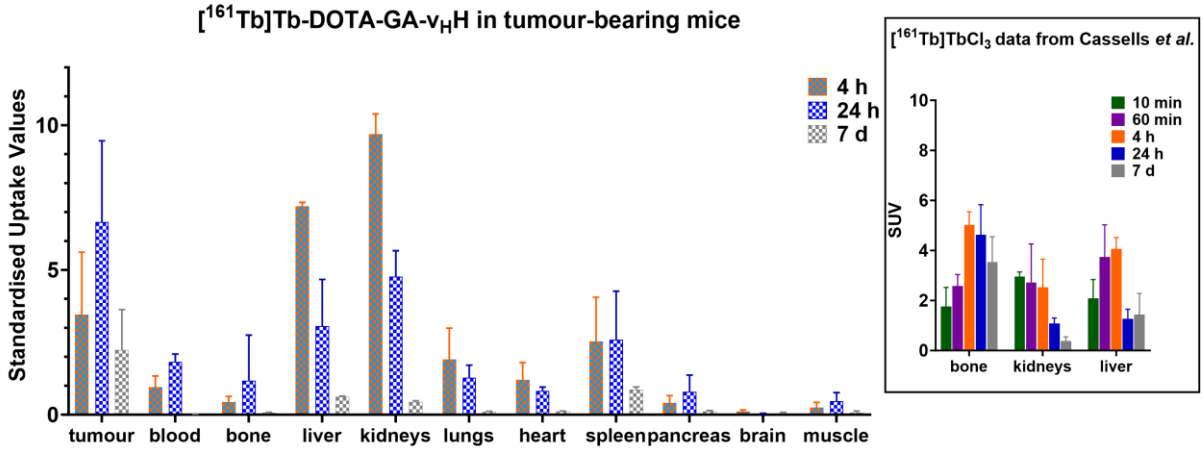


Figure 3.9. Standardised uptake values of **[^{161}Tb]Tb-DOTA-GA-v$_H$H** in tumour-bearing mice. Uncomplexed **[^{161}Tb]TbCl$_3$** is provided for reference (9).

3.3.6 *μ*SPECT/ CT scans

Low activity μSPECT/CT images of a healthy mice (n = 1), injected with **[^{155}Tb]Tb-DOTA-GA-v$_H$H,** were obtained with co-registration of CT. The μSPECT/CT images were centred on the abdominal region, where most of the activity was observed in the *ex vivo* biodistribution. After 4 h *p.i.*, most of the activity was observed in the liver and kidney regions. In addition, other blood rich organs, such as the lungs, are observed to have an accumulation of activity. Uptake in blood-rich organs could be expected since most of the activity was expected to be in blood due to the half-life extending albumin binding v$_H$H Moreover, μSPECT/CT images in the healthy mouse are remarkably similar to that of albumin-directed tracers, which circulate in the pulmonary regions without a distinctive organ uptake (47). Large uptake in the

heart was expected, particularly the main chamber (left ventricle). But the low activity used in this experiment (0.6 MBq) crippled our ability to distinguish between the different chest regions. Furthermore, a good correlation between the image and biodistribution data is observed, where most of the radioconjugate was observed in blood or blood-rich organs. The maximal intensity projection fused µSPECT/CT is provided in **Figure 3.10.**

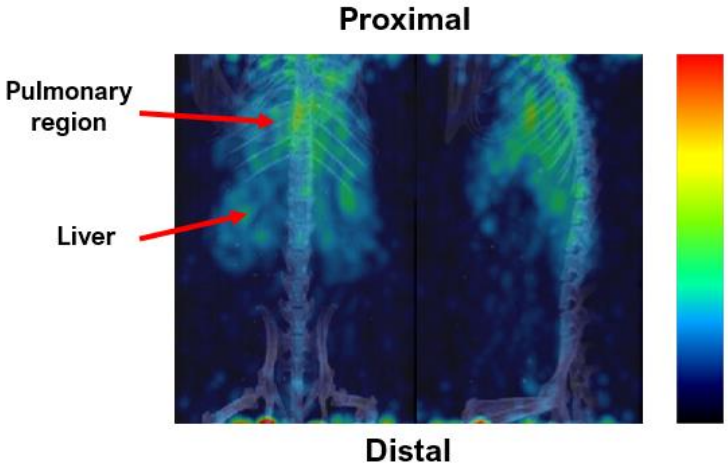


Figure 3.10. Maximum intensity projection fused µSPECT/CT scan (left: anterior, right: lateral) of **[^{155}Tb]Tb-DOTA-GA-v$_H$H** in a healthy mouse, centred on abdominal region, after 4 h p.i..

High-activity µSPECT/CT scans (~20 MBq of **[^{161}Tb]Tb-DOTA-GA-v$_H$H**) were performed on tumour-bearing mice (n = 3), and were recorded after 4, 24, 48 and 72 h p.i. (**Figure 3.11**). After 4 h, most of the activity was observed in the liver, which corresponds to the *ex vivo* biodistribution and ^{155}Tb µSPECT/CT imaging scans in healthy mice. Images obtained at later time points showed a gradual washout of radioactivity from the abdominal and chest regions. In contrast, we expect slower washout from the tumour, as it has been shown that c-Met bound tracers often slowly dissociate from the receptor (22,36). Slow dissociation of v$_H$H from the tumour was observed between 24h p.i. (SUV_{tumour} = 1.04 ± 0.40 g/mL) and 72 h p.i. (SUV_{tumour} = 0.78 ± 0.39 g/mL). A constant decrease of the activity in the kidney over 72 h (SUV_{4h} = 2.15, SUV_{72h} = 0.48) suggest that the v$_H$H is excreted through the urinary tract, without long-term retention in the kidney (>72h). Furthermore, these data were not consistent with the biodistribution data, where we observed much higher SUV values p.i.. This result was expected as quantification of SPECT data is challenging (**Table 3.1**). Moreover, the low abundance of gamma rays from ^{161}Tb adds to the complexity of accurate quantification. In therapeutic applications, nephrotoxicity is a limiting factor in the success of a therapeutic radiopharmaceutical (48–51), which in this case could also be a major concern, as after 24 hours a large amount of the radionuclides (both as radiometabolites and as the intact compound) are still in the kidney region; a common issue of v$_H$H (17,52–54). In a clinical setting, this limitation may be overcome using kidney retention blocking agents such as Gelofusin® or lysine/arginine consumption prior to administration. In addition, performing a pre-clinical test in mice

using these methods would be vital in optimising the selective tumour uptake of the radioconjugate, which is important as we see great potential using ^{161}Tb in reducing cell viability for c-Met upregulated cancers.

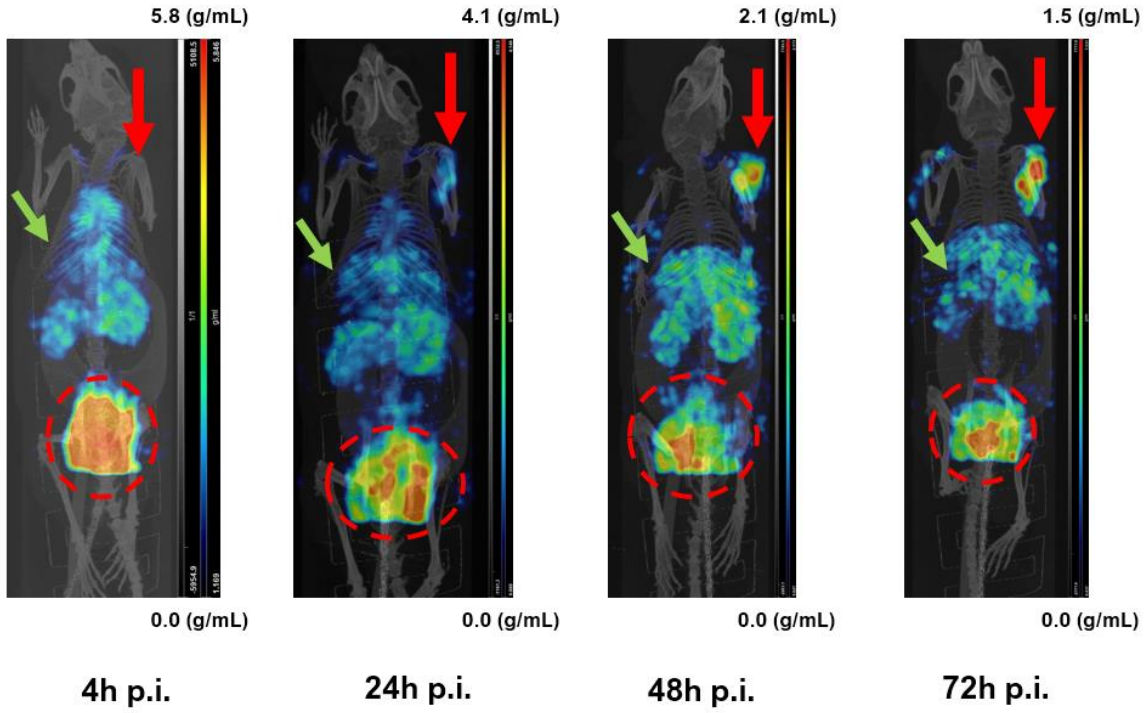


Figure 3.11. Maximum intensity projection fused μSPECT/CT scan of **[^{161}Tb]Tb-DOTA-GA-v$_H$H** in a tumour-bearing mouse over the 72 h. Tumour is indicated by means of a red arrow. Kidney, liver and lung region is indicated by green arrow. Images are scaled individually for better visual representation. Red dotted circle indicates the injection site of the animal (perivenous injection).

Table 3.1. Estimated SUV values (g/mL) of tumour and kidney uptake of **[^{161}Tb]Tb-DOTA-GA-v$_H$H** in tumour mice.

Timepoint (h)	Tumour	Kidneys	Tumour-to-kidney ratio
4	0.39 ± 0.23	2.01 ± 0.38	0.19 ± 0.12
24	1.04 ± 0.40	1.48 ± 0.33	0.70 ± 0.31
48	0.91 ± 0.49	0.89 ± 0.38	1.02 ± 0.70
72	0.78 ± 0.39	0.54 ± 0.41	1.44 ± 1.31

3.4 Conclusion

In conclusion, we have successfully radiolabelled a bivalent v$_H$H targeting anti-c-Met v$_H$H with [^{161}Tb]TbCl$_3$ using the low-temperature labelling method described in our previous work (9). Additionally, we have also used our radiolabelling protocol with ^{155}Tb, broadening the scope to the full terbium isotope series for radiopharmaceutical implementation. *In vitro* studies show a clear inverse proportionality between the activity applied and cell viability. This was observed with the c-Met binding **[^{161}Tb]Tb-DOTA-GA-v$_H$H** and non-c-Met binding **[^{161}Tb]Tb-DOTA-GA-Mal**, suggesting unspecific medium-related radiation effects dominate the observed therapeutic efficacy of ^{161}Tb. The fact that therapeutic effect of is **[^{161}Tb]Tb-DOTA-GA-v$_H$H** is higher than that of **[^{161}Tb]Tb-DOTA-GA-Mal** is promising, however presence of therapeutic effects of non-targeted Tb-161 also clearly shows the limitation of the *in vitro* assays performed in these studies. In the healthy mouse model, we observed uptake and retention in the kidneys, an organ known to have high uptake of v$_H$H. Additionally, the **[^{161}Tb]Tb-DOTA-GA-v$_H$H** construct was observed to circulate in the bloodstream with an estimated plasma half-life of ~10h. This is a shorter circulation time than conventional antibodies, and longer circulation time than v$_H$H with no half-life extension moiety and may provide a favourable pharmacokinetic profile for therapeutic radiopharmaceuticals in general. In tumour models, we observed tumour accumulation (SUV ~ 1 g/mL), extending beyond 7 days p.i., which was similar to findings reported earlier in literature for c-MET targeted probes. **[^{161}Tb]Tb-DOTA-GA-v$_H$H** µSPECT studies were possible with detection of the low energy gamma rays emitted by ^{161}Tb, potentially enabling the estimation of the radiation dose to the tumour and healthy tissues. For a greater understanding of the therapeutic potential, a direct *in vivo* comparison to other β^- emitting isotopes, such as lutetium-177, should be performed, similar to Muller et al. (5,6). Additionally, exploring cross-reactive c-Met carriers will help predict potential off-target effects which can occur in humans. Though no comparison data was explored in this study, the data obtained in this study paint a positive outlook for combining terbium radionuclides with biologicals, as we observed no change in the biological functionality after highly efficient radiolabelling – an important result towards the development of potent terbium radiopharmaceuticals.

3.5 Conflict of Interest Declaration

The authors declare that the research was conducted without any conflict of interest.

3.6 Ethical Statement

Animal experiments were conducted according to the Belgian code of practice for the care and the use of animals, after approval from the animal ethics committees of KU Leuven (P054/2019) and SCK CEN (LA 1100614).

3.7 Acknowledgements

The authors would like to acknowledge the contributions of Julie Cornelis (KU Leuven, Leuven, Belgium), and Nathalie Heynickx, Anthony Waked and Amelie Coolkens (SCK CEN, Mol, Belgium) to the research reported. This research was funded by the Research Foundation – Flanders (FWO)-SBO project: Terbium Isotopes for Medical Applications in Flanders (Tb-IRMA-V).

3.8 References

1. Rahman AKMR, Awal A. Production of ^{149}Tb, ^{152}Tb, ^{155}Tb and ^{161}Tb from gadolinium using different light-particle beams. *J Radioanal Nucl Chem* (2020) **323**:731–740. doi:10.1007/s10967-019-06973-0

2. Mishiro K, Hanaoka H, Yamaguchi A, Ogawa K. Radiotheranostics with radiolanthanides: Design, development strategies, and medical applications. *Coord Chem Rev* (2019) **383**:104–131. doi:10.1016/j.ccr.2018.12.005

3. Gracheva N, Müller C, Talip Z, Heinitz S, Köster U, Zeevaart JR, Vögele A, Schibli R, van der Meulen NP. Production and characterization of no-carrier-added ^{161}Tb as an alternative to the clinically-applied ^{177}Lu for radionuclide therapy. *EJNMMI Radiopharm Chem* (2019) **4**:12. doi:10.1186/s41181-019-0063-6

4. Lehenberger S, Barkhausen C, Cohrs S, Fischer E, Grünberg J, Hohn A, Köster U, Schibli R, Türler A, Zhernosekov K. The low-energy β - and electron emitter ^{161}Tb as an alternative to ^{177}Lu for targeted radionuclide therapy. *Nucl Med Biol* (2011) **38**:917–924. doi:10.1016/j.nucmedbio.2011.02.007

5. Müller C, Reber J, Haller S, Dorrer H, Bernhardt P, Zhernosekov K, Türler A, Schibli R. Direct in vitro and in vivo comparison of ^{161}Tb and ^{177}Lu using a tumour-targeting folate conjugate. *Eur J Nucl Med Mol Imaging* (2014) **41**:476–485. doi:10.1007/s00259-013-2563-z

6. Müller C, Umbricht CA, Gracheva N, Tschan VJ, Pellegrini G, Bernhardt P, Zeevaart JR, Köster U, Schibli R, van der Meulen NP. Terbium-161 for PSMA-targeted radionuclide therapy of prostate cancer. *Eur J Nucl Med Mol Imaging* (2019) **46**:1919–1930. doi:10.1007/s00259-019-04345-0

7. Rosar F, Maus S, Schaefer-Schuler A, Burgard C, Khreish F, Ezziddin S. New Horizons in Radioligand Therapy. *Clin Nucl Med* (2023) **48**:433–434. doi:10.1097/RLU.0000000000004589

8. Al-Ibraheem A, Scott AM. 161Tb-PSMA Unleashed: a Promising New Player in the Theranostics of Prostate Cancer. *Nucl Med Mol Imaging (2010)* (2023) **57**:168–171. doi:10.1007/s13139-023-00804-7

9. Cassells I, Ahenkorah S, Burgoyne AR, Van de Voorde M, Deroose CM, Cardinaels T, Bormans

G, Ooms M, Cleeren F. Radiolabeling of Human Serum Albumin With Terbium-161 Using Mild Conditions and Evaluation of in vivo Stability. *Front Med* (2021) **8**:1–12. doi:10.3389/fmed.2021.675122

10. Parakh S, Lee ST, Gan HK, Scott AM. Radiolabeled Antibodies for Cancer Imaging and Therapy. *Cancers (Basel)* (2022) **14**:1–23. doi:10.3390/cancers14061454

11. Mondello P, Cuzzocrea S, Navarra M, Mian M. ^{90}Y-ibritumomab tiuxetan: A nearly forgotten opportunity. *Oncotarget* (2016) **7**:7597–7609. doi:10.18632/oncotarget.6531

12. Bensch F, Brouwers AH, Lub-de Hooge MN, de Jong JR, van der Vegt B, Sleijfer S, de Vries EGE, Schröder CP. ^{89}Zr-trastuzumab PET supports clinical decision making in breast cancer patients, when HER2 status cannot be determined by standard work up. *Eur J Nucl Med Mol Imaging* (2018) **45**:2300–2306. doi:10.1007/s00259-018-4099-8

13. Cheung MC, MacEachern JA, Haynes AE, Meyer RM, Imrie K. ^{131}I-tositumomab in lymphoma. *Curr Oncol* (2009) **16**:32–47. doi:10.3747/co.v16i5.385

14. Carter LM, Poty S, Sharma SK, Lewis JS. Preclinical optimization of antibody-based radiopharmaceuticals for cancer imaging and radionuclide therapy-Model, vector, and radionuclide selection. *J Label Compd Radiopharm* (2018) **61**:611–635. doi:10.1002/jlcr.3612

15. Kijanka M, Dorresteijn B, Oliveira S, Van Bergen En Henegouwen PMP. Nanobody-based cancer therapy of solid tumors. *Nanomedicine* (2015) **10**:161–174. doi:10.2217/nnm.14.178

16. Bannas P, Hambach J, Koch-Nolte F. Nanobodies and nanobody-based human heavy chain antibodies as antitumor therapeutics. *Front Immunol* (2017) **8**:1–13. doi:10.3389/fimmu.2017.01603

17. Hambach J, Fumey W, Stähler T, Gebhardt AJ, Adam G, Weisel K, Koch-Nolte F, Bannas P. Half-Life Extended Nanobody-Based CD38-Specific Bispecific Killercell Engagers Induce Killing of Multiple Myeloma Cells. *Front Immunol* (2022) **13**:1–12. doi:10.3389/fimmu.2022.838406

18. Saad KM, Shaker ME, Shaaban AA, Abdelrahman RS, Said E. The c-Met inhibitor capmatinib alleviates acetaminophen-induced hepatotoxicity. *Int Immunopharmacol* (2020) **81**:106292. doi:10.1016/j.intimp.2020.106292

19. Wu JG, Yu JW, Wu HB, Zheng LH, Ni XC, Li XQ, Du GY, Jiang BJ. Expressions and clinical significances of c-MET, p-MET and E2f-1 in human gastric carcinoma. *BMC Res Notes* (2014) **7**: doi:10.1186/1756-0500-7-6

20. Organ SL, Tsao MS. An overview of the c-MET signaling pathway. *Ther Adv Med Oncol* (2011) **3**:S7–S19. doi:10.1177/1758834011422556

21. Van Der Steen N, Zwaenepoel K, Mazzaschi G, Luirink RA, Geerke DP, De Beeck KO, Hermans C, Tiseo M, Van Schil P, Lardon F, et al. The role of c-met as a biomarker and player in innate

and acquired resistance in non-small-cell lung cancer: Two new mutations warrant further studies. *Molecules* (2019) **24**: doi:10.3390/molecules24244443

22. Viticchiè G, Muller PAJ. c-Met and other cell surface molecules: Interaction, activation and functional consequences. *Biomedicines* (2015) **3**:46–70. doi:10.3390/biomedicines3010046

23. Goyal L, Muzumdar MD, Zhu AX. Targeting the HGF/c-MET pathway in hepatocellular carcinoma. *Clin Cancer Res* (2013) **19**:2310–2318. doi:10.1158/1078-0432.CCR-12-2791

24. You W-K, Lee DH, Sung E-S, Ahn J-H, An S, Huh J. Development of antibody-based c-Met inhibitors for targeted cancer therapy. *ImmunoTargets Ther* (2015) **18**:35. doi:10.2147/ITT.S37409

25. Luyten K, Van Loy T, Cawthorne C, Deroose CM, Schols D, Bormans G, Cleeren F. D-peptide-based probe for cxcr4-targeted molecular imaging and radionuclide therapy. *Pharmaceutics* (2021) **13**: doi:10.3390/pharmaceutics13101619

26. Webster B, Ivanov P, Russell B, Collins S, Stora T, Ramos JP, Köster U, Robinson AP, Read D. Chemical Purification of Terbium-155 from Pseudo-Isobaric Impurities in a Mass Separated Source Produced at CERN. *Sci Rep* (2019) **9**:1–9. doi:10.1038/s41598-019-47463-3

27. Formento-Cavaier R, Haddad F, Alliot C, Sounalet T, Zahi I. New excitation functions for proton induced reactions on natural gadolinium up to 70 MeV with focus on ^{149}Tb production. *Nucl Instruments Methods Phys Res Sect B Beam Interact with Mater Atoms* (2020) **478**:174–181. doi:10.1016/j.nimb.2020.06.029

28. Catherall R, Andreazza W, Breitenfeldt M, Dorsival A, Focker GJ, Gharsa TP, T J G, Grenard J-L, Locci F, Martins P, et al. The ISOLDE facility. *J Phys G Nucl Part Phys* (2017) **44**:094002. doi:10.1088/1361-6471/aa7eba

29. Webster BL. The Chemical Separation of Terbium for Applications in Nuclear Medicine. (2021) doi:https://doi.org/10.15126/thesis.900310

30. Duchemin C, Ramos JP, Stora T, Ahmed E, Aubert E, Audouin N, Barbero E, Barozier V, Bernardes A-P, Bertreix P, et al. CERN-MEDICIS: A Review Since Commissioning in 2017. *Front Med* (2021) **8**:1–11. doi:10.3389/fmed.2021.693682

31. Li Z, Tyrpak DR, Park M, Okamoto CT, MacKay JA. A new temperature-dependent strategy to modulate the epidermal growth factor receptor. *Biomaterials* (2018) **183**:319–330. doi:10.1016/j.biomaterials.2018.07.063

32. Brix N, Samaga D, Hennel R, Gehr K, Zitzelsberger H, Lauber K. The clonogenic assay: robustness of plating efficiency-based analysis is strongly compromised by cellular cooperation. *Radiat Oncol* (2020) **15**:1–12. doi:10.1186/s13014-020-01697-y

33. Fernandes C, Palma E, Silva F, Belchior A, Pinto CIG, Guerreiro JF, Botelho HM, Mendes F,

Raposinho P, Paulo A. Searching for a Paradigm Shift in Auger-Electron Cancer Therapy with Tumor-Specific Radiopeptides Targeting the Mitochondria and/or the Cell Nucleus. *Int J Mol Sci* (2022) **23**: doi:10.3390/ijms23137238

34. Fritzberg AR, Whitney WP, Kuni CC, Klingensmith W. Biodistribution and renal excretion of 99mTc-N,N'-bis-(mercaptoacetamido) ethylenediamine. Effect of renal tubular transport inhibitors. *Int J Nucl Med Biol* (1982) **9**:79–82. doi:10.1016/0047-0740(82)90081-X

35. Vaissier PEB, Beekman FJ, Goorden MC. Similarity-regulation of OS-EM for accelerated SPECT reconstruction. *Phys Med Biol* (2016) **61**:4300–4315. doi:10.1088/0031-9155/61/11/4300

36. Tang Y, Xu H, Dai Y, Wang F, Huang W, Liu P, Gu Y. A novel peptide targeting c-Met for hepatocellular carcinoma diagnosis. *J Mater Chem B* (2021) **9**:4577–4586. doi:10.1039/d1tb00408e

37. Ku A, Facca VJ, Cai Z, Reilly RM. Auger electrons for cancer therapy – a review. *EJNMMI Radiopharm Chem* (2019) **4**: doi:10.1186/s41181-019-0075-2

38. Hasenauer S, Malinger D, Koschut D, Pace G, Matzke A, von Au A, Orian-Rousseau V. Internalization of Met Requires the Co-Receptor CD44v6 and Its Link to ERM Proteins. *PLoS One* (2013) **8**:e62357. doi:10.1371/journal.pone.0062357

39. Johnstone RW, Andrew SM, Hogarth MP, Pietersz GA, McKenzie IFC. The effect of temperature on the binding kinetics and equilibrium constants of monoclonal antibodies to cell surface antigens. *Mol Immunol* (1990) **27**:327–333. doi:10.1016/0161-5890(90)90045-2

40. Rico F, Chu C, Abdulreda MH, Qin Y, Moy VT. Temperature modulation of integrin-mediated cell adhesion. *Biophys J* (2010) **99**:1387–1396. doi:10.1016/j.bpj.2010.06.037

41. Encarnação JC, Barta P, Fornstedt T, Andersson K. Impact of assay temperature on antibody binding characteristics in living cells: A case study. *Biomed Reports* (2017) **7**:400–406. doi:10.3892/br.2017.982

42. Borgna F, Haller S, Rodriguez JMM, Ginj M, Grundler P V., Zeevaart JR, Köster U, Schibli R, van der Meulen NP, Müller C. Combination of terbium-161 with somatostatin receptor antagonists—a potential paradigm shift for the treatment of neuroendocrine neoplasms. *Eur J Nucl Med Mol Imaging* (2022) **49**:1113–1126. doi:10.1007/s00259-021-05564-0

43. Grünberg J, Lindenblatt D, Dorrer H, Cohrs S, Zhernosekov K, Köster U, Türler A, Fischer E, Schibli R. Anti-L1CAM radioimmunotherapy is more effective with the radiolanthanide terbium-161 compared to lutetium-177 in an ovarian cancer model. *Eur J Nucl Med Mol Imaging* (2014) **41**:1907–1915. doi:10.1007/s00259-014-2798-3

44. Desouky O, Ding N, Zhou G. Targeted and non-targeted effects of ionizing radiation. *J Radiat Res Appl Sci* (2015) **8**:247–254. doi:10.1016/j.jrras.2015.03.003

45. Vermeulen K, Van de Voorde M, Segers C, Coolkens A, Rodriguez Pérez S, Daems N, Duchemin C, Crabbé M, Opsomer T, Saldarriaga Vargas C, et al. Exploring the Potential of High-Molar-Activity Samarium-153 for Targeted Radionuclide Therapy with [^{153}Sm]Sm-DOTA-TATE. *Pharmaceutics* (2022) **14**: doi:10.3390/pharmaceutics14122566

46. Alcocer-Ávila ME, Ferreira A, Quinto MA, Morgat C, Hindié E, Champion C. Radiation doses from ^{161}Tb and ^{177}Lu in single tumour cells and micrometastases. *EJNMMI Phys* (2020) **7**:33. doi:10.1186/s40658-020-00301-2

47. Hu H, Quintana J, Weissleder R, Parangi S, Miller M. Deciphering albumin-directed drug delivery by imaging. *Adv Drug Deliv Rev* (2022) **185**:114237. doi:10.1016/j.addr.2022.114237

48. Umbricht CA, Benešová M, Schmid RM, Türler A, Schibli R, van der Meulen NP, Müller C. ^{44}Sc-PSMA-617 for radiotheragnostics in tandem with ^{177}Lu-PSMA-617—preclinical investigations in comparison with ^{68}Ga-PSMA-11 and ^{68}Ga-PSMA-617. *EJNMMI Res* (2017) **7**:9. doi:10.1186/s13550-017-0257-4

49. Müller C, Singh A, Umbricht CA, Kulkarni HR, Johnston K, Benešová M, Senftleben S, Müller D, Vermeulen C, Schibli R, et al. Preclinical investigations and first-in-human application of ^{152}Tb-PSMA-617 for PET/CT imaging of prostate cancer. *EJNMMI Res* (2019) **9**:1–10. doi:10.1186/s13550-019-0538-1

50. Sartor O, Herrmann K. Prostate Cancer Treatment: ^{177}Lu-PSMA-617 Considerations, Concepts, and Limitations. *J Nucl Med* (2022) **63**:823–829. doi:10.2967/jnumed.121.262413

51. Roberts MJ, Maurer T, Perera M, Eiber M, Hope TA, Ost P, Siva S, Hofman MS, Murphy DG, Emmett L, et al. Using PSMA imaging for prognostication in localized and advanced prostate cancer. *Nat Rev Urol* (2023) **20**:23–47. doi:10.1038/s41585-022-00670-6

52. Dekempeneer Y, Bäck T, Aneheim E, Jensen H, Puttemans J, Xavier C, Keyaerts M, Palm S, Albertsson P, Lahoutte T, et al. Labeling of Anti-HER2 Nanobodies with Astatine-211: Optimization and the Effect of Different Coupling Reagents on Their in Vivo Behavior. *Mol Pharm* (2019) **16**:3524–3533. doi:10.1021/acs.molpharmaceut.9b00354

53. Tchouate Gainkam LO, Caveliers V, Devoogdt N, Vanhove C, Xavier C, Boerman O, Muyldermans S, Bossuyt A, Lahoutte T. Localization, mechanism and reduction of renal retention of technetium-99m labeled epidermal growth factor receptor-specific nanobody in mice. *Contrast Media Mol Imaging* (2011) **6**:85–92. doi:10.1002/cmmi.408

54. D'Huyvetter M, Vincke C, Xavier C, Aerts A, Impens N, Baatout S, De Raeve H, Muyldermans S, Caveliers V, Devoogdt N, et al. Targeted radionuclide therapy with A ^{177}Lu-labeled anti-HER2 nanobody. *Theranostics* (2014) **4**:708–720. doi:10.7150/thno.8156

Chapter 4 – Auger electron therapy of prostate cancer using ^{111}In and ^{161}Tb labelled compounds targeting the mitochondria of prostate specific membrane antigen (PSMA) overexpressing cells

Irwin Cassells[1,2], Joana F. Santos[3], Paula Raposinho[3,4], Simon Leekens[2], Maarten Ooms[1], Michiel Van de Voorde[1], Filipa Mendes[3,4], Célia Fernandes[3,4], António Paulo*[3,4] and Frederik Cleeren*[2]

[1] NURA Research Group, Belgian Nuclear Research Centre (SCK CEN), Mol, Belgium [2] Laboratory for Radiopharmaceutical Research, Department of Pharmacy and Pharmacology, University of Leuven, Leuven, Belgium [3] C^{2}TN – Centro de Ciências e Tecnologias Nucleares, Instituto Superior Técnico, U. Lisboa, Portugal [4] DECN – Departamento de Engenharia e Ciências Nucleares, Instituto Superior Técnico, U. Lisboa, Portugal

*Corresponding authors

[The work presented here is part of an ongoing PRISMAP collaborative project between KU Leuven, SCK CEN and C^{2}TN (Lisbon, Portugal)]

Part of the results are published in Santos, J., Braz, M., Raposinho, P., Cleeren, F., **Cassells, I.**, Leekens, S., Cawthorne, C., Mendes, F., Fernandes, C., and Paulo, A. (2023) Synthesis and Preclinical Evaluation of PSMA-Targeted ^{111}In-Radioconjugates Containing a Mitochondria-Tropic Triphenylphosphonium Carrier. *Mol. Pharmaceutics* 2024, 21, 1, 216−233

4.1 Introduction

In the past decade, radiopharmaceuticals have played an increasingly important role in diagnosis or treatment in oncology (1,2). Prostate-specific membrane antigen, commonly referred to as PSMA, is a type II metalloprotease and a useful clinical biomarker of prostate cancer (3,4). Its expression is highly upregulated with androgen deprivation and is well-correlated with the aggressiveness of prostate cancer (4). Many radiolabelled, small organic molecules (e.g. PSMA-617) which target the PSMA receptor have been developed for both diagnostic and therapeutic applications. Therapeutic radiopharmaceuticals, such as [^{177}Lu]Lu-PSMA-617 (Pluvicto®), which is EMA and FDA approved, are successfully used for the treatment of metastatic castration-resistant prostate cancer (mCRPC) (5). Though highly promising, some patients do not respond to the [^{177}Lu]Lu-PSMA-617 therapy or patients develop tolerance to this therapy resulting in progression of disease after multiple treatment cycles (6). This general trend with β^- emitting therapy is often attributed to the low linear energy transfer (LET) of β^- particles resulting in a relatively small local energy deposit spread over a long range. This results in a limited chance of causing fatal irreparable damage to the target cells. In addition, the long pathway of β^- energy deposition implies

that surrounding healthy tissues are also irradiated, which might lead to radiotoxicity of healthy tissue, as observed in the VISION phase II clinical trial of [^{177}Lu]Lu-PSMA-617 (7). Other PSMA-617 derivatives, such as [^{161}Tb]Tb-PSMA-617 and [^{225}Ac]Ac-PSMA-617, have shown promise in (pre)clinical studies as alternatives to their ^{177}Lu counterpart, and, though in a small number of patients, there is still a positive therapeutic response against mCRPC in patients who no longer respond to [^{177}Lu]Lu-PSMA-617 treatments (8,9).

Alpha emitter based radionuclide therapy has shown great promise in recent years, delivering a potent dose to their target (3,10,11) because of the high LET values of alpha particles. Moreover, many alpha emitting isotopes have daughter radioisotopes which can deliver an additional therapeutic dose to the target. However, supply of these promising alpha emitting radionuclides is generally limited. An alternative to alpha emitting isotopes are Auger electron emitters, which emit low-energy electrons as a result of a transfer of energy after an electron is kicked out of its orbital following electron capture or internal conversion (12). The cascading electrons deposit high LET radiation (4−26 keV/µm) over a very short distance (0.1-5.0 µm) (12). Many Auger emitting isotopes are currently used for SPECT applications, one of which is indium-111 (^{111}In). ^{111}In decays via electron capture, with a half-life of 2.83 days and emits gamma rays (Eγ = 171 keV (91%) and Eγ = 245 keV (94%)) upon its decay. A fraction of the gamma rays transfers its energy to electrons (internal conversion) producing conversion electrons of 144 keV or 218 keV and low energy X-rays in turn generating Auger electrons which will contribute to a therapeutic effect. Additionally, isotopes such as ^{161}Tb (β^- emitter, $t_{1/2}$ = 6.95 days, $E\beta^-_{average}$ = 197 keV) (13,14), which co-emits two Auger and five conversion electrons (total E_{e^-} = 36 keV) in addition to its main β^- decay, has shown increased therapeutic potency when compared to more established beta emitting isotopes such as ^{177}Lu (β^- emitter, $t_{1/2}$ = 6.7 days, $E\beta^-_{average}$ = 134 keV) that are often used in the clinic (15,16).

Because of the short range of conversion and Auger electrons, most of the energy is deposited in the cell the radiopharmaceutical is bound to, without affecting neighbouring cells. Due to its short range however, it is also assumed that maximal efficacy can only be achieved when these electrons are in close proximity of the DNA so that double-stranded DNA breaks can occur. However, recent reports by Müller *et al.* indicate that the cell membrane itself might also be a good target to cause radiation induced cytotoxic effects (17). This result suggests that DNA is not the only potential subcellular target, but other vital organelles such as mitochondria could be promising targets. In a study by Paulo and co-workers, ^{99m}Tc-labelled acridine orange derivatives, a known DNA targeting group, was observed to cause DNA double stranded breaks (18). To our knowledge, this is the first study which showcased the therapeutic power of ^{99m}Tc (E_e- = 14-18 keV) as an Auger emitter. The success of this study sparked a follow-up study by the authors, where they investigated targeting mitochondria using the mitotropic group triphenyl phosphonium (19). This study was the first to indicate that preferential uptake in cell organelles can be an effective strategy using an Auger emitter, even with low yielding Auger emitters such as ^{99m}Tc

(19). However, no therapeutic Auger electron emitting radiopharmaceutical is used in clinical routine yet.

In this study, we extended the work of Paulo and co-workers, by targeting mitochondria. We have designed dual-targeted radioconjugates carrying a PSMA binding motif and a triphenyl phosphonium (TPP) group to promote 1) selective uptake by prostate cancer (PCa) cells and 2) subsequent accumulation in the mitochondria post internalisation (**Figure 4.1**). We report the radiolabelling of three compounds, **DOTAGA(TPP), DOTA-PSMA, DOTAGA(TPP)-PSMA** (**Figure 4.2**) with two radioisotopes, ^{111}In (Auger emitter) and ^{161}Tb (conversion, Auger and β^- emitter). In addition, we evaluated the cell binding, internalisation, and subcellular localisation of the radiolabelled complexes in PSMA expressing cells. We then investigated the radiobiological effects and assessed the potential pathways of cell death. Lastly, we evaluated the biodistribution of the ^{111}In-labelled compounds in PSMA-positive PCa xenografts *using* μSPECT/CT to evaluate the *in vivo* pharmacokinetics and tumour accumulation of the novel constructs. For future studies, an additional compound will be included containing a tri-glycine moiety between the DOTAGA and the PSMA binding motif. The aim of this linker is that it can be cleaved enzymatically by Cathepsin B in the lysosomal compartment of the cell, so that the radioactive-DOTAGA(TPP) radiometabolite might be directed more efficiently to the mitochondria (**Figure 4.2**). However, the synthesis of this construct was not completed when ^{161}Tb experiments were performed.

4.2 Material and Methods

4.2.1 General

All reagents and solvents were purchased from Sigma-Aldrich (Bornem, Belgium or Lisboa, Portugal) or VWR (Leuven, Belgium), and used without further purification. Radiolabelling buffers were stirred with chelex (Chelex 100 sodium form, 50-100 mesh, Sigma Aldrich), to remove trace metals, for 30 minutes before being filtered and degassed prior to use. DOTA-based compounds (**DOTAGA(TPP), DOTA-PSMA, DOTAGA(TPP)-PSMA**) were synthesised by C^{2}TN team (IST, Lisbon, Portugal)(20).

4.2.2 Instrumentation and Characterisation

Quality control and evaluation of radiochemical conversion (decay corrected) of the ^{161}Tb-labelled compounds were carried out using high-performance liquid chromatography (HPLC, Perkin Elmer, Waltham, MA, USA), which consisted out of a Perkin–Elmer LC pump 200 coupled to a LC 290 tuneable UV–Vis detector and a Berthold LB-509 radiometric detector in series, with an analytical Macherey-Nagel C_{18} reversed-phase column (Nucleosil 100–10, 250 × 4 mm) using a flow rate of 0.7 mL/min and gradient method using 0.1% TFA in H_2O (eluent A) and 0.1% TFA in acetonitrile (eluent B) (Method: t = 0–25 min, 5–100% eluent B; 25–27 min,100% eluent B; 27–30 min, 100-5% eluent B). For ^{111}In-labelled

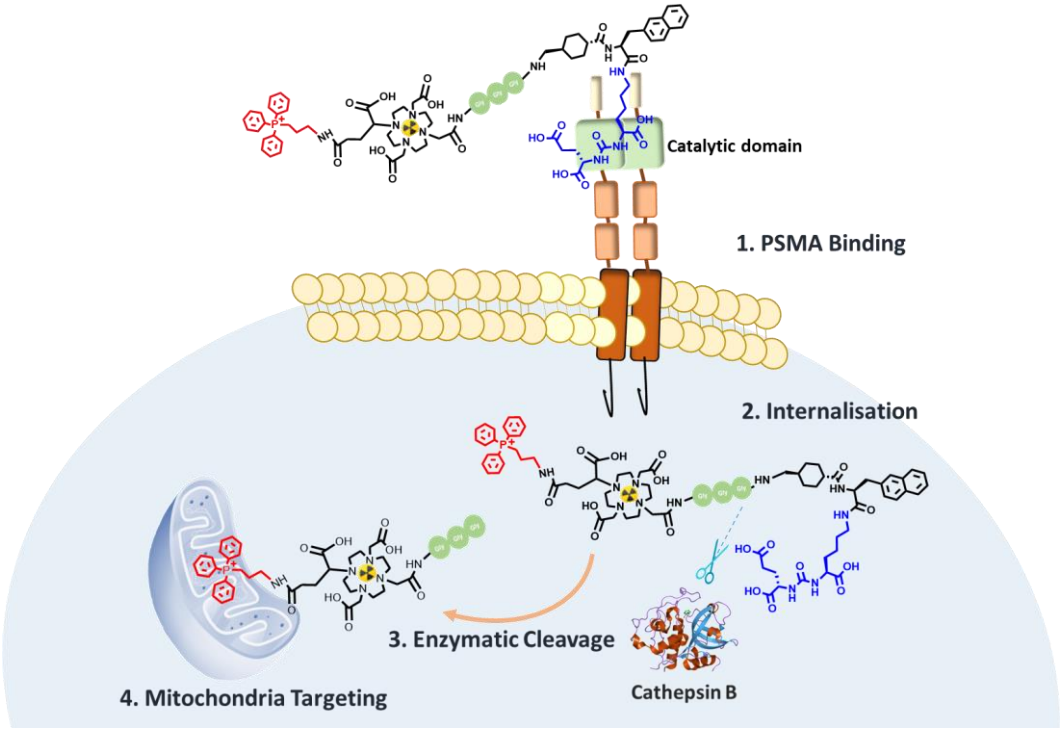


Figure 4.1. Illustration of the subcellular targeting approach. (1) PSMA-617 binds PSMA, and (2) gets internalised into the cells. (3) In the lysosome, the TPP-PSMA-617 molecule is enzymatically cleaved (tri-glycine is cleaved by Cathepsin B), and (4) the TPP moiety of the radioactive-DOTAGA(TPP) radiometabolite directs the radionuclide to the mitochondria. Image designed by Prof. A. Paulo, Dr C. Fernandes and Dr F. Mendes.

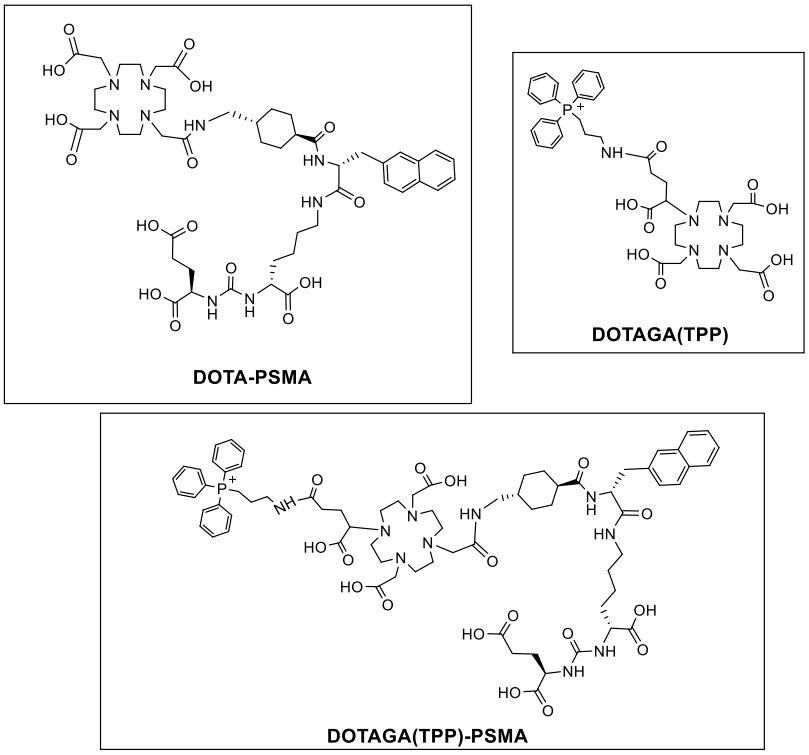


Figure 4.2. Compounds used in this study.

compounds, an XBridge C_{18} column (Waters, Antwerp, Belgium) was used at the same conditions, passing through a UV detector (2998 PDA detector, Waters, Milford, Massachusetts) in series with a 3-inch NaI(Tl) radioactivity detector. Gamma counting was performed on a Wizard^2 3470 (crystal: NaI(Tl), 50 mm in height, 32 mm in diameter, dead time 2.5 μs; Perkin Elmer, Rodgau, Germany) or HIDEX AMG (Hidex, Turku, Finland) with a detection profile with an energy window of 50-400 keV, and counting time of 60 seconds. Counts were corrected for background radiation, physical decay, counter dead time and referenced to a ^{137}Cs source. Mass spectrometry analysis was performed using an electrospray ionization/quadrupole ion trap (ESI/QITMS) Bruker HCT mass spectrometer (Bruker, Billerica, MA, USA). Samples were injected as mixtures of water:acetonitrile or water:methanol and injected at a flow rate of 150 $\mu L \cdot h^{-1}$. Colorimetry cell-based assays were quantified using Varioskan™ LUX microplate reader (Thermo Fisher Scientific).

4.2.3 Cell Culture

PSMA-positive transfected PC-3 cells (PC3-PIP) and PSMA-negative PC-3 cells (PC3-flu) were received from Dr M. Pomper at the John Hopkins Medicine Centre (Baltimore, MD). Cells were maintained under 5% CO_2 atmosphere at 37 ºC, in RPMI 1640 medium (Thermo Fisher, Gibco, cat. no. A1049101, Merelbeke, Belgium), which was supplemented with 10% foetal bovine serum (FBS, Thermo Fisher, cat. no. A5256701) and 20 μg/mL puromycin (Fisher Scientific, Gibco, cat. no. 12122530). Both cell lines were subcultured according to ATCC specifications for unmodified PC3 cells.

4.2.4 Radioisotopes

[^{161}Tb]$TbCl_3$ was produced at the Belgian Nuclear Research Centre (SCK CEN) using the method described in Cassells *et. al*. (21). Enriched $^{160}Gd_2O_3$ (1.0 mg, 98.2 %, Isoflex, San Francisco, CA) was dissolved in nitric acid and sealed in a quartz ampoule. The sealed ampoule was placed inside an aluminium capsule and irradiated for 7 days in the BR2 Reactor at SCK CEN at a thermal neutron flux of approx. 3.0 x 10^{14} $n \cdot cm^{-2} \cdot s^{-1}$. After 24 hours cooling, the sample is diluted in ultra-pure water. High-pressure ion chromatography (HPIC, Shimadzu), with a strong cation exchange column (ø: 6 mm, l: 50 mm, Shodex IC R-621), was used to separate the ^{161}Tb from unconverted ^{160}Gd and ^{161}Dy target matrix by elution with α-hydroxyisobutyric acid (α-HIBA) / ammonium hydroxide (trace-metal grade, pH 4.5) solution. The resulting [^{161}Tb]Tb-(α-HIBA)n complex is converted to the chloride salt by trapping the terbium source on an extraction resin (ø: 2.1 mm, l: 30 mm, LN3, TrisKem International, Bruz, France) and eluting with 50 mM hydrochloric acid (trace-metal free). This procedure yields [^{161}Tb]$TbCl_3$ with a high radionuclidic purity (> 99.999%). [^{111}In]$InCl_3$ was purchased from Curium (Petten, The Netherlands), and used without purification.

4.2.5 Complexation reactions with $^{nat}InCl_3$ and $^{nat}TbCl_3$

General method: DOTA-based compounds (**DOTAGA(TPP), DOTA-PSMA, DOTAGA(TPP)-PSMA**) were reacted with $^{nat}InCl_3$ or $^{nat}TbCl_3$ (1:5 molar equivalent) in a sodium acetate solution (0.4M NaOAc, pH 4.7, 0.5 mL) for 15 minutes at 95°C. The solution was left to cool to room temperature. The unreacted metal chloride was removed by Sep-Pak purification (Sep-Pak C_{18} light, Waters, Antwerp, Belgium) by applying the reaction mixture to the column and rinsing with 5 mL of high purity water. The final construct was eluted with 0.5 mL of acetonitrile. The complexes were analysed by UV-HPLC and mass spectrometry.

^{nat}In-**DOTAGA(TPP):** DOTAGA(TPP) (720.0 µg, 0.9 µmol) was reacted with indium chloride (1020.0 µg, 4.6 µmol) to form ^{nat}In-DOTAGA(TPP). Purity: >99%. ESI MS(+) : m/z 890.4 ($[M]^+$, calculated 890.2), 445.7 ($[M+H]^{2+}$, calculated 445.6). ^{nat}In-**DOTA-PSMA:** DOTA-PSMA (300.0 µg, 0.29 µmol) was reacted with indium chloride (318.0 µg, 1.4 µmol) to form ^{nat}In-DOTA-PSMA. Purity: >99%. ESI MS(+) : m/z 1154.4 ($[M+H]^+$, calculated 1154.4). ^{nat}In-**DOTAGA(TPP)-PSMA:** DOTAGA(TPP)-PSMA (50.0 µg, 0.03 µmol) was reacted with indium chloride (38.9 µg, 0.17 µmol) to form ^{nat}In-DOTAGA(TPP)-PSMA. Purity: >99%. ESI MS(+) : m/z 1527.6 ([M]+, calculated 1527.5), 764.6 ($[M+H]^{2+}$, calculated 764.7).

^{nat}Tb-**DOTAGA(TPP):** DOTAGA(TPP) (100.0 µg, 0.13 µmol) was reacted with terbium chloride (242.0 µg, 0.64 µmol) to form ^{nat}Tb-DOTAGA(TPP). Purity: >99%. ESI MS(+) : m/z 934.4 ($[M]^+$, calculated 934.4), 467.8 ($[M+H]^{2+}$, calculated 467.6). ^{nat}Tb-**DOTA-PSMA:** DOTA-PSMA (100.0 µg, 0.9 µmol) was reacted with terbium chloride (180.0 µg, 0.48 µmol) to form ^{nat}Tb-DOTA-PSMA. Purity: >99%. ESI MS(+) : m/z 1198.57 ($[M+H]^+$, calculated 1198.41). ^{nat}Tb-**DOTAGA(TPP)-PSMA:** DOTAGA(TPP)-PSMA (50.0 µg, 0.03 µmol) was reacted with terbium chloride (65.0 µg, 0.18 µmol) to form ^{nat}Tb-DOTAGA(TPP)-PSMA. Purity: >99%. ESI MS(+) : m/z 786.67 ($[M+H]^{2+}$, calculated 786.28).

4.2.6 Radiolabelling with $[^{111}In]InCl_3$ and $[^{161}Tb]TbCl_3$

DOTA-based compounds (**DOTAGA(TPP), DOTA-PSMA, DOTAGA(TPP)-PSMA**) (5 nmol) were reacted with $[^{111}In]InCl_3$ or $[^{161}Tb]TbCl_3$ (25-100 MBq) in a sodium acetate solution (0.4M NaOAc, pH 4.7, 0.5 mL) for 15 minutes at 95°C. The solution was left to cool to room temperature. The unreacted radioactive metal salt was removed by Sep-Pak purification by applying the reaction mixture on the column and rinsing with 5 mL high purity water. The final construct was eluted with 0.6 mL absolute ethanol and dried using a gentle dry dinitrogen gas flow at room temperature. The final sample is redissolved in a solution of phosphate buffered saline (PBS) containing sodium ascorbate (25.2 mM). The integrity of the complexes was analysed by radio-HPLC and referenced against cold complexes.

4.2.7 Partition coefficient

The partition coefficient of the radiolabelled constructs was determined by concentration ratios in octanol/water mixtures (22). Radiolabelled compound solution (~500 kBq, 25 µL) was added to a mixture of n-octanol (1 mL) and water (pH 7.0, 1 mL). The radiolabelled mixture was vortexed and then centrifuged to separate water and octanol phases. Once separated, and in triplicate, 0.05 mL of each phase was isolated, and the amount of γ-radiation determined in each sample using a gamma counter. The logarithm of partition coefficient ($\log_{10}P_{o/w}$) was determined by taking the log10 of the ratio of γ-counts found in octanol and PBS ($\log_{10} P_{\frac{o}{water}} = \log_{10}(\gamma_o/\gamma_{water})$).

4.2.8 *In vitro* stability studies

The stability of the radiolabelled compounds was evaluated in PBS and cell culture medium (RPMI 1640 with 10% FBS and 20 µg/mL puromycin). The radiolabelled compound (5-10 MBq, diluted to 0.1 mL with PBS or cell culture medium) was added to 0.4 mL of PBS or cell culture medium, which was pre-heated to 37°C. The radioactive solution was incubated for 48 hours at 37°C, with a sample removed at 24 hours for analysis. The stability was assessed using radio-HPLC.

4.2.9 Cell binding assays

Cells were seeded in a 24-well plate, at a cell density of 0.5-1.5 x 10^5 cells per well and allowed to attach over 16 hours at 37 °C, in a 5% CO_2 atmosphere. Culture medium (previously described) was replaced 60 minutes before the experiment. Cells were treated with ^{161}Tb-labelled constructs (~7.4 kBq, total volume per well = 0.5 mL), and incubated at 37 °C for 5 minutes to 4 hours. For PSMA receptor-blocked experiments, cells were pre-treated with 2-(phosphonomethyl)pentanedioic acid (2-PMPA) (50 nmol, 0.25 mL) for 30 minutes before the radiolabelled construct was added. After each incubation period, the unbound tracer was removed, and cells washed with cold (4 °C) cell culture medium. Cell surface-bound tracer was removed by incubating the cells with an acid wash solution (50 mM glycine-HCl, 100 mM NaCl, pH 2.8) at room temperature for 4 minutes. The detached cell membrane proteins were collected, cells washed with PBS and wash solutions were combined. Cells were lysed by incubating the cells with 1M NaOH for 10 minutes and the remaining cell matter (internalised activity) collected. The γ-counts in each fraction were determined by an automatic γ-counter and reported as a ratio of the total activity (unbound + surface bound + internalised). Assays were performed in triplicate for reproducibility, regressed to 2 x 10^5 cells, and represented as mean and standard deviation.

4.2.10 Mitochondria Uptake Assay

The mitochondrial uptake was assessed by compartmental fractionation studies in PC3-pip cells, using the same method outlined in Fernandes *et. al*. (19). Cells were incubated with the radiolabelled PSMA-

containing compounds (~7.4 MBq) in 2 mL of RPMI 1640 medium (supplemented with 10% FBS, 20 µg/mL puromycin dichloride) for 1 h and 3 h at 37 °C and 5% CO_2. The incubation solution was removed, and cells were washed with 3 x 1 mL of culture medium, after which the cells were harvested by scraping the adhered cells and suspending them in 6 mL of cold non-supplemented cell culture medium. The suspension was split into 3 fractions, centrifuged (850 x g, 2 min at 4°C) and the resulting pellet washed with cold PBS to remove unbound radiolabelled PSMA construct. To obtain the mitochondrial uptake fraction, cells were treated with the *Mitochondria Isolation Kit for Cultured cells* (Thermo Scientific, Walthman, MA) without modification to the manufacturer's protocol. In short, the pellet was divided into three, and each dividend was resuspended in reagent A from the kit, which was supplemented with protease inhibitors (Roche, Basel, Switzerland), vortexed, and rested on ice. To the cold suspension, reagent B was added, and the samples were aggressively vortexed, after which samples were incubated on ice and vortexed periodically. Reagent C, which was supplemented with protease inhibitors, was added, and the resulting suspension centrifuged for 10 minutes at 700 × g at 4 °C to obtain the nucleus fraction. The nucleus pellet was isolated, and the supernatant was centrifuged for 15 minutes at 3 000 x g at 4 °C to remove the lysosomal and peroxisomal material. The pellet was carefully removed, and the supernatant was centrifuged for 5 minutes at 12 000 x g to recover the mitochondria of the cells. After isolation of the mitochondria pellet, the activity in all fractions were counted using an automatic γ-counter.

4.2.11 Cell viability assay

Cells were seeded in a 96-well plate, at a cell density of 2 x 10^3 cells per well and allowed to attach over 18 hours at 37 °C in 5% CO_2. Cells were treated with ^{161}Tb-labelled constructs (0.002-18.5 MBq/mL, total volume: 100 µL) and incubated for 4 hours. The non-cell bound activity was removed, replaced with fresh medium, and incubated for 5 days. To each well, 10 µL of MTT (3-(4,5-dimethylthiazol-2-yl)-2,5-diphenyltetrazolium bromide) was added to assess the impact of the radiation dose on cell viability. The resulting formazan salt was dissolved in dimethyl sulfoxide and the absorbance (490 nm) was determined for each well and normalised to the absorbance from cell culture medium. The experiment was performed in sextuplicate, and then mean cell viability was calculated by using the ratio of the absorbance of treated and untreated cells.

4.2.12 Clonogenic assay

Clonogenic survival assays were performed based on the methods described by Brix *et. al*. (23). Cells were seeded in a 6-well plate, at a cell density of 0.3 x 10^3 cells per well and allowed to attach over 18 hours at 37 °C in 5% CO_2. Cells were treated with ^{161}Tb-labelled PSMA constructs (0.025 – 1.23 MBq/mL) and incubated for 4 hours, in triplicate. The activity was removed, wells washed with phosphate buffered saline (3 x 3 mL), complete medium was added (3 mL), and incubated for 10 days. Cells were fixed

using a solution of methanol and glacial acetic acid (3:1) and colonies were stained with Giemsa (4%). Wells were dried by gravity, colonies counted (minimum of 50 cells per colony) and the plating efficiency (PE) and survival fraction (SF) calculated (19):

$$PE(\%) = 100 \times N_{colonies} \text{ without treatment} / N_{cells} \text{ seeded}$$

$$SF(\%) = 100 \times N_{colonies} \text{ after treatment} / N_{cells} \text{ seeded} \times PE$$

4.2.13 Tumour inoculation

Mice (SCID beige, age: 6-12 weeks, Envigo, Gannat, France) were housed in individually ventilated cages (IVC) in a regulated environment (22 ºC, humidity, 12h day/night cycle), with food and water *ad libitum*. Mice were subcutaneously inoculated on both shoulders with 1-2 million cells (PC3-PIP or PC3-flu) suspended in 0.1 mL of Cultrex (Bio-Techne, 3432-010-01) and 0.1 mL RPMI 1640 (non-supplemented media). Tumours were left to grow for 3-4 weeks (tumour size: 200 – 350 mm^3) before experiments were conducted on the mice. Animal experiments were conducted according to the Belgian code of practice and use of animal experiments were approved by the ethical committee for animal care from KU Leuven (P112/2020/038).

4.2.14 µSPECT/CT acquisition and image processing and analysis

Tumour-bearing mice were injected via a tail vein with 22-25 MBq of **[^{111}In]In-DOTAGA(TPP)**, **[^{111}In]In-DOTAGA(TPP)-PSMA** or **[^{111}In]In-DOTA-PSMA** (1-2 nmols). After 1h or 24h p.i., mice were anaesthetised using 2.5% isoflurane carrier by of O_2 at steady flow of 1 L/min. Static µSPECT imaging was performed using a γ-CUBE (Molecubes, Ghent, Belgium) in a headfirst-prone position (energy peaks: 171 keV, 246 keV, window: ±10 %, 30 minutes) at 1 h and 24 h *p.i.* Following the SPECT imaging, a 5-min CT scan was acquired using the X-CUBE (Molecubes, Ghent, Belgium) for attenuation correction. The acquired SPECT images were reconstructed through a maximum-likelihood expectation-maximization (MLEM) algorithm using 10 iterations. The resulting images were then processed to generate fused SPECT/CT images for anatomical co-registration. The reconstruction, fusion and analysis of these images were performed using the PMOD biomedical image quantification software (PMOD Technologies, Zurich, Switzerland). For calculation of standardised uptake value (SUV), a calibration sample (400 µL, 1.5 MBq ^{111}In-labeled construct) was introduced in each scan and referenced for activity correlation.

4.2.15 Statistical analysis

Quantitative data are expressed as mean ± standard deviation, unless stated otherwise. For intercomparison of results, means were compared using a mixed model ANOVA analysis in GraphPad

Prism 9.3.1, corrected using Sidak's or Tukey multiple comparison test. Values were determined to be statistically significant for p-values less than the threshold value of 0.05.

4.3 Results and Discussion

4.3.1 Complexation with natural terbium chloride and indium chloride

Naturally occurring (stable) terbium chloride ($^{nat}TbCl_3$) or indium chloride ($^{nat}InCl_3$) was reacted with **DOTAGA(TPP)**, **DOTAGA(TPP)-PSMA, DOTA-PSMA** to afford the non-radioactive Tb-complexes. These complexes serve as the reference compounds for identification purposes using radio-HPLC. Compound purity was assessed using HPLC. **Tb-DOTAGA(TPP) and Tb-DOTA-PSMA** had similar retention times of 14.7 and 14.1 minutes, respectively. **Tb-DOTAGA(TPP)-PSMA** had a retention time of 17.0 minutes, reflecting its lowest hydrophilicity (see **Table 1)**. This change might influence the pharmacokinetics and tumour accumulation of the compound. Additionally, indium labelled variants were observed at the same retention times, which does not correlate to the trend in log*P* (**Table 4.1**). It is important to note that lipophilicity is not the only factor to influence the retention of the compound, but also charge can influence the interaction between the metal complex and the packing material.

Confirmation of the integrity of the compounds was afforded using ESI-MS. **Tb-DOTAGA(TPP)**, which carries a permanent positive charge, was observed in the mass spectrum as $[M]^+$, with a *m/z* of 934.4. Unlike the **Tb-DOTAGA(TPP)**, **Tb-DOTAGA(TPP)-PSMA** was observed as a doubly charged $[M+H]^{2+}$ species, with *m/z* 786.67. Similarly, the **Tb-DOTA-PSMA** was protonated in the ionisation process, and was observed as a $[M+H]^+$ species with *m/z* 1198.57. All *m/z* values were within 0.1% of their calculated values. A similar trend was observed with the indium complexes, and the data is provided in **Table 4.1**.

Table 4.1. Analytical data of compounds used in this study.

Compound	Retention time (min)	Dominant ionisation species	*m/z* (calculated *m/z*)	Log*P*
^{nat}Tb-DOTAGA(TPP)	14.7	$[M]^+$	934.4 (934.4)	-3.27
^{nat}Tb-DOTA-PSMA	14.1	$[M+H]^+$	1198.57 (1198.41)	-2.29
^{nat}Tb-DOTAGA(TPP)-PSMA	17.0	$[M+H]^{2+}$	786.67 (786.28)	-2.08
^{nat}In-DOTAGA(TPP)	14.5	$[M]^+$	890.4 (890.2)	-3.40
^{nat}In-DOTA-PSMA	13.9	$[M+H]^+$	1154.4 (1154.4)	-3.56
^{nat}In-DOTAGA(TPP)-PSMA	16.9	$[M+H]^{2+}$	764.6 (764.7)	-1.90

4.3.2 Radiolabelling with [^{161}Tb]$TbCl_3$ and [^{111}In]$InCl_3$ and *in vitro* stability

Radiolabelling of **DOTAGA(TPP), DOTA-PSMA** and **DOTAGA(TPP)-PSMA** with [^{161}Tb]$TbCl_3$ and [^{111}In]$InCl_3$ was performed using the same conditions used in the cold reactions. Reactions with [^{111}In]$InCl_3$ were non-quantitative with PSMA-617 containing compounds, with radiochemical conversions of 94.3% and 94.5%, respectively for **[^{111}In]In-DOTA-PSMA** and **[^{111}In]In-DOTAGA(TPP)-PSMA.** Similarly, **[^{111}In]In-DOTAGA(TPP)** was observed to have high variance in the complexation yields, ranging between 80% to 90%. Because of this non-quantitative radiochemical conversions, labelled compounds were purified using solid phase extraction. Radiochemical purity post purification was determined to be >99.9%. In contrast, reactions with [^{161}Tb]$TbCl_3$ showed radiolabelling conversion yields >99.5%, which was confirmed using radio-HPLC. To allow direct comparison between indium and terbium complexes, the ^{161}Tb-labelled compounds were subjected to the same purification method as used for the ^{111}In-labelled compounds.

The stability of the radiocomplexes in PBS and RPMI 1640 cell culture medium at 37°C (10-20 MBq/mL) was monitored over 48 hours. All ^{111}In- and ^{161}Tb-labelled compounds showed excellent stability (>95% after 48h). Additionally, no change in the retention time was observed, strongly suggesting that the complex remains in the same chemical form throughout the experiment. The stability data of **[^{111}In]In-DOTAGA(TPP)-PSMA** and **[^{161}Tb]Tb-DOTAGA(TPP)-PSMA** are provided in **Figure 4.3**.

4.3.3 Cell binding and sub-cellular uptake

Cell binding studies were performed by incubating the ^{161}Tb-labelled PSMA with PC3-PIP, a transduced cell line with high PSMA expression, and PC3-flu, a control cell line without PSMA expression. **[^{161}Tb]Tb-DOTAGA(TPP)-PSMA** showed excellent binding to the PC3-PIP cells, with 15.9% ± 0.7% of the added activity bound to the surface of the cells after 5 minutes of incubation. Gradual increase in the binding was observed over the following 4 hours, with a maximum binding of 42.7% of the incubated activity being associated with the cells (**Figure 4.4**). A quarter of the incubated activity was found to be internalised in the cells, which is similar to literature data for [^{152}Tb]Tb-PSMA-617 (24). **[^{161}Tb]Tb-DOTA-PSMA** followed a similar trend, with 19.2% ± 1.0% of the activity surface bound after 5 minutes, and a maximum receptor-association of 74.5%, with a quarter of it internalised in the cell (17.4% ± 0.4%) after 4h of incubation, indicating that the TPP moiety does have a negative effect on the maximum receptor-association. This result in accordance with the results obtained by Paulo *et. al.*(20), where the TPP negatively impacted the PSMA receptor-association. No binding for **[^{161}Tb]Tb-DOTAGA(TPP)** was observed. This was expected as no PSMA binding moiety is present. In addition, all constructs showed no cell binding to PC3-flu, which is expected as no PSMA are present. Similar cell binding experiments were performed by C^2TN using ^{111}In-variants, and the results were congruent with the data obtained in this experiment.

2-phosponomethylpentanedioic acid, commonly known as 2-PMPA, is a non-structurally related organic compound with high affinity for PSMA. To assess the PSMA specific uptake of the ^{161}Tb-labelled

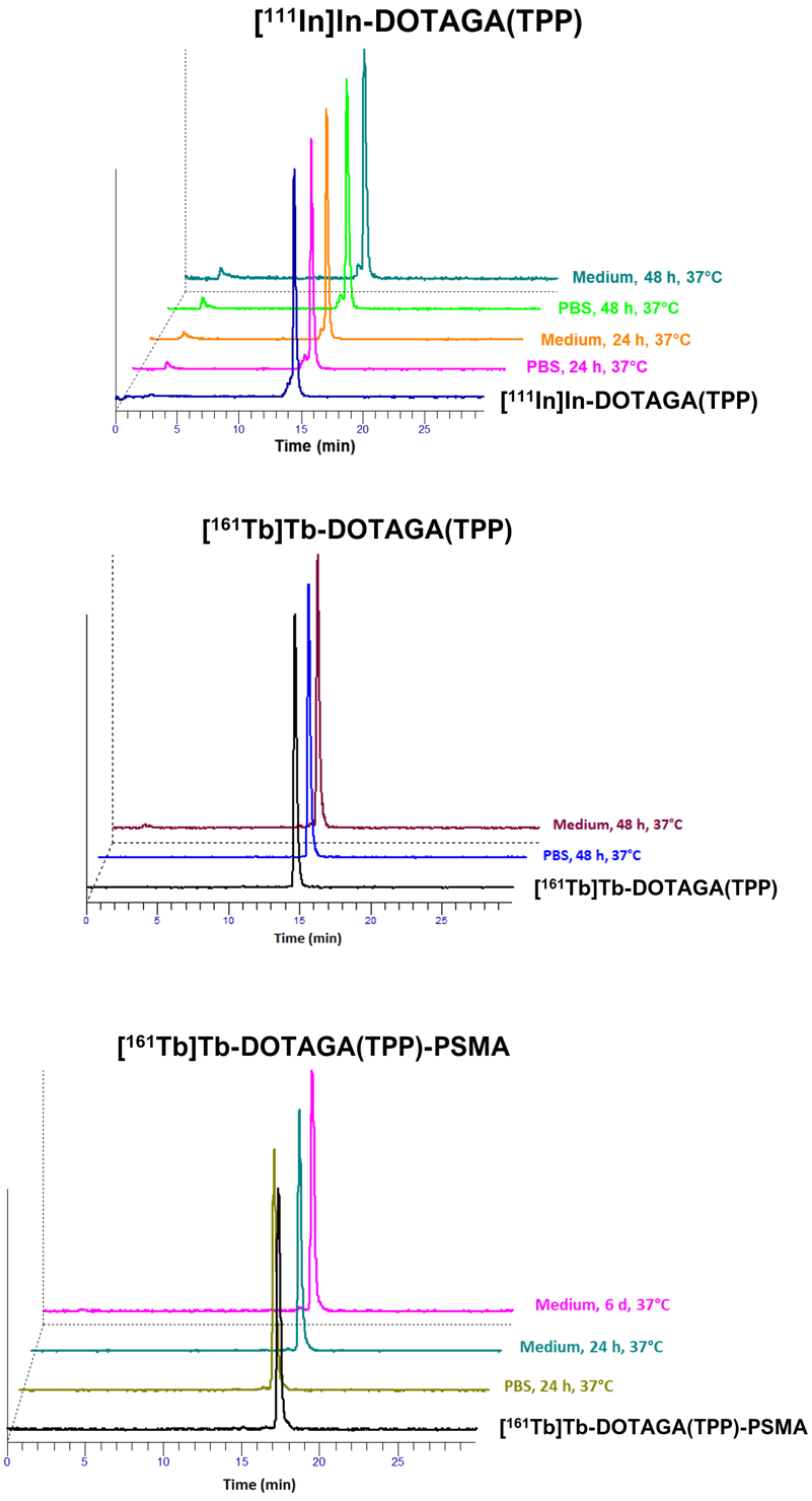


Figure 4.3. Stability of ^{111}In/^{161}Tb-labelled **DOTAGA(TPP)** and **[^{161}Tb]Tb- DOTAGA(TPP)-PSMA** in PBS and RPMI 1640 cell culture medium.

constructs, cells were incubated with 2-PMPA, in high molar excess to obtain a blocking effect, prior to incubation with the ^{161}Tb-labelled constructs. No binding of either ^{161}Tb-labelled PSMA construct was observed (**Figure 4.5**), a result which suggests the lack of non-specific binding of **[^{161}Tb]Tb-DOTAGA(TPP)-PSMA** and **[^{161}Tb]Tb-DOTA-PSMA** .

The TPP moiety has been associated with mitochondrial uptake, which is an essential design strategy in this project. Therefore, we were interested in the sub-cellular uptake of these constructs. The fractional uptake of the tracer of the internalised fraction at 1h and 3h exposure to the compound in the cytosol, mitochondria and nucleus was analysed. Small amounts of the activity were observed in the mitochondria after 1h, with only 3.0% ± 0.1% of **[^{161}Tb]Tb-DOTAGA(TPP)-PSMA** and 2.6% ± 0.1% of **[^{161}Tb]Tb-DOTA-PSMA** of the internalised activity found in the mitochondria (**Figure 4.6**). TPP has been proven as a mitochondrial targeting agent, therefore this low mitochondria binding was not anticipated. It has been reported that a high lipophilicity of the compound is required to diffuse over the mitochondrial membrane, the relatively high hydrophilicity of **[^{161}Tb]Tb-DOTAGA(TPP)-PSMA** may prevent uptake of the compound in the mitochondria (25). As this is an essential component for our therapeutic vision, a study investigating the improvement of mitochondria interaction is currently ongoing. In the cytosol region, between 8-11% of the activity was found after 1h incubation. Incubating for 3h sees most of the compound binding to the nucleus, with only 4-6% of the radioactivity in the cytosol. A large portion of the activity of was found in the nucleus after 1h for both **[^{161}Tb]Tb-DOTAGA(TPP)-PSMA** (79.0% ± 1.9% and **[^{161}Tb]Tb-DOTA-PSMA (**83.2% ± 0.9%). Incubating the compounds for an additional 2h saw 3-4% increase in the activity associated with the nucleus. However, these data are an overestimation of the nucleus uptake due to the large size of the nucleic matter, which could trap smaller organelles upon isolation (26). Additionally, we had no measurable means to evaluate the mitochondria during the experiment, which has shown to be a key component of mitochondria isolation experiments (26). This would negatively impact the mitochondrial uptake as well, as the data obtained would be an underestimate of mitochondria bound radioconjugate. To accurately determine the activity in the nucleus, alternative cell fractionation assays or non-isolation methods, such fluorescent microscopy and high-resolution emulsion autoradiography, needs to be explored.

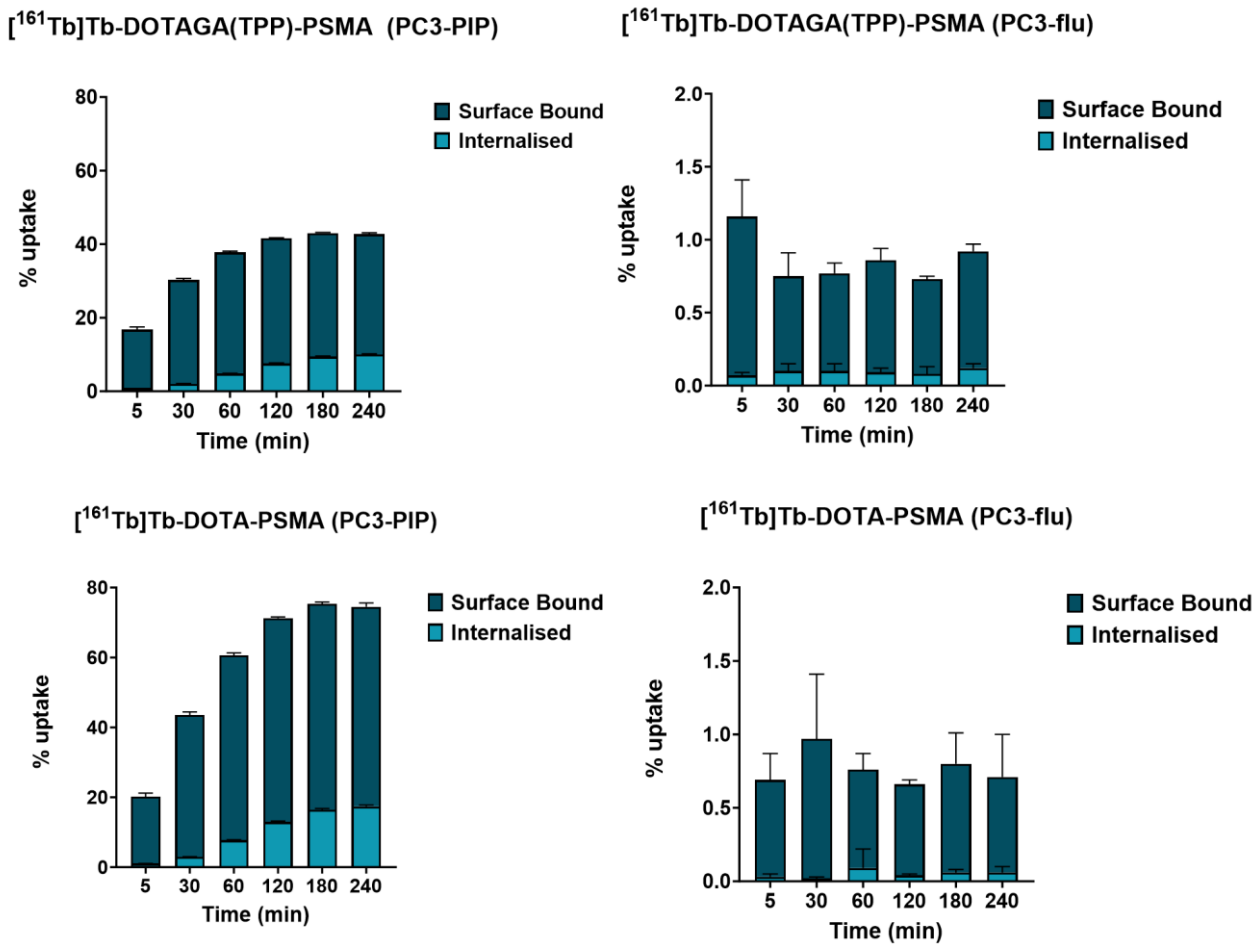


Figure 4.4 Cell binding of **[^{161}Tb]Tb-DOTA-PSMA** (below) and **[^{161}Tb]Tb-DOTAGA(TPP)-PSMA** (above) to PC3-PIP (left) and PC3-flu (right).

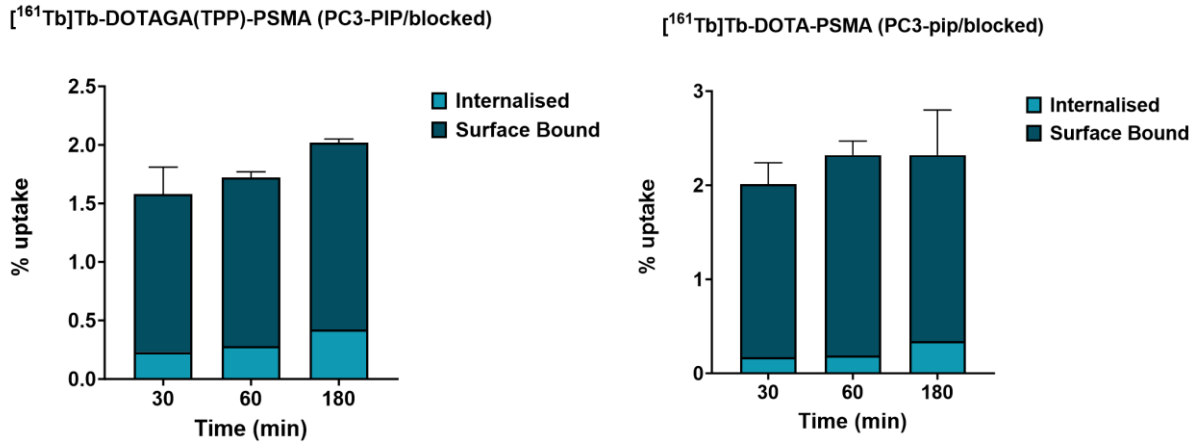


Figure 4.5 Cell binding of **[^{161}Tb]Tb-DOTA-PSMA** (left) and **[^{161}Tb]Tb-DOTAGA(TPP)-PSMA** (right) after pre-treatment with 2-PMPA, a known PSMA binding agent.

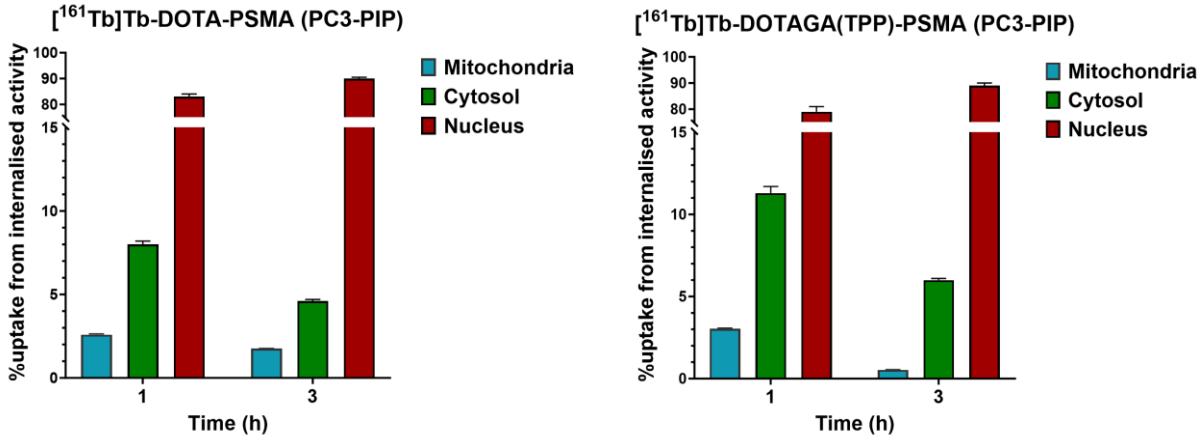


Figure 4.6 Fractional uptake of the internalised fraction of **[^{161}Tb]Tb-DOTA-PSMA** (left) and **[^{161}Tb]Tb-DOTAGA(TPP)-PSMA** (right).

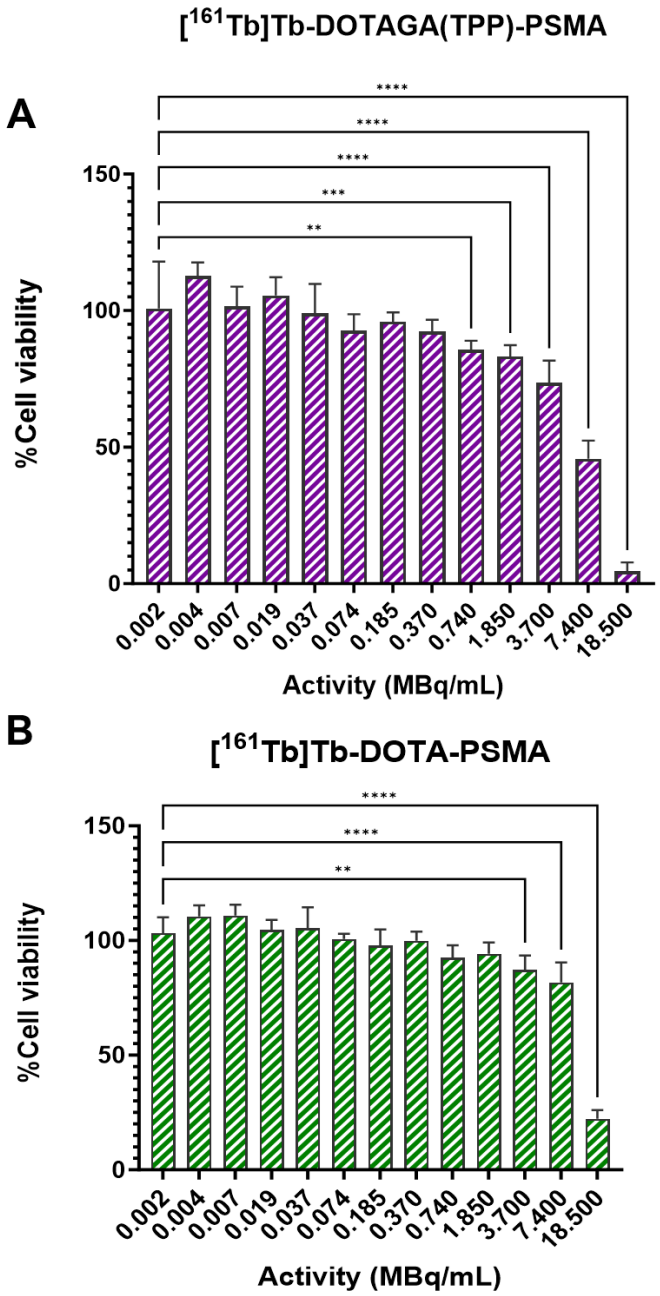
4.3.4 Cell viability

In vitro cell viability after modified PC3 cells was exposed to **[^{161}Tb]Tb-DOTA-PSMA** was evaluated using an MTT assay. Exposing cells for 4 hours to **[^{161}Tb]Tb-DOTA-PSMA** resulted in a activity concentration dependent decrease of cell viability (EC_{50} = 16.16 MBq/mL). After addition of 3.7 MBq/mL, cell viability was already significantly lower compared to baseline cells (87.0% ± 3.3%, P < 0.01). At the highest concentration applied (18.5 MBq/mL), cell viability was further reduced to 22.3% ± 3.8% compared to the baseline (P<0.001)(**Figure 4.7B**).

In addition, we evaluated the **[^{161}Tb]Tb-DOTAGA(TPP)-PSMA** (**Figure 4.7A**), which contains a TPP moiety, which was designed to increase accumulation of the ^{161}Tb source closer to the mitochondria. The addition of **[^{161}Tb]Tb-DOTAGA(TPP)-PSMA** resulted in a more pronounced effect on the cell viability (EC_{50} = 5.38 MBq/mL). Even at 0.74 MBq/mL**, [^{161}Tb]Tb-DOTAGA(TPP)-PSMA** resulted already in a significant decrease in cell viability (85.6%± 3.3%, P < 0.01), a fifth of the activity required for the non-TPP construct. At the highest activity concentration (18.5 MBq/ml), cell viability decreased to 4.5% ± 3.3% (P<0.001). The large difference (-5x) in the cytotoxic behaviour cannot be directly associated with mitochondria interaction, as our mitochondria uptake tests remain inconclusive.

4.3.5 Clonogenic Assay

Additionally, the effect on the clonogenic potential of PC3-PIP cells was evaluated after exposure to **[^{161}Tb]Tb-DOTA-PSMA**. Exposing the cells to **[^{161}Tb]Tb-DOTA-PSMA** for 4 hours resulted in a activity concentration-dependent decrease in the clonogenic potential (**Figure 4.8**). After addition of 0.37 MBq/mL, a significantly reduced survival fraction was observed (87.5 ± 2.8 %, P < 0.05) compared



MBq/mL	*P* between [^{161}Tb]Tb-DOTA-PSMA and [^{161}Tb]Tb-DOTAGA(TPP)-PSMA
0.00185	ns
0.0037	ns
0.0074	*
0.0185	ns
0.037	ns
0.074	*
0.185	ns
0.37	ns
0.74	ns
1.85	**
3.7	***
7.4	****
18.5	***

Figure 4.7 Cell viability as a function of activity of **[^{161}Tb]Tb-DOTAGA(TPP)-PSMA** (**A**) and **[^{161}Tb]Tb-DOTA-PSMA** (**B**).

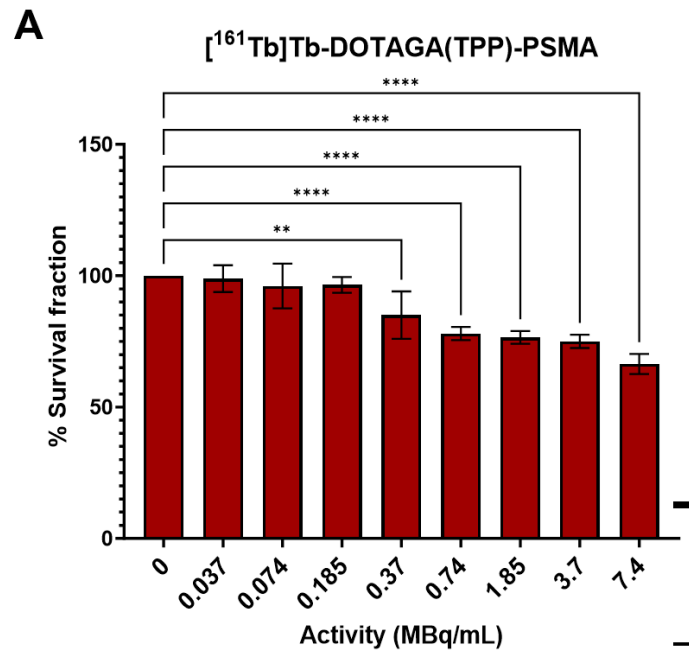
to baseline cells. At the highest concentration tested (7.4 MBq/mL), the clonogenic potential was reduced to 75.6 ± 2.1 % (P<0.001).

Analogous to this, we repeated the experiment using the mitochondria targeting **[^{161}Tb]Tb-DOTAGA(TPP)-PSMA** to ascertain if this targeting group makes a difference. The effect of the **[^{161}Tb]Tb-DOTAGA(TPP)-PSMA** was comparable to that of **[^{161}Tb]Tb-DOTA-PSMA**, with 0.37 MBq/mL needed for a significant decrease in the clonogenic potential (85.0% ± 9.0%, P < 0.01). At concentrations >0.74 MBq/mL of **[^{161}Tb]Tb-DOTAGA(TPP)-PSMA**, the survival fraction was observed to be less than 75%. At the highest concentration tested, the clonogenic potential was reduced to 66.4% ± 3.8% (P<0.001).

These data complements the data obtained in the cell viability tests, where exposure to **[^{161}Tb]Tb-DOTAGA(TPP)-PSMA** resulted in a significantly more potent effect on the cell viability at 0.74 MBq/mL (P<0.0001) and 3.7 MBq/mL (P<0.001). The results of the clonogenic assay can help ascertain whether or not the cells survive the treatment, which is different from cell viability studies, which only indicates the inhibition of cell proliferation. The data obtained suggest that once the cells are exposed to the **[^{161}Tb]Tb-DOTAGA(TPP)-PSMA** they cannot recover as well as they can when exposed to **[^{161}Tb]Tb-DOTA-PSMA.**

4.3.6 Mechanism of action

Further studies into the mechanism of action were performed. Apoptosis is the cell's natural pathway to death and can be induced by stress (27). During this process, an upregulation of caspase 3/7 is observed, which triggers a cell death event (27). High levels of caspase 3/7 were observed in treatments with **[^{161}Tb]Tb-DOTA-PSMA** at activity concentrations of 7.4 MBq/mL (**Figure 4.9).** At concentrations below 3.7 MBq/mL, the caspase 3/7 levels were below those induced by cisplatin (50 µM) treatment, a known apoptosis inducer (28). No significant increase in the Caspase 3/7 levels was observed with increasing in the activity concentration of **[^{161}Tb]Tb-DOTAGA(TPP)-PSMA** (**Figure 4.9**), suggesting that **[^{161}Tb]Tb-DOTAGA(TPP)-PSMA** does not induce apoptosis.



MBq/mL	*P* between [161Tb]Tb-DOTAGA(TPP)-PSMA and [161Tb]Tb-DOTA-PSMA
0	ns
0.037	ns
0.074	ns
0.185	ns
0.37	ns
0.74	***
1.85	ns
3.7	***
7.4	*

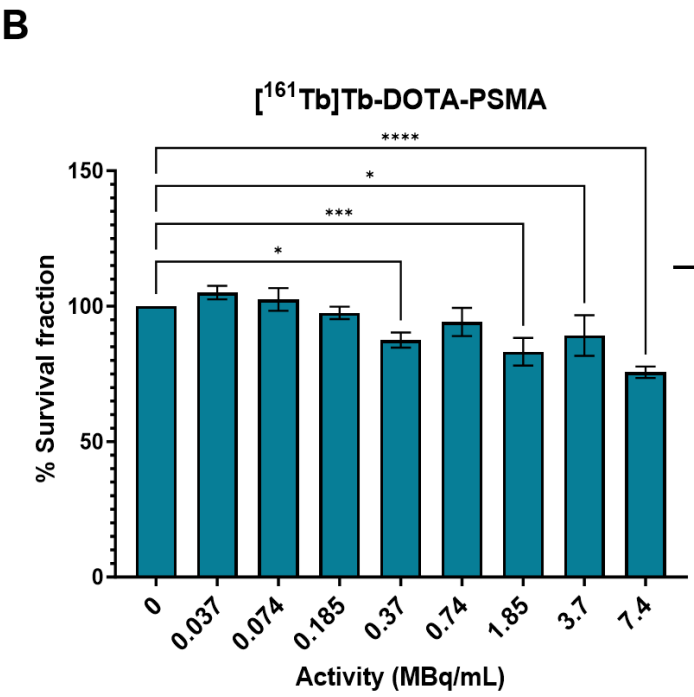


Figure 4.8 Survival fraction as a function of activity of **[^{161}Tb]Tb-DOTAGA(TPP)-PSMA** (A) and **[^{161}Tb]Tb-DOTA-PSMA** (B).

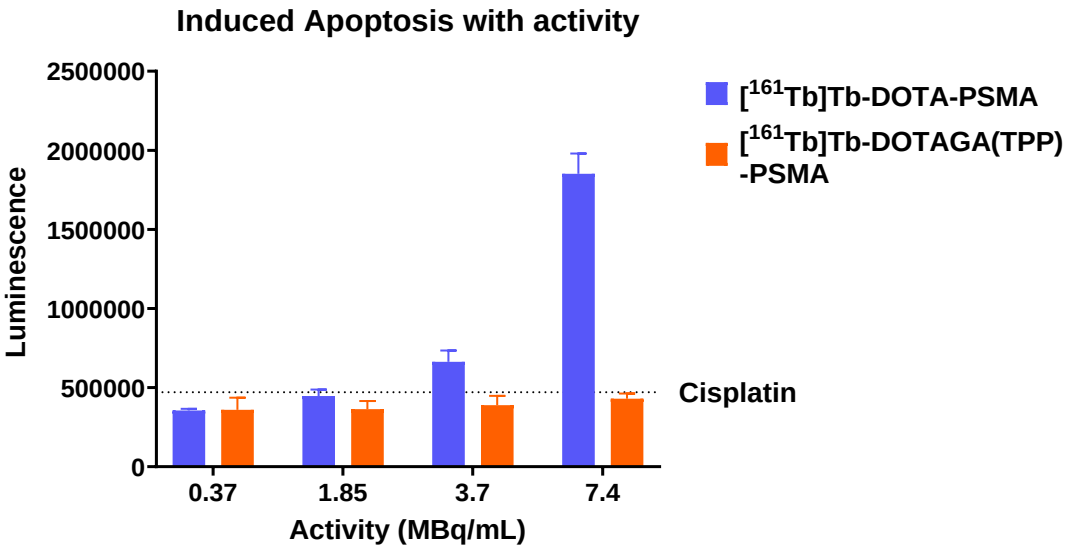


Figure 4.9 Upregulation of Caspase 3/7 after exposure to **[^{161}Tb]Tb-DOTA-PSMA** (blue) and **[^{161}Tb]Tb-DOTAGA(TPP)-PSMA** (orange). As reference, 50μM of cisplatin, a metal-based chemotherapeutic known for upregulating caspase 3/7, is displayed using a dotted-line.

Another potential cell death pathway that was investigated is mitochondrial dysfunction. This was quantified using an assay (mitochondria ToxGlo®) that monitors the drop in ATP levels in the cells, which indicates if the compound has mitochondrial toxicity. In addition, a cytotoxicity study was done in parallel to determine if the drop in ATP levels was due to necrosis or mitochondria dysfunction. An inverse correlation between the activity of the compounds and ATP levels was observed in the assay for both **[^{161}Tb]Tb-DOTA-PSMA** and **[^{161}Tb]Tb-DOTAGA(TPP)-PSMA** (**Figure 4.10**). This result was expected since both compounds had shown to affect the cell viability at the tested concentrations. Conversely, an increase in cytotoxicity parameters was observed, indicating that the cells are dying from exposure to the radiation dose. This synergic effect is indicative of cell necrosis, as the drop in ATP levels is not due to mitochondria dysfunction, but rather due to cells dying. This result is expected as we observed minimum activity bound to the mitochondria when internalised. Therefore, we can expect a minimum effect of the conversion and Auger electrons on the mitochondria and following a more traditional β^- mechanism of action. Furthermore, a similar result was observed by Paulo *et al.* whereby [^{99m}Tc]-TPP-BBN generated significantly higher H2AX foci, a biomarker for double-stranded DNA breaks, than the nucleus targeting [^{99m}Tc]-AO-BBN, which showed signs of repairable damage to cells (19). To date, the reason for the increased cytotoxicity of **[^{161}Tb]Tb-DOTAGA(TPP)-PSMA** could not be determined. One plausible reason could be the effect of the TPP moiety, as it has been shown to interact with various proteins which disturb ordinary cell activity (25,29). Therefore, quantification of the internalised radiopharmaceutical, cytotoxicity of the cold complex and H2Ax foci is imperative for understanding the effect on cell viability.

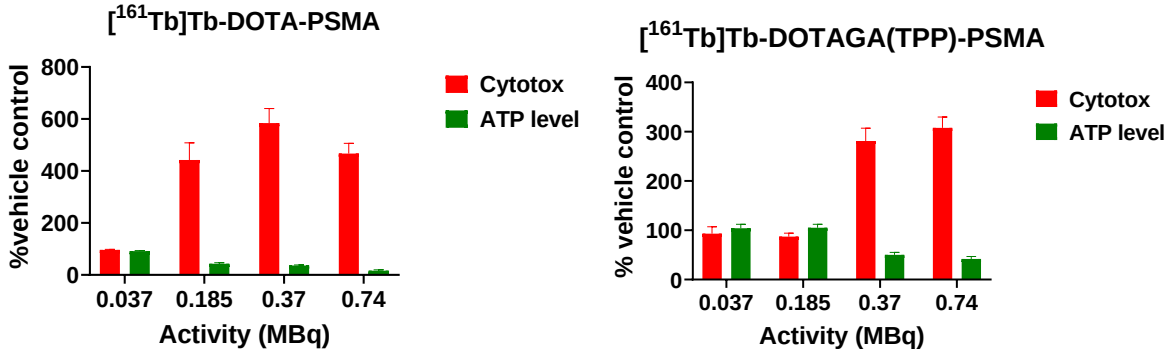


Figure 4.10 Cytotoxicity and ATP concentrations post exposure to **[^{161}Tb]Tb-DOTA-PSMA** (left) and **[^{161}Tb]Tb-DOTAGA(TPP)-PSMA** (right).

4.3.7 µSPECT/CT imaging

µSPECT/CT scans after injection of ^{111}In-labelled PSMA constructs were performed on tumour-bearing mice to assess if the TPP moiety had any major influence on the pharmacokinetics and tumour accumulation of the novel constructs. Due to the complications with µSPECT ^{161}Tb scanning (low resolution images, gamma vs lead scatter energy differentiation, etc.), we opted to use ^{111}In for better image resolution. In addition, cell binding studies with ^{111}In-variants showed no change in the binding profile, therefore receptor binding of the ^{161}Tb and ^{111}In conjugates can be assumed to be similar. However, it is important to note that the biodistributions of these conjugates can be different, and therefore ^{161}Tb-conjugates should be tested in the future. Static images were recorded after 1 and 24 hours p.i. These images were collected to assess the biodistribution of the constructs *in vivo*, with key emphasis on the tumour uptake and clearance pathway of the tracer. To ascertain the specific uptake of the construct, a dual-tumour model, containing one tumour (left flank) with PC3-flu and one tumour (right flank) with PC3-PIP, was used.

The ^{111}In-labelled PSMA-617 containing constructs were shown to rapidly concentrate in the PC3-PIP tumour 1h p.i, with **[^{111}In]In-DOTA-PSMA** and **[^{111}In]In-DOTAGA(TPP)-PSMA** shown to have comparable uptake to each other (SUV_{1hr}: 1.59 ± 0.86 g/mL and 1.39 ± 0.60 g/mL, respectively) (**Figure 4.11**). In addition, slow washout of these complexes was observed, with SUV values of >1.0 g/mL of the ^{111}In-labelled constructs (SUV_{24h}: **[^{111}In]In-DOTA-PSMA** = 1.14 ± 0.30 g/mL; **[^{111}In]In-DOTAGA(TPP)-PSMA** = 1.04 ± 0.34 g/mL) still present in the tumour 24h p.i.. No uptake was observed in the left tumour (PC3-flu), which was expected as no binding to PC3-flu cells of the constructs was observed *in vitro* (**Figure 4.11**). **[^{111}In]In-DOTAGA(TPP)** showed no uptake in either tumour for the duration of the experiment, confirming that the PSMA-binding group is indeed essential for specific uptake.

Renal clearance was determined to be the excretory pathway of all constructs. Nephrotoxicity is a major concern for therapeutic radiopharmaceuticals, as kidney damage is irreversible and can lead to long

lasting renal treatments (5,8). As many PSMA-targeting compounds have shown renal clearance as the major excretory pathway (7,24,30,31), we expect our compounds to exhibit similar behaviour. Moreover, hydrophilic compounds are prone to follow renal excretion, where lipophilic compounds follow hepatic clearance (32). In our study, compounds followed the same pathway as known PSMA radiopharmaceuticals, which was an expected result as **[^{111}In]In-DOTA-PSMA** was found to be highly hydrophilic (logP = -3.56). After 1h, the kidney SUV value for **[^{111}In]In-DOTAGA(TPP)-PSMA** construct was 2.36 ± 0.73 g/mL, which is ~1.7x the activity concentration in the tumour (**Table 4.2**). For **[^{111}In]In-DOTA-PSMA**, an SUV value of only 0.65 ± 0.11 g/mL was observed in the kidneys. Though this might suggest that the TPP moiety plays a role in the kidney retention, further tests are currently performed to investigate this matter. Washout of the activity from the kidney was observed, resulting in lower kidney SUV values after 24 hours p.i. (SUV_{24h}: **[^{111}In]In-DOTA-PSMA** = 0.04 ± 0.01 g/mL; **[^{111}In]In-DOTAGA(TPP)-PSMA** = 0.97 ± 0.15 g/mL). This high retention is a concern for ^{161}Tb derivatives of these constructs, as nephrotoxicity is a major hurdle for clinical translation. It should be noted that few studies have been conducted investigating the nephrotoxicity of hybrid therapeutic isotopes, such ^{161}Tb. Moreover, the only reported study on nephrotoxicity was performed by Muller *et al.*, where no conclusions could be drawn from the added effect from the conversion/Auger electrons (33). However, it can be postulated that negligible renal damage occurs from the conversion/Auger electrons, as shown in a clinical study with [^{111}In]In-octreotide, where high renal dose did not impair any kidney function (34). The co-registered μSPECT/CT MIP images are provided in **Figure 4.11**.

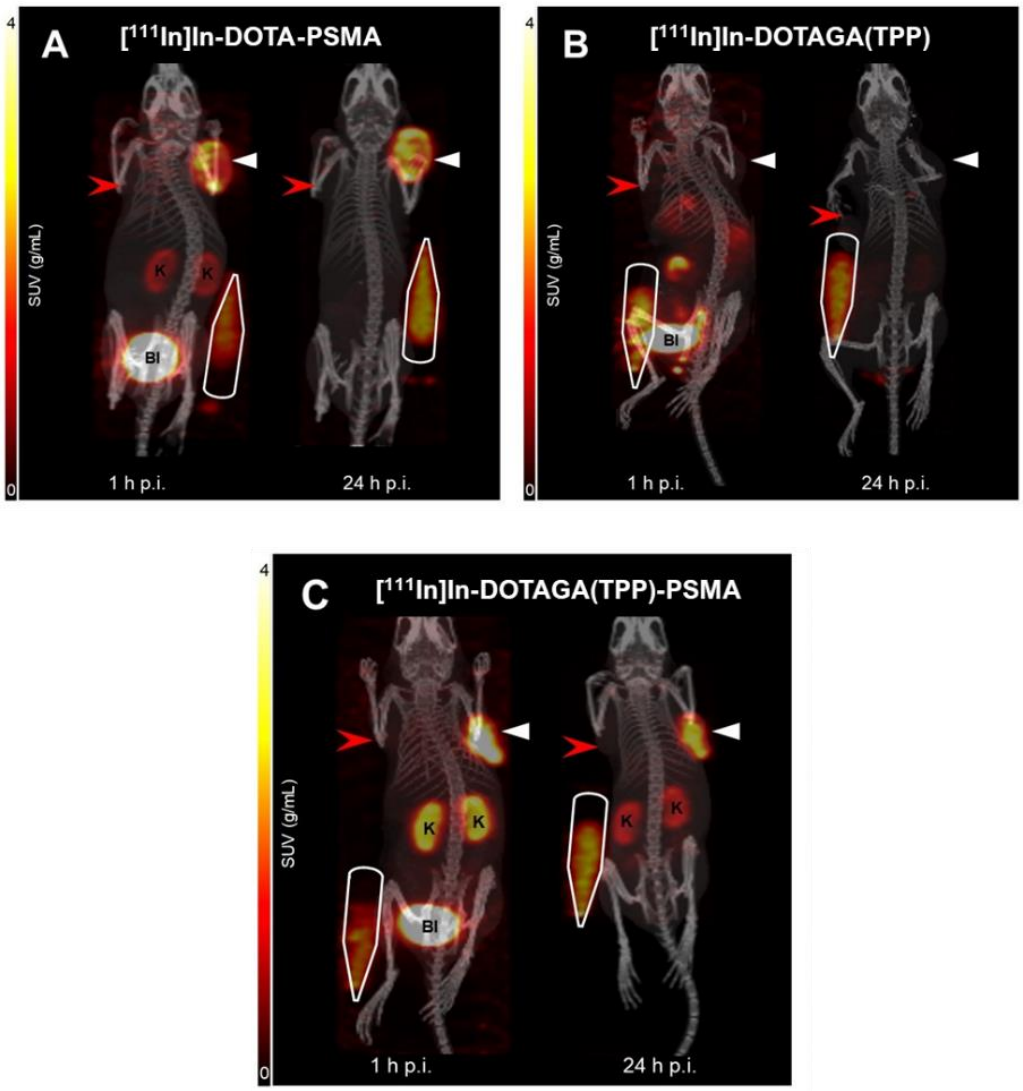


Figure 4.11 Maximum intensity projection μSPECT/CT after 1 hour and 24 hour p.i. of **[^{111}In]In-DOTAGA(TPP), [^{111}In]In-DOTA-PSMA** and **[^{111}In]In-DOTAGA(TPP)-PSMA**. PSMA-positive tumours (PC3-PIP) and PSMA-negative (PSMA-flu) are indicated with white and red arrows, respectively. Kidneys are indicated by 'KI' and bladder by 'Bl'. Vial (left of the left hindleg) is used as a standard for SUV estimation.

Table 4.2. Estimated SUV values (g/mL) of tumour and kidney uptake of ^{111}In-labelled complexes in tumour mice.

	1h			24h		
	Kidneys	Tumour (flu)	Tumour (PIP)	Kidneys	Tumour (flu)	Tumour (PIP)
[^{111}In]In-DOTAGA(TPP)	0.67 ± 0.73	0.06 ± 0.04	0.07 ± 0.86	0.12 ± 0.15	0.01 ± 0.05	0.01 ± 0.35
[^{111}In]In-DOTA-PSMA	0.65 ± 0.11	0.14 ± 0.05	1.39 ± 0.6	0.04 ± 0.01	0.08 ± 0.05	1.14 ± 0.3
[^{111}In]In-DOTAGA(TPP)-PSMA	2.36 ± 0.73	0.2 ± 0.045	1.59 ± 0.86	0.97 ± 0.15	0.1 ± 0.05	1.04 ± 0.35

4.4 Conclusion

This study focussed on the incorporation of TPP, a mitochondrial targeting agent, with ^{111}In/^{161}Tb-labelled PSMA constructs for conversion/Auger therapy. Radiolabelling of PSMA constructs with ^{111}In and ^{161}Tb was successful and the labelled complexes remained stable in culture medium. As a first step, we investigated the mitochondrial uptake and the effect on cell viability. Subcellular uptake studies showed minimal uptake in the mitochondria, regardless of the addition of the TPP moiety. Research into introducing cleavable linking systems (e.g. Tri-glycine linker) to further increase mitochondria uptake is currently being investigated. However, the incorporation of TPP had a pronounced effect on the cytotoxicity of the **[^{161}Tb]Tb-DOTAGA(TPP)-PSMA** construct. This effect on the viability could be due to a different mechanism of action, as it was observed by Paulo *et. al.* (19). Though we did observe a decrease in cell viability, this was not a result of mitochondrial damage from the low energy electrons (conversion and Auger) emitted from the ^{161}Tb. More work needs to be completed to fully understand the mechanism of action of the complex carrying the TPP moiety. Constructs were excreted through the renal tract with **[^{161}Tb]Tb-DOTA-PSMA** excreting quickly post injection, which is a favourable pharmacokinetic parameter for imaging and limiting off-target radiation dose for therapy. In contrast, the **[^{161}Tb]Tb-DOTAGA(TPP)-PSMA** was retained in the kidney after 24 hours p.i., calling for concern in further pre-clinical applications. Minute adjustments to the final complex are currently being investigated to mitigate the high kidney retention, which can be a concern when ^{161}Tb-labelled constructs are used, and to increase mitochondria uptake for a more effective targeted conversion/Auger therapy.

4.5 Funding

This research was funded by the Precision and Intelligent Systems in Medicine Research Partnership (PRISMAP) European collaboration (project number: WP12) and Research Foundation – Flanders (FWO)-SBO project: Terbium Isotopes for Medical Applications in Flanders (Tb-IRMA-V).

4.6 Ethical Statement

Animal experiments were conducted according to the Belgian code of practice for the care and the use of animals, after approval from the animal ethics committee of KU Leuven (P112/2020/038).

4.7 Acknowledgements

The authors would like to acknowledge the contributions of Julie Cornelis (KU Leuven, Leuven, Belgium), Ana Rita Julião (IST, Lisbon, Portugal) and Caterina Pinto (IST, Lisbon, Portugal) for their contributions to the research reported.

4.8 References

1. Mishiro K, Hanaoka H, Yamaguchi A, Ogawa K. Radiotheranostics with radiolanthanides: Design, development strategies, and medical applications. *Coord Chem Rev* (2019) **383**:104–131. doi:10.1016/j.ccr.2018.12.005

2. Weber WA, Czernin J, Anderson CJ, Badawi RD, Barthel H, Bengel F, Bodei L, Buvat I, DiCarli M, Graham MM, et al. The future of nuclear medicine, molecular imaging, and theranostics. *J Nucl Med* (2020) **61**:263S-272S. doi:10.2967/jnumed.120.254532

3. Morgenstern A, Apostolidis C, Kratochwil C, Sathekge M, Krolicki L, Bruchertseifer F. An Overview of Targeted Alpha Therapy with ^{225}Actinium and ^{213}Bismuth . *Curr Radiopharm* (2018) **11**:200–208. doi:10.2174/1874471011666180502104524

4. Chang SS. Overview of prostate-specific membrane antigen. *Rev Urol* (2004) **6 Suppl 10**:S13-8. Available at: http://www.ncbi.nlm.nih.gov/pubmed/16985927%0Ahttp://www.pubmedcentral.nih.gov/articlerender.fcgi?artid=PMC1472940

5. Emmett L, Willowson K, Violet J, Shin J, Blanksby A, Lee J. Lutetium 177 PSMA radionuclide therapy for men with prostate cancer: a review of the current literature and discussion of practical aspects of therapy. *J Med Radiat Sci* (2017) **64**:52–60. doi:10.1002/jmrs.227

6. Rahbar K, Essler M, Pabst KM, Eiber M, Fougère C la, Prasad V, Rassek P, Hasa E, Dittmann H, Bundschuh RA, et al. Safety and Survival Outcomes of ^{177} Lu-Prostate-Specific Membrane Antigen Therapy in Patients with Metastatic Castration-Resistant Prostate Cancer with Prior 223 Ra treatment: The RALU Study. *J Nucl Med* (2023) **64**:574–578. doi:10.2967/jnumed.122.264456

7. Sartor O, Herrmann K. Prostate Cancer Treatment: ^{177}Lu-PSMA-617 Considerations, Concepts, and Limitations. *J Nucl Med* (2022) **63**:823–829. doi:10.2967/jnumed.121.262413

8. Ma J, Li L, Liao T, Gong W, Zhang C. Efficacy and Safety of ^{225}Ac-PSMA-617-Targeted Alpha Therapy in Metastatic Castration-Resistant Prostate Cancer: A Systematic Review and Meta-Analysis. *Front Oncol* (2022) **12**: doi:10.3389/fonc.2022.796657

9. Rosar F, Maus S, Schaefer-Schuler A, Burgard C, Khreish F, Ezziddin S. New Horizons in Radioligand Therapy. *Clin Nucl Med* (2023) **48**:433–434. doi:10.1097/RLU.0000000000004589

10. Dekempeneer Y, Caveliers V, Ooms M, Maertens D, Gysemans M, Lahoutte T, Xavier C, Lecocq Q, Maes K, Covens P, et al. Therapeutic Efficacy of ^{213}Bi-labeled sdAbs in a Preclinical Model of Ovarian Cancer. *Mol Pharm* (2020) **17**:3553–3566. doi:10.1021/acs.molpharmaceut.0c00580

11. Pruszynski M, D'Huyvetter M, Bruchertseifer F, Morgenstern A, Lahoutte T. Evaluation of an

Anti-HER2 Nanobody Labeled with ^{225}Ac for Targeted α-Particle Therapy of Cancer. *Mol Pharm* (2018) **15**:1457–1466. doi:10.1021/acs.molpharmaceut.7b00985

12. Ku A, Facca VJ, Cai Z, Reilly RM. Auger electrons for cancer therapy – a review. *EJNMMI Radiopharm Chem* (2019) **4**: doi:10.1186/s41181-019-0075-2

13. Müller C, Umbricht CA, Gracheva N, Tschan VJ, Pellegrini G, Bernhardt P, Zeevaart JR, Köster U, Schibli R, van der Meulen NP. Terbium-161 for PSMA-targeted radionuclide therapy of prostate cancer. *Eur J Nucl Med Mol Imaging* (2019) **46**:1919–1930. doi:10.1007/s00259-019-04345-0

14. Gracheva N, Müller C, Talip Z, Heinitz S, Köster U, Zeevaart JR, Vögele A, Schibli R, van der Meulen NP. Production and characterization of no-carrier-added ^{161}Tb as an alternative to the clinically-applied ^{177}Lu for radionuclide therapy. *EJNMMI Radiopharm Chem* (2019) **4**:12. doi:10.1186/s41181-019-0063-6

15. Ballinger JR. Theranostics and precision medicine special feature: Review Article Theranostic radiopharmaceuticals: established agents in current use. *Br J Radiol* (2018) **91**:20170969. Available at: http://europepmc.org/backend/ptpmcrender.fcgi?accid=PMC6475961&blobtype=pdf

16. Müller C, Reber J, Haller S, Dorrer H, Bernhardt P, Zhernosekov K, Türler A, Schibli R. Direct in vitro and in vivo comparison of ^{161}Tb and ^{177}Lu using a tumour-targeting folate conjugate. *Eur J Nucl Med Mol Imaging* (2014) **41**:476–485. doi:10.1007/s00259-013-2563-z

17. Borgna F, Haller S, Rodriguez JMM, Ginj M, Grundler P V., Zeevaart JR, Köster U, Schibli R, van der Meulen NP, Müller C. Combination of terbium-161 with somatostatin receptor antagonists—a potential paradigm shift for the treatment of neuroendocrine neoplasms. *Eur J Nucl Med Mol Imaging* (2022) **49**:1113–1126. doi:10.1007/s00259-021-05564-0

18. Pereira E, Do Quental L, Palma E, Oliveira MC, Mendes F, Raposinho P, Correia I, Lavrado J, Di Maria S, Belchior A, et al. Evaluation of Acridine Orange Derivatives as DNA-Targeted Radiopharmaceuticals for Auger Therapy: Influence of the Radionuclide and Distance to DNA. *Sci Rep* (2017) **7**:1–16. doi:10.1038/srep42544

19. Fernandes C, Palma E, Silva F, Belchior A, Pinto CIG, Guerreiro JF, Botelho HM, Mendes F, Raposinho P, Paulo A. Searching for a Paradigm Shift in Auger-Electron Cancer Therapy with Tumor-Specific Radiopeptides Targeting the Mitochondria and/or the Cell Nucleus. *Int J Mol Sci* (2022) **23**: doi:10.3390/ijms23137238

20. Santos JF, Braz MT, Raposinho P, Cleeren F, Cassells I, Leekens S, Cawthorne C, Mendes F, Fernandes C, Paulo A. Synthesis and Preclinical Evaluation of PSMA-Targeted ^{111}In-Radioconjugates Containing a Mitochondria-Tropic Triphenylphosphonium Carrier. *Mol Pharm* (2023) doi:10.1021/acs.molpharmaceut.3c00787

21. Cassells I, Ahenkorah S, Burgoyne AR, Van de Voorde M, Deroose CM, Cardinaels T, Bormans G, Ooms M, Cleeren F. Radiolabeling of Human Serum Albumin With Terbium-161 Using Mild Conditions and Evaluation of in vivo Stability. *Front Med* (2021) **8**:1–12. doi:10.3389/fmed.2021.675122

22. Troutner DE, Volkert WA, Hoffman TJ, Holmes RA. A neutral lipophilic complex of ^{99m}Tc with a multidentate amine oxime. *Int J Appl Radiat Isot* (1984) **35**:467–470. doi:10.1016/0020-708X(84)90165-0

23. Brix N, Samaga D, Hennel R, Gehr K, Zitzelsberger H, Lauber K. The clonogenic assay: robustness of plating efficiency-based analysis is strongly compromised by cellular cooperation. *Radiat Oncol* (2020) **15**:1–12. doi:10.1186/s13014-020-01697-y

24. Müller C, Singh A, Umbricht CA, Kulkarni HR, Johnston K, Benešová M, Senftleben S, Müller D, Vermeulen C, Schibli R, et al. Preclinical investigations and first-in-human application of ^{152}Tb-PSMA-617 for PET/CT imaging of prostate cancer. *EJNMMI Res* (2019) **9**:1–10. doi:10.1186/s13550-019-0538-1

25. Zielonka J, Joseph J, Sikora A, Hardy M, Ouari O, Vasquez-Vivar J, Cheng G, Lopez M, Kalyanaraman B. Mitochondria-Targeted Triphenylphosphonium-Based Compounds: Syntheses, Mechanisms of Action, and Therapeutic and Diagnostic Applications. *Chem Rev* (2017) **117**:10043–10120. doi:10.1021/acs.chemrev.7b00042

26. Liao P-CC, Bergamini C, Fato R, Pon LA, Pallotti F. "Isolation of mitochondria from cells and tissues," in *Methods in Cell Biology*, 3–31. doi:10.1016/bs.mcb.2019.10.002

27. Shim MK, Yoon HY, Lee S, Jo MK, Park J, Kim JH, Jeong SY, Kwon IC, Kim K. Caspase-3/-7-Specific Metabolic Precursor for Bioorthogonal Tracking of Tumor Apoptosis. *Sci Rep* (2017) **7**:1–15. doi:10.1038/s41598-017-16653-2

28. Reedijk J. Platinum Anticancer Coordination Compounds: Study of DNA Binding Inspires New Drug Design. *Eur J Inorg Chem* (2009) **2009**:1303–1312. doi:10.1002/ejic.200900054

29. Ozsvari B, Sotgia F, Lisanti MP. Exploiting mitochondrial targeting signal(s), TPP and bis-TPP, for eradicating cancer stem cells (CSCs). *Aging (Albany NY)* (2018) **10**:230–240. doi:10.18632/aging.101384

30. Umbricht CA, Benešová M, Schmid RM, Türler A, Schibli R, van der Meulen NP, Müller C. ^{44}Sc-PSMA-617 for radiotheragnostics in tandem with ^{177}Lu-PSMA-617—preclinical investigations in comparison with ^{68}Ga-PSMA-11 and ^{68}Ga-PSMA-617. *EJNMMI Res* (2017) **7**:9. doi:10.1186/s13550-017-0257-4

31. Roberts MJ, Maurer T, Perera M, Eiber M, Hope TA, Ost P, Siva S, Hofman MS, Murphy DG, Emmett L, et al. Using PSMA imaging for prognostication in localized and advanced prostate cancer. *Nat Rev Urol* (2023) **20**:23–47. doi:10.1038/s41585-022-00670-6

32. Tafreshi NK, Kil H, Pandya DN, Tichacek CJ, Doligalski ML, Budzevich MM, Delva NC, Langsen ML, Vallas JA, Boulware DC, et al. Lipophilicity Determines Routes of Uptake and Clearance, and Toxicity of an Alpha-Particle-Emitting Peptide Receptor Radiotherapy. *ACS Pharmacol Transl Sci* (2021) **4**:953–965. doi:10.1021/acsptsci.1c00035

33. Haller S, Pellegrini G, Vermeulen C, van der Meulen NP, Köster U, Bernhardt P, Schibli R, Müller C. Contribution of Auger/conversion electrons to renal side effects after radionuclide therapy: preclinical comparison of ^{161}Tb-folate and ^{177}Lu-folate. *EJNMMI Res* (2016) **6**:1–11. doi:10.1186/s13550-016-0171-1

34. Valkema R, De Jong M, Bakker WH, Breeman WAP, Kooij PPM, Lugtenburg PJ, de Jong FH, Christiansen A, Kam BLR, de Herder WW, et al. Phase I study of peptide receptor radionuclide therapy with [^{111}In-DTPA0]octreotide: The Rotterdam experience. *Semin Nucl Med* (2002) **32**:110–122. doi:10.1053/snuc/2002.31025

Chapter 5 – General discussion & prospects

Terbium-labelled Radiopharmaceuticals: A perspective of the advances towards routine clinical application

5.1 General Discussion

Advances of the use of terbium radionuclides

Radiopharmaceuticals have become compelling non-invasive clinical tools for routine diagnosis and treatment for various diseases in the past three decades. Additionally, for radiopharmaceuticals which are intravenously administered to the patient, radionuclides with different decay modes/emissions can be used depending on if diagnostic or therapeutic applications are desired. Terbium has four medically interesting isotopes which cover all the possible diagnostic and therapeutic applications commonly used in clinics today. As terbium chemistry is remarkably similar to other lanthanide chemistry, the development pathway is often similar to that of other radiolanthanides, particularly ^{177}Lu. Though the terbium family is a relatively new series of isotopes that received attention, substantial advance in the production, radiopharmaceutical and clinical avenues have been made over the last few years (**Figure 5.1**). Since the proposition of the terbium quadruplet in 2012, terbium has become a topic at the forefront of theragnostics in nuclear medicine. Currently, few theragnostic pairs exist and are used in clinics. The main advantage of the terbium isotope series is that the development of a single radiopharmaceutical can be translated to all facets of the nuclear medicine space, namely diagnostic application in SPECT and PET imaging, and therapeutic avenues in α, β^- and Auger therapy. In 2011, Lehenberger reported the production of ^{161}Tb through neutron bombardment of enriched [^{160}Gd]GdO_3 (1), which can produce 12-15 GBq per mg of target material; enough for multiple clinical doses for patients. More recently, ^{161}Tb is produced in much larger quantities (50-150 GBq) at various institutions such as NTP Radioisotopes (South Africa), and SCK CEN (Belgium). A recent collaboration between SCK CEN and Terthera (The Netherlands) even resulted in the first commercial supply of [^{161}Tb]$TbCl_3$. For ^{155}Tb, highly isotopically pure ^{155}Tb was produced from high energy protons (480 MeV) bombarding with a tantalum target, which was mass separated and deposited on Zn/Au foils, which was successfully recovered through chemical separation (2). However, facilities with such cyclotrons are far-and-few between, with transport of these targets posing a potential challenge. To overcome this barrier, the production of ^{155}Tb was investigated by irradiating enriched $^{155}GdO_3$ foils with accelerated protons from a medical PET cyclotron (18 MeV), which is successfully converted to ^{155}Tb (3), supporting clinical application of terbium. With these advances in the field, it might be possible to use terbium in a theragnostic approach in clinics.

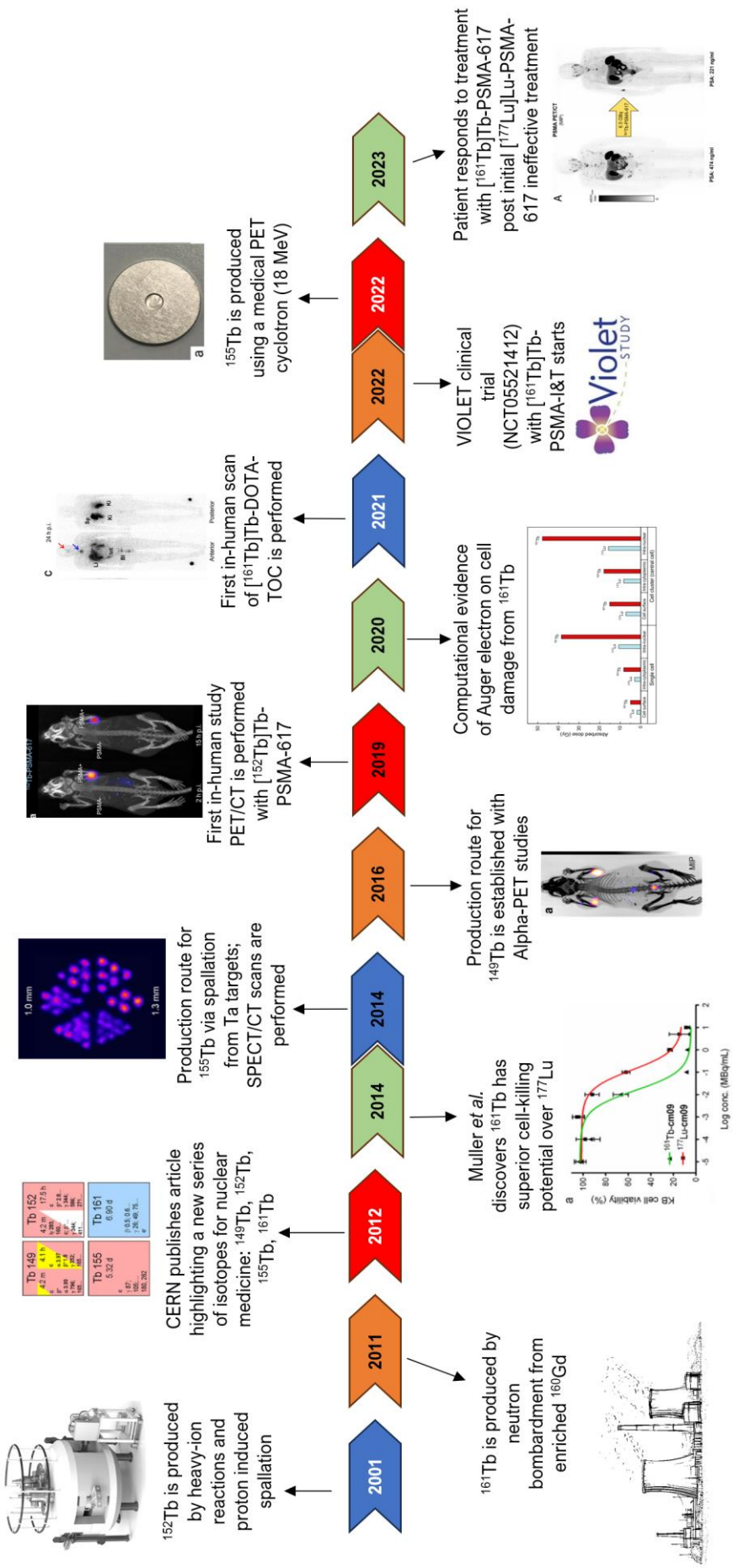


Figure 5.1. A roadmap showing some of the most significant advances of terbium isotopes over the last 23 years (3–12).

Given the excellent production pathway of ^{161}Tb, most of the developmental work with these radionuclides have been completed using ^{161}Tb. Additionally, because ^{161}Tb is a lanthanide with mainly decays via β^-, ^{161}Tb often follows a similar trajectory as ^{177}Lu, which has become a staple for β^- therapy. Hence, of the successful radiopharmaceuticals labelled with terbium isotopes, there are few which are not targeting PSMA (prostate specific membrane antigen) and somatostatin, limiting the reach of the potential of terbium isotopes in the field. One way to increase this reach is to use other carrier molecules such as antibodies or antibody-fragments. Antibodies and antibody-fragments are great carrier groups for targeted therapy and have mostly high affinity and selectivity towards their target. However, the implementation of biomolecules as carriers in radiopharmaceutical research presents a few challenges, meaning that very few radiolanthanide / biomolecule combinations have been researched (13). The current labelling conditions for radiolanthanides make use of temperatures more than 80 °C to ensure rapid labelling and to overcome the energy barrier for the radiometal to enter the rigid ligand core. These high temperatures often exceed the degradation/denaturation temperature limit of proteins. Also, the use of organic solvents can lead to protein denaturing, in turn resulting in a loss of affinity for the target receptor. Therefore, more gentle methods are needed to replace these harsh radiolabelling conditions, providing compatibility with biological carriers.

In our study, we aimed to address two major challenges associated with terbium radiolabelling of protein-based carriers: 1) harsh radiolabelling conditions, and 2) the stability of the radioconjugates *in vivo*. These are two very important aspects that need to be addressed to achieve advances in the field. Prior to this investigation, and to the best of our knowledge, only one case of biological radiolabelling with ^{161}Tb was investigated, whereby the radiolabelling was not quantitative (14). This study explored the development of an optimised protocol using ^{161}Tb, the most readily available isotope in the terbium family of radioisotopes. Additionally, ^{161}Tb decays through β^- decay with Auger electron emission for therapeutic application and one diagnostic decay mode (γ), therefore it was chosen for incorporation in this preclinical evaluation. The current application and prospects of terbium radiopharmaceuticals are discussed in the next section.

Mild condition Radiolabelling with terbium radionuclides

To develop a radiolabelling protocol whereby mild temperatures and aqueous media can be used, a better understanding of the reactivity of various ligand systems for radiometal complexation is needed. Orvig *et al.* discussed the importance of metal-ligand thermodynamic stability and kinetic inertness of chelators *in vivo* (15). Macrocyclic ligands such as 1,4,7,10-tetraazacyclododecane-1,4,7,10-tetraacetic acid (more commonly known as DOTA) have rigid coordination geometries, which lowers the entropic loss of the metal coordination, which is more thermodynamically favoured. In contrast, the non-rigid

coordination with acyclic ligands, such as diethylenetriamine pentaacetate (commonly referred to as DTPA), undergoes significant geometric changes during complexation, drastically lowering the entropic loss, which is thermodynamically unfavourable and preferentially forming the more kinetic product. Moreover, the stability of the final complex is heavily influenced by parameters such as temperature and pH, and because of that, it is difficult to predict the biological stability.

Therefore, in our search for a mild temperature radiolabelling method, it was imperative to include both acyclic and cyclic ligands, as the labelling conditions will influence the final complex structure. Additionally, hybrid chelating agents, where both cyclic and acyclic coordination modes are available was of great interest to us, as they have fast reaction kinetics commonly associated with acyclic ligands, and the thermodynamic stability of cyclic ligands. Thus, in this study, three commercially available ligands, commonly used in nuclear medicine, and one non-commercial hybrid ligand were utilised in first instance.

DOTA, DOTA-GA (a glutaric acid derivative of DOTA), DTPA and 3p-C-NETA bifunctional chelators (isocyanate derivatives with no biomolecule attached) were investigated at 25 °C and 40 °C at a pH of 4.7, a pH commonly used in radiolabelling conditions with radiolanthanides (13,15). DOTA, DOTA-GA, DTPA and 3p-C-NETA isocyanate derivatives were successfully radiolabelled with ^{161}Tb at 25 °C in an aqueous buffered solution (0.1M sodium acetate, pH 4.7), generating the desired product in high conversion yields (90%). Increasing temperatures to 40 °C resulted in optimal conversion yields of >95% so that no further optimisation of the conditions was required. Prior to our protocol, the classical radiolanthanide labelling conditions used temperatures >80 °C in an aqueous solution at pH 4-6. Hens *et al.* did investigate radiolabelling DOTA and DTPA at 25 °C using ^{177}Lu (16); however, they were only able to achieve moderate radiochemical conversion yields of 73-86%. To the best of our knowledge, our protocol was the first reported result where quantitative Tb-radiolabelling of DOTA, DOTA-GA and 3p-C-NETA was performed in aqueous media at mild temperatures. Additionally, we were able to extend these radiolabelling conditions to biologicals, which have previously had not been possible. Moreover, ^{161}Tb-labelled biological constructs of DOTA, DOTA-GA and 3p-C-NETA containing human serum albumin (HSA) were found to be highly stable in mice, with no dissociation of the terbium.

However, this high stability was not observed with the ^{161}Tb-labelled DTPA-HSA construct, which demonstrated low *in vivo* stability. Previous studies suggest that some radiometals readily dissociate from DTPA in the presence of other binding agents (17). This behaviour is associated with the acyclic nature of DTPA, as it is known to prefer the formation of open metal complexes which leaves the metal exposed for competitive interactions with numerous nitrogen/oxygen rich molecules. However, it is important to note that many other acyclic compounds do not exhibit the same behaviour as the metal-ligand bonds formed require more energy to break them (15,18). Ligands such as the "-pa" family of compounds (H_2dedpa, H_4octapa, and H_5decapa, which were synthesised by Orvig *et al.* (19), **Figure 5.2**) encloses the metal centre and provides a high electron-rich environment, preventing transchelation with serum proteins. Macrocyclic ligands, such as "crown"-amines, have also shown promise in to stably

binding the radiometal, without the need for harsh radiolabelling conditions. These ligands, such as crown and macropa (20,21), have multiple oxygen donor atoms, which increase the bond strength to the radiometal. Additionally, these ligands have shown great stability with actinides, making them useful for situations where the same carrier is used for different applications, such as α- and β-therapy and PET/SPECT application. Other, more established ligands such as NOTA and NODA have not been directly labelled with ^{161}Tb but are part of hybrid systems and therefore their contribution cannot be isolated.

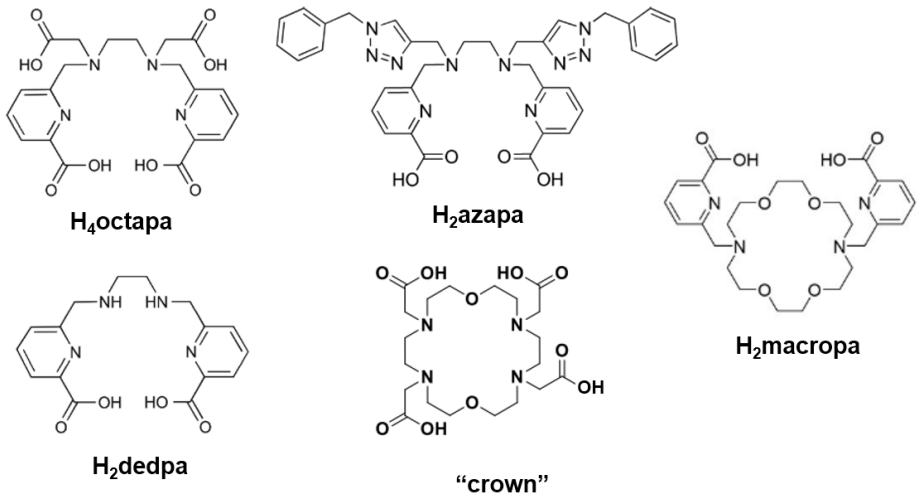


Figure 5.2. A small sample of ligands which have shown promise with lanthanide and actinide (18,19,21). Images used from original manuscripts without edit.

However, in our tests, we observed that DOTA, DOTA-GA and 3p-C-NETA were all compatible with our mild radiolabelling procedure. Of the three ligands tested, DOTA-GA was found to be the most economical ligand to use, since the compound can easily be obtained commercially, in contrast to 3p-C-NETA. DOTA-GA performed excellent in achieving the goals of our study, which was to form stable complexes at low temperatures. Therefore, based on the data we collected, DOTA-GA is the most suitable ligand for terbium, and lanthanides in general.

In recent years, more complex ligand systems, such as the previous discussed ligands in **Figure 5.2**, have been developed to overcome the high labelling temperature barrier (15,22). These ligands have not been evaluated here, as the goal was primarily to develop a protocol whereby the target compounds are easily attainable. Indeed, the complex synthetic pathways of these non-conventional ligands is an additional hurdle, especially if GMP implementation is required. It is also important to note that no pH stability was performed on the radiolabelled DOTA-GA complexes. Further, we have also not evaluated the influence of pH on radiochemical conversion. Hydrolysis of the terbium from $TbCl_3$ to $Tb(OH)_3$ occurs in the pH range 6-8. To the best of our knowledge, the pH dependency on radiolabelling with terbium has not been reported, therefore, further optimisation of our radiolabelling protocol is possible.

Towards using terbium radionuclide in theragnostics

Currently, there are very few true theragnostic radiopharmaceuticals used in a clinical setting. Often, a heteronuclear pairing of radiopharmaceuticals is used, which can potentially result in different biodistribution of the radiopharmaceutical, despite using the same vector molecule. For example, radiopharmaceuticals such as [^{177}Lu]Lu-PSMA-617 and [^{177}Lu]Lu-DOTA-TATE, are often paired with a ^{68}Ga-labelled analogues of the same or slightly different molecular structure, which have similar biodistribution profiles to the ^{177}Lu analogue (23–27). In other cases, a modification to the base molecule is necessary to counteract the effect on the biodistribution profile by changing the radionuclide. This is best demonstrated for radiopharmaceuticals targeting the chemokine receptor 4 (CXCR4). [^{68}Ga]Ga-Pentixafor is an established diagnostic radiopharmaceutical targeting CXCR4 (28), but the substitution of the ^{68}Ga with ^{177}Lu surprisingly resulted in a loss of affinity. Therefore, an iodine was incorporated in the structure, forming [^{177}Lu]Lu-Pentixather, to maintain the high binding affinity for CXCR4. However, this structural adjustment severely changes the pharmacokinetic profile of the radiopharmaceutical. And due to these changes in the pharmacokinetics, [^{177}Lu]Lu-Pentixather and [^{68}Ga]Ga-Pentixafor cannot be considered as a true theragnostic pair.

The main decay pathway of ^{161}Tb is via β^- decay which results in the emission of a β^- particle ($E(\beta^-)_{average}$ = 154 keV), which can be used for therapeutic applications. As both ^{161}Tb and ^{177}Lu are lanthanides which decay via β^- emission, ^{161}Tb is often compared or referenced to ^{177}Lu, which has become the gold standard for β^-- therapy. Additionally, the average beta energy of ^{177}Lu ($E(\beta^-)_{average}$ = 133 keV) is similar that of ^{161}Tb (10). Furthermore, both isotopes co-emit γ-rays, which have been used for whole-body SPECT/CT imaging of cancer patients (11,29,30). Of the terbium series, ^{161}Tb has been at the forefront to drive interest. This is largely due to the high production yields which can be achieved from an enriched ^{160}Gd precursor (31,32). ^{161}Tb is more biologically advantageous compared to ^{177}Lu, as it has been shown that ^{161}Tb has a greater therapeutic potential (6,33) in various studies. It is often speculated that this increased potential is due to the co-emission of ~2 Auger electrons per decay, which accounts for approximately 8.9 keV per decay (10). Additionally, the co-emission of 5 conversion electrons (total E_{e^-} = 31 keV) provide an even more potent dose to the targeted tumour. In preclinical studies, ^{161}Tb has shown to be more therapeutically efficient preclinically compared to ^{177}Lu. In the initial studies by Müller *et al.* with cm-09 (a folate-targeting carrier), [^{161}Tb]Tb-cm-09 was observed to be ~1.8 times more cytotoxic to IGROV-1 cells than [^{177}Lu]Lu-cm-09. In preclinical studies, it was also shown that animals treated with [^{161}Tb]Tb-PSMA-617 showed a greater effect on reducing tumour growth and rodent death than [^{177}Lu]Lu-PSMA-617 (34), speculating that the conversion/Auger electrons from ^{161}Tb decay contribute to cell death inducing effect. This was postulated to be due to the additional conversion/Auger electrons, which can deposit an additional total therapeutic energy per decay (Auger: 5.16 keV (88%); CE: 16.6 keV (41%), 40 keV (42%)) (10). Similarly, a patient was successfully treated with [^{161}Tb]Tb-

PSMA-617, after no response to [^{177}Lu]Lu-PSMA-617 treatment (**Figure 5.4**)(12). These findings have sparked a series of clinical trials using ^{161}Tb, namely the VIOLET trial (NCT05521412), which evaluates [^{161}Tb]Tb-PSMA-I&T in 24 participants as an potential alternative or replacement to [^{177}Lu]Lu-PSMA-617 (35).

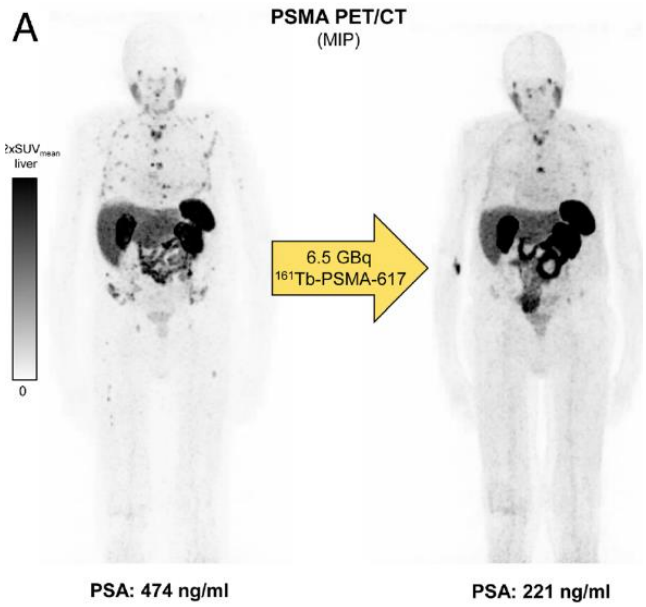


Figure 5.4. An 85-year old patient with advanced metastatic castration-resistant prostate cancer who showed a positive response to being treated with a single dose of 6.5 GBq of [^{161}Tb]Tb-PSMA-617. The patient was previously treated with 8 cycles of [^{177}Lu]Lu-PSMA-617, after which treatment showed no effect.

Though there are multiple studies showcasing the superiority of ^{161}Tb over ^{177}Lu, the claim that this is a result of the conversion and Auger electrons has only been researched computationally, and no empirical experiments have been conducted to understand the isolated contributions of these electrons to the overall therapeutic potential. To achieve this goal, the therapeutic effect was monitored by evaluating the cell response when ^{161}Tb was cell bound (or internalised) against non-cell bound ^{161}Tb. Comparing the therapeutic effect of the [^{161}Tb]Tb-DOTA-GA-v$_H$H (c-Met targeting) and [^{161}Tb]Tb-DOTA-GA-Mal (no-specific target) at radioactive concentrations below 1.25 MBq/mL, we observed a ~20% increase in the therapeutic effect from the targeted radiopharmaceutical. However, increasing the radioactive concentration above this threshold yielded negligible differences in the therapeutic effect. This result is in agreement with data obtained by Vermeulen *et al.*, where cell death by ^{153}Sm decay were independent of the carrier molecule (comparing [^{153}Sm]Sm-DOTA-TATE and [^{153}Sm]Sm-DTPA) (36). The results show that at high activities, the absorbed dose generated from conversion and Auger electrons is negligible compared to the reactive oxygen species (ROS, etc.) generated (37). Therefore to isolate the contribution from conversion and Auger electrons, another study was conducted using [^{161}Tb]Tb-PSMA-617, which is known to internalise into the cell. Alcocer-Ávila *et al.* calculated that a maximum absorbed dose (80%-90% of absorbed dose) was delivered inside the cell, and was therefore attributed

to the conversion/Auger electrons (10). Additionally, these calculations also showed that there is 3-4 times greater absorbed dose from ^{161}Tb, which concurred with the results obtained in both Müller studies (6,10,34). However, in order to take advantage of the Auger/conversion electrons, the radiometal needs to be as close to the target as possible. It was believed that internalisation was a requirement. This theory was debunked in the study by Müller *et al.,* whereby AR42 cells showed the similar response to SSTR-targeting agents which localised on either the cell membrane, cytoplasm/nucleus or cytoplasm only (38). This result changed the outlook of Auger/conversion electron-based therapies, which predominantly uses internalisation carrier molecules (39). In our study, we observed no isolated organelle damage leading to cell death, which was expected as most of the internal absorbed dose should be due to the conversion/Auger electrons. To confirm this, in future, collecting additional information by evaluating ^{111}In (Auger electron decay only) and ^{177}Lu (β^- decay) derivatives of the conjugates for comparison is necessary.

In our study, the experiments were conducted with a human c-MET expressing cell line. A common attribute of v_HH is renal clearance from plasma followed by renal retention, which could result in nephrotoxicity for a ^{161}Tb labelled v_HH, (40,41). Renal retention is often mitigated through megalin/cubilin receptor saturation through lysine or gelofusin pre-administration or co-infusion (42). In experiments in healthy mice using the ^{161}Tb-labelled half-life extended bivalent v_HH, moderate activity was found to accumulate in the kidneys, suggesting that renal retention might not be a problem in this case. In our tumour models with BxPC-3 cells, moderate tumour accumulation was observed over a 72-hour period post injection, with most of the activity cleared from the body via renal/urinary excretion. Further, the low abundance of γ-radiation from ^{161}Tb decay and low energy (<100 keV) makes it challenging to provide high resolution SPECT images. This was also illustrated in the study conducted by Müller and co-workers, where low resolution images of [^{161}Tb]Tb-cm09 were obtained (6). Novel developments in medical physics (e.g. optimisation of preclinical and clinical SPECT systems), might improve the quality of SPECT images in the future.

Finally, a way to obtain high contrast SPECT/CT images is to ensure a high concentration of the radiopharmaceutical at the tumour site and clearance from non-target tissue. Therefore, a higher apparent molar activity might be required to further increase the tumour uptake. A higher apparent molar activity ensures that a lower number of non-radioactive molecules are bound to targeted receptors, reducing the chance of receptor saturation and thus increasing non-bound radiopharmaceutical in circulation, which contributes to poor contrast between tumour and background. In this study conducted with anti-c-Met [^{161}Tb]Tb-v_HH, receptor saturation occurred with molar activities below 10 MBq/nmol. When molar activities above this threshold were utilised, higher *in vitro* binding was observed but this effect has not been evaluated in an *in vivo* setting.

In whole-body SPECT/CT acquisitions of patients, high contrast SPECT/CT images were obtained using molar activities between 10-14 MBq/nmol [^{161}Tb]Tb-DOTATOC in two patients with tumour metastases (11). Another possibility to increase tumour accumulation in a preclinical setting is to use cell lines which have higher receptor expression, as Tang *et al*. showcased in their studies targeting c-MET, where contrast was significantly better when using HepG2 (high c-Met receptor expression) compared to BxPC-3 (low c-Met receptor expression) (43).

Based on the evidence presented in this thesis, and the results of ^{161}Tb in (pre)clinical settings, we see a positive avenue for the integration of ^{161}Tb in the clinical radiopharmaceutical space. The latest advances in radiolabelling techniques (investigated and developed in Chapter 2), therapeutic profiling of ^{161}Tb in the radiolanthanide space (Chapter 3 and 4, results published by other authors) and the ongoing and future planned clinical trials with ^{161}Tb-radiopharmaceuticals form a great foundation for the promising and exciting future of terbium-based radiopharmaceuticals.

5.2 References

1. Lehenberger S, Barkhausen C, Cohrs S, Fischer E, Grünberg J, Hohn A, Köster U, Schibli R, Türler A, Zhernosekov K. The low-energy β - and electron emitter ^{161}Tb as an alternative to 177Lu for targeted radionuclide therapy. *Nucl Med Biol* (2011) **38**:917–924. doi:10.1016/j.nucmedbio.2011.02.007

2. Wharton L, McNeil SW, Merkens H, Yuan Z, Van de Voorde M, Engudar G, Ingham A, Koniar H, Rodríguez-Rodríguez C, Radchenko V, et al. Preclinical Evaluation of [155/161Tb]Tb-Crown-TATE—A Novel SPECT Imaging Theranostic Agent Targeting Neuroendocrine Tumours. *Molecules* (2023) **28**:3155. doi:10.3390/molecules28073155

3. Dellepiane G, Casolaro P, Favaretto C, Grundler P V., Mateu I, Scampoli P, Talip Z, van der Meulen NP, Braccini S. Cross section measurement of terbium radioisotopes for an optimized ^{155}Tb production with an 18 MeV medical PET cyclotron. *Appl Radiat Isot* (2022) **184**:110175. doi:10.1016/j.apradiso.2022.110175

4. Allen BJ, Goozee G, Sarkar S, Beyer G, Morel C, Byrne AP. Production of terbium-152 by heavy ion reactions and proton induced spallation. *Appl Radiat Isot* (2001) **54**:53–58. doi:10.1016/S0969-8043(00)00164-0

5. Lehenberger S, Barkhausen C, Cohrs S, Fischer E, Grünberg J, Hohn A, Köster U, Schibli R, Türler A, Zhernosekov K. The low-energy β − and electron emitter ^{161} Tb as an alternative to Lu for targeted radionuclide therapy. *Nucl Med Biol* (2011) **38**:917–924. doi:10.1016/j.nucmedbio.2011.02.007

6. Müller C, Reber J, Haller S, Dorrer H, Bernhardt P, Zhernosekov K, Türler A, Schibli R. Direct in vitro and in vivo comparison of ^{161}Tb and ^{177}Lu using a tumour-targeting folate conjugate. *Eur J Nucl Med Mol Imaging* (2014) **41**:476–485. doi:10.1007/s00259-013-2563-z

7. Müller C, Fischer E, Behe M, Köster U, Dorrer H, Reber J, Haller S, Cohrs S, Blanc A, Grünberg J, et al. Future prospects for SPECT imaging using the radiolanthanide terbium-155 - production and preclinical evaluation in tumor-bearing mice. *Nucl Med Biol* (2014) **41**:58–65. doi:10.1016/j.nucmedbio.2013.11.002

8. Müller C, Vermeulen C, Köster U, Johnston K, Türler A, Schibli R, van der Meulen NP. Alpha-PET with terbium-149: evidence and perspectives for radiotheragnostics. *EJNMMI Radiopharm Chem* (2016) **1**:2–6. doi:10.1186/s41181-016-0008-2

9. Müller C, Singh A, Umbricht CA, Kulkarni HR, Johnston K, Benešová M, Senftleben S, Müller D, Vermeulen C, Schibli R, et al. Preclinical investigations and first-in-human application of ^{152}Tb-PSMA-617 for PET/CT imaging of prostate cancer. *EJNMMI Res* (2019) **9**:1–10. doi:10.1186/s13550-019-0538-1

10. Alcocer-Ávila ME, Ferreira A, Quinto MA, Morgat C, Hindié E, Champion C. Radiation doses from ^{161}Tb and ^{177}Lu in single tumour cells and micrometastases. *EJNMMI Phys* (2020) **7**:33. doi:10.1186/s40658-020-00301-2

11. Baum RP, Singh A, Kulkarni HR, Bernhardt P, Rydén T, Schuchardt C, Gracheva N, Grundler P V., Köster U, Müller D, et al. First-in-human application of terbium-161: A feasibility study using 161Tb-DOTATOC. *J Nucl Med* (2021) **62**:1391–1397. doi:10.2967/jnumed.120.258376

12. Rosar F, Maus S, Schaefer-Schuler A, Burgard C, Khreish F, Ezziddin S. New Horizons in Radioligand Therapy. *Clin Nucl Med* (2023) **48**:433–434. doi:10.1097/RLU.0000000000004589

13. Kostelnik TI, Orvig C. Radioactive Main Group and Rare Earth Metals for Imaging and Therapy. *Chem Rev* (2019) **119**:902–956. doi:10.1021/acs.chemrev.8b00294

14. Grünberg J, Lindenblatt D, Dorrer H, Cohrs S, Zhernosekov K, Köster U, Türler A, Fischer E, Schibli R. Anti-L1CAM radioimmunotherapy is more effective with the radiolanthanide terbium-161 compared to lutetium-177 in an ovarian cancer model. *Eur J Nucl Med Mol Imaging* (2014) **41**:1907–1915. doi:10.1007/s00259-014-2798-3

15. Price EW, Orvig C. Matching chelators to radiometals for radiopharmaceuticals. *Chem Soc Rev* (2014) **43**:260–290. doi:10.1039/c3cs60304k

16. Hens M, Vaidyanathan G, Zhao XG, Bigner DD, Zalutsky MR. Anti-EGFRvIII monoclonal antibody armed with ^{177}Lu: In vivo comparison of macrocyclic and acyclic ligands. *Nucl Med Biol* (2010) **37**:741–750. doi:10.1016/j.nucmedbio.2010.04.020

17. Hijnen NM, de Vries A, Blange R, Burdinski D, Grüll H. Synthesis and in vivo evaluation of ^{201}Tl(III)-DOTA complexes for applications in SPECT imaging. *Nucl Med Biol* (2011) **38**:585–592. doi:10.1016/j.nucmedbio.2010.10.009

18. Price EW, Cawthray JF, Adam MJ, Orvig C. Modular syntheses of H4octapa and H2dedpa, and yttrium coordination chemistry relevant to86Y/90Y radiopharmaceuticals. *J Chem Soc Dalt Trans* (2014) **43**:7176–7190. doi:10.1039/c4dt00239c

19. Bailey GA, Price EW, Zeglis BM, Ferreira CL, Boros E, Lacasse MJ, Patrick BO, Lewis JS, Adam MJ, Orvig C. H2azapa: A versatile acyclic multifunctional chelator for 67Ga, 64Cu, 111In, and 177Lu. *Inorg Chem* (2012) **51**:12575–12589. doi:10.1021/ic302225z

20. Yang H, Zhang C, Yuan Z, Rodriguez-Rodriguez C, Robertson A, Radchenko V, Perron R, Gendron D, Causey P, Gao F, et al. Synthesis and Evaluation of a Macrocyclic Actinium-225 Chelator, Quality Control and In Vivo Evaluation of ^{225} Ac-crown-αMSH Peptide. *Chem – A Eur J* (2020) **26**:11435–11440. doi:10.1002/chem.202002999

21. Thiele NA, Brown V, Kelly JM, Amor-Coarasa A, Jermilova U, MacMillan SN, Nikolopoulou A, Ponnala S, Ramogida CF, Robertson AKHH, et al. An Eighteen-Membered Macrocyclic Ligand for Actinium-225 Targeted Alpha Therapy. *Angew Chemie - Int Ed* (2017) **56**:14712–14717.

doi:10.1002/anie.201709532

22. Wharton L, Kurakina E, Radchenko V, Schaffer P, Orvig C. Chemical Promiscuity of Non-Macrocyclic Multidentate Chelating Ligands for Radiometal Ions: H 4 neunpa-NH 2 vs H 4 noneunpa. *Inorg Chem* (2021) **60**:4076–4092. doi:10.1021/acs.inorgchem.1c00152

23. A.P. Breeman W, Sze Chan H, M.S. de Zanger R, K. Konijnenberg M, de Blois E. Overview of Development and Formulation of ^{177}Lu-DOTA-TATE for PRRT . *Curr Radiopharm* (2015) **9**:8–18. doi:10.2174/1874471008666150313111131

24. Banerjee SR, Kumar V, Lisok A, Chen J, Minn I, Brummet M, Boinapally S, Cole M, Ngen E, Wharram B, et al. ^{177}Lu-labeled low-molecular-weight agents for PSMA-targeted radiopharmaceutical therapy. *Eur J Nucl Med Mol Imaging* (2019) **46**:2545–2557. doi:10.1007/s00259-019-04434-0

25. Sartor O, Herrmann K. Prostate Cancer Treatment: ^{177}Lu-PSMA-617 Considerations, Concepts, and Limitations. *J Nucl Med* (2022) **63**:823–829. doi:10.2967/jnumed.121.262413

26. Emmett L, Willowson K, Violet J, Shin J, Blanksby A, Lee J. Lutetium 177 PSMA radionuclide therapy for men with prostate cancer: a review of the current literature and discussion of practical aspects of therapy. *J Med Radiat Sci* (2017) **64**:52–60. doi:10.1002/jmrs.227

27. Umbricht CA, Benešová M, Schmid RM, Türler A, Schibli R, van der Meulen NP, Müller C. ^{44}Sc-PSMA-617 for radiotheragnostics in tandem with ^{177}Lu-PSMA-617—preclinical investigations in comparison with ^{68}Ga-PSMA-11 and ^{68}Ga-PSMA-617. *EJNMMI Res* (2017) **7**:9. doi:10.1186/s13550-017-0257-4

28. Osl T, Schmidt A, Schwaiger M, Schottelius M, Wester HJ. A new class of pentixa for and pentixa ther-based theranostic agents with enhanced CXCR4-targeting efficiency. *Theranostics* (2020) **10**:8264–8280. doi:10.7150/thno.45537

29. Bailey DL, Hennessy TM, Willowson KP, Henry EC, Chan DLH, Aslani A, Roach PJ. In vivo quantification of ^{177}Lu with planar whole-body and SPECT/CT gamma camera imaging. *EJNMMI Phys* (2015) **2**:20. doi:10.1186/s40658-015-0123-2

30. Pathmanandavel S, Crumbaker M, Ho B, Yam AO, Wilson P, Niman R, Ayers M, Sharma S, Hickey A, Eu P, et al. Evaluation of ^{177}Lu-PSMA SPECT Quantitation as a Response Biomarker within a Prospective ^{177}Lu-PSMA-617 and NOX66 Combination Trial (LuPIN). *J Nucl Med* (2023) **64**:221–226. doi:10.2967/jnumed.122.264398

31. Cassells I, Ahenkorah S, Burgoyne AR, Van de Voorde M, Deroose CM, Cardinaels T, Bormans G, Ooms M, Cleeren F. Radiolabeling of Human Serum Albumin With Terbium-161 Using Mild Conditions and Evaluation of in vivo Stability. *Front Med* (2021) **8**:1–12. doi:10.3389/fmed.2021.675122

32. Rahman AKMR, Awal A. Production of ^{149}Tb, ^{152}Tb, ^{155}Tb and ^{161}Tb from gadolinium using

different light-particle beams. *J Radioanal Nucl Chem* (2020) **323**:731–740. doi:10.1007/s10967-019-06973-0

33. Gracheva N, Müller C, Talip Z, Heinitz S, Köster U, Zeevaart JR, Vögele A, Schibli R, Meulen NP Van Der. Production and characterization of no- carrier-added ^{161}Tb as an alternative to the therapy. *EJNMMI Radiopharm Chem* (2019) **4:12**:1–16.

34. Müller C, Umbricht CA, Gracheva N, Tschan VJ, Pellegrini G, Bernhardt P, Zeevaart JR, Köster U, Schibli R, van der Meulen NP. Terbium-161 for PSMA-targeted radionuclide therapy of prostate cancer. *Eur J Nucl Med Mol Imaging* (2019) **46**:1919–1930. doi:10.1007/s00259-019-04345-0

35. Al-Ibraheem A, Scott AM. ^{161}Tb-PSMA Unleashed: a Promising New Player in the Theranostics of Prostate Cancer. *Nucl Med Mol Imaging (2010)* (2023) **57**:168–171. doi:10.1007/s13139-023-00804-7

36. Vermeulen K, Van de Voorde M, Segers C, Coolkens A, Rodriguez Pérez S, Daems N, Duchemin C, Crabbé M, Opsomer T, Saldarriaga Vargas C, et al. Exploring the Potential of High-Molar-Activity Samarium-153 for Targeted Radionuclide Therapy with [153Sm]Sm-DOTA-TATE. *Pharmaceutics* (2022) **14**: doi:10.3390/pharmaceutics14122566

37. Milkovic L, Gasparovic AC, Cindric M, Mouthuy PA, Zarkovic N. Short overview of ROS as cell function regulators and their implications in therapy concepts. *Cells* (2019) **8**:1–14. doi:10.3390/cells8080793

38. Borgna F, Haller S, Monné JM, Mihaela R, Pascal G, Rijn J, Ulli Z, Roger K, Meulen NP Van Der, Müller C. Combination of terbium - 161 with somatostatin receptor antagonists — a potential paradigm shift for the treatment of neuroendocrine neoplasms. *Eur J Nucl Med Mol Imaging* (2022)1113–1126. doi:10.1007/s00259-021-05564-0

39. Ku A, Facca VJ, Cai Z, Reilly RM. Auger electrons for cancer therapy – a review. *EJNMMI Radiopharm Chem* (2019) **4**: doi:10.1186/s41181-019-0075-2

40. Gotthardt M, Van Eerd-Vismale J, Oyen WJG, De Jong M, Zhang H, Rolleman E, Maecke HR, Béhé M, Boerman O. Indication for different mechanisms of kidney uptake of radiolabeled peptides. *J Nucl Med* (2007) **48**:596–601. doi:10.2967/jnumed.106.036020

41. Ma J, Li L, Liao T, Gong W, Zhang C. Efficacy and Safety of ^{225}Ac-PSMA-617-Targeted Alpha Therapy in Metastatic Castration-Resistant Prostate Cancer: A Systematic Review and Meta-Analysis. *Front Oncol* (2022) **12**: doi:10.3389/fonc.2022.796657

42. Tchouate Gainkam LO, Caveliers V, Devoogdt N, Vanhove C, Xavier C, Boerman O, Muyldermans S, Bossuyt A, Lahoutte T. Localization, mechanism and reduction of renal retention of technetium-99m labeled epidermal growth factor receptor-specific nanobody in mice. *Contrast Media Mol Imaging* (2011) **6**:85–92. doi:10.1002/cmmi.408

43. Tang Y, Xu H, Dai Y, Wang F, Huang W, Liu P, Gu Y. A novel peptide targeting c-Met for hepatocellular carcinoma diagnosis. *J Mater Chem B* (2021) **9**:4577–4586. doi:10.1039/d1tb00408e

Summary

Targeted radionuclide therapy (TRNT) has been a growing field in nuclear medicine for the past decade. Therapeutic radioisotopes which decay via alpha, beta, or Auger/conversion electron (A/CE) emission have emerged as viable treatment strategies for cancer. Radiopharmaceuticals such as Xofigo® ($^{223}RaCl_3$) and Pluvicto™ ([^{177}Lu]Lu-DOTA-PSMA-617) have shown evidence of TRNT being an effective way to treat cancer. Additionally, radiopharmaceuticals with β^+ or gamma-emitting isotopes can be used to visualise cancers non-invasively through imaging techniques such as single photon emission computed tomography (SPECT) and positron emission tomography (PET). To ensure that diagnostic and therapeutic radiopharmaceuticals have the same biodistribution and pharmacokinetics, homonuclear pairings (same element, different isotope) for diagnostic and therapeutic applications are best suited. One of the most promising homonuclear pairings is terbium, which has four medically interesting isotopes (^{149}Tb, ^{152}Tb, ^{155}Tb and ^{161}Tb) which span the entire radiopharmaceutical space (TRNT, PET and SPECT imaging).

The carrier molecule plays a vital role in the pharmacokinetics of the radiopharmaceutical. For a carrier molecule to be suitable for TRNT, it needs to bind with a high affinity and selectivity to the molecular target expressed on tumour cells. Ideally, these targets should be present only in the cancer cells to avoid off-target binding and potential adverse effects. Antibody-based carriers have high selectivity and affinity for their biological target, which limits off-target binding, limiting potential radiotoxicity. However, antibody-based carriers are mostly sensitive to temperature and harsh chemical conditions required for radiolabelling, making it a challenge to use them for TRNT applications. In the second chapter, we focussed on developing a terbium labelling method that is compatible with sensitive carriers such as antibody-based compounds, as current reported labelling methods require elevated temperatures (>80 °C) and harsh conditions. Chelating compounds *p*-SCN-Bn-CHX-A´´-DTPA, *p*-SCN-Bn-DOTA, *p*-NCS-Bz-DOTA-GA and *p*-SCN-3*p*-C-NETA were conjugated to human serum albumin (HSA), the most abundant protein in blood, via a lysine coupling method. All HSA-constructs were labelled with [^{161}Tb]$TbCl_3$ at 40 °C with radiochemical yields greater than 98%. The radiolabelled constructs were stable in human serum for at least 24 hours at 37 °C in PBS. The labelled ^{161}Tb-HSA-constructs were injected in mice to evaluate their *in vivo* stability. Increasing bone accumulation as a function of time was observed for [^{161}Tb]$TbCl_3$ and [^{161}Tb]Tb-DTPA-CHX-A´´-Bn-HSA, while negligible bone uptake was observed with the DOTA, DOTA-GA and NETA variants over a 7-day period. Increasing uptake in the liver was also identified as a feature of dissociation of ^{161}Tb from the HSA construct, which was observed with [^{161}Tb]Tb-DTPA-CHX-A´´-Bn-HSA. The results indicate that the *p*-SCN-Bn-DOTA, *p*-NCS-Bz-DOTA-GA and *p*-SCN-3*p*-C-NETA are suitable bifunctional ligands for Tb-based radiopharmaceuticals, allowing for high yield radiolabelling in mild conditions.

Based on the availability and stability of the [^{161}Tb]Tb-DOTA-GA-Bz-*p*-NCS construct, we extended our work by using the bifunctional chelator maleimide-DOTA-GA in combination with smaller biologicals. Combining this bifunctional chelator with a single domain heavy-chain antigen fragment (v_HH) as a carrier molecule can be a promising approach for highly specific and selective targeting of cancer cells. In the third chapter we focussed on the preclinical evaluation of a terbium-161 labelled half-life extended anti-c-Met nanobody. c-Met is a mesenchymal-epithelial transition factor which is responsible for migration and is upregulated in many cancers such as pancreatic and liver cancers. Terbium-161 was successfully coupled to a half-life extended anti-c-Met v_HH with the introduction of a DOTA-GA moiety at the *C*-terminal of the v_HH. *In vitro* studies showed a clear inverse proportionality between the applied activity and cell viability. The effect was observed with both a directing (anti-c-Met v_HH) and non-directing (DOTA-GA-Mal) moiety, suggesting non-specific binding related radiotoxicity effects dominate the efficacy of ^{161}Tb TRNT in cell culture. Furthermore, it suggests that having the terbium near the target will produce a response, and the directing group only serves to get the terbium at a high concentration close to the target cells *in vivo*. In a healthy mouse model, we observed uptake in the kidneys, an organ known to have high uptake and retention of v_HH. Additionally, the [^{161}Tb]Tb-DOTAGA-v_HH construct was observed to circulate for 24 hours before complete expulsion from the bloodstream. This is a shorter circulation time than the radiolabelled HSA compounds in the previous section, which suggests that the pharmacokinetic profile can be tuned for v_HH-based radiopharmaceuticals. In tumour mouse models, we observed good tumour accumulation, even after 7 days p.i. μSPECT studies were possible by detection of the low energy γ of ^{161}Tb, which makes dosimetric follow-up possible after administration of a single dose of the therapeutic ^{161}Tb radiopharmaceutical.

Auger electron emitters, which emit low-energy electrons, deposit a high dose of energy (4−26 keV/μm) over a very short distance (0.1-5.0 μm), and can be advantageous isotopes in the therapeutic space, as there short range limit off-target radiation to healthy tissues during *in vivo* circulation and accumulation in tumour tissue. Many isotopes that do emit Auger electrons are currently used in SPECT (single photon emission computed tomography) applications, such as ^{99m}Tc (E_e- = 14-18 keV), as they co-emit gamma energies suitable for imaging. ^{161}Tb (β^- emitter, $t_{1/2}$ = 6.95 days) emits two Auger and five conversion electrons (total E_{e^-} ~ 36 keV) in addition to its main β^- decay. In our study, we are interested in understanding the contribution of the conversion and Auger electrons to the therapeutic efficacy of ^{161}Tb. To evaluate this, we designed dual-targeting radio-conjugates consisting of a PSMA binding motive and a triphenyl phosphonium (TPP) group to selectively bind to cancer cells expressing PSMA and promote intracellular accumulation in the mitochondria after the radio-conjugate is internalised. Radiolabelling of the PSMA constructs with [^{161}Tb]$TbCl_3$ was successful and the constructs remained stable for at least 48 hours in cell culture medium. We investigated the mitochondrial uptake and the effect on cell viability. Subcellular uptake studies showed marginal uptake in the mitochondria, regardless of the addition of the TPP moiety. The [^{161}Tb]Tb-TPP construct showed a greater radiocytotoxic effect on the cells than the ^{161}Tb construct not containing a TPP group. Though we did observe a decrease in cell viability, this was not a result of mitochondria damage from the low energy

conversion and Auger electrons emitted from the ^{161}Tb, and potentially an effect of TPP directing post internalisation. In addition, the TPP group did not play a role in the biodistribution of the construct, which was determined by μSPECT/CT studies using ^{111}In-labelled derivatives of the constructs. Constructs were found to be excreted rapidly through the renal tract, which is a favourable pharmacokinetic parameter for future nuclear medicine applications.

Samenvatting

Doelgerichte radionuclidetherapie heeft de afgelopen tien jaar een groei gekend in het domein van de nucleaire geneeskunde. Therapeutische radio-isotopen die vervallen via alfa-, bèta- of Auger/conversie-elektronenemissie (A/CE) zijn veelbelovende behandelingsstrategieën voor kanker. Radiofarmaca zoals Xofigo® ($^{223}RaCl_3$) en Pluvicto™ ([^{177}Lu]Lu-DOTA-PSMA-617) hebben aangetoond dat doelgerichte radionuclide therapie een effectieve manier is om kanker te behandelen. Bovendien kunnen radiofarmaca ook gebruikt worden om kankers niet-invasief te visualiseren door middel van beeldvormingstechnieken zoals computertomografie met enkelvoudige fotonemissie (SPECT) en positronemissietomografie (PET). Om ervoor te zorgen dat diagnostische en therapeutische radiofarmaca dezelfde biodistributie en farmacokinetiek hebben, zijn homonucleaire paren (hetzelfde element, verschillende isotoop) voor diagnostische en therapeutische toepassingen het meest geschikt. Een van de meest veelbelovende homonucleaire paren is terbium, dat vier medisch interessante isotopen heeft (^{149}Tb, ^{152}Tb, ^{155}Tb en ^{161}Tb).

Het vectormolecuul speelt een belangrijke rol in de farmacokinetiek van het radiofarmaceutisch preparaat. Het vectormolecuul moet met een hoge affiniteit en selectiviteit binden aan het moleculaire doelwit dat tot expressie komt op tumorcellen. Idealiter zijn deze doelwitten alleen in de kankercellen aanwezig zodat off-target binding en toxische effecten voorkomen kunnen worden. Op antilichaam gebaseerde vectormoleculen hebben meestal een hoge selectiviteit en affiniteit voor hun biologische doelwit, wat off-target binding beperkt en waardoor potentiële radiotoxiciteit wordt vermeden. Echter, biomolecules zoals antilichamen zijn meestal gevoelig voor hoge temperatuur dat nodig is voor efficiënte merking, waardoor het een uitdaging is om ze efficiënt te gebruiken.

In het tweede hoofdstuk was het doel een generische merkingsmethode te ontwikkelen voor terbium isotopen die compatibel is met hittegevoelige vectormoleculen zoals antilichamen. De bifunctionele liganden p-SCN-Bn-CHX-A''-DTPA, p-SCN-Bn-DOTA, p-NCS-Bz-DOTA-GA en p-SCN-3p-C-NETA werden via een lysinekoppelingsmethode geconjugeerd aan humaan serumalbumine (HSA), het meest voorkomende eiwit in het bloed. Alle HSA-constructen werden gemerkt met [^{161}Tb]$TbCl_3$ bij 40 °C met radiochemische opbrengsten van meer dan 98%. De radioactief gemerkte constructen waren stabiel in humaan serum gedurende ten minste 24 uur bij 37 °C. Vervolgens werden de gemerkte ^{161}Tb-HSA-constructen geïnjecteerd in muizen om hun *in vivo* stabiliteit te evalueren. Toenemende botaccumulatie als functie van de tijd werd waargenomen voor [^{161}Tb]$TbCl_3$ en [^{161}Tb]Tb-DTPA-CHX-A''-Bn-HSA, terwijl een verwaarloosbare botopname werd waargenomen met de DOTA-, DOTA-GA- en NETA-varianten gedurende een periode van 7 dagen. Toenemende opname in de lever werd ook geïdentificeerd als een kenmerk van dissociatie van ^{161}Tb van het HSA-construct, wat werd waargenomen met [^{161}Tb]Tb-DTPA-CHX-A''-Bn-HSA. De resultaten geven duidelijk aan dat p-SCN-Bn-CHX-A''-DTPA niet geschikt is als

ligand maar dat p-SCN-Bn-DOTA, p-NCS-Bz-DOTA-GA en p-SCN-3p-C-NETA geschikte bifunctionele liganden zijn voor de bereiding van terbium gemerkte radiofarmaceutische preparaten.

In het derde hoofdstuk werd de geoptimaliseerde merkingsmethode voor terbiumisotopen gebruikt voor het merken van een nanobody. Het nanobody heeft een verlengde half-waarde tijd en vergelijking met standaard nanobodies en is gericht tegen het moleculaire doelwit c-MET. c-MET is een mesenchymale-epitheliale overgangsfactor die verantwoordelijk is voor migratie en het komt tot over-expressie bij veel kankers, zoals pancreas- en leverkanker. Het construct werd succesvol gemerkt met terbium-161 en *in vitro* studies toonden aan dat hoe hoger de activiteit dat werd toegediend aan de cellen, hoe groter de cel sterfte. De cel sterfte werd echter ook waargenomen met controle constructen die niet binden aan cMET wat suggereert dat niet-specifieke radiotoxiciteits effecten de werkzaamheid *in vitro* domineren.

In gezonde muizen observeerden we een klaring en retentie in de nieren, wat een gekend profiel is voor nanobodies. Zoals verwacht werd een verlengde biologische half-waarde tijd waargenomen in vergelijking met standaard nanobodies. In tumormuizen zagen we een goede tumoraccumulatie, zelfs 7 dagen na injectie. Dit werd bevestigd met behulp van µSPECT-studies en toont aan dat de nieuwe constructen veelbelovend zijn voor de behandeling van gemetastaseerde tumoren.

Auger-elektronenstralers, die laag-energetische elektronen uitzenden, deponeren een hoge dosis energie (4−26 keV/µm) over een zeer korte afstand (0,1-5,0 µm). Dit kan voordelig zijn om off-target bestraling van gezonde weefsels te vermijden. Veel isotopen die Auger-elektronen uitzenden, worden momenteel gebruikt in SPECT-toepassingen, een voorbeeld hiervan is ^{99m}Tc (E_e- = 14-18 keV). ^{161}Tb (β-emitter, $T_{1/2}$ = 6,95 dagen) zendt ook twee Auger/conversie-elektronen (Ee- ~ 9 keV) uit.

In hoofdstuk 4 was het doel de bijdrage van Auger-elektronen te bepalen in functie van de totale therapeutische werkzaamheid van terbium-161. Om dit te evalueren werden dual-targeting radioconjugaten ontworpen die enerzijds bestaan uit een PSMA-bindend motief, om selectief te binden aan prostaat kankercellen die PSMA tot expressie brengen, en anderzijds uit een trifenylfosfonium (TPP)-groep om intracellulaire accumulatie in de mitochondriën te bevorderen. Merking van de PSMA-constructen met [^{161}Tb]$TbCl_3$ was succesvol en de constructen waren ten minste 48 uur stabiel. De opname in de mitochondriën en het effect op de levensvatbaarheid van cellen werd vervolgens onderzocht. Subcellulaire opnamestudies toonden beperkte opname in de mitochondriën, ongeacht de aanwezigheid van de TPP-groep. Het terbium-161 gemerkte construct met TPP vertoonde echter een groter radiocytotoxisch effect op de cellen dan het ^{161}Tb-construct dat geen TPP-groep bevatte. Bijkomende studies zijn noodzakelijk om dit effect te verklaren. Tenslotte toonden µSPECT-CT studies aan dat de incorporatie van de TPP groep geen grote effecten had op de farmacokinetiek van het radiofarmaceutisch preparaat. Alle constructen vertoonden een gunstige biologische distributie met renale klaring.



Curriculum Vitae

Personal Details

Full Name:	Irwin Cassells
Contact Details:	irwincassells@gmail.com
Date of Birth:	08 April 1992
Sex:	Male
Nationality:	South African
Residency:	United Kingdom
Languages:	English, Afrikaans

Specific Skills

Analytical Techniques

- Homo- and heteronuclear magnetic resonance (NMR) spectroscopy
- Infrared (IR) spectroscopy
- Mass spectrometry
- XRD analysis
- Gamma spectroscopy
- HPLC (gamma, size exclusion, normal and reverse phase, method development)
- SPECT imaging

Chemistry and Biology

- Radiochemical synthesis and method development (^{11}C, ^{18}F, radiometals)
- Chemical synthesis (organic, inorganic, coordination, organometallic, bioconjugation)
- Production of PET isotopes form cyclotron (GE PETtrace)
- Cell culturing
- Human and cell biological assays (cell proliferation, cell survival, cell and cell organelle uptake, apoptosis, Western blot)
- FELASA B certification, L/E1 PIL ABC (rodent)
- *Ex vivo* and *in vivo* biodistribution

Statistical Analysis

- Standard error and uncertainty estimation
- Regression analysis
- Optimisation and simulation
- Curve-fitting and structural equation modelling
- Data visualisation
- Monte-Carlo simulation

Computer Literacy

- Microsoft Office (Word, Excel, Access, Outlook, OneNote, SharePoint, Automate)
- Object-oriented programming (vPython, MATLAB/Octave, R, Shiny, C#, VBA)
- Other programming (SQL (mySQL, bigQuery, Oracle), gnuPlot, task scheduler and .bat commands for automation)
- Typesetting languages ($LaTeX$, Markdown)
- Chemical, biological and statistical programming (GraphPad Prism, ChemOffice Suite, MestreNova, Topspin, ACD Labs Suite)

Tertiary Education

Institution:	Katholieke Universiteit Leuven
Period:	2018-present
Degree:	PhD Pharmaceutical and Pharmacological Sciences

Institution:	University of Cape Town
Period:	2015-2016
Degree:	MSc Chemistry (w/ Distinction)
Awards:	NRF Scarce Skills Scholarship (2015-2016)

Institution:	University of Cape Town
Period:	2014
Degree:	BSc Chemistry (Hons)
Awards:	NSFAS Post-Graduate Bursary (2014), SASOL Inzalo Foundation Scholarship (2014), Harry Crossley Foundation Post-Graduate Scholarship (2014)

Institution:	University of Cape Town
Period:	2010-2013
Degree (Majors):	BSc (Chemistry)
Extra-curricular:	Township Debating League (TDL) Trainer and Adjudicator (2010)
Awards:	UCT Science Entrance Scholarship (2010), UCT Merit/Achievement Award (2010), SASOL Inzalo Foundation Scholarship (2010-2013), Dean's Merit List (2011), NSFAS Bursary (2013).

Published Work

Publications

Year:	2024

Authors:	J. F. Santos, M. T. Braz, P. Raposinho, F. Cleeren, **I. Cassells**, S. Leekens, C. Cawthorne, F. Mendes, C. Fernandes, and A. Paulo*
Title:	Synthesis and Preclinical Evaluation of PSMA-Targeted 111In-Radioconjugates Containing a Mitochondria-Tropic Triphenylphosphonium Carrier
Journal:	Molecular Pharmaceutics

Year:	2021
Authors:	**I. Cassells**, S. Ahenkorah, A. R. Burgoyne, M. Van De Voorde, C. M. Deroose, T. Cardinaels, G. Bormans, M. Ooms and F. Cleeren
Title:	Radiolabeling of human serum albumin with terbium-161 using mild conditions and evaluation of in vivo stability
Journal:	Frontiers in Medicine

Year:	2021
Authors:	S. Ahenkorah, **I. Cassells**, C. M. Deroose, T. Cardinaels, A. R. Burgoyne, G. Bormans, M. Ooms and F. Cleeren
Title:	Bismuth-213 for Targeted Radionuclide Therapy: From Atom to Bedside
Journal:	Pharmaceuticals

Year:	2018
Authors:	**I. Cassells**, T. Stringer, A. T. Hutton, S. Prince, G.S. Smith
Title:	Impact of various lipophilic substituents on ruthenium(II), rhodium(III) and iridium(III) salicylaldimine-based complexes: synthesis, in vitro cytotoxicity studies and DNA interactions
Journal:	Journal of Biological Inorganic Chemistry

Year:	2015
Authors:	E. Ekengard, L. Glans, **I. Cassells**, T. Fogeron, P. Govender, T. Stringer, P. Chellan, G. C. Lisensky, W. H. Hersh, I. Doverbratt, S. Lidin, C. de Kock, P. J. Smith, G. S. Smith and E. Nordlander
Title:	Antimalarial activity of ruthenium(II) and osmium(II) arene complexes with mono- and bidentate chloroquine analogue ligands
Journal:	Dalton Transactions

Conference Participations

Year:	2022

Type:	Poster Presentation
Event:	Terachem 2022
Title:	Evaluating the in vivo distribution and stability of a ^{161}Tb-labelled Nanobody® for potential cancer therapy
Location:	Bressanone, Italy
Year:	2022
Type:	Poster Presentation
Event:	iSRS 2022
Title:	Mild condition radiolabelling and in vivo stability of Nanobody® constructs with terbium-161 and terbium-155
Location:	Nantes, France
Year:	2020
Type:	Oral Presentation
Event:	EANM 2020
Title:	Tb-IRMA-V: Low temperature radiolabelling of human serum albumin constructs with terbium-161 and ex vivo biodistribution to assess in vivo stability
Location:	Online
Year:	2020
Type:	Oral Presentation
Event:	NRKV Eindhoven 3
Title:	Tb-IRMA-V: Radiolabelling of human serum albumin constructs with ^{161}Tb as a framework for sensitive peptide configurations
Location:	Eindhoven, The Netherlands
Year:	2019
Type:	Poster Presentation
Event:	MedChem2019
Title:	Tb-IRMA-V: Radiolabelling of human serum albumin constructs with ^{161}Tb as a framework for sensitive peptide configurations
Location:	Brussels, Belgium
Year:	2019
Type:	Poster Presentation
Event:	Metals in Medicine
Title:	Tb-IRMA-V: Radiolabelling of heat-sensitive molecules bearing macroor acyclic ligands with ^{161}Tb
Location:	Paris, France
Year:	2019
Type:	Oral Presentation

Event:	Medicis ProMed Conference
Title:	Tb-IRMA-V: Towards the labelling of heat-sensitive biomolecules with terbium radionuclides: Chelation studies of DOTA-NHS with natural Tb and ^{161}Tb
Location:	Erice, Italy
Year:	2016
Type:	Poster Presentation
Event:	8th International Symposium of Bio-organometallic Chemistry
Title:	Synthesis and Biological Evaluation of PGM Complexes Based on Derivatised PTA Scaffolds
Location:	Moscow, Russia

Dissertations

Year:	2015-2016
Degree:	MSc
Supervisor(s):	Assoc. Prof. G. S. Smith, Assoc. Prof. A. T. Hutton, Assoc. Prof. S. Prince, Dr T. Stringer
Title:	Synthesis and Biological Evaluation of PGM Complexes Based on Derivatised PTA Scaffolds
Year:	2014
Degree:	B. Sc (Hons)
Supervisor(s):	Assoc. Prof. G. S. Smith, Assoc. Prof. A. T. Hutton
Title:	A Study Towards the Synthesis, Characterisation and Electrochemical Nature of Homo- and Heterometallic Ferrocenyl-derived Dendrimers

Summary of Work Experience

Company:	King's College London
Department:	Imaging Chemistry and Biology
Supervisor:	Antony Gee
Role:	Research Associate
Period:	2023 - present
Company:	Media24
Department:	Customer insights
Supervisor:	JanDirk Engelbrecht
Role:	Data Analyst
Period:	2017 - 2018
Company:	Permoseal

Department:	Customer Services: Laboratory
Supervisor:	Paul Jacobs
Role:	Product Developer
Period:	2017

Company:	University of Cape Town
Department:	Department of Chemistry (Organometallics Research Group)
Supervisor:	Gregory Smith
Role:	Research Assistant (chemistry)
Period:	2011-2014

Referees

Full Name:	Prof. Antony Gee
Relationship:	Manager (Principal Investigator, King's College London)
Contact Information:	+44 20 7188 8366 (work)
	antony.gee@kcl.ac.uk

Full Name:	Prof. Frederik Cleeren
Relationship:	PhD Supervisor (KU Leuven)
Contact Information:	+32 16 37 72 37 (work)
	frederik.cleeren@kuleuven.be

Full Name:	Dr Maarten Ooms
Relationship:	PhD Supervisor (SCK CEN)
Contact Information:	+32 14 33 32 83 (work)
	maarten.ooms@sckcen.be

Full Name:	Prof. Guy Bormans
Relationship:	PhD Supervisor (KU Leuven)
Contact Information:	+32 16 33 04 47 (work)
	guy.bormans@kuleuven.be